DISSERTATION

Search for Standard Model $H \to \tau^+\tau^-$ Decays in the Lepton–Hadron Final State in Proton–Proton Collisions with the ATLAS Detector at the LHC

Nils Ruthmann

Fakultät für Mathematik und Physik
Albert-Ludwigs-Universität Freiburg

Search for Standard Model $H \rightarrow \tau^+\tau^-$ Decays in the Lepton–Hadron Final State in Proton–Proton Collisions with the ATLAS Detector at the LHC

Dissertation
zur Erlangung des Doktorgrades der
Fakultät für Mathematik und Physik der

Albert-Ludwigs-Universität
Freiburg im Breisgau

vorgelegt von
Nils Ruthmann

Oktober 2014

Dekan: Prof. Dr. Kröner
Betreuer der Arbeit: Prof. Dr. Karl Jakobs
Prüfer: Prof. Dr. Karl Jakobs
Prof. Dr. Markus Schumacher
Prof. Dr. Stefan Dittmaier

Datum der mündlichen Prüfung:
18. Dezember 2014

Contents

Introduction

To gain insight into what constitutes matter and to understand the dynamics of interactions between these building blocks is one of the oldest questions in fundamental science. The elementary particles as known today interact by means of four distinct forces, namely the weak, electromagnetic, strong and gravitational force. Throughout the 1960's a unified description of the electromagnetic and weak interactions was established by Glashow, Salam and Weinberg. Along with a model of the strong interaction, it forms the core of the modern description of elementary particle physics, also known as the Standard Model (SM). With the exception of gravity, for which no consistent quantum theory has been established yet, the SM describes accurately nearly all known particle physics phenomena. A successful demonstration of the predictive power of the SM and its theoretical consistency was the prediction of several previously unknown particles which were subsequently experimentally discovered. The last particle in this series is the Higgs boson, which plays a crucial role in the electroweak theory.

The theoretical foundation for the description of the dynamical structure of the electroweak and strong interactions is the so-called gauge symmetry. In its version without a Higgs field, the electroweak theory describes the interaction between massless matter particles, called fermions, by the exchange of massless force mediators, called gauge-bosons. The gauge-bosons of the weak interaction, the $W^{\pm}$ and Z bosons, are experimentally well understood and their masses are a multitude larger than the mass of an electron or even a proton. The description of massive gauge-bosons though would violate the gauge-symmetry, and thus the foundation of the theory. This contradiction is solved by the Higgs mechanism, which modifies the theory by introducing the Higgs field. While the gauge-symmetry of the theory stays intact, the weak gauge-bosons as well as the fermions obtain their masses through interactions with the Higgs field. As a consequence, the existence of a Higgs boson is predicted. The Higgs boson interacts with all massive particles of the SM. The corresponding coupling strengths are predicted by the theory once the Higgs boson mass, m_H, is determined by experiment.

Despite the large experimental effort put into the search for the Higgs boson, no evidence for its existence was found until 2012, when the *ATLAS* [1] and *CMS* [2] experiments at the Large Hadron Collider (LHC) at CERN discovered a particle consistent with the expectations for a SM Higgs boson with a mass of approximately

---

[1] **A** **T**oroidal **L**HC **A**pparatu**S**

[2] **C**ompact **M**uon **S**olonoid

$m_H \approx 125$ GeV. The LHC is a particle accelerator, colliding protons at centre-of-mass energies of up to $\sqrt{s} = 14$ TeV in order to study fundamental particle interactions at the high-energy frontier. It started operation in 2009 and in its first years of running it already delivered collision data corresponding to integrated luminosities of up to 5.5 fb^{-1} at $\sqrt{s} = 7$ TeV and 22.8 fb^{-1} at $\sqrt{s} = 8$ TeV to the experimental collaborations. Four large detectors, among them the two general-purpose experiments ATLAS and CMS, record the particles which emerge from the p-p collisions, in order to reconstruct the scatter events between the protons' constituents. Following the discovery of the new boson in its decay modes to pairs of photons, Z and W bosons, the focus of the experiments lies on identifying the particle with the Higgs boson of the SM by verifying as many predictions made by the theory as experimentally accessible. Besides the determination of the spin and CP quantum numbers, especially the measurement of the coupling strength of the particle to fermions plays a crucial role in this step. While the coupling between the Higgs boson and gauge-bosons is determined by the gauge-structure, the coupling to fermions is described by so-called Yukawa couplings. A direct observation and measurement of these Yukawa couplings therefore provides crucial information about the mechanism responsible for the fermion mass generation. Higgs boson decays into a pair of tau leptons provide one of the most promising decay channels to observe these couplings. Since tau leptons decay further into either leptons or hadrons, three distinct final states emerge from $H \to \tau\tau$ decays and the lepton-hadron final state ($H \to \tau\tau \to (\tau_{\text{had}}\nu)(\ell\nu\nu)$) accounts for approximately 46% of all decays.

This thesis presents a search for $H \to \tau\tau$ decays in the lepton-hadron final state with the ATLAS detector, and was optimised, implemented and carried out in collaboration with the ATLAS experiment in the course of this thesis. In this search, a multivariate classification algorithm is trained to discriminate signal-like from background-like events and provides a significant sensitivity improvement with respect to previous analyses of the same final state. The structure of the thesis follows the logical order of the analysis. Chapter 1 gives a brief theoretical introduction into the SM and into the phenomenological aspects of Higgs boson searches. In Chapters 2 and 3 the LHC and the ATLAS experiment are introduced and an overview of the particle and event reconstruction is given. Since sizeable systematic uncertainties arise from the reconstruction of hadronic tau decays, dedicated studies towards a better understanding of the tau-energy scale were carried out and are presented in Chapter 4. Chapter 5 finally presents the analysis strategy with a focus on the methodology employed to separate signal from background events. In Chapter 6, the statistical methods used to interpret the results of the analysis are introduced and the results are presented. As similar analyses are carried out by the ATLAS collaboration in the fully leptonic and fully hadronic final states, a combination of all $H \to \tau\tau$ search channels is performed and presented in Chapter 7.

1 Theoretical Overview

This chapter briefly introduces the structure of the Standard Model (SM) of particle physics. Being the framework of high energy physics phenomenology, it provides the theoretical foundation for predictions to be probed in the experimental context. Throughout Section 1.1 the particle content and the interactions of the SM are described with an emphasis on the electroweak symmetry breaking mechanism and the Higgs boson. Section 1.2 gives an overview of the phenomenology and the tools and concepts used in the simulation of proton-proton collisions. A summary of the most important Higgs boson production mechanisms at the LHC and its decay modes is given in Section 1.3. The chapter closes with a brief overview of the experimental status of Higgs boson searches in ditau final states.

1.1. The Standard Model of Particle Physics

The Standard Model of Particle Physics evolved throughout the 20th century due to a fertile interplay between fundamental theoretical developments and experimental input guiding the way. It consists of a gauge theory of strong interactions, called quantum chromodynamics (QCD) [1–3] and a unified theory of electromagnetism and the weak interaction based on a spontaneously broken gauge symmetry completed in the 1960's by Glashow, Salam and Weinberg [4–6]. It was the description of a symmetry breaking mechanism that allowed for constructing a theory of massive weak vector bosons using the theoretically attractive and successful gauge theories. This spontaneous symmetry breaking mechanism described by Brout, Englert [7], Higgs [8, 9] and Guralnik, Hagen, Kibble [10] will be denoted as *Higgs mechanism* throughout this thesis. Since then, the SM has proven to be a highly predictive theory as it not only correctly predicted the existence of the b-quark [11, 12], the top quark [13, 14] and the τ neutrino [15] but is also able to correctly predict interaction rates at high precision. It further predicts the existence of a scalar particle, the *Higgs boson*, whose mass is one of the 19 free parameters of the SM. Experimental searches for this particle were performed with large efforts at the Large Electron Positron Collider (LEP) at CERN from 1989-2000 and the Tevatron at Fermilab from 2002-2011. Both programs could exclude significant mass ranges without giving a conclusive answer about the actual existence of the Higgs boson. The search for the Higgs boson at the Large Hadron Collider (LHC) at CERN, which started operation in 2009, led to the discovery of a Higgs boson candidate in 2012 by the ATLAS and CMS collaborations [16, 17] in the bosonic decay channels $H \to \gamma\gamma$,

$H \to ZZ^*$ and $H \to WW^*$. The search for $H \to \tau\tau$ decays is the topic of this thesis, which presents an important direct test of fermionic Higgs boson couplings. While it is instructive to follow the developments leading to the formulation of the SM in a historical order, this section cannot attempt to give a full review of this topic. Instead, a brief qualitative introduction into the basic concepts of the SM is given. Several textbooks provide a more complete and more rigorous introduction [18–20]. This section closely follows Refs. [19–21]. Throughout this document, natural units are used. Velocities are measured in units of the speed of light c, while actions are expressed in units of the reduced Planck constant $\hbar$. Furthermore, the Einstein summation notation is used.

1.1.1. Particle Content and Interactions

The Standard Model describes the electromagnetic and weak interactions, as for example responsible for the binding of electrons to atomic nuclei and radioactive beta decays, respectively, as well as the strong interaction which confines quarks into hadrons. The electromagnetic force is described together with the weak interaction in a unified electroweak theory with a single characteristic energy scale. The SM does not provide a description of gravitation, for which no consistent quantum theory exists up to now. In any case, gravity acts with a coupling strength far too weak to play any role at high energy physics experiments. The particle content of the SM consists of twelve fundamental fermions of spin 1/2 and their respective antiparticles, twelve gauge bosons and one scalar particle. The fermions are further grouped into leptons, participating in electroweak interactions only, and quarks, which interact via the strong as well as the electroweak interactions. Both, quarks and leptons appear in three generations, copies of the first one with increasing masses but identical other quantum numbers. Approximate masses of the fermions are given in Table 1.1 and span a range between 10^{-3}eV and 10^{11}eV. The ordinary matter surrounding us consists basically exclusively of fermions of the first generation, as the heavier particles subsequently decay into them. For each of these fermions a corresponding antiparticle with conjugated additive quantum numbers exists. In the remainder of this thesis, the particle name refers to both, the particle and its antiparticle if not stated otherwise.

The first generation of leptons consists of the electrically charged electron and the electrically neutral electron neutrino. While the SM describes neutrinos as massless particles, the observation of neutrino oscillations implies non-vanishing neutrino masses [23–27]. Even though, terms describing finite neutrino masses can be added to the SM relatively easily, the exact realisation is yet unclear and represents one clear hint for physics not yet described by the SM. Quarks were originally proposed in 1964 by Gell-Mann and Zweig to allow for a symmetry-based description of meson and baryon systems. It was only later, during the formulation of QCD, that these quarks were actually identified with the strongly interacting constituents of hadrons which were discovered in deep inelastic lepton-hadron scattering experiments. They come as so-called up- and down-type quarks, carrying fractional electric charge

Quarks	El. charge [e]	Mass [GeV]
u	2/3	$\approx 2.49 \times 10^{-3}$
d	$-1/3$	$\approx 5.05 \times 10^{-3}$
c	2/3	≈ 1.27
s	$-1/3$	≈ 0.10
t	2/3	≈ 172.0
b	$-1/3$	≈ 4.19
Leptons		
ν_e	-	$< 2 \times 10^{-9}$
e^-	-1	$\approx 0.5 \times 10^{-3}$
ν_μ	-	$< 0.19 \times 10^{-3}$
μ^-	-1	$\approx 105 \times 10^{-3}$
ν_τ	-	$< 18 \times 10^{-3}$
τ^-	-1	≈ 1.7

Table 1.1. *Fundamental fermions of the SM and their electric charge and approximative mass, demonstrating the large mass range covered by the fermions. The quark masses are given as so-called current masses in the* $\overline{MS}$ *renormalisation scheme, apart from the top-quark mass, which is given as pole mass. Mass values are taken from Ref. [22].*

of $-1/3e$ and $2/3e$, respectively. Quarks are confined inside hadrons due to the structure of QCD, which prohibits direct experimental observation of free quarks. They rather hadronise into a spray of hadrons.

The interactions are mediated by the gauge bosons of spin one, which are summarised in Table 1.2. Electromagnetism is mediated by the massless photon, which couples to electrically charged particles, while the weak interaction is transmitted by the massive $W^\pm$ and Z bosons. Their heavy masses of $m_W = 80.4\,\text{GeV}$ and $m_Z = 91.2\,\text{GeV}$, respectively, is what limits the range of the weak interaction and makes it appear weakly coupled at low energies. The charge associated to the weak interaction is the so-called *weak isospin*. The strong interaction is mediated by eight massless gluons, which couple to colour charge[1]. In addition to the gauge bosons, the SM contains one scalar spin zero particle, the Higgs boson.

---

[1] Interestingly, the concept of colour was originally proposed in the quark model by O.W. Greenberg [28] to allow for a Pauli principle obeying description of the Δ^{++} baryon without actually constructing a theory of the strong force based on colour-charge.

Interaction	Boson	Mass [GeV]	Associated charge
strong	8 gluons g_{ij}	0	colour
electromagnetic	photon γ	0	electric charge
weak	$W^{\pm}$ bosons	≈ 80.4	weak isospin
	Z^0 boson	≈ 91.2	

Table 1.2. *The interactions of the SM and their mediating gauge bosons. Masses taken from Ref. [22].*

1.1.2. Quantum Electrodynamics

The successful combination of Maxwell's theory of electromagnetism, its symmetries and a consistent relativistic and quantum-mechanical description of electrons was pioneering for the development of quantum field theories. Quantum electrodynamics (QED) is based on the well known gauge invariance of electrodynamics. The Maxwell equations

$$\partial_\xi F_{\mu\nu} + \partial_\mu F_{\nu\xi} + \partial_\nu F_{\xi\mu} = 0 \tag{1.1}$$

$$\partial_\mu F^{\mu\nu} = j^\nu \tag{1.2}$$

where $F_{\mu\nu} = \partial_\mu A_\nu - \partial_\nu A_\mu$ denotes the field strength tensor, are invariant under gauge transformations of the form $A_\mu \to A_\mu - \partial_\mu \alpha$. The symmetry group is the $U(1)$, and A_μ transforms like a four-vector. The Lagrange density function of a free Dirac fermion, however, is not invariant. Considering the Lagrange density

$$\mathcal{L}_0 = \bar{\Psi}(i\not{\partial} - m)\Psi \tag{1.3}$$

where $\not{\partial} := \gamma_\mu \partial^\mu$ denotes the contraction with the Dirac matrices γ_μ, under local $U(1)$ transformations of the form

$$\Psi(x) \to \mathrm{e}^{-ie\alpha(x)}\,\Psi(x) \qquad \bar{\Psi}(x) \to \bar{\Psi}(x)\,\mathrm{e}^{ie\alpha(x)} \tag{1.4}$$

the density acquires an additional term $\bar{\Psi} e \not{\partial} \alpha \Psi$.

To arrive at a $U(1)$ invariant Lagrange density, this behaviour suggests to introduce a coupling between the vector field A_μ and the Dirac fermion to compensate this term:

$$\mathcal{L} = \bar{\Psi}[i\gamma^\mu(\partial_\mu - ieA_\mu) - m]\Psi \tag{1.5}$$

Adding the free field dynamics, as described by the Maxwell equation (1.2) in absence of any external sources, the Lagrange density of QED reads:

$$\mathcal{L}_{QED} = -\frac{1}{4}F^{\mu\nu}F_{\mu\nu} + \bar{\Psi}[i\gamma^\mu(\partial_\mu - ieA_\mu) + m]\Psi \tag{1.6}$$

The equation of motion can be derived from the Euler-Lagrange equations for Eq. (1.6) with respect to A_μ. This yields Maxwell's equations (1.2) so that the conserved current $j^\nu = -e\bar{\Psi}\gamma^\nu\Psi$ can be identified with the electron current. This is a remarkable result, since it was the requirement of local gauge invariance of the Lagrange density, which correctly produced the field-fermion interaction term. The current j^ν is the conserved quantity of the $U(1)$ symmetry of the theory. In fact, this offers a well-defined way to construct gauge theories. Once the gauge group is chosen, the interaction structure is fixed as well. One can absorb the interaction term in the definition of the covariant derivative $D_\mu = \partial_\mu - ieA_\mu$, which transforms like the vector field itself. Additional fermions can be added to the theory by simply adding the corresponding interaction and kinetic terms for each of them to Eq. (1.6). A mass term for the vector field of the form $-\frac{1}{2}m^2 A_\mu A^\mu$ is not gauge invariant and therefore forbidden.

Even though, the dynamical structure of QED is completely fixed by Eq. (1.6), solving the equations of motion is highly non-trivial and is usually performed in perturbation theory. This is possible due to the small numerical value of the coupling strength $\alpha = e^2/4\pi \approx 1/137$, so that expansions in α converge quickly. A convenient way to construct transition amplitudes in fixed order perturbation theory is offered by the so-called Feynman rules, which associate, based on the Lagrange density of the theory, mathematical terms to propagators and interaction vertices.

1.1.3. Quantum Chromodynamics

Deep inelastic scattering experiments, like electron-proton scattering, gave strong indications that the proton is a composite particle of point-like spin 1/2 constituents, so-called partons. In parallel, baryon and meson spectroscopy under the quark hypothesis has lead to the introduction of a colour charge, expressed in dimensions (red, green, blue). Indeed, both concepts describe the same particles. Quantum chromodynamics is the gauge theory of a local $SU(3)$ invariance, describing the dynamics of the strong interaction. Its gauge bosons are called *gluons*. Under local $SU(3)$ transformations a free quark field transforms as:

$$q(x) \rightarrow Uq(x) = \mathrm{e}^{i\alpha_a T_a}\, q(x) \tag{1.7}$$

In analogy to QED gauge fields, G^a_μ and the covariant derivative D_μ are introduced

$$D_\mu = \partial_\mu + ig_s \frac{\lambda_a}{2} G^a_\mu \tag{1.8}$$

defining the structure of interactions between quarks and gluons with a coupling strength g_s. In the fundamental representation of $SU(3)$, the generators T_a can be written as

$$T_a = \frac{1}{2}\lambda_a \tag{1.9}$$

$$[T_a, T_b] = if_{abc}T_c \tag{1.10}$$

where λ_a denote the Gell-Mann matrices and the colour index a runs from $1-8$. In contrast to $U(1)$, the generators of $SU(3)$ do not commute. This is expressed by the non-vanishing structure constants f_{abc} in Eq. (1.10). In general, groups with this property are referred to as *non-abelian* groups. As an important consequence, the gluon field strength tensor $G^a_{\mu\nu}$ acquires an additional term with respect to its electromagnetic counterpart

$$G^a_{\mu\nu} = \partial_\mu G^a_\nu - \partial_\nu G^a_\mu - g_s f^{abc} G^b_\mu G^c_\nu \tag{1.11}$$

so that finally, the Lagrangian of QCD reads

$$\mathcal{L}_{QCD} = \bar{q}(i\gamma^\mu \partial_\mu - m)q - g_s(\bar{q}\gamma^\mu T_a q)G^a_\mu - \frac{1}{4}G^a_{\mu\nu}G^{a,\mu\nu} \tag{1.12}$$

Due to the non-abelian structure of $SU(3)$ Eq. (1.12) includes terms of order $g_s G^3$ and $g_s^2 G^4$ describing three and four gluon self-interaction vertices. As a consequence, QCD has a completely different energy scaling behaviour than QED. In QED, the electromagnetic coupling α falls with decreasing energy scale Q of the process, as the electron charge is screened by vacuum polarisation effects. In QCD though, the strong coupling α_s grows for lower scales. This scaling behaviour of the coupling strength is described by the renormalisation group equation (RGE):

$$Q^2 \frac{\partial \alpha_s(Q^2)}{\partial Q^2} = \beta(\alpha_s) \tag{1.13}$$

The β-function can be computed in perturbation theory and in leading order one obtains

$$\beta(\alpha_s) = -\alpha_s^2(Q^2)\frac{33 - 2N_f}{12\pi} \tag{1.14}$$

where N_f denotes the number of light quark flavours participating at energy scales Q^2. This prediction can be tested and an example is shown in Fig. 1.1 where the scaling behaviour of QCD is compared to experimental measurements. The negative sign in Eq. (1.14) has important consequences: At very low energy scales, corresponding to large spatial separation, QCD becomes a strongly coupled theory. This leads to quark *confinement* inside hadrons. Trying to dissolve a hadron into its constituents, e.g. in scattering experiments, will result in the *hadronisation* of the scattered parton and the hadron remnants, as the separated colour charges will be so strongly coupled at large distances that neutralising colour charges will be created out of the vacuum. Therefore, all experimentally observable particles will be colour neutral states. At high energy scales in contrast, QCD becomes weakly coupled, which is referred to as *asymptotic freedom.* In high energy experiments, like deep inelastic scattering the partons appear as free particles. Most importantly for the calculation of observables in perturbation theory, the numerical value of the coupling constant at $Q^2 = m_Z^2$ is $\alpha_s = 0.1184(7)$ [22], which is low enough to allow a perturbative treatment of QCD scattering amplitudes. In the strongly coupled regime though, perturbation expansions in α_s do not converge, therefore QCD is *non-perturbative* at low energy scales.

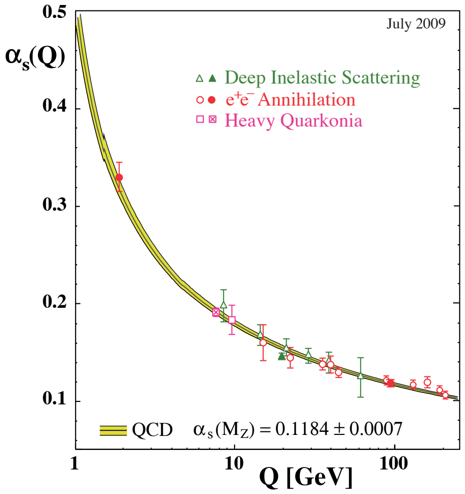

Figure 1.1. *Experimental measurements of α_s at different scales Q compared to the scaling prediction by QCD [29].*

1.1.4. Electroweak Unification and the Gauge Group of the Standard Model

The weak interaction observed in the radioactive beta decay ($pe^- \rightarrow n\nu_e$) was interpreted by Fermi in 1933, as a four-fermion interaction vertex with a coupling strength given by the Fermi constant G_f. It was later suggested by Lee, Yang [30] and Wu [31] that the weak interaction violates parity, giving the first experimental hints about the coupling structure of weak interactions. In fact, weak interactions do violate parity maximally and only left-handed particles (and right-handed antiparticles) take part in it. Glashow, Salam and Weinberg proposed a unified theory of electroweak interactions able to describe the observed weak and electromagnetic forces from a single underlying gauge group $SU(2)_L \times U(1)_Y$, also known as the GSW model, where Y denotes the hypercharge, and L refers to the coupling to left-handed particles. Together with the gauge group of QCD the SM gauge group reads

$$SU(3)_C \times SU(2)_L \times U(1)_Y \tag{1.15}$$

With this in mind, the fermion content of the SM can be written down in weak isospin multiplets of identical hypercharge, which is related to the electric charge Q and weak isospin I^3 via the Gell-Mann-Nishijima relation: $Y = 2Q - 2I^3_W$.

$$\begin{array}{ccc|cc}
 & \text{Quarks} & & I^3_W & Y \\
\begin{pmatrix} u \\ d \end{pmatrix}_L & \begin{pmatrix} c \\ s \end{pmatrix}_L & \begin{pmatrix} t \\ b \end{pmatrix}_L & \begin{array}{c} 1/2 \\ -1/2 \end{array} & \begin{array}{c} 1/3 \\ 1/3 \end{array} \\
u_R & c_R & t_R & 0 & 4/3 \\
d_R & s_R & b_R & 0 & -2/3
\end{array} \tag{1.16}$$

Leptons

$$\begin{array}{ccc|cc} \begin{pmatrix} \nu_e \\ e^- \end{pmatrix}_L & \begin{pmatrix} \nu_\mu \\ \mu^- \end{pmatrix}_L & \begin{pmatrix} \nu_\tau \\ \tau^- \end{pmatrix}_L & \begin{array}{c} 1/2 \\ -1/2 \end{array} & \begin{array}{c} -1 \\ -1 \end{array} \\ e_R & \mu_R & \tau_R & 0 & -2 \end{array} \tag{1.17}$$

The right-handed particles appear as singlets under the $SU(2)_L$. Since right-handed, massless neutrinos would be singlets under $SU(3)_C$, $SU(2)_L$ and $U(1)_Y$ they are dropped from Eq. (1.17) since they would not take part in any interaction of the SM. In addition, the left- (right-) handed quark fields are grouped in $SU(3)_C$ (anti-)triplets, which is suppressed here. Denoting the gauge fields of $SU(2)_L$ by W^i (i=1,2,3) and the gauge field of $U(1)_Y$ by B, the Lagrangian of the pure field dynamics reads

$$\mathcal{L}_{\text{YM}} = -\frac{1}{4}W^i_{\mu\nu}W^{i,\mu\nu} - \frac{1}{4}B_{\mu\nu}B^{\mu\nu} - \frac{1}{4}G^a_{\mu\nu}G^{a,\mu\nu} \tag{1.18}$$

where the field strength tensors are defined as usual:

$$W^i_{\mu\nu} = \partial_\mu W^i_\nu - \partial_\nu W^i_\mu - g\epsilon^{ijk}W^j_\mu W^k_\nu \tag{1.19}$$

$$B_{\mu\nu} = \partial_\mu B_\nu - \partial_\nu B_\mu \tag{1.20}$$

$$G^a_{\mu\nu} = \partial_\mu G^a_\nu - \partial_\nu G^a_\mu - g_s f^{abc}G^b_\mu G^c_\nu \tag{1.21}$$

with ϵ^{ijk},f^{abc} denoting the structure constants of $SU(2)$ and $SU(3)$, respectively. The coupling to the fermion sector can be schematically written as

$$\mathcal{L}_{\text{f}} = i\bar{\Psi}_L \not{D}\Psi_L + i\bar{\Psi}_{l_R}\not{D}\Psi_{l_R} + i\bar{\Psi}_Q\not{D}\Psi_Q + i\bar{\Psi}_{u_R}\not{D}\Psi_{u_R} + i\bar{\Psi}_{d_R}\not{D}\Psi_{d_R} \tag{1.22}$$

where Ψ_L are the left-handed lepton $SU(2)$-doublets and Ψ_{l_R} the right-handed lepton $SU(2)$-singlets of flavour e, μ, τ as summarised in Eq. (1.17), and similarly Ψ_Q the left-handed quark $SU(2)$-doublets, Ψ_{u_R} the right-handed quark $SU(1)$-singlets for the up-type quarks and Ψ_{d_R} for the down-type quarks, respectively. The covariant derivative contains one term per generator of the full gauge group:

$$D_\mu = \partial_\mu + igI^i_W W^i_\mu + ig'\frac{Y}{2}B_\mu + ig_s T^a_c G^a_\mu \tag{1.23}$$

I^i_W,Y and T^a_c are denoting the representations of the generators as defined by the fermion multiplet they are acting on, for instance $T^a_c = \lambda^a/2$ for the $SU(3)$ colour quark triplets but $T^a_c = 0$ for colour singlets, like leptons.

There are two neutral vector fields connected to the electroweak sector, B_μ and W^3_μ. The existence of a neutral weak current was one of the predictions made by the GSW model. Since these two vector fields carry the same quantum numbers it is natural to parametrise their mixing. As the B_μ field interacts symmetrically with left- and right-handed particles one expects a right-handed component in the weak neutral current and indeed experiments do observe such a contribution. With the weak mixing angle θ_w, the physical photon, Z^0 and $W^\pm$ fields are expressed as:

$$\begin{aligned}\begin{pmatrix} Z_\mu \\ A_\mu \end{pmatrix} &= \begin{pmatrix} \cos\theta_W & -\sin\theta_W \\ \sin\theta_W & \cos\theta_W \end{pmatrix}\begin{pmatrix} W_\mu^3 \\ B_\mu \end{pmatrix} \quad (1.24)\\ W_\mu^\pm &= \frac{1}{\sqrt{2}}(W_\mu^1 \mp iW_\mu^2) \quad (1.25)\end{aligned}$$

The electric charge can be written in terms of the couplings g,g' as:

$$e = \frac{gg'}{\sqrt{g^2+(g')^2}} = g'\cos\theta_W \quad (1.26)$$

This theory includes interaction terms between all fermions and the electroweak gauge bosons, as well as between the quarks and gluons. Furthermore, there is a non-trivial self-coupling sector with couplings between the electroweak bosons as well as between the gluons. Nevertheless, the vector fields are massless since any mass term bilinear in the fields violates gauge invariance as already discussed in Section 1.1.2. In contrast to the QED or QCD models discussed above, in which the left and right-handed fermions transform identical under the respective gauge transformations, the electroweak model also forbids fermion mass terms of the form $\bar{\Psi}_{f_L}\Psi_{f_R}+\Psi_{f_L}\bar{\Psi}_{f_R}$ which violate gauge invariance due to the different transformation properties of left- and right-handed fermions. The mechanism introduced in the GSW model to achieve a spontaneous breaking of the $SU(2)_L \times U(1)_Y$ into the observed $U(1)_{\text{EM}}$ symmetry group, while preserving the gauge invariance of the Lagrangian, is discussed in Subsection 1.1.5.

1.1.5. Electroweak Symmetry Breaking

The general idea of spontaneous symmetry breaking is that a symmetric system can evolve into a ground state which is not invariant under the full symmetry group of the theory. To achieve this in the framework of the SM, an additional complex scalar $SU(2)_L$ doublet $\Phi = (\phi^+,\phi^0)^T$ of hypercharge $Y = 1$ is introduced into the theory

$$\begin{aligned}\mathcal{L}_{\text{Higgs}} &= (D_\mu\Phi)^\dagger(D^\mu\Phi) - V(\Phi) \quad (1.27)\\ &= (D_\mu\Phi)^\dagger(D^\mu\Phi) + \mu^2(\Phi^\dagger\Phi) - \frac{\lambda}{4}(\Phi^\dagger\Phi)^2 \quad (1.28)\end{aligned}$$

where D_μ is the covariant derivative introduced in Eq. (1.23) and $V(\Phi)$ describes the self-interaction of Φ. In order to respect the gauge symmetries (1.15) it depends only on $\Phi^\dagger\Phi$. It is further restricted to terms of dimension four or less to ensure the renormalisability of the model. While $\lambda > 0$ is required to allow for a stable vacuum, μ^2 can be chosen to describe two different scenarios. For $\mu^2 < 0$ the potential has a minimum for vanishing values of Φ, but if μ^2 is chosen to be positive the vacuum expectation value (vev) Φ_0 of Φ is finite and corresponds to a scenario in which the gauge symmetry is broken in the expected vacuum state. Figure 1.2 shows a

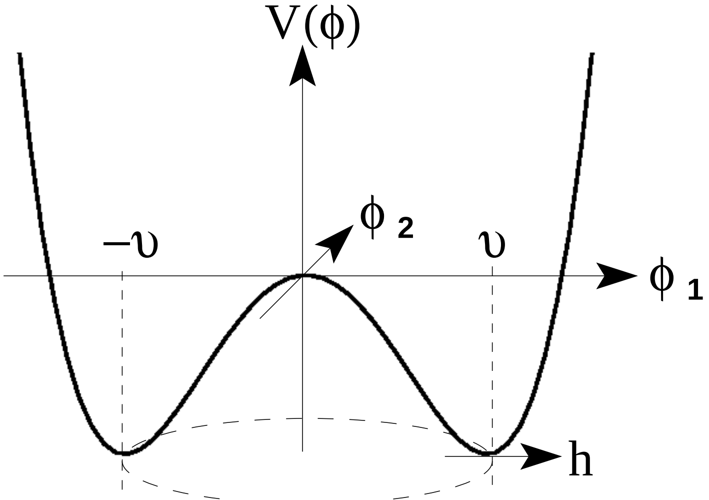

Figure 1.2. *Two dimensional Higgs potential of the form of Eq. 1.28 with* $\lambda > 0$ *and* $\mu^2 < 0$*. There is a set of equivalent minima connected via rotations in the* (ϕ_1, ϕ_2) *plane [19].*

simplified example of such a potential in two real dimensions. Minimising V with respect to $\Phi^\dagger\Phi$ yields:

$$\Phi_0^\dagger\Phi_0 = \frac{v^2}{2}, \qquad v = 2\sqrt{\frac{\mu^2}{\lambda}} \tag{1.29}$$

Since the vacuum should be electrically neutral, the ϕ_0^+ component should vanish and Φ_0 is fixed up to an arbitrary phase. Parametrising the field around the vev

$$\Phi = \begin{pmatrix} \phi^+ \\ (v + H + i\chi)/\sqrt{2} \end{pmatrix} \tag{1.30}$$

allows to identify the Higgs field H and two additional fields, a complex one (ϕ^+) and a real one (χ). Fixing the gauge so that ϕ^+ and χ vanish is called the *unitary gauge*. It breaks $SU(2)$ invariance, so that the Lagrangian (1.27) in the vacuum reads

$$\begin{aligned}\mathcal{L}_{\text{Higgs,U-gauge}} =& \frac{1}{2}(\partial_\mu H)(\partial^\mu H) + \frac{g^2}{4}(v+H)^2 W_\mu^+ W^{-,\mu} \\ &+ \frac{g^2}{8(\cos\theta_W)^2}(v+H)^2 Z_\mu Z^\mu \\ &+ \frac{\mu^2}{2}(v+H)^2 - \frac{\lambda}{16}(v+H)^4\end{aligned} \tag{1.31}$$

where the physical $W^\pm$ and Z fields are used as introduced in Section 1.1.4. In this form, one can directly identify a kinetic term for the Higgs field, bilinear mass terms for the $W^\pm$, Z and H bosons and a number of interaction terms.

In this gauge, the vacuum is invariant under a $SU(2)_L$ rotation of angle α around the z-axis followed by a $U(1)_Y$ rotation of $\alpha/2$:

$$\Phi_0 \to \exp\Big(i\alpha(\frac{1}{2}\mathbb{1}_{1\times 2} + \frac{\sigma_3}{2})\Big)\Phi_0 = \Phi_0 \tag{1.32}$$

where $\sigma_3/2$ is the $SU(2)$ generator for rotations around the z-axis and $\mathbb{1}_{1\times 2}$ the generator of $U(1)$ rotations. This symmetry reflects the unbroken $U(1)_{\mathrm{EM}}$ symmetry of the vacuum and one finds the Gell-Mann-Nishijima relation introduced above.

Expressed in terms of coupling constants, the vev v and one of the parameters of the Higgs potential μ, the masses of the bosons are given by

$$m_W = \frac{gv}{2}, \qquad m_Z = \frac{m_W}{\cos\theta_W}, \qquad m_H = \sqrt{2\mu^2} \tag{1.33}$$

Neither the gluons nor the photon acquire a mass as desired, and the mass ratio of W and Z bosons is fully determined by the weak mixing angle θ_W. An additional physical particle appears in Eq. (1.31), the Higgs boson, whose mass m_H is a free parameter of the SM and is driven by the steepness of the Higgs potential.

The value of the vacuum expectation value v can be determined using precise measurements of the muon lifetime. Compared to the small momenta involved in the muon decay, m_W is large and the process can be expressed as an effective four fermion vertex with a coupling strength given by the Fermi constant $G_F = 1/\sqrt{2}v^2 \propto 1/m_W^2$. The vacuum expectation value is determined to be $v \approx 246.22$ GeV[22].

In addition, interaction terms between the weak vector bosons and the Higgs boson are included in Eq. (1.31). Writing these out by making use of relations (1.33) yields:

$$\begin{aligned}\mathcal{L}_{\mathrm{Higgs,U-gauge}} =& \frac{1}{2}(\partial_\mu H)(\partial^\mu H) - \frac{1}{2}m_H^2 H^2 + \frac{1}{2}m_W^2 W_\mu^+ W^{-,\mu} + \frac{1}{2}m_Z^2 Z_\mu Z^\mu \\ &+ g m_W H W_\mu^+ W^{-,\mu} + \frac{g^2}{4} H^2 W_\mu^+ W^{-,\mu} \\ &+ \frac{g m_Z}{2\cos\theta_W} H Z_\mu Z^\mu + \frac{g^2}{4(\cos\theta_W)^2} H^2 Z_\mu Z^\mu \\ &- \frac{g m_H^2}{4 m_W} H^3 - \frac{g^2 m_H^2}{32 m_W^2} H^4 + \mathrm{const.}\end{aligned} \tag{1.34}$$

Also cubic ($HV^\dagger V$) and quartic ($HHV^\dagger V$) interaction terms between the weak vector bosons (V) and the Higgs boson can be identified. The coupling strength is proportional to the squared mass of the boson[2]. Furthermore cubic and quartic Higgs self-coupling terms appear. The corresponding vertices are shown in Fig. 1.3.

---

[2] The coupling between the vector bosons and the Higgs boson is a gauge coupling and proportional to $(-igm_W)$. As the coupling constant g can be expressed as $g = \frac{2m_W}{v}$, a quadratic dependence on the vector boson mass follows.

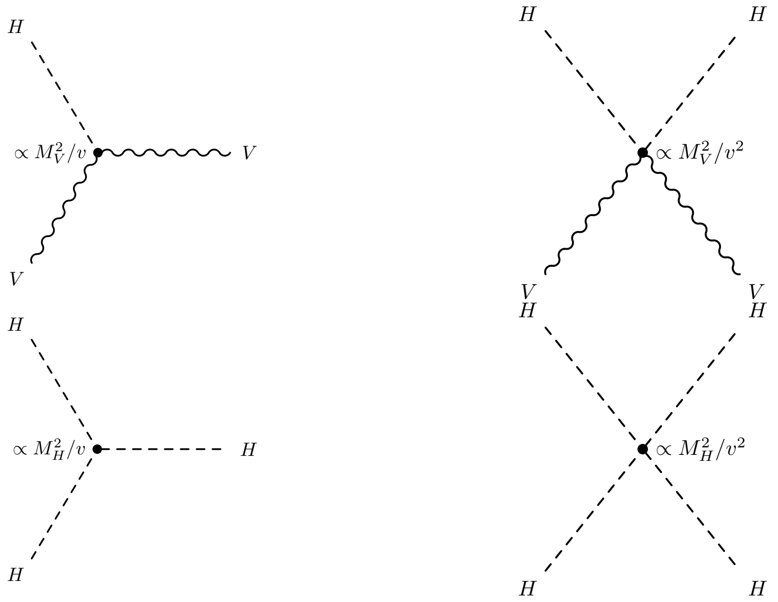

Figure 1.3. *Triple and quartic vertices between the weak vector bosons and the Higgs boson (top) as well as the Higgs boson self interaction vertices (bottom). V denotes the weak vector bosons* $W^{\pm}, Z$.

1.1.6. Fermion Masses

As last missing part of the SM Lagrangian, fermion mass terms need to be added in a way respecting the symmetries of the theory. This is accomplished by so-called *Yukawa couplings* between the Higgs $SU(2)$ doublet Φ, the left-handed fermion $SU(2)$ doublets and right-handed fermion singlets. In the most general form one writes

$$\mathcal{L}_{\text{Yukawa}} = -\bar{\Psi}_L G_l \Psi_{l_R} \Phi - \bar{\Psi}_Q G_u \Psi_{u_R} \Phi^C - \bar{\Psi}_Q G_d \Psi_{d_R} \Phi + \text{h.c.} \tag{1.35}$$

where Φ^C is the charge conjugated Higgs doublet. These terms couple left and right-handed fermions which is possible in the Higgs mechanism since Φ allows the contraction of the $SU(2)$ indices of the left-handed fermion fields. G_l, G_u and G_d are 3×3 generation matrices defining the coupling strengths for all terms. In particular, they allow for mixing across the generations. After unitary transformations $U^{f_{L/R}}$ of the fermion fields into a mass basis in which the mass matrices are diagonal and after fixing the gauge, the Yukawa terms simply become

$$\mathcal{L}_{\text{Yukawa,U-gauge}} = -\sum_f \frac{v}{\sqrt{2}} \lambda_f \left(\hat{\bar{\Psi}}_{f_L} \hat{\Psi}_{f_R} - \hat{\bar{\Psi}}_{f_R} \hat{\Psi}_{f_L}\right)\left(1 + \frac{H}{v}\right) \tag{1.36}$$

where the hat indicates that the fermion fields are in the mass basis. The dimensionless coupling constant λ_f is directly proportional to the fermion mass:

$$\frac{v}{\sqrt{2}} \lambda_f = m_f \tag{1.37}$$

Only the charged weak interaction terms involving quarks are affected by these transformations and hence need to be modified so that the fermion fields are rotated back into the interaction basis

$$\Psi_{u_L} = (U^{u_L})^\dagger \hat{\Psi}_{u_L} \qquad \bar{\Psi}_{u_L} = \hat{\bar{\Psi}}_{u_L} U^{u_L} \tag{1.38}$$

$$\Psi_{d_L} = (U^{d_L})^\dagger \hat{\Psi}_{d_L} \qquad \bar{\Psi}_{d_L} = \hat{\bar{\Psi}}_{d_L} U^{d_L} \tag{1.39}$$

The product $V := U^{u_L}(U^{d_L})^\dagger$ is called Cabibbo-Kobayashi-Maskawa (CKM) matrix [32, 33] and describes the quark mixing. As a unitary complex matrix it can be parametrised by four independent parameters, for example by three mixing angles and one CP violating phase. Measurements do show though, that the mixing is relatively weak and the diagonal elements of V are close to one.

The neutral weak currents remain unchanged by this change of basis since the matrices $U^{f_{L/R}}$ are unitary. Because the neutrinos are assumed to be massless particles in the SM, the charged current in the lepton sector does not involve mixing between the generations. In extensions of the SM involving neutrino masses, mixing occurs and the corresponding matrix is called Maki-Nakagawa-Sakata (MNS) matrix [34].

The fermion mass terms (1.36) also lead to Higgs-fermion interactions with a coupling strength proportional to the fermion mass (Fig. 1.4). This prediction can be tested experimentally and is one important test to identify the Higgs mechanism as being responsible for electroweak symmetry breaking. While the Higgs mechanism offers a theoretical consistent description of vector boson and fermion masses, it cannot explain or motivate the large spread between the fermion mass values which appear as free parameters in the theory. In case of the electron for example the dimensionless Yukawa coupling yields $\sqrt{2}m_e/v \approx 3 \times 10^{-6}$ while for the top quark $\sqrt{2}m_t/v \approx 1$. The SM does not offer any explanation for the variety of the fermion mass scales.

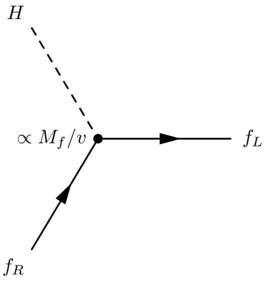

Figure 1.4. *Leading order feynman diagram of the Higgs boson coupling to fermions with a coupling strength proportional to* m_f*.*

1.1.7. Theoretical Bounds on the Mass of the Higgs Boson

Once all 19 free parameters[3] of the SM are fixed, predictions for experimentally accessible observables can be calculated. The phenomenology of Higgs boson production and decays does of course heavily depend on its mass. While being a free parameter in general, bounds on the allowed range of possible values of m_H can be constructed based on theoretical arguments. These are briefly reviewed in the following.

Unitarity Constraints

As discussed above, the Higgs mechanism is responsible for the generation of the weak vector boson masses. The additional longitudinal degrees of freedom of a massive vector boson compared to a massless one, were introduced into the theory with the postulation of the Higgs doublet Φ. In high energy forward scattering of two vector bosons (e.g. $W^+W^- \to W^+W^-$) the longitudinal component dominates the scattering amplitude. The cross section of this process grows with the centre-of-mass energy $\sqrt{s}$. It turns out that this process would even violate unitarity, if diagrams involving the exchange of a Higgs boson did not cancel the divergency. It is remarkable, that for this cancellation to hold, the coupling strength of the Higgs boson to the W boson is required to be proportional to the squared W mass, just as realised in the Higgs mechanism.

The energy scale above which these cancellations appear depends of course on the mass of the Higgs boson. Therefore, requiring unitarity sets an upper bound on the Higgs boson mass of approximately $m_H \lesssim 1$ TeV [35].

Vacuum Stability and Triviality

Interestingly, the mass of the Higgs boson can have important consequences for the self-consistency of the SM. As discussed for QCD in Section 1.1.3, also the coupling strength $\lambda(Q)$ of the Higgs boson self interaction receives quantum corrections and therefore exhibits a dependence on the energy scale Q, described by the RGE. Two concurrent terms contribute, dominating the behaviour in two different limits. For large values of m_H it is the Higgs boson self-interaction vertices which cause $\lambda(Q)$ to grow with rising energy scales, while for small values it is the top-quark Yukawa coupling which drives the behaviour of the quartic coupling to fall at high energies.

---

[3] Section 1.1 has only discussed 18 parameters so far. The three gauge couplings g, g', g_s, the parameters of the Higgs potential μ, λ, nine fermion masses and four CKM matrix parameters. QCD nevertheless allows for a 19th parameter, usually denoted as QCD vacuum angle θ. For finite values of θ, CP violation occurs in strong interactions, which so far has been not observed experimentally. This is referred to as the *strong CP problem* and will be touched upon in Section 1.1.8.

In the first scenario of large m_H, $\lambda(Q)$ reaches a non-perturbative regime in the high energy limit. At leading order, it even diverges at a so-called Landau-pole. While the exact appearance of such a divergence can change with higher order corrections, it is clear that the theory becomes strongly coupled at high energies. Avoiding this can only be achieved by a *trivial*, non-interacting theory corresponding to $\lambda = 0$. The requirement of the SM to remain perturbative up to a scale Λ therefore puts an upper bound on the Higgs boson mass. One can rather interpret the SM as effective theory, valid up to some scale at which new contributions to the correction of $\lambda(Q)$ become relevant, curing the high energy behaviour.

In contrast to this, a low mass of the Higgs boson would lead to negative corrections to λ dominated by the top-quark Yukawa coupling. For large energies, these corrections would drive the quartic self interaction to become negative. In such scenarios, no stable vacuum exists in the theory since the Higgs potential would fall to infinitely large negative values. In such cases new physics effects, becoming relevant at energy scales Λ, would need to change the effective potential to allow a stable vacuum configuration. This puts a lower bound on the Higgs boson mass with a residual dependence on the top-quark mass. In the transition regime metastable configurations exist, where the lifetime of the metastable vacuum exceeds the age of the universe.

Figure 1.5 shows both, the high and low mass bounds on m_H based on these two arguments. If the SM should remain a (meta-)stable theory in a perturbative regime up to $\Lambda \sim 10^{19}$ GeV, the mass of the Higgs boson m_H should lie in a narrow band between 120 GeV $\lesssim m_H \lesssim$ 170 GeV. A more rigorous discussion of the stability and triviality arguments can be found in Refs. [35–38].

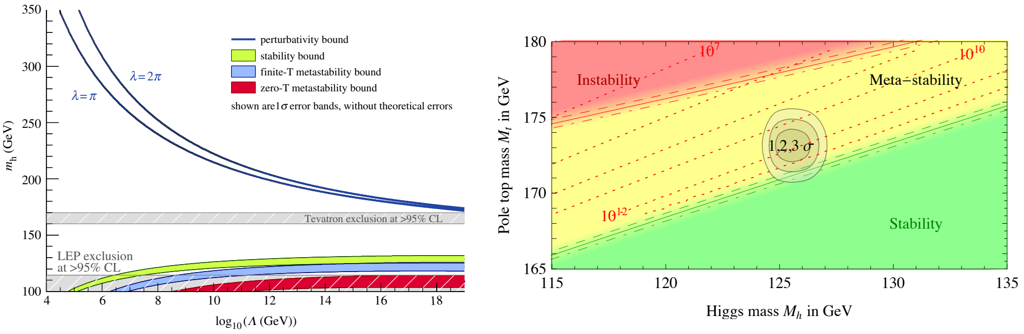

(a) (b)

Figure 1.5. *Upper and lower bounds on m_H derived from the perturbativity and vacuum-stability arguments as a function of the scale Λ up to which the SM remains a stable and perturbative theory (a). The shaded bands indicate the exclusion range from direct searches at LEP and Tevatron, which are discussed in Chapter 1.4 [35]. The right Figure shows the stable, meta-stable and instable configurations of the Higgs potential for given top quark and Higgs boson masses. The dotted lines represent the field energies measured in GeV for which the instability occurs [38].*

Constraints from Electroweak Precision Measurements

Due to the Higgs boson couplings to the weak vector bosons $W^{\pm}$ and Z^0, basically all electroweak observables acquire loop corrections involving the exchange of Higgs bosons. Due to these corrections, indirect constraints on m_H can be drawn from a careful analysis of electroweak precision data taken at LEP[4] and other experiments. A logarithmic dependence on m_H for example is present in the one loop correction Δr to the W boson mass m_W [37]

$$m_W^2 = \frac{\pi\alpha}{\sqrt{2}G_F \sin^2\theta_W}(1+\Delta r) \tag{1.40}$$

$$\Delta r \propto \frac{\sqrt{2}G_F}{16\pi^2}\left(\frac{11}{3}\ln\frac{m_H^2}{m_Z^2}+...\right) \tag{1.41}$$

In general, such corrections to electroweak observables depend strongly on the electroweak mixing angle and the top-quark mass. While the electroweak mixing angle is constrained by measurements of the forward-backward and τ polarisation asymmetries at the Z^0 pole, the top-quark mass is directly measured at the Tevatron[5]. Performing a fit to a combined set of electroweak precision data [39], including direct measurements of m_W, the W decay width Γ_W and the top-quark mass, allows to indirectly constrain also the mass of the Higgs boson. Figure 1.6 shows the $\Delta\chi^2$ value as a function of m_H of such a combined fit. The width of the blue band corresponds to uncertainties from missing higher order corrections in the theory calculations summarised in Refs. [40–42]. The best-fit value lies at a relatively low Higgs boson mass of $m_H = 94^{+29}_{-24}$ GeV, which is consistent with the observation of a Higgs boson candidate made in 2012 at the LHC experiments of a mass of approximately $m_H \approx 125.5$ GeV [16, 17] which is discussed in Chapter 1.4.

1.1.8. Limitations of the Standard Model

Since its formulation in the 1960s the SM was tested experimentally in various ways. Most of its free parameters are by now over-constrained, so that direct and indirect measurements can be tested against each other, indicating a high degree of self consistency of the theory. Higher and higher accuracy in theoretical calculations due to improved technical skills allow the theory predictions to keep up with the growing experimental precision achieved in the last decades. Despite this success, there are experimental and theoretical observations suggesting physical phenomena not described by the SM, usually referred to as *physics beyond the SM* (BSM). An incomplete overview of some of these observations is briefly given here.

---

[4] The Large Electron Positron Collider was an e^+e^- collider at CERN running from 1989 - 2000. The LEP experiments performed detailed analyses of the electroweak sector of the SM.

[5] The Tevatron was a $p\bar{p}$ collider at Fermilab running from 1983-2011 at which the top quark was discovered in 1995.

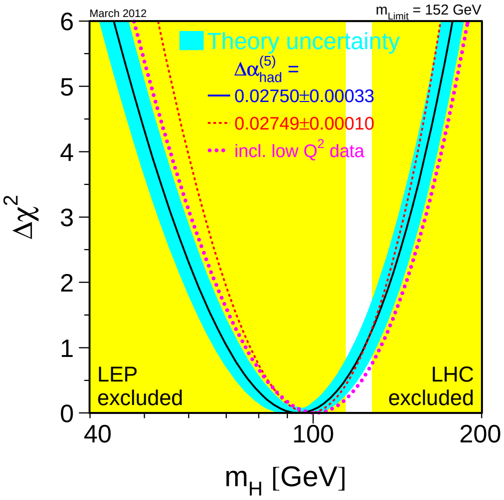

Figure 1.6. $\Delta\chi^2$ *as a function of* m_H *of a global fit of the SM to electroweak precision data. The blue band corresponds to uncertainties in the theory calculations due to missing higher orders. Even without including knowledge from direct searches the experimental data favours a light Higgs boson mass of* $m_H < 152$ *GeV [39].*

Neutrino Masses

As discussed in Section 1.1.6, neutrinos are described as massless particles in the SM. This is why the rotation into the mass basis, when constructing the fermion mass terms, does not change the leptonic weak charged current (CC) structure, while the quark sector is modified by the introduction of the CKM matrix describing generation mixing in quark CC interactions. Experiments studying the flux of solar neutrinos ν_e (e.g. the Homestake [23] and GNO experiments [24]), anti-neutrinos from reactors $\bar{\nu}_e$ (e.g. KamLAND [25]) and atmospheric (anti-) neutrinos $\nu_\mu, \bar{\nu}_\mu$ (e.g. Super-Kamiokande [26]) do all observe *disappearance effects*. In contrast, *appearance* of ν_τ [27] and ν_e [43, 44] in beams of neutrinos created in their muonic interaction state is observed as well. All current experimental data is in compelling agreement with the hypothesis of neutrino oscillation. Such oscillations are indeed predicted by extensions of the SM in which neutrinos appear as massive particles, so that the weak interaction eigenstates ν_{lL} appear as a linear combination of the mass eigenstates ν_{jL}

$$\nu_{lL} = \sum_j U_{lj} \nu_{jL} \tag{1.42}$$

The oscillation probabilities $P(\nu_l \to \nu_{l'})$, depend on the the mass difference between the two neutrino states $\Delta m^2_{l,l'}$, the distance to energy ratio $L/2E$ of the system under study and of course the mixing matrix U. In the scenario of three neutrinos ν_{jL}, fits to the experimental data allow to constrain the mass differences between the species to be [22]:

$$\begin{aligned} |\Delta m^2_{21}| &\approx 7.5 \cdot 10^{-5}\ \mathrm{eV} \\ |\Delta m^2_{31}| &\approx 2.3 \cdot 10^{-3}\ \mathrm{eV} \\ |\Delta m^2_{21}|/|\Delta m^2_{31}| &\approx 0.032 \end{aligned} \tag{1.43}$$

As electrically neutral particles, neutrinos could in principle be described as Dirac or Majorana spinors. While in the former description the neutrino would be its own anti-particle, the latter one makes use of the same formalism as used to describe charged leptons. Therefore, lepton number would not be a conserved quantity. Neutrino oscillation experiments do not allow to conclude on these questions, but searches for neutrinoless double beta decay, for example, might provide insight into this. Besides the open question about the exact realisation of neutrino mass terms, searches for additional sterile neutrino species, measurements of the absolute neutrino mass scale and theoretical models trying to explain the extreme mass ratios between neutrinos and the charged leptons, provide a large field of developments for physics beyond the SM.

Dark Matter

From measurements of the rotation velocities of galaxies, gravitational lensing effects and the bullet cluster observation, it is well established that dark matter exists, a form of matter which interacts only very weakly with the electromagnetic sector and is stable on cosmological time-scales. Performing a fit of cosmological models to the power spectrum of the cosmic microwave background (CMB) and other experimental data, allows to extract the contribution of dark matter to the overall energy density. One finds a contribution of approximately 26.8%, while ordinary baryonic matter only accounts for about 4.9% [45]. The largest contribution to the overall energy density is accounted for by a cosmological constant in the standard cosmological model. Several models exist, trying to explain dark matter by *Weakly Interacting Massive Particles*, *Axions*, *sterile neutrinos* or *primordial black holes*. None of these models has yet been experimentally proven to be realised in nature. The prediction of a dark matter candidate is one attractive feature of R-parity conserving super-symmetric extensions of the SM, which are searched for by the LHC experiments.

Baryon Asymmetry

Our universe seems to be completely dominated by matter. The three Sakharov conditions [46] need to be met for a baryon asymmetry to occur. One of these conditions requires baryon number violation, which is absent in perturbative descriptions of the SM. In addition, CP violating processes must be present. The CP violation in the weak interaction though, is not strong enough to explain the observed baryon asymmetry. Both conditions therefore suggest that physics beyond the SM accounting for strong CP and baryon number violating effects becomes relevant at higher energy scales than experimentally probed today.

Fine Tuning of Parameters

The dimensionless parameters of the SM span a huge numerical range, which is not motivated by any underlying principle. For example a CP violating term $(F_{\mu\nu}\tilde{F^{\mu\nu}})$ in the Lagrangian of QCD is consistent with gauge symmetry, but strong interactions seem to be invariant under CP. This is referred to as the strong CP problem. The relative strength of the CP violating interaction term is described by the QCD vacuum angle θ, which is constrained by measurements of the electric dipole moment of the neutron to be $|\theta| < 1.5^{-10}$ [47]. Another parameter which seems to be unnaturally tuned is the bare Higgs boson mass parameter m_H^0. This bare mass, receives large quantum corrections due to H, W, Z and top-quark loop contributions. These loop diagrams diverge quadratically with the cut-off scale Λ introduced in the renormalisation procedure. This is not an inconsistency of the theory since the renormalisability guarantees that the divergent part can be cancelled by a counterterm. But it is troublesome if the cutoff scale is interpreted physically as the typical energy scale, at which the SM as effective theory breaks down. In that case, choosing large values for the cut-off scale Λ requires the bare Higgs boson mass parameter to be fine tuned to a high precision to balance the quantum corrections to arrive at a mass at the electroweak scale.

1.2. Phenomenology of Proton-Proton Collisions

Analyses of high energy physics experiments are mostly based on measuring event rates in certain phase space regions. The number of scattering events of a particular process in collisions in a collider like the LHC is proportional to the scattering cross section σ and the integrated *luminosity*

$$N_{\text{scatter}} = \sigma \times \int \mathcal{L} dt \tag{1.44}$$

The luminosity $\mathcal{L}$, combines the experimental parameters of the collider and for two colliding beams of proton bunches it is roughly given by

$$\mathcal{L} = \frac{f n N_1 N_2}{2\pi \Sigma_x \Sigma_y} \tag{1.45}$$

where f denotes the revolution frequency, n the number of bunches, $N_{1/2}$ the number of protons per bunch in the two beams and $\Sigma_{x/y}$ the horizontal and vertical beam widths under the assumption of a Gaussian density profile. The time integrated luminosity is measured in units of (cm^{-2})[6]. Due to the direct proportionality between the expected number of events and the luminosity, a precise measurement of the luminosity is crucial for measuring cross sections and event rates. Chapter 2.2.5 briefly introduces the detectors used to measure the luminosity in ATLAS.

---

[6] In high energy physics it is common to measure cross sections in units of barns [1 b $\equiv 10^{-24}$ cm^2]

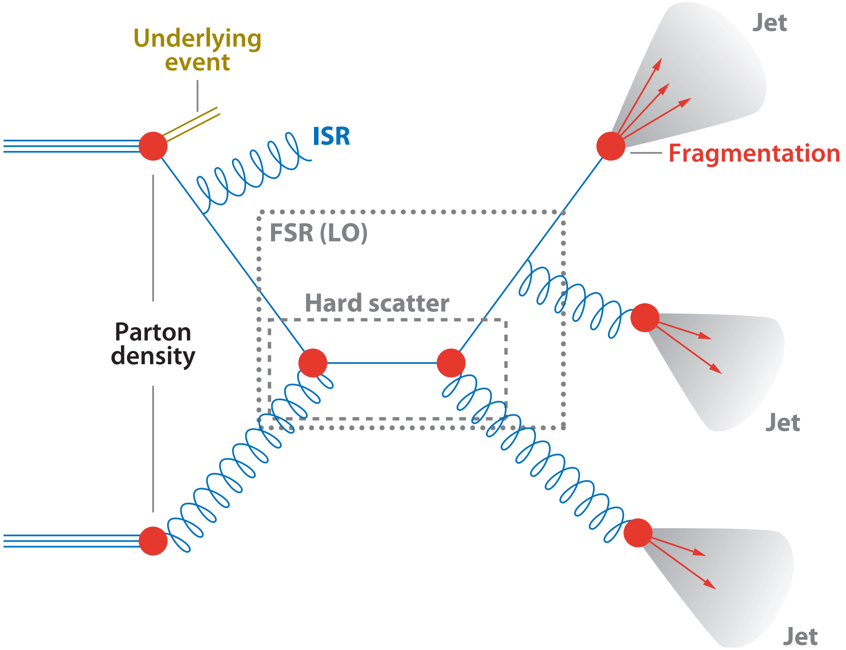

Figure 1.7. *Schematic view of a proton-proton collision. The momentum distributions of two initial state partons are described by the PDFs, the hard scatter event is described by a matrix element calculated in perturbation theory followed by phenomenological models for soft QCD effects as parton showering and hadronisation (fragmentation). Taken from Ref. [48].*

The cross section σ of the process under study is the quantity which is predictable by theory. In proton-proton collisions, composite hadrons are colliding and therefore the cross section depends on the dynamics of the compound proton system as well as on the *hard scattering* process between quarks and gluons. The factorisation theorem allows to treat these domains separately, making use of *parton-density functions* (PDF) and the partonic cross section (see also Ref. [49] for a detailed discussion of the factorisation theorem). Figure 1.7 shows a schematic overview of a proton-proton collision. The proton remnants undergo a series of low energy interactions, denoted as *underlying event*. The initial or final state particles of the hard scatter might carry colour and electric charge, so that additional *initial* (ISR) or *final state* radiation (FSR) may occur. Finally, the colour charged final-state partons will *hadronise* into a spray of colour neutral hadrons, due to confinement. In this series, interactions of many typical energy scales are involved and to describe them, phenomenological models of non-perturbative effects must interplay with theoretical predictions for the hard scattering process. To compare theoretical predictions with data, the instrumental detector effects need to be taken into account. Thus, a detailed detector simulation accurately models the particle-matter interactions in the various sub-detectors of ATLAS. The following section gives an overview of the chain of various tools needed to accurately simulate proton-proton collisions.

1.2.1. Parton-Density Functions and Factorisation

In the parton model of QCD, the hadronic cross section of two colliding hadrons $h_{1,2}$ can be written as [50, 51]

$$\sigma_{h_1,h_2} = \sum_{a,b} \int_0^1 dx_1 \int_0^1 dx_2 f_{a/h_1}(x_1, \mu_F) f_{b/h_2}(x_2, \mu_F) \int d\hat{\sigma}_{a_1,a_2}(x_1 P_1, x_2 P_2, \mu_F) \tag{1.46}$$

where the functions $f_{a/h}(x, \mu_F)$ are the parton-density functions, giving the probability of finding a parton a of momentum $x \times P$ in a hadron h of momentum P. These PDFs are convoluted with the partonic cross section $d\hat{\sigma}_{a_1,a_2}$ and the sum runs over all initial state partons a, b. Formula (1.46) is known as the factorisation theorem, since it states that the dynamics of the hadronic substructure can be described by PDFs independent of the hard scatter process under study. The dynamics of this hard scatter is described in a partonic cross section of fundamental initial state particles. This quantity can be calculated in perturbation theory. The factorisation scale μ_F determines the boundary between soft physics described as hadronic structure and what is regarded as being part of the hard scatter. Most importantly, the logarithmic divergencies for soft gluon emission of the incoming partons can be truncated at this scale and are so absorbed in a redefinition of the PDFs. The choice of μ_F is of course arbitrary and the scaling behaviour of the PDFs with the momentum transfer scale Q^2 ensures the independence of physical observables. This scaling is described by the Dokshitzer–Gribov–Lipatov–Altarelli–Parisi (DGLAP) evolution equations [52–54]. At finite order in perturbation theory, a remaining dependence on μ_F is present, indicating the uncertainty of the prediction due to missing higher order corrections. Since PDFs cannot be calculated in perturbative QCD, they need to be extracted from experimental data, mainly from deep inelastic scattering experiments. Several collaborations perform combined fits to such datasets, with small differences in the exact choice of input data and the chosen parametrisation of the parton-density functions. Among others, the following sets provide recent results: CTEQ[55, 56], MSTW[57], NNPDF[58]. Experimental uncertainties of the input data, uncertainties on the strong coupling α_s and the functional form used as parametrisation are the major uncertainties in PDF fits. Figure 1.8 shows the parton density as a function of x as provided by the MSTW2008 PDF set and its uncertainty at two different momentum transfer scales, visualising the scaling behaviour. Probing the proton structure at higher energy scales, enhances the soft gluon and sea quark contributions.

1.2.2. Partonic Cross Sections and Event Generation

If the energy scale of the hard scattering process is large enough to allow for a perturbative treatment of QCD, the partonic cross section $\hat{\sigma}_{a_1,a_2}(\mu_F)$ can be

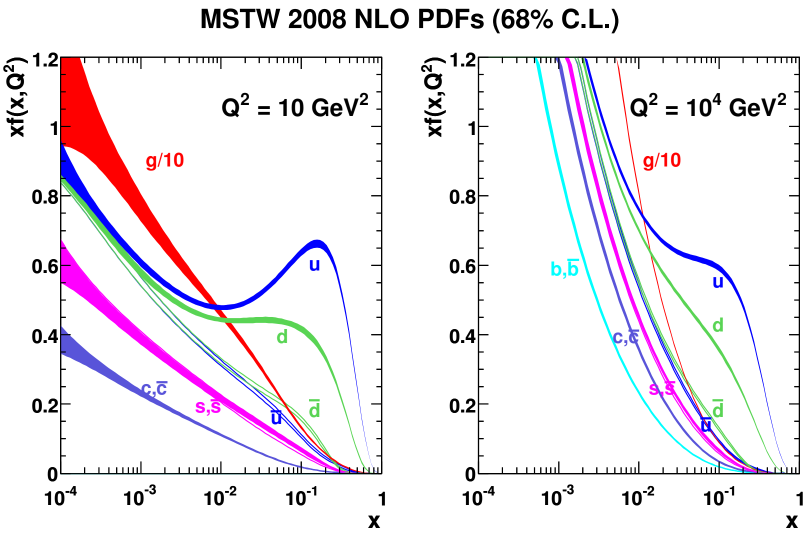

Figure 1.8. *Parton densities as a function of* x*, as provided by the MSTW2008 PDF set at* $Q^2 = 10$ *GeV* ^{2} *(left) and* $Q^2 = 10^4$ *GeV* ^{2} *(right), visualising the scaling behaviour. The* x*-dependence is extracted from a combined fit to experimental data [57].*

expanded in powers of the strong coupling constants

$$\hat{\sigma}_{a_1,a_2}(\mu_F) = \sum_{n=1}^{\infty} \alpha_s^n(\mu_R)\hat{\sigma}_n(\mu_F, \mu_R) \tag{1.47}$$

where μ_R denotes the renormalisation scale which has already been touched upon in Section 1.1.3. The SM as renormalisable theory allows, order by order, to absorb certain divergencies in a redefinition of the coupling constants. Again, the physical observable does not depend on the choice of μ_R as it is the case for μ_F, but in fixed order calculations residual dependencies remain. In practice, the scale choices are usually varied to estimate the uncertainty due to missing higher order corrections in fixed order calculations. Reviews about renormalisation procedures can be found in textbooks, e.g. Ref. [18].

At fixed order in α_s, the cross sections can be constructed using the Feynman rules of the theory. Higher order corrections to the leading order calculation involve loop (virtual corrections) and real emission diagrams. The necessary integrations are often carried out numerically. To compare the theoretical predictions with the experimental observation, detector acceptance and experimental efficiency effects need to be taken into account. Furthermore, measurements often involve differential distributions, so that a proper modelling of a multi dimensional phase space is required. So called *Monte Carlo Event Generators* perform the numerical integrations and generate sets of four-momenta of the final state particles such that whole event samples are generated, allowing for detailed studies of differential distributions. Figure 1.9 gives an overview of typical cross sections of SM processes at the LHC, spanning many orders of magnitude. The production of multiple jets by QCD processes is a dominant contribution to the total cross section at the LHC and therefore is an important background in nearly every physics analysis. Such events will be referred to as QCD multijet events in the following.

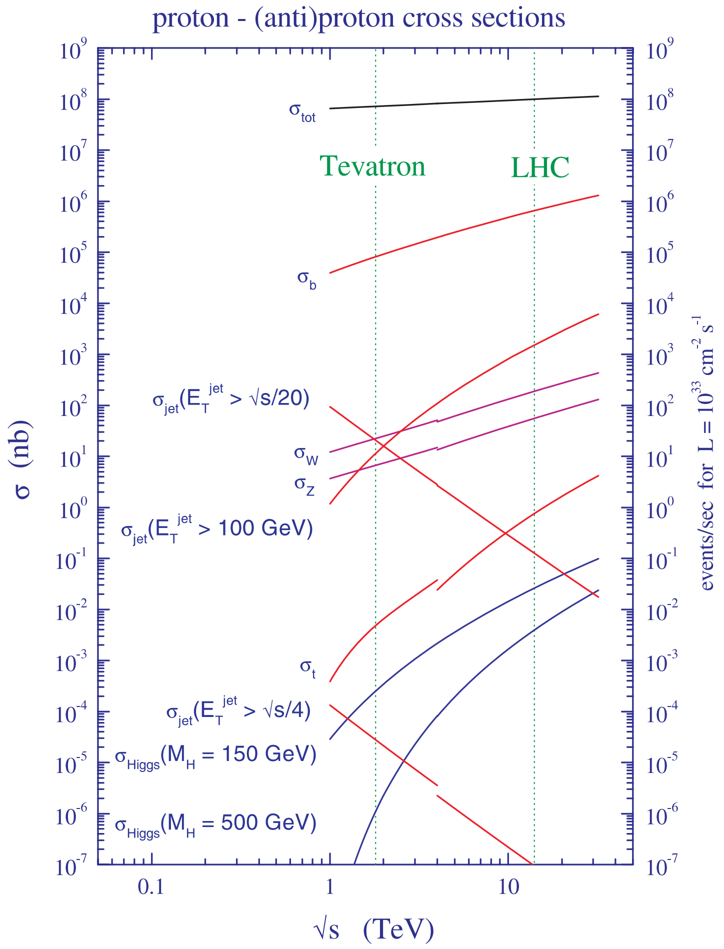

Figure 1.9. *Standard model cross sections for typical processes under study at the LHC as a function of the centre-of-mass energy [50]. The discontinuity at* $\sqrt{s} = 4$ *TeV occurs from assuming* $p - \bar{p}$ *collisions as used at the Tevatron for lower energies, while* $p - p$ *collisions are assumed for higher energies.*

1.2.3. Parton Shower

In hadron collider experiments, typical event selection criteria are inclusive in the number of final-state partons. The emission of additional quarks, gluons, as well as photons, is therefore an important property, since these can significantly alter the leading order cross sections. For most important SM processes, NLO calculations are available, describing one extra emission, which often does not suffice. Due to the large phase space available in high energy hadron collisions, the number of partons in the final state can easily exceed two or more. To model inclusive final states, tree-level calculations can be used, which include the desired final state plus additional partons whose kinematics are described by the full matrix element. The Alpgen [59] event generator for instance, implements processes with additional parton emission, as $pp \to Z/\gamma^* \to \tau^+\tau^- + \mathrm{n}$ partons with $n \leq 6$.

Real emissions exhibit divergencies in the soft (emissions of partons with negligible momentum) and colinear limit (emissions of partons under a very small opening angle with respect to the emitting parton), which would be cancelled by corresponding interference terms involving loop contributions. To realistically describe radiation in these enhanced phase space region, parton shower algorithms model the emission of quarks and gluons based on a re-summation of the leading logarithms to all orders. The splitting functions $P_{i\to jk}$ describe the probability of parton i to split into partons j, k [60]. An additional emission of a parton on top of a process with LO cross section σ_0 can so be written as

$$d\sigma \approx \sigma_0 \sum_{i\to jk} \frac{\alpha_s}{2\pi} \frac{d\theta^2}{\theta^2} P_{i\to jk}(z,\theta) d\phi dz \tag{1.48}$$

where z is the energy fraction carried by the emitted parton j and θ and ϕ denote the opening angles with respect to the parent. Such expressions can be written down for different parametrisations of the emission phase space, like for example the virtuality $q = z(1-z)\theta^2 E^2$ of the internal parton line, instead of its opening angle. Different parton shower algorithms do indeed use different parametrisations. The parton shower approach is based on an ordered evolution of splittings, starting with the original final-state partons evolving down in the quantity chosen for the ordering. The splitting procedure is stopped, once a resolution criteria is met. This defines a cut-off to avoid the soft and colinear divergencies. The implementation of such algorithms is based on the *Sudakov form factors* $\Delta_i(Q^2, q^2)$ giving the probability of having no splitting, which would lead to virtualities between Q and q (depending on the chosen ordering of course). For $q \to 0$ the Sudakov form factor will vanish, pointing at the divergent probability for colinear emissions. Drawing random numbers ρ between $[0,1]$ and solving $\Delta_i(Q^2, q^2)$ for q, generates a potential splitting, which is performed if q is greater than the chosen cut-off scale $q > Q_0$. The procedure is repeated on the new final-state partons, but starting now at the scale q. The starting scale Q for the first emission is chosen differently among different implementations, but it is usually of the order of the scale of the hard scatter event to prevent situations where the emission is harder than the scattering process described by the matrix element.

Different implementations exists, all making specific choices and therefore yielding slightly different results. Most commonly used are Pythia [61, 62], Herwig [63] and Sherpa [64], where interfaces allow showering of events produced from different event generators. Complications arise when the matrix element final state was generated using higher order precision (e.g. NLO). Then a significant overlap exists, between the emission included in the matrix element calculation and the ones from the parton showering. Matching algorithms need to be defined to allow a coherent treatment of such generators by the parton shower and are implemented for example in MC@NLO [65], POWHEG [66, 67] for NLO matrix elements and in ALPGEN [59] for leading order n-parton tree level generation.

Even though the different algorithms differ in detail, they all separate phase space regions described by the matrix element from phase space regions described by the parton shower by some resolution measure, for example the transverse momentum with respect to the emitting parton. A detailed discussion of different implementations can be found for example in Ref. [68].

1.2.4. Hadronisation

Colour charged partons in the final state of the hard scattering process hadronise due to the confinement property of QCD. As discussed in Section 1.1.3 such interactions of small momentum transfers are far beyond the perturbative regime of QCD. Instead, they are strongly coupled and non-perturbative approaches are necessary to model them. In the simulation of strong interactions this step is denoted as *hadronisation*. Different phenomenological approaches exist, all relying on the universality of the hadronisation, that it is independent of the perturbative physics at larger scales. PYTHIA applies the Lund-String-Model [61, 69]. Schematically it is based on an effective potential energy model, linearly increasing with the spatial separation of colour charges. Once this potential exceeds the quark-pair creation threshold, these strings create a pair of quarks. This procedure is repeated until stable, colourless hadrons are formed once the kinetic energy of the partons is low enough. Especially the flavour distribution during the string fragmentation is controlled via free parameters, which need to be tuned to reproduce experimental data. An alternative procedure is implemented in HERWIG: The cluster hadronisation model. In cluster hadronisation models, gluons are forced to split into quark-antiquark pairs at the shower cutoff scale and the adjacent colour lines form colour neutral clusters. These clusters can be regarded as superposition of hadron states, so that a subsequent decay of such clusters into stable hadrons can be constructed based on their properties, like lifetimes and spin states. The shower cut off scale represents the most important parameter in this approach. For a more thorough discussion of these hadronisation models see Refs. [60, 61, 70]. Both approaches are followed by the decay of the unstable hadrons into hadrons with sufficiently large lifetimes to be regarded as stable.

The decay of τ-leptons requires some care due to polarisation effects and the low relative momenta between the decay products and is handled within TAUOLA [71].

1.2.5. Underlying Event

Since the initial state of the hard scatter interaction is extracted from the two incoming protons, the remnants of these undergo soft interactions denoted as *underlying event* (UE). An accurate model of the underlying event is of high interest, since soft particles from the UE can impact the performance of high momentum measurements significantly, like for instance the determination of missing E_T (see Sec. 3.7) and jet-energy calibrations. As all strong interactions at low energy scales, the underlying event can only be modelled on a phenomenological basis. Several such models exist and are implemented in the common multi-purpose Monte Carlo event generators. Usually these models include various parameters which can be used to tune the model to reproduce certain experimentally accessible observables like the charged particle multiplicity [72, 73].

1.2.6. Pile-up

Besides the underlying event, another origin of soft QCD interactions exists: *Pile-up*. Pile-up denotes multiple proton-proton interactions per bunch-crossing and presents a major issue in the high luminosity environment of the LHC. In the LHC, bunches of up to 10^{11} protons with a transverse size of about 16μ m collide. The expected number of interactions per bunch crossing varies with the exact run conditions, but easily exceeds the mean value of 20 as obtained during the 2012 data taking period. This large number of interactions makes it crucial to also model these additional interactions. This is done by generating an inclusive sample of proton-proton collision events and by overlaying them with the hard scatter event. To mimic as close as possible the conditions in data, the number of overlaid events is varied and later reweighted to match the actual distribution of the number of interactions per bunch crossing in data. Details about the LHC run conditions are presented in Section 2.3.

1.2.7. Detector Simulation

ATLAS is an extremely complex detector, consisting of multiple sub-detectors and millions of readout channels. Generated events including non-perturbative corrections like parton showering, hadronisation and pile-up overlay are therefore passed through a detailed detector simulation based on GEANT4 [74]. This detector simulation fully simulates the particle-matter interaction and produces output data in the same format as produced by the actual experiment. That way it is ensured that simulated event samples can be passed through the same reconstruction and analysis chain as actual data. This simulation includes trigger conditions in varying data taking periods as well as known detector defects. The ATLAS simulation infrastructure is described in detail in Refs. [75, 76].

1.3. Phenomenological Overview of Higgs Boson Production and Decay

The general structure of the Higgs mechanism and the couplings between the predicted Higgs boson and other SM particles were discussed in Section 1.1.5. For

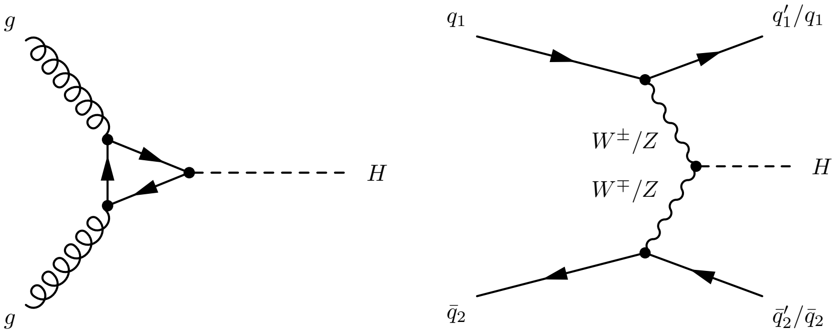

(a) Gluon fusion (b) Vector boson fusion

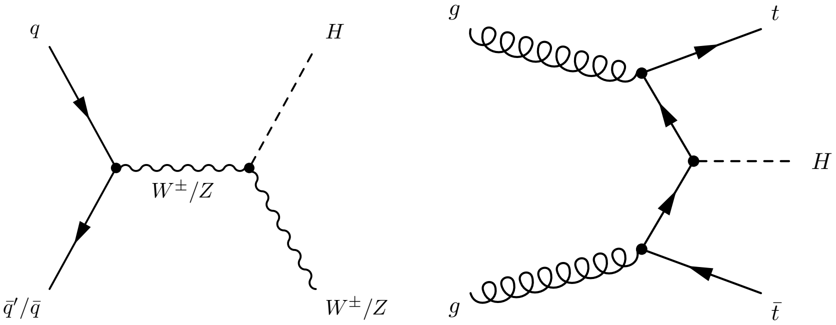

(c) Higgs-strahlung (d) Associated production

Figure 1.10. *Feynman diagrams of the four main production mechanisms of Higgs bosons at the LHC.*

experimental searches, in addition a precise phenomenological picture is needed to develop and optimise analysis strategies and of course to compare results with the SM predictions at high accuracy. In the following, the main production mechanisms and decay channels of Higgs bosons at the LHC are discussed, as well as the SM predictions used in the course of this thesis. A short overview over the main experimental search channels closes the section.

1.3.1. Higgs Boson Production at the LHC

Higgs boson production at the LHC is dominated by four mechanisms: Gluon (ggF) and vector-boson-fusion (VBF), the Higgs-strahlung (VH) process and the production in association with a top-quark pair (ttH). The leading order Feynman diagrams of these processes are shown in Fig. 1.10.

For Higgs boson masses $m_H < 1$ TeV, the gluon fusion process via a heavy quark loop is the dominant production mode, mainly due to the large contribution of gluons to the proton PDF at small momentum fractions x. Due to the large top-quark Yukawa coupling, the loop is dominated by the top-quark contribution. The VBF production cross-section is one order of magnitude smaller than the corresponding ggF cross section. This process is initiated by two quarks radiating weak vector bosons which then annihilate into a Higgs boson. The final state contains two quarks at tree level, widely separated in pseudorapidity η, so that this process provides a distinct signature exploited in experimental searches to suppress background processes. Higgs-strahlung denotes the annihilation of a quark pair into a weak vector boson, which radiates a Higgs boson. If decaying leptonically, the vector boson provides a high p_T lepton, which can be used for trigger purposes for example in the search for hadronically decaying Higgs bosons. Production in association with a top-quark pair is initiated by two gluons at tree level, each splitting into a top-quark pair of which two quarks annihilate into a Higgs boson. The two heavy top quarks in the final state limit the available phase space, so that the ttH process has the smallest cross section of all relevant Higgs boson production mechanisms at the LHC and is expected to not contribute significantly to the final state and signal regions discussed in this thesis.

The Higgs cross-section working group, founded in 2010, aims at providing a set of state-of-the-art theory calculations and SM predictions of Higgs boson phenomenology to the LHC experiments. It summarised recent developments on higher order corrections on Higgs boson production cross-sections, as well as Higgs boson decay branching ratios (BR) in three reports [77–79]. Their recommendations are followed throughout this thesis. Details on the calculations can be found in these reports and the Refs. therein.

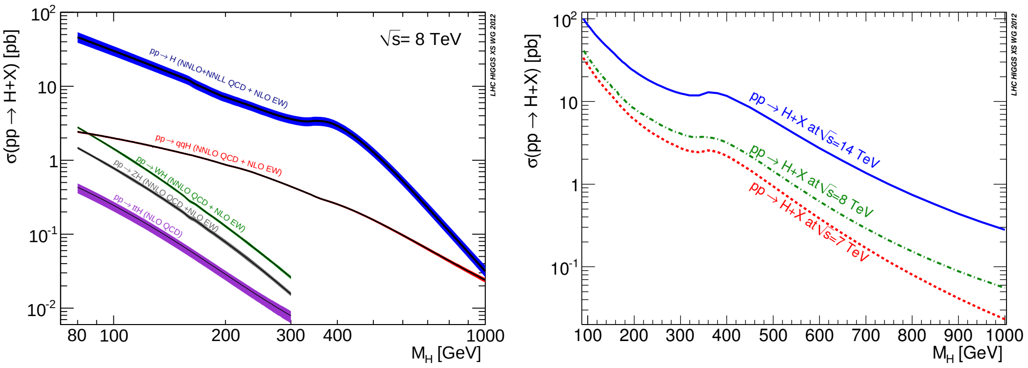

(a) (b)

Figure 1.11. *Production cross-section of a Higgs boson at the LHC. Shown are the contributions of the main production mechanisms at* $\sqrt{s} = 8$ *TeV including NNLO QCD and NLO EW corrections (a) and the inclusive cross section for centre-of-mass energies of 7,8 and 14 TeV (b) as a function of the Higgs boson mass* m_H*. Figures taken from Ref. [77–79].*

The gluon fusion cross section is calculated at NLO in α_s including the effects of finite top and bottom quark masses. The size of the NLO correction is large and of the order of $80-100\%$. Contributions from soft gluon emissions are resummed consistently to all orders at the next-to-leading-log (NLL) approximation. Further QCD corrections at NNLO and NNLL are included in the heavy top-quark limit and yield corrections of about $\sim 25-35\%$. In addition, electroweak (EW) corrections are added and their size depends strongly on the Higgs boson mass. At $m_H = 125$ GeV and $\sqrt{s} = 8$ TeV, the ggF process has a cross section of $\sigma_{\mathrm{ggF}} = 19.27$ pb. Theoretical uncertainties arise from missing higher order corrections, the uncertainties of the PDF and the numerical value of the strong coupling constant, as well as from finite quark mass effects. Differential distributions and cross sections, exclusive in the number of jets, are subject to larger uncertainties than the inclusive cross sections. A NNLO calculation for example effectively describes a two jet final state at leading order only. The Higgs boson production cross-section uncertainties are therefore estimated taking into account the specific selection criteria applied in the analysis and are summarised in Section 5.7.

The VBF cross section is fully calculated at NLO in the strong as well as in electroweak couplings. The NLO QCD corrections are relatively small and of the order of $5-10\%$. Electroweak corrections depend strongly on the renormalisation scheme and are of the order of -5%. In addition, NNLO QCD corrections are known approximately, from a structure-function based calculation which misses certain contributions and interference effects. These are nevertheless expected to be small. Like this, the remaining scale dependence can be reduced to about $\pm 1\%$.

The cross sections of the WH and ZH processes include the full QCD corrections up to NNLO as well as electroweak corrections at NLO. The scale uncertainties on the inclusive cross sections are of the order of $\pm(1-3)\%$.

Figure 1.11(a) shows the Higgs boson production cross-sections at the LHC as a function of m_H, and Table 1.3 summarises them for a Higgs boson mass of $m_H = 125$ GeV as well as the inclusive scale and PDF uncertainties. The dependence of the inclusive production cross-section on the centre-of-mass energy is visualised in Fig. 1.11(b) for the two main configurations of LHC Run 1 (7 TeV, 8 TeV) and the design centre-of-mass energy of $\sqrt{s} = 14$ TeV.

Process	$\sigma_{\mathrm{incl.}}$ [pb]	δ_{μ_R,μ_F}	$\delta_{\mathrm{PDF}+\alpha_s}$
ggF	19.27	$^{+7.2\%}_{-7.8\%}$	$^{+7.5\%}_{-6.9\%}$
VBF	1.58	$^{+0.2\%}_{-0.8\%}$	$^{+2.6\%}_{-2.9\%}$
WH	0.705	$\pm 1\%$	$\pm 2.3\%$
ZH	0.415	$\pm 3.1\%$	$\pm 2.5\%$

Table 1.3. *Inclusive Higgs boson production cross-sections and their main uncertainties at the LHC at $\sqrt{s} = 8$ TeV and $m_H = 125$ GeV. The numbers are based on calculations at NNLO in QCD and NLO in EW. The calculations are summarised in Ref. [79].*

1.3.2. Higgs Boson Decays

As seen in Section 1.1.5, the Higgs boson couplings to vector bosons and fermions are proportional to m_V^2/v and m_f/v respectively. Therefore, the branching ratios of direct Higgs boson decays is driven by the masses of the decay products. The total width and branching ratios are determined including higher order corrections from QCD and EW processes. The partial widths are calculated with two software packages HDECAY [80, 81] and PROPHECY4F [82, 83], implementing the highest accuracy calculations available for each process. Theoretical uncertainties on the branching ratios arise from missing higher order corrections and parametric uncertainties, denoting uncertainties on SM input parameters like α_s or quark masses, propagated to the branching ratios. The branching ratio $BR(H \rightarrow \tau^+\tau^-)$ is determined up to NNNLO QCD and NLO EW corrections. It contributes significantly at low Higgs boson masses with a value of 6.3% at $m_H = 125$ GeV with an uncertainty of the order of ±6% [78]. The branching ratios of a SM Higgs boson as a function of m_H are shown in Fig. 1.12 (a), where the bands indicate the size of the corresponding uncertainties. At low values of m_H, decays into a pair of b-quarks dominate. Approaching the threshold for on-shell decays into a pair of W bosons, this decay mode takes over and dominates the total decay width over the mass range up to 1 TeV. Indirect decays via vector boson and quark loops to two photons or gluons contribute at low masses.

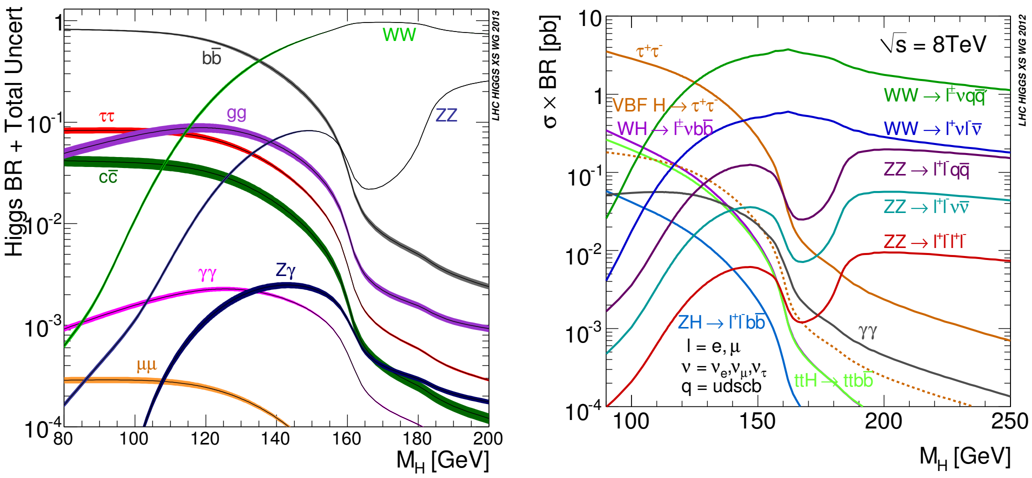

(a) (b)

Figure 1.12. *Branching ratios of a SM Higgs boson as a function of m_H (a) and the product of production cross-section times branching ratio for most important experimental search channels at the LHC (b). For $H \rightarrow \tau^+\tau^-$ the VBF (solid orange line) and ggF production (dashed orange line) are included. For Higgs boson masses around $m_H \approx 125$ GeV the decay into a pair of tau leptons is one of the major, experimentally accessible, decay modes. Taken from Ref. [79].*

1.3.3. Experimental Search Channels

Taking into account experimental considerations like triggering limitations and background-to-signal ratios, only certain combinations of production and decay modes are accessible in LHC Higgs boson searches.

Figure 1.12 (b) shows the product of production cross-section and decay branching ratio for the most common of such combinations. Despite the small branching ratio, the decay into two photons plays a crucial role in the LHC Higgs boson search programme due to its clean experimental signature. Photons can be reconstructed accurately with a very small misidentification rate from hadronic processes and feature an excellent energy resolution. The ability to differentiate between primary photons and photons from π^0 decays, by the use of finely segmented detectors further reduces the background level in this channel. The di-photon final state is accessible only in a narrow mass range between $110 - 140$ GeV. In this region though, it offers not only a good sensitivity to the overall signal strength but also a precise handle on the Higgs boson mass. The $H \to ZZ^* \to \ell\ell\ell'\ell'$ channel, where ℓ denotes either an electron or muon, is an important search channel in a broad mass range. As in the di-photon channel, the full event can be reconstructed with the advantage that the decays of the Z bosons provide access to additional polarisation information for spin and CP quantum number measurements. The four lepton final state is relatively background free, as nearly no hadronic background processes contribute, and offers a high mass resolution due to the high muon momentum and electron-energy scale resolutions. Due to the low branching ratio though, the sensitivity of this search channel is limited by the data-sample size. The Higgs boson mass is measured by the LHC experiments, by statistically combining the individual results of the di-photon and four-lepton final state measurements.

Higgs boson decays into a pair of W bosons is the dominant decay mode over a large mass range. To reject high rate backgrounds from $W+$jets events, the search focuses on the fully leptonic final state $WW^* \to \ell\nu\ell'\nu$. Due to the two neutrinos in the final state, the event cannot be fully reconstructed and the mass resolution is poor. The dominant backgrounds arise from diboson and top-pair production processes. Due to the high branching ratio, the WW^* search channel is sensitive to the spin quantum number of the Higgs boson as the shape of angular distributions of the decay products can be exploited.

Fully hadronic final states like $H \to b\bar{b}$ are difficult to isolate from the large background arising from multijet processes. To suppress such background events and to allow for an effective triggering using a leptonic signature, the search for $H \to \bar{b}b$ decays focuses on the associated Higgs boson production with a leptonically decaying vector boson. Apart from the ditau final state, the search for $H \to \bar{b}b$ is the only search channel in leptonic decay modes.

Among these experimentally accessible combinations of production and decay modes, the VBF $H \to \tau\tau$ channel offers the largest $\sigma \times$ BR at low Higgs boson masses. Background events arise from $Z \to \tau\tau$ decays with kinematic properties very similar to those of the signal process. The VBF production mechanism offers a distinct event topology which can be used to suppress these backgrounds to a large extent. Together with the WW^* channel, the $H \to \tau\tau$ decay mode provides the strongest sensitivity to this production mechanism. Given the amount of data collected at LHC Run 1, the decay into a pair of tau leptons is furthermore the only accessible decay mode into leptons. It therefore directly probes the Yukawa coupling of the Higgs boson to tau leptons and is an important component to test the responsible mechanism for fermion mass generation. As a down-type SU(2) particle, a measurement of the Higgs boson coupling strength to tau leptons also allows for comparisons to the relative coupling strength to up-type SU(2) fermions like top quarks, which is accessible via the top-quark loop contribution in the ggF production process. In the following section, a brief overview over tau-lepton decays is given. Experimental considerations and the overall analysis strategy is discussed below in Section 5.1.

Tau Lepton Decays and Combined $\tau\tau$ Final State Branching Ratios

Decay mode	Branching fraction [%]
$\tau^- \to e^-\bar{\nu}_e\nu_\tau$	17.83 ± 0.04
$\tau^- \to \mu^-\bar{\nu}_\mu\nu_\tau$	17.41 ± 0.04
$\tau^- \to \pi^-\pi^0\nu_\tau$	25.52 ± 0.09
$\tau^- \to \pi^-\nu_\tau$	10.83 ± 0.06
$\tau^- \to \pi^-\pi^0\pi^0\nu_\tau$	9.30 ± 0.11
$\tau^- \to \pi^-\pi^0\pi^0\pi^0\nu_\tau$	1.05 ± 0.07
$\tau^- \to K^-\nu_\tau$	0.700 ± 0.010
$\tau^- \to K^-\pi^0\nu_\tau$	0.429 ± 0.015
$\tau^- \to \pi^-\pi^-\pi^+\nu_\tau$	8.99 ± 0.06
$\tau^- \to \pi^-\pi^-\pi^+\pi^0\nu_\tau$	2.70 ± 0.08

Table 1.4. *Main decay modes and the corresponding branching ratios of tau leptons. They equally apply to the charge conjugate decays. The branching fractions are the result of a combined fit to experimental data, taken from Ref. [22].*

Tau leptons are the heaviest leptons with a mass of $m_\tau = 1776.82 \pm 0.16$ MeV[22]. They decay after a mean life time of $\tau = (290.6 \pm 1.0) \times 10^{-15}$ s via weak charged current interactions into leptons or hadrons. This lifetime leads to a mean decay length of $\beta\gamma c\tau = 2.45$ mm in the laboratory frame for an energy of $E_\tau = 50$ GeV. The main leptonic decay modes are three body decays $\tau^\pm \to l^\pm\nu_\tau\bar{\nu}_l$ $(l = e, \mu)$, with a combined branching ratio of 35.24% ± 0.08% [22]. Leptonic decays with multiple charged particles are very rare with branching ratios below 3×10^{-5}. A variety of hadronic tau decay modes exist, where the majority proceed into final states with pions and in rare cases kaons. They can be further distinguished by the number of charged particles among the decay products. Hadronic decays with three charged particles have a combined branching ratio of approximately 15.2% and are denoted as *3-prong decays* ($\tau_{3-\mathrm{prong}}$), while hadronic decays into one charged particle contribute approximately 49.5% to the total decay width and are referred to as *1-prong decays* ($\tau_{1-\mathrm{prong}}$). Table 1.4 lists the dominant decay modes of tau leptons together with the corresponding branching ratios. Throughout this thesis, leptonically decaying tau leptons will be referred to as τ_{lep}, hadronic decays as τ_{had}.

The combined branching ratios for fully leptonic, fully hadronic and lepton-hadron final states in $H \to \tau\tau$ events are 12.4%, 42% and 45.6%, respectively. The lepton-hadron final state therefore provides the highest event rate. It has one light lepton and three neutrinos in the final state, while the fully hadronic decay mode accounts for nearly the same branching ratio but suffers from a larger multijet background and the need of complex triggers.

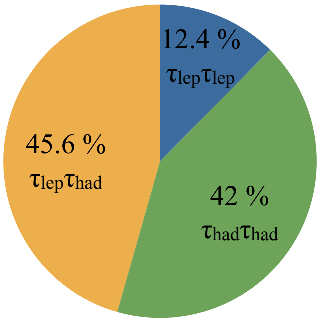

Figure 1.13. *Branching ratios of a ditau system grouped into fully leptonic, fully hadronic and lepton-hadron final states.*

1.4. Experimental Status of Higgs Boson Searches

Even though experimental evidence for the existence of the scalar particle of the Higgs mechanism has already been searched for in the early days of the SM, it was the availability of electroweak precision data from LEP and first measurements of the top-quark mass at the Tevatron, which opened a high intensity phase in the search for the Higgs boson. From electroweak fits it became clear that a light Higgs boson mass is favoured by the majority of experimental data, so that direct searches at collider experiments deemed promising. This chapter attempts to give a brief overview of the status of Higgs boson searches performed prior to the LHC programme, with a focus on $H \to \tau\tau$ searches.

1.4.1. LEP

In the second phase of the LEP programme the centre-of-mass energy was subsequently increased to up to $\sqrt{s} = 209$ GeV, pushing the kinematic boundaries of Higgs boson production to larger values of m_H. In the year 2000, LEP was shut down to allow for the beginning of construction works preparing for the LHC programme. The ALEPH, DELPHI, L3 and OPAL collaborations all performed direct and model-independent searches for Higgs bosons being produced mainly in Higgs-strahlung processes in association with a Z boson $e^+e^- \to ZH$. They were able to exclude the low mass region up to $m_H > 114.4$ GeV at 95% confidence level (CL) [84]. For such low masses, the Higgs boson decays predominantly into a pair of b-quarks, so that the four jet final state $(H \to b\bar{b})(Z \to q\bar{q})$ provided the largest sensitivity. For a mass of $m_H = 115$ GeV the branching ratio into b-quarks is approximately 74%, while it is about 7% for the decay into a pair of tau leptons. Nevertheless, searches did consider ditau final states as well, where either the Higgs or the Z boson decayed into a pair of tau leptons $(H \to \tau^+\tau^-)(Z \to q\bar{q})$, $(H \to b\bar{b})(Z \to \tau^+\tau^-)$ to maximise the sensitivity. Due to the well defined initial state, events were fully reconstructed, including the Higgs boson candidate mass. The ALEPH experiment observed an 3σ excess consistent with the presence of a Higgs boson of $m_H = 115$ GeV while the DELPHI experiment measured a deficit of events in this region. In the full combination no significant excess could be established.

1.4.2. Tevatron

The Tevatron was a proton-antiproton accelerator at Fermilab, delivering collisions at centre-of-mass energies of up to $\sqrt{s} = 1.96$ TeV until 2011. Due to the different initial state particles, the Higgs boson production mechanisms contribute differently compared to the case of p-p collisions at the LHC. Especially the Higgs-strahlung processes WH/ZH are of a comparable cross section as the VBF production for low Higgs boson masses. Therefore, the Tevatron experiment searches put a special emphasis on searches for $H \to b\bar{b}$ decays in in WH/ZH events. The lower multijet background compared to the LHC further increases the importance of this search channel. At higher masses of $m_H > 130$ GeV, Higgs boson decays to a pair of leptonically decaying W bosons presented the most sensitive search channel. The CDF and D0 experiments performed direct searches for the Higgs boson with integrated luminosities of up to 10 fb^{-1}. In the last years of running they were able to exclude the presence of a Higgs boson in two mass regions between 90 GeV $< m_H <$ 109 GeV and 149 GeV $< m_H <$ 182 GeV at 95% CL and observed a broad excess of data compared to the background expectation in a mass range between 115 GeV – 140 GeV with a local significance of about 3σ [85]. Both experiments performed dedicated searches for $H \to \tau\tau$ decays based on multivariate analysis techniques.

The CDF experiment searched for an excess in ditau final states with one tau decaying hadronically and one decaying leptonically [86]. Two dedicated boosted decision trees (BDT) were trained to separate the signal process from the dominant $Z \to \tau\tau$ background and the rest of background processes, respectively. An upper limit on the product of production cross-section times branching ratio at a mass hypothesis of $m_H = 125$ GeV of approximately $16.4 \times \sigma_{\text{SM}} \times \text{BR}_{\text{SM}}$ was set, where $\sigma_{\text{SM}} \times \text{BR}_{\text{SM}}$ denotes the SM prediction.

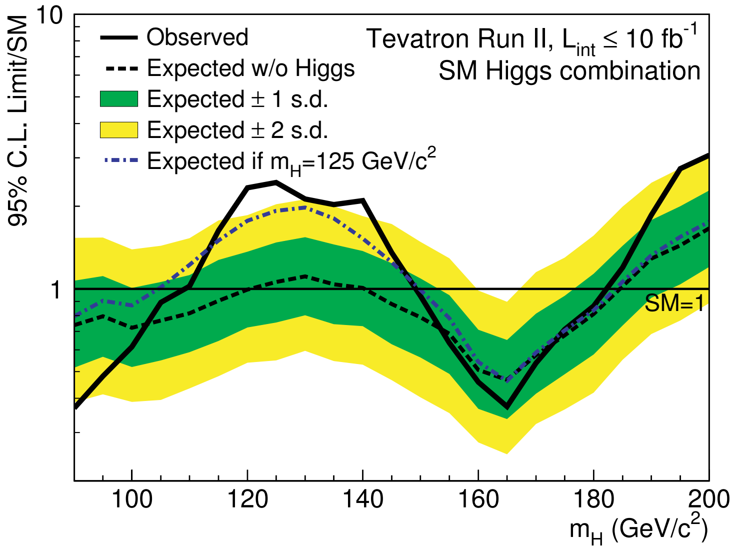

Figure 1.14. *Expected and observed exclusion limits on the product of Higgs boson production cross-section and decay branching ratio as a function of the hypothesised Higgs boson mass as resulting from the statistical combination of all search channels studied by the CDF and D0 collaborations [85].*

The D0 experiment exploited the specific topology of Higgs-strahlung events with an analysis of trilepton final states [87] and in addition performed a search in events with one light lepton, one hadronically decaying tau and at least two jets [88]. The trilepton analysis included the $\mu\tau_h\tau_h$ final state, where τ_h denotes a hadronically decaying tau lepton, and $ee\mu$ as well as $\mu\mu e$ final states, both sensitive to $H \to \tau\tau$ events with leptonic tau decays. Similar to the CDF analysis two different BDTs, trained against the dominant diboson background and other backgrounds, are used to define a region enhanced in signal process events. A limit on the production cross-section times branching ratio was set at $m_H = 125$ GeV, corresponding to 8.4 times the SM expectation while a limit of 6.3 was expected. The second analysis focused on final states with one hadronically decaying tau, one electron or a muon and at least two jets. This final state is sensitive to Higgs bosons produced via ggF, VBF and VH processes and decaying into either two tau leptons or two W bosons, of which at least one decays further into a tau lepton. This approach allows the analysis to achieve a good sensitivity over a broad mass range between 105 GeV $< m_H <$ 150 GeV. While for low Higgs boson masses the decay into a pair of taus dominates the sensitivity of the analysis, the consideration of $H \to W^+W^-$ events, allows to maintain the sensitivity also at higher mass hypotheses, where the Higgs boson decays predominantly into a pair of W bosons. A BDT is used to separate two event samples enhanced in either $H \to \tau^+\tau^-$ and $H \to W^+W^-$ decays. For both samples an additional BDT is trained to separate signal from background processes and is used in the final likelihood fit. For $m_H = 125$ GeV an upper limit on the ratio of cross section times branching ratio to the SM expectation of 11.3 was observed while a limit of 9.0 was expected.

1.4.3. LHC

Shortly after the LHC began operation in 2010 the ATLAS and CMS experiments collected a significant amount of data at centre-of-mass energies of $\sqrt{s}$ = 7 TeV and $\sqrt{s}$ = 8 TeV. This allowed to rapidly exclude broad regions of Higgs boson masses. In July 2012, both experiments announced the observation of a resonance with a mass of about 125 GeV, mainly based on analyses of the ZZ^* and $\gamma\gamma$ final states of datasets corresponding to 4.8 (5.1) fb^{-1} at $\sqrt{s} = 7$ TeV and 5.8 (5.3) fb^{-1} at $\sqrt{s}$ = 8 TeV for the ATLAS (CMS) experiments [16, 17]. Figure 1.15 shows the p-value of the background-only hypothesis[7] as a function of the hypothesised Higgs boson mass, as resulting from the statistical combination of the searches for $H \to \gamma\gamma$,$H \to ZZ^*$ and $H \to WW^*$ decays. With the full dataset of the first run period of LHC, corresponding to up to 25 fb^{-1}, the ATLAS experiment measured the mass of this particle to be $m_H = 125.36 \pm 0.37(\text{stat.}) \pm 0.18(\text{sys})$ GeV [89], while CMS measures $m_H = 125.03 \pm 0.27(\text{stat.}) \pm 0.15(\text{sys})$ GeV[90]. Evidence for the decay of the discovered particle into a pair of W bosons was found by the ATLAS and CMS collaborations for fully leptonic W decays [91, 92]. Detailed studies of the kinematic properties of events in the ZZ^*,WW and $\gamma\gamma$ final states allow to constrain both spin and parity quantum numbers of the resonance. Both experiments show clear preference for the $J^P = 0^+$ hypothesis [93–96].

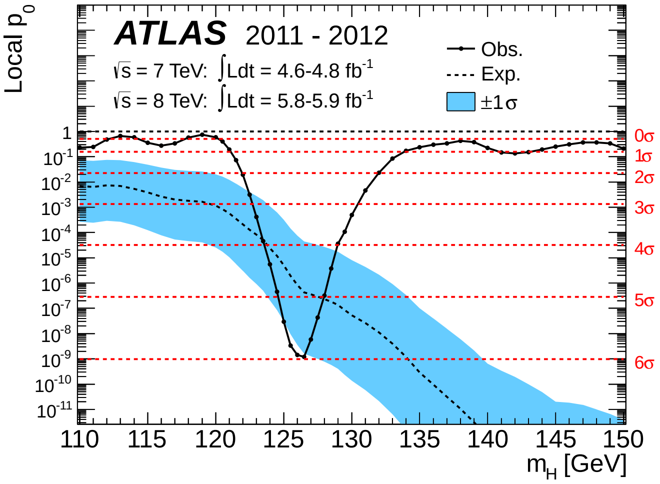

Figure 1.15. *Local p-value of the background-only hypothesis as a function of the Higgs boson mass hypothesis, as resulting from a statistical combination of the search for Higgs boson decays in the $H \to \gamma\gamma$, $H \to ZZ^* \to \ell\ell\ell'\ell'$ and $H \to WW^* \to \ell\nu\ell\nu$ channels by the ATLAS experiment, as of July 2012. The observed data disfavours the background-only hypothesis at a level of nearly* 6 *standard deviations [16] around a Higgs boson mass of $m_H \approx 125$ GeV.*

---

[7] The p-value quantifies the probability, under the assumption of the background-only hypothesis, to observe greater incompatibility to the background expectation than actually present in data. For a detailed discussion see Section 6.3.

2 The ATLAS Experiment at the LHC

The *ATLAS* experiment [97] is one of the four large experiments at the Large Hadron Collider (*LHC*) [98], located at the European Organisation for Nuclear Research *CERN* in Geneva, Switzerland. This chapter introduces the accelerator complex used to accelerate and collide the particles in the LHC in Section 2.1, as well as the various subdetectors of the ATLAS experiment in Section 2.2. Section 2.3 summarises the run conditions during the data taking periods in the years 2011 and 2012 in which the data sample analysed in this thesis was collected.

2.1. The Large Hadron Collider

The LHC at CERN is a particle accelerator which allows to accelerate and collide protons and heavy ions at highest energies. It can provide proton-proton, proton-Pb and Pb-Pb collisions. While heavy ion collisions are studied in order to gain insights into the dynamics of QCD in a dense and hot environment, the proton-proton collisions are studied to probe the fundamental interactions between partons at high energy scales. The accelerator is designed to provide centre-of-mass energies of up to $\sqrt{s} = 14$ TeV in proton-proton collisions and a whole chain of accelerators is needed to achieve this. The LHC is located in an underground tunnel with a circumference of about 27 km, which previously hosted the LEP collider. In contrast to electron-positron storage rings, proton acceleration in circular colliders is not limited by the energy loss during circulation from synchrotron radiation due to the much larger proton mass[1].

The particle beams circulating in two evacuated beam pipes are bent by a magnetic field created by 1232 super-conducting dipole magnets operating at a temperature of 1.9 K. Their field strength limits the maximum beam energy of the LHC. At the design energy of 7 TeV per proton beam, the dipoles provide field strengths of up to 8.33 T. 392 quadrupole magnets are used to focus the beams and eight superconducting cavities operating at 400 MHz are generating the electric fields used for the particle acceleration and for compensating the energy loss due to synchrotron radiation. During the acceleration phase, the particles gain 485 keV energy per turn. Once accelerated, the life time of the beams is mainly limited by the luminosity loss due to collisions in the interaction points (IP) to about $\tau = 14.9$ h. The beams are collided at four interaction points hosting the four main LHC experiments.

---

[1] The radiated power due to synchrotron radiation is proportional to $\propto 1/m^4$

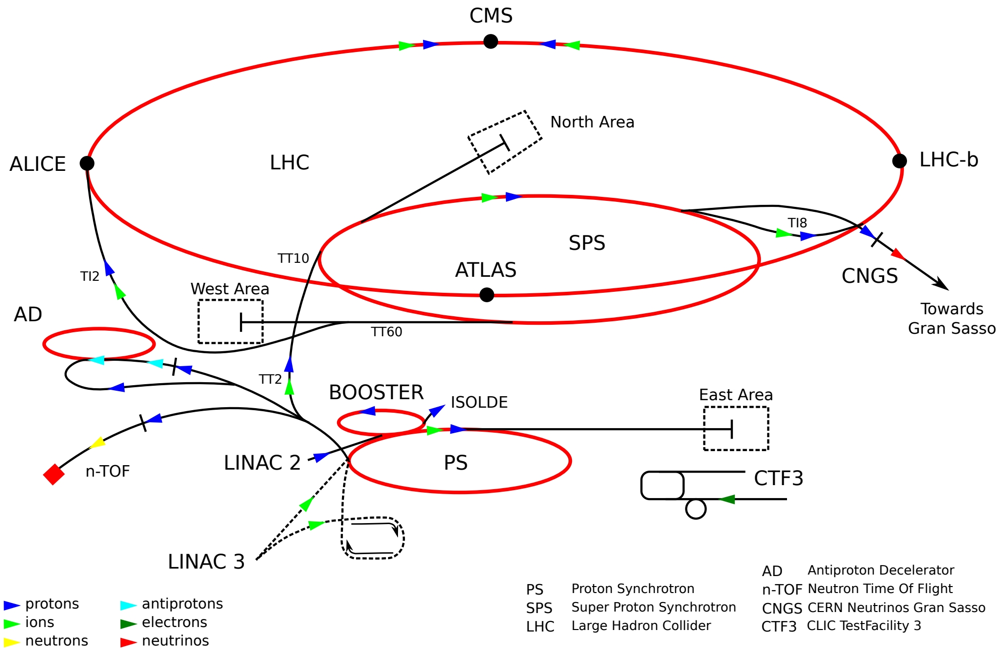

Figure 2.1. *Schematic view of the CERN accelerator complex, including the LHC injection chain consisting of the accelerators LINAC2, BOOSTER, PS and SPS [99].*

A whole chain of accelerators is used to deliver particles to the LHC. Protons, obtained by ionising hydrogen gas, are subsequently accelerated by linear accelerators to 50 MeV and grouped into bunches using radiofrequency (RF) quadrupoles. The Proton Synchrotron Booster (PSB) accelerates them further to 1.4 GeV, the injection energy for the Proton Synchrotron (PS) which provides protons of 25 GeV and generates the *bunch train* structure used at the LHC. If operated at design specifications, bunch trains consist of 72 neighbouring bunches, separated by a spacing of 25 ns followed by empty buckets corresponding to a gap of 320 ns. However, there are different filling schemes, and the LHC was mainly operated with bunch spacings of 50 ns in 2011 and 2012. The PS is followed by the Super Proton Synchrotron (SPS), which accelerates the particles to 450 GeV, the LHC injection energy. Figure 2.1 shows a schematic overview over this accelerator complex.

In total, 39 bunch trains are filled into the LHC at design conditions, so that 2808 bunches per beam are brought to collision in the LHC. Each bunch contains about 10^{11} protons. Instantaneous luminosities of $\mathcal{L} = 10^{34}$ cm^{-2}s^{-1} are achieved at the two high luminosity interaction points where the beams are crossing each other at a crossing angle of 285 μrad at design specifications. At these points, the two general purpose detectors ATLAS and CMS[100] reside, both constructed to search directly for new physics phenomena.

Besides ATLAS and CMS the LHC hosts two other large detectors, the *ALICE* detector [101] built especially for the heavy ion programme of the LHC, and *LHCb* [102], an asymmetric detector built with excellent vertex detectors for secondary vertex reconstruction to study rare b-hadron decays. Due to the higher cross sections of the processes under study, these two experiments are located at interaction points with lower instantaneous luminosities than provided for ATLAS and CMS. This limits the number of secondary collision events to ease the reconstruction of the complex event topologies.

In addition to the four large experiments, a few smaller experiments are located at the LHC. *LHCf* [103] is a far forward detector intended to study physics of cosmic rays and to deepen the understanding of forward scattering. *TOTEM* [104] aims at measuring the total elastic and diffractive cross section of proton-proton collisions which cannot be calculated by perturbative approaches. And finally *MOEDAL* [105], an experiment searching for exotic particles like magnetic monopoles.

2.2. The ATLAS Detector

ATLAS is a multi-purpose detector covering a solid angle of nearly 4π. It is intended to provide excellent resolution of basically all final state objects needed to reconstruct hard scatter events and to search for physical phenomena beyond the SM. The aim to achieve a good sensitivity in the search for the Higgs boson of the SM already in the first years of running provided performance goals which needed to be met, including:

- Good spatial resolution in vertex reconstruction for efficient identification of secondary vertices from b hadron and τ lepton decays, as well as for the identification of the primary interaction vertex.

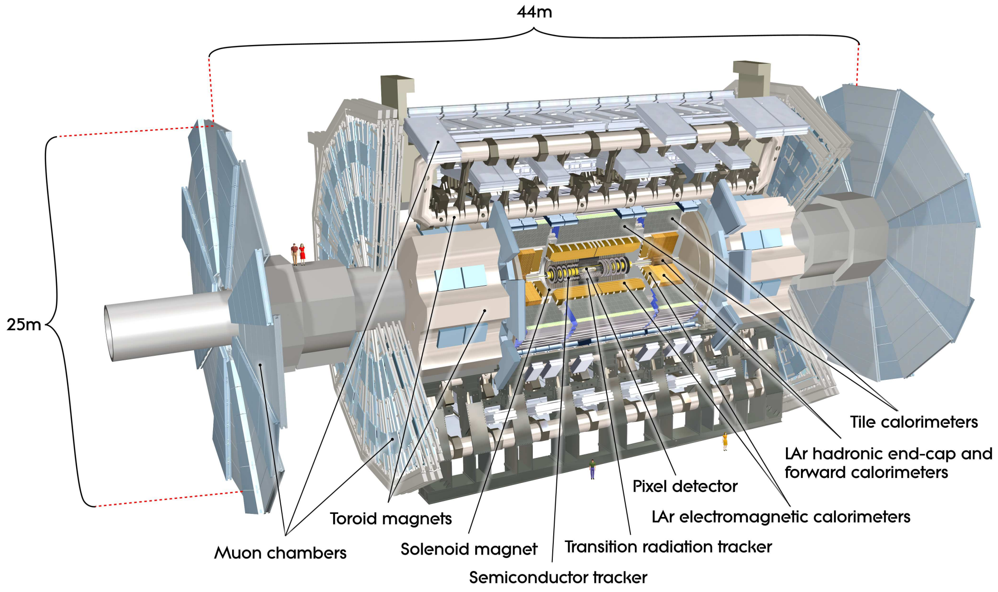

Figure 2.2. *Schematic view of the ATLAS detector and its various sub-systems [97].*

- Fine transverse segmentation of the electromagnetic calorimeter for good angular resolution in photon and electron reconstruction and for distinction of $\pi^0 \to \gamma\gamma$ decays from primary photons.
- High energy resolution for both, the electromagnetic and hadronic calorimetry for electron, photon and hadronic jet energy measurements and a precise reconstruction of missing transverse energy.
- Extremely high geometrical coverage to maximise the total detector acceptance.
- High muon momentum resolution over a wide range of momenta.
- Fast and efficient triggering to cope with the high luminosity delivered by the LHC.

Figure 2.2 gives a schematic view of the ATLAS detector consisting of the inner detector containing the vertexing and tracking subdetectors, the electromagnetic and hadronic calorimeters and the muon spectrometer. In total, ATLAS weighs about 7 kT, is about 44 m long and has a diameter of 25 m. ATLAS is a forward backward symmetric detector and contains a solenoid as well as three toroid magnets. The superconducting solenoid encloses the inner detector and provides a 2 T magnetic field to bend the trajectory of charged particles in order to allow for a momentum measurement by the tracking system. It is hosted in the same cryostat as the electromagnetic barrel calorimeter. The toroidal magnets provide the magnetic field for additional bending of the muon trajectories for a precise momentum measurement in the muon barrel and endcap spectrometers. In the following, the subdetectors are briefly introduced, based on Refs. [97, 106].

2.2.1. Coordinate System

The ATLAS coordinate system is a right-handed cartesian system, with its z-axis pointing along the beam pipe, the x-axis towards the centre of the LHC ring and its y-axis pointing upwards. Spherical coordinates are better suited to describe rotational invariant properties. The coordinates (r, ϕ, θ) are defined by $r = \sqrt{x^2 + y^2}$, $\phi = \arctan(y/x)$ and $\theta = \arctan(r/z)$. Often the pseudorapidity η is used instead of the polar angle θ where $\eta = -\ln\tan(\theta/2)$. For massless particles, the pseudorapidity coincides with the rapidity y. Since rapidity differences Δy are Lorentz-invariant, η provides a physically better suited measure of the polar angle. Table 2.1 lists a few of the most commonly used variables in the description of particle and event topologies and their definitions.

2.2.2. The Inner Detector

The inner detector measures tracks of charged particles with three sub-detectors with a coverage up to pseudorapidities of $|\eta| < 2.5$. It measures tracks of charged particles in a wide momentum range starting at about 500 MeV and provides high

Variable	Description	Definition
$\mathbf{p}$	Momentum	$p_\mu := (E, p_x, p_y, p_z)$
p_T	Transverse momentum	$p_T := \sqrt{p_x^2 + p_y^2}$
ϕ	Azimuthal angle	$\phi := \arctan\left(\frac{p_y}{p_x}\right)$
θ	Polar angle	$\theta := \arctan\left(\frac{p_T}{p_z}\right)$
y	Rapidity	$y := \frac{1}{2}\ln\left(\frac{E+p_z}{E-p_z}\right)$
η	Pseudorapidity	$\eta := -\ln\left(\tan\frac{\theta}{2}\right)$
$\Delta\phi_{ij}$	Opening angle in ϕ	$\Delta\phi_{ij} := \min\left(\lvert\phi_i - \phi_j\rvert, \pi - \lvert\phi_i - \phi_j\rvert\right)$
$\Delta\eta_{ij}$	Separation in η	$\Delta\eta_{ij} := \lvert\eta_i - \eta_j\rvert$
R_{ij}	Opening in (η, ϕ) space	$R := \sqrt{\Delta\phi_{ij}^2 + \Delta\eta_{ij}^2}$
E_T^{miss}	Missing transverse energy	$\mathbf{E}_T^{\text{miss}} := \sqrt{\left(\sum_{\text{Deposits}} E_x\right)^2 + \left(\sum_{\text{Deposits}} E_y\right)^2}$

Table 2.1. *Definitions of commonly used variables in the description of particle and event properties in the ATLAS coordinate system. For a detailed discussion of the reconstruction of* E_T^{miss} *see also Section 3.7.*

spatial resolution for primary and secondary vertex reconstruction. Figure 2.3 shows an outline of the inner detector including the pixel and semiconductor strip detectors (SCT) and the transition radiation tracker (TRT).

Pixel Detector

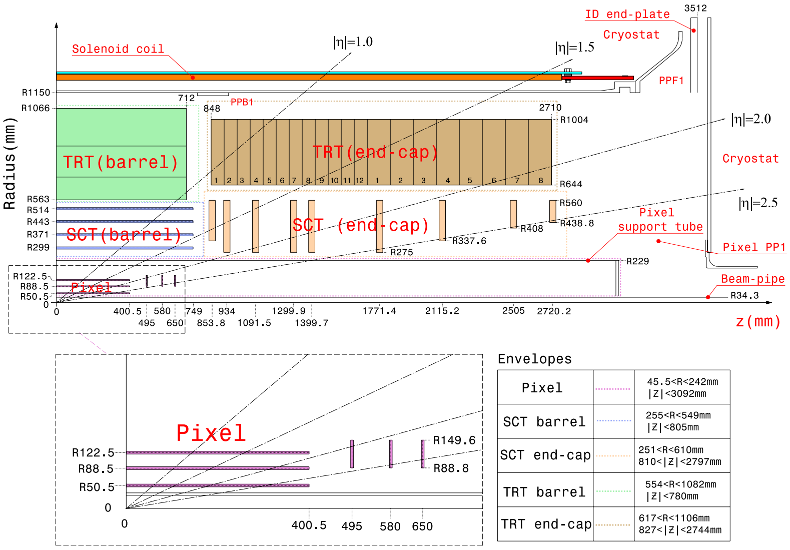

Figure 2.3. *Schematic view of one quadrant of the inner detector (top) and a detailed scheme of the pixel detector layout (bottom) [97].*

The silicon *pixel detector* is the closest detector component to the interaction vertex and is made up of three cylindrical layers located between 5 cm – 12 cm in radial distance from the beam pipe. The innermost layer is often also referred to as B-layer, as it is a crucial detector component for secondary vertexing for b-hadron decay reconstruction. In the forward region, three discs provide coverage up to $|\eta| < 2.5$. In total, the pixel detector consists of 80.4 million pixels, each with a nominal size of 50×400 μm^2. They are organised on staves, containing 13 modules each. A charged particle produces on average to three hits in the pixel detector, each with an intrinsic resolution of 10 μm in the $\mathrm{R} - \phi$ plane and 115 μm along the z-axis. To suppress electronic noise, the pixels are operated at a temperature of 0°C.

The Silicon Microstrip Tracker

The SCT is a silicon strip detector made up of four cylindrical layers in the barrel region and two endcaps of nine disks each in the forward region. In total, the SCT provides an active area of 63 m^2 to measure four space points over the full inner detector coverage. Two sensors, each containing 768 active strips, 285 μm thick and of a strip pitch of 80 μm are mounted back-to-back on the modules tilted against each other by a small stereo angle of 40 mrad. This angle breaks the degeneracy along the z-direction and allows to measure three-dimensional space points with an accuracy of 17 μm in the $\mathrm{R} - \phi$ plane, 580 μm along the z-axis and R direction for the end caps, respectively. As outlined in Fig. 2.3, the end cap disks differ slightly in their geometry and are build from an inner wheel of 40 modules for disks 2-6, a middle wheel for disks 1-8 and an outer wheel for all disks. The sensors are single sided p-in-n silicon detectors with an applied bias voltage of about 150 V which can be increased during the lifetime of the experiment to maintain a high charge collection efficiency after a few years of high luminosity running. The SCT is operated at -10°C to -5°C to suppress electronic noise.

Transition Radiation Tracker

The concept of the TRT is based on transition radiation, which is emitted by charged particles passing a boundary of two dielectric materials. It is made of polymide drift tubes, 144 cm long and interleaved with polyproyplen/polyethylen fibres. Each tube has a diameter of 4 mm and is filled with a xenon-based gas mixture and contains a gold plated tungsten wire to collect the charge from the gas ionisation. Both, high- and low-threshold TRT hits are recorded, where the low threshold is optimised to detect ionisation from primary traversing particles while the high-threshold hits indicate transition radiation. The intensity of the transition radiation is proportional to the Lorentz factor γ of the particle, so that the TRT can provide particle identification and especially $e^{\pm}/\pi^{\pm}$ separation over a wide momentum range of 0.5 GeV to 150 GeV by counting the number of high-threshold hits along the path of flight. The tubes measure hits with an accuracy of 130 μm in the $\mathrm{R} - \phi$ plane. In comparison to the silicon tracking detectors, the accuracy per hit is quite poor. Nevertheless, the TRT can provide valuable information for track reconstruction, given that each particle provides about 36 hits in the TRT easing pattern recognition in the dense tracking environment. The TRT covers pseudorapidities up to $|\eta| < 2$.

Inner Detector Material Budget

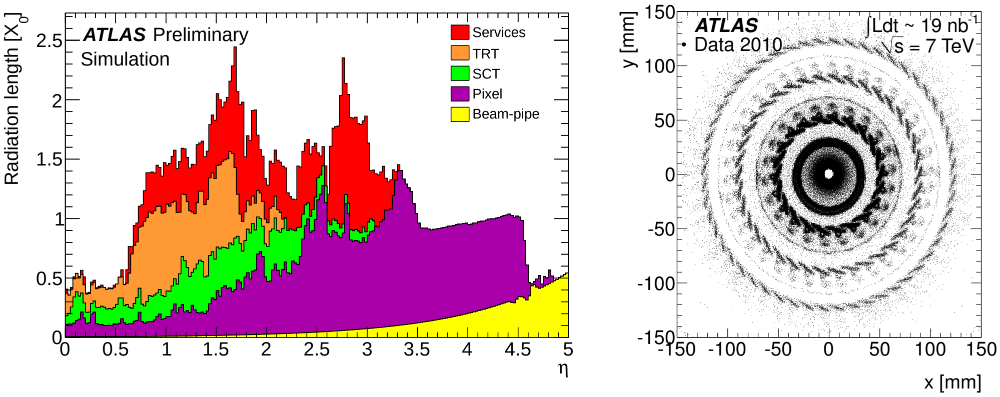

Figure 2.4. *Material budget in the inner detector visualised by the radiation length of the various subdetectors and service structures (a) [107] and by the distribution of secondary vertices as measured in p-p collisions in 2010 (b) [108]. The inner detector is clearly visible from hadronic interactions in the material.*

The material budget of the inner detector is large enough to significantly limit the track reconstruction efficiencies at low momenta and impact particle identification and energy momentum measurements. The material budget of the subsystems and the necessary service structures is shown in Fig. 2.4 (a), in units of radiation lengths for a straight track as a function of η. A precise knowledge of the material budget and its modelling in the detector simulation, is important to correct for such effects. Figure 2.4 (b) shows the distribution of secondary vertices in $\sqrt{s} = 7$ TeV proton-proton collision data collected in 2010. The visible structure of the ID emerges from hadronic interactions with the material of the ID [108]. In addition, about 40% of photons undergo conversions in the material in front of the calorimeter. The material leads further to early hadronic interactions of hadrons and to electron bremsstrahlung processes in front of the calorimeter. In-depth studies of observables sensitive to the material budget help to measure the position of the detector components as well as the material distribution, and to include these in the complex simulation model.

2.2.3. The Calorimeter System

The calorimeter system is intended to provide an accurate measurement of particle energies by absorbing them and measuring the shower properties, which also eases particle identification. The electromagnetic calorimeter is designed to fully absorb and precisely measure electromagnetic cascades of subsequent e^+e^- pair production and bremsstrahlung processes as initiated from electrons and photons. The hadronic calorimeter is intended to fully contain hadronic showers of high energy hadrons. The calorimeter system provides coverage up to the far forward region with $|\eta| < 4.9$. It is built as sampling calorimeter with alternating samples of passive material, inducing showering, and active scintillating material to detect the secondary particles. Besides a precise measurement of energy depositions, it is furthermore required to also provide accurate spatial resolution, for a precise photon reconstruction as well as for the detection of missing transverse energy from stable, weakly interacting particles escaping detection, like neutrinos. Therefore, the ATLAS calorimeter system is finely segmented, both in the longitudinal and azimuthal direction. This allows to reconstruct the three-dimensional shower position, using so-called topological clusters, and to use dedicated calibration schemes based on this three dimensional spatial resolution. Figure 2.5 shows the different calorimeter sub-systems in a cut-away view.

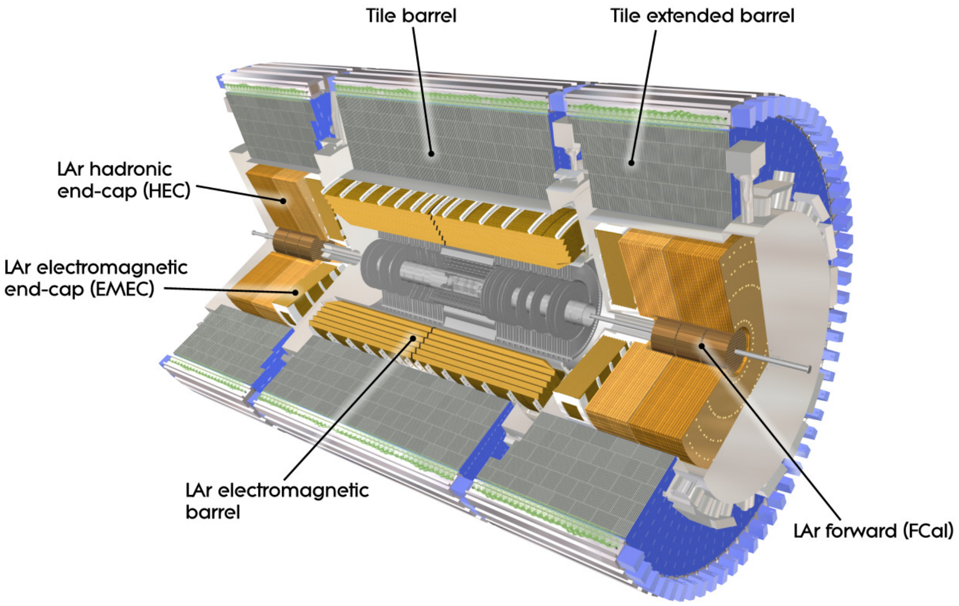

Figure 2.5. *Cut-away view of the ATLAS calorimeter system [97].*

The Electromagnetic Calorimeter

The electromagnetic calorimeter is a finely segmented high-resolution device. It consists of the EM central barrel calorimeter covering pseudorapidities up to $|\eta| < 1.4$ with a small gap of 4 mm at $|z| = 0$, the EM endcap calorimeters covering the forward region $|\eta| < 3.2$. The cylindrical barrel has inner and outer diameters of $r = 2.8$ m and 4 m , respectively and covers the full azimuthal angle, while the endcaps are ranging from $r = 0.33$ m to 2.1 m with respect to the beam pipe. The EM calorimeter is fully built as liquid argon (LAr) sampling calorimeter, intersected with lead absorber plates. It is constructed in an accordion shaped way for its natural phi symmetry as shown in Fig. 2.6. It provides an excellent energy resolution of about $\sigma_E/E = 10\%/\sqrt{E/\mathrm{GeV}} \oplus 0.7\%$. The lead plates are 1.13 mm to 1.53 mm thick, depending on the module. Three copper layers are used as readout electrodes in the gaps between the absorber material, where high voltage is applied to the outer layers. The inner plate is used as readout using capacitive coupling. Given the gap thickness and the drift velocities, the charge drift time is about 450 ns.

Three different calorimeter layers of rising granularity allow high angular resolution, and in parallel full shower containment.The layered structure provides additional information about the shower development, also referred to as shower shapes, like the longitudinal depth of the shower. The first layer is referred to as *strip layer* with a granularity of $\Delta\eta \times \Delta\phi = 0.0031 \times 0.098$ in the barrel and allows an excellent identification of $\pi^0 \rightarrow \gamma\gamma$ decays as one important background to primary photons. The second layer has a granularity of $\Delta\eta \times \Delta\phi = 0.025 \times 0.0245$ and is the thickest layer with 16 radiation lengths X_0[2]. The third layer measures the tails of electromagnetic showers and can therefore be used to distinguish electromagnetic from hadronic deposits. In addition, one 11 mm thin LAr layer, denoted as presampler, is mounted in front of the EM calorimeter in the central region ($0 < |\eta| < 1.8$) to provide an additional measurement before the first sampling layer to correct for energy loss in the inner detector and the solenoid coil. It features a fine η-granularity of 0.2.

Each endcap calorimeter consists of two wheels, the inner and outer EM endcap calorimeter wheel with a spacing of about 3 mm in between. The layout of the endcaps follows the barrel geometry. Three layers are available between ($1.5 < |\eta| < 2.5$) including a strip layer, while only two layers of a coarser granularity are used in the outermost part of the outer wheel and the inner wheel.

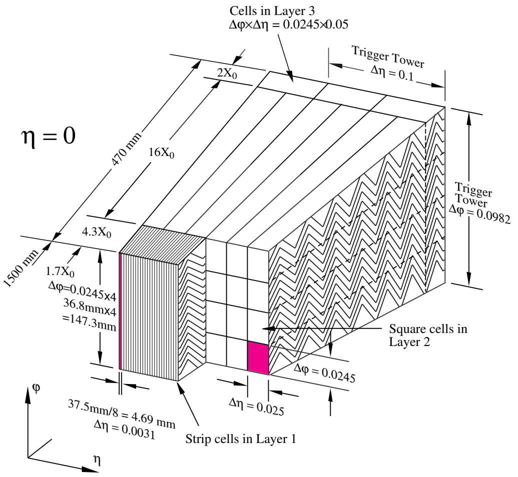

Figure 2.6. *Drawing of a EM LAr calorimeter barrel module. Shown are the three layers and the cell granularity [97].*

---

[2] Mean path length after which the energy of an electron has reduced by a factor of $1/e$ due to bremsstrahlung.

The Hadronic Calorimeter

The hadronic calorimeter is divided into the hadronic tile, the hadronic endcap and the liquid argon forward calorimeter. Like the EM calorimeter all hadronic calorimeters are sampling calorimeters. The typical energy resolution of the hadronic barrel and endcap calorimeters for hadronic jets is $\sigma_E/E = 50\%/\sqrt{E/\mathrm{GeV}} \oplus 3\%$, while it is about $\sigma_E/E = 100\%/\sqrt{E/\mathrm{GeV}} \oplus 10\%$ for the forward calorimeter. The tile barrel calorimeter uses steel as absorber and scintillating tiles as active material, which are read out by photomultiplier tubes at the tile edges, using wavelength shifting fibres. It is built cylindrical around the EM calorimeter with an inner radius of $r = 2.3$ m and an outer radius of 4.3 m. It is divided into the central barrel, 5.8 m in length, and two extended barrel parts each 2.6 m long, covering pseudorapidities of up to $|\eta| < 1.7$, as depicted in Fig. 2.5. Between the central and extended barrel calorimeter service cables for the inner detector and LAr pipes are mounted, so that a gap of 60 cm provides only limited instrumentation. All barrel parts consist of three layers. In general, the granularity of the hadronic calorimeter is coarser than the one of the EM calorimeter as hadronic showers tend to be wider than EM showers and the angular resolution of hadronic energy deposits is not expected to limit the reconstruction performance. The tile barrel cell granularity is $\Delta\eta \times \Delta\phi = 0.1 \times 0.1$ in the first two layers and twice as coarse in $\Delta\eta$ for the third layer.

The hadronic endcap calorimeter is made of two disks for the for- and backward region covering $1.5 < |\eta| < 3.2$ and is built as copper/liquid-argon sampling calorimeter. It is hosted in the same cryostat structure as the electromagnetic endcap and the forward calorimeters. The cell size is $\Delta\eta \times \Delta\phi = 0.1 \times 0.1$ for $|\eta| < 2.5$ and twice as coarse beyond that point.

The liquid-argon forward calorimeter is a combined electromagnetic and hadronic calorimeter. It consists of three layers. The first uses copper as absorber material and is optimised for electromagnetic interactions, the second and third utilises tungsten, predominantly to absorb hadronic showers. It covers the far forward region $3.1 < |\eta| < 4.9$ and overlaps significantly with the hadronic endcap calorimeters for a smooth transition. Liquid argon is used as active material and is filled in small gaps which are drilled inside the absorber material.

The overall material budget of the calorimeter is depicted in Fig. 2.7 in units of the interaction length[3]. Over the full acceptance, the calorimeter provides ten interaction lengths material at minimum for optimal shower containment. Due to the large geometrical acceptance and the fine segmentation, it is well suited for the reconstruction of missing transverse energy, which is described in Section 3.7.

---

[3] The interaction length represents the mean path length travelled by a hadron before undergoing a hadronic interaction.

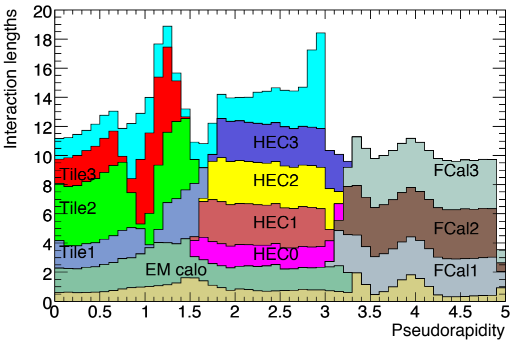

Figure 2.7. *Material profile of the ATLAS detector as a function of $|\eta|$ measured in interaction lengths. Besides the layers of the electromagnetic and hadronic calorimeters the material in front of the calorimeter (olive) and of the muon chambers (blue) are shown as well [97].*

2.2.4. The Muon Spectrometer

The outermost part of the ATLAS detector is the muon spectrometer containing various sub-detectors to efficiently detect muons and measure their momentum over a broad range. It provides an overall acceptance up to $|\eta| < 2.7$ and measures momenta ranging from 3 GeV to 1 TeV. At design specifications, it offers a relative momentum resolution of 10% for muons of 1 TeV.

Three air-core toroid magnets, covering the barrel ($|\eta| < 1.7$) and the two endcap regions ($1.6 < |\eta| < 2.7$), provide the magnetic field to bend the muon trajectories. In the barrel region, the integrated field strength $\int B_{\perp} dl$ ranges from 1.5 Tm to 5.5 Tm and between 1.0 Tm to 7.5 Tm in the endcaps. Each toroid consists of eight coils.

The flight path of muons are measured by monitored drift tubes (MDT), cathode strip chambers (CSC) and thin gap chambers (TGC) all providing differing response times and resolution parameters, while resistive plate chambers (RPC) are used as fast trigger detectors. Monitored drift tubes are installed over the full coverage ($|\eta| < 2.7$). In the barrel region they are arranged in three cylindrical layers at radii between 5 m to 10 m from the beam pipe, while in the endcap region they are arranged in four wheels located at $|z| = 7.4$ m, 10.8 m, 14 m and 21.5 m. The drift tubes are made of aluminium tubes, filled with a Ar/CO$_2$ gas mixture pressurised at about 3 bar and the electrons from ionisation processes are collected by tungsten-rhenium wires held at a voltage of 3080 V. The drift time in these chambers is about 700 ns and hence much larger than the bunch-spacing in nominal LHC conditions. Their average in situ spatial resolution per chamber is 35 μm though, so that they are providing very precise hit information. This requires an enormous precision in the alignment of these detectors to a level of about 30 μm. A special optical alignment system was build to achieve this goal.

The cathode strip chamber detectors are used in the most inner spectrometer layer, for the forward region between $2.0 < |\eta| < 2.7$ where the total particle flux exceeds the rate limitations of the drift tubes. The strip chambers are multi-wire proportional chambers, with orthogonal splitted cathodes to provide a two-dimensional spatial resolution of the hits.

In addition, the resistive plate chambers are covering a pseudorapidity range of $|\eta| < 2.4$, in order to provide fast triggering information and to complete the MDT measurement with a second position measurement. Two parallel electrode plates are held at a spacing of 2 mm, where the gap is filled by a gas mixture. The plates are operated with an electric field of 4.9 kV/mm and are both orthogonaly segmented, to provide two-dimensional hits. The chambers are mounted in front and on the back of the middle drift tube layer, as well as on the back of the outermost drift tube layer. The inner and middle layers of the end cap wheels are further equipped with thin gap chambers, multi-wire proportional chambers providing triggering information and an additional hit for the muon-momentum measurement. Both trigger detectors provide a good timing resolution of a few ns.

2.2.5. The Luminosity and Forward Detectors

Two dedicated detectors measure the luminosity of the collisions in ATLAS. The *LUCID*[4] and the *ALFA*[5] detectors. LUCID consists of two components on each side of ATLAS, located 17 m from the interaction vertex measuring the number of inelastic p-p interactions with 20 Cherenkov tubes. This measurement provides an online determination of the luminosity, by counting the number of charged particles in the far forward region. The ALFA detectors are located 240 m from the interaction point and measure the elastic scattering amplitude at extremely small scattering angles, which can be related to the total cross section using the optical theorem. The scattering angles of about 3 μrad are actually smaller than the nominal beam divergence and therefore special runs with specific beam conditions are carried out for the ALFA measurements. The detectors are located in so-called *Roman-pots*, a volume connected to the beam pipe via bellows so that it can be moved as close as 1 mm to the beams . The active detector volume is made of scintillating fibres. The ATLAS luminosity measurement is based on a two step procedure: An absolute luminosity calibration using machine parameters at simplified LHC run conditions is combined with the relative luminosity measurements during nominal data taking. The horizontal and vertical beam profiles needed to determine the absolute luminosity scale are measured in dedicated beam separation scans called *van der Meer scans* (vdM) using the ALFA detectors. The luminosity calibration in 2011 yielded uncertainties of about ±1.5% from the vdM scans [109]. Combined with uncertainties on the extrapolation procedure, including long term stability effects, the luminosity measurement in 2011 was performed with a remarkable precision of ±1.8%, while preliminary studies for the 2012 calibration following the same methodology as that detailed in Ref. [109] yield an uncertainty of ±2.8%.

---

[4] LUminosity measurement using Cherenkov Integrating Detector

[5] Absolute Luminosity for ATLAS

Another far forward detector is the zero-degree calorimeter (ZDC) used to measure the centrality in heavy ion collisions.

2.2.6. The Trigger System

The high collision rate of 40 MHz at nominal LHC running conditions does not allow to continuously read out the full detector due to limitations in the readout, computing and storage infrastructure. Instead, a dedicated trigger system selects events of interesting, predefined topologies to reduce the event rate by a factor 2×10^5 to 200 Hz. The trigger consists of the level 1 hardware trigger (L1) and the high level software trigger containing the level 2 (L2) and event filter triggers (EF). In nominal conditions, the L1 system reduces the event rate to 75 kHz, L2 reduces it further to 3.5 kHz and the EF achieves the final reduction to 200 Hz. A detailed description of the trigger system can be found in Refs. [97, 110].

The L1 trigger makes use of information from the calorimeters (L1Calo), the muon chambers (L1Muon) and the minimum bias scintillators. Within 2.5 μs it takes decisions based on simplified detector information. It is searched for local maxima of energy deposits in the calorimeter, by using fixed size sliding window algorithms operating on so-called *trigger towers*. Such local maxima are denoted as regions of interest (ROI). Only a coarse granularity of $\Delta\eta \times \Delta\phi = 0.1 \times 0.1$ (in most parts, but slightly coarser at higher values of $|\eta|$) is used for the projective trigger towers, which are built from the electromagnetic and hadronic barrel and endcap calorimeters separately. These objects are used for example to define electron and tau trigger objects, while groups of 2×2 trigger towers of the EM and hadronic calorimeters make up jet elements which are further used in the L1 jet trigger, which searches for energy maxima in typical windows sizes of 4×4 jet elements. L1 electron and photon objects are defined as windows of 2×2 EM calorimeter trigger towers, where horizontal or vertical sums of 1×2 blocks exceed predefined thresholds, while in parallel the neighbouring 12 towers are required to fulfil certain isolation criteria. Trigger objects optimised for the identification of hadronic tau decays, make use of the same procedure while considering towers from EM and hadronic calorimeters. The procedure is visualised in Fig. 2.8 (a). The signal processing already starts at the front-end electronics of the calorimeters, ensuring an optimal parallelisation of the tasks. The L1 Muon trigger is based on coincidence requirements between the different trigger chambers. A hit found in the first layer, defines a coincidence window in which another hit is searched for in the outer layers. The window is centred around the expected impact point of an infinite momentum track originating at the nominal interaction point. The size of the window is defined by the momentum threshold of the trigger item, so that the momentum dependence of the expected bending of the trajectory is taken into account. This is depicted in Fig. 2.8 (b). In addition, L1 calculates the scalar and vectorial sum of the energy deposits, enabling sensitivity towards missing transverse energy.

Information from the muon and calorimeter trigger processors are gathered by the central trigger processor (CTP), which takes decisions based on logical expressions stored in look-up tables. Every trigger item may be penalised by a *prescale* p to artificially reduce its acceptance rate by a factor p.

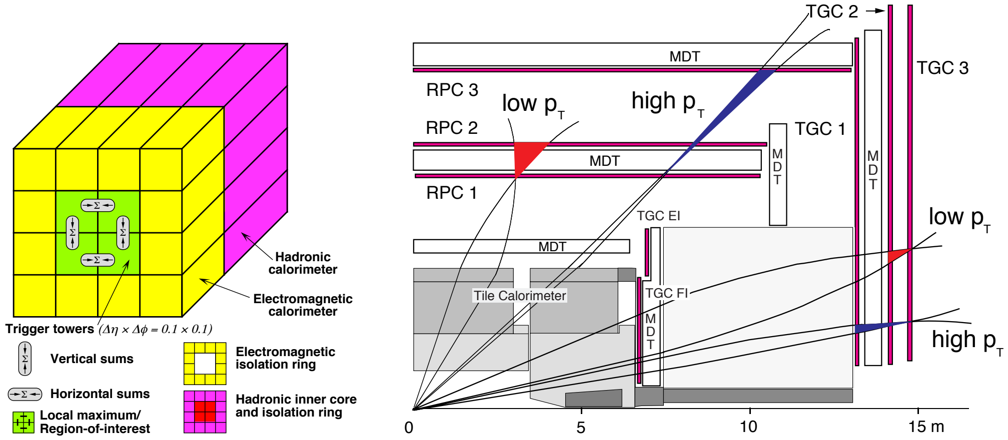

(a) (b)

Figure 2.8. *Visualisation of the electron/photon and hadronic τ trigger algorithms at L1 (a) and the concept of the L1 muon trigger based on coincidences in momentum threshold dependent windows (b) [97].*

Events passing L1 are further analysed by L2, which makes use of the full detector information in the ROIs. Within about 40 ms it can use more complex reconstruction algorithms including information from the ID for track reconstruction. The algorithms performed on each event depend on the actual trigger item under study. A distinct L1 decision triggers a dedicated L2 algorithm configuration. Finally, the EF performs a full event reconstruction using the full detector granularity. The trigger objects on EF level are based on complex object definitions closely related to the objects actually reconstructed offline. For this step, a processing time of about 4 s is available at the EF. The HLT runs on a dedicated computing farm. During data taking between 2009 to 2012, the availability of storage and computing resources exceeded the design specifications, so that the EF output rate was increased to 400 Hz during 2012 [111]. Events passing the trigger system are finally stored permanently and subsequently reconstructed at the CERN Tier 0 computing facility.

2.3. Data Taking during LHC Run 1

The first run period of the LHC was successfully completed in 2013. Since November 2009, proton collisions were established in the LHC, first at the injection energy of $\sqrt{s} = 900$ GeV, later at $\sqrt{s} = 2.36$ TeV and $\sqrt{s} = 7$ TeV. In the year 2010, proton-proton collisions corresponding to an integrated luminosity of 48.1 pb^{-1} were delivered to ATLAS, of which 93.6% were recorded [112]. This first year of data

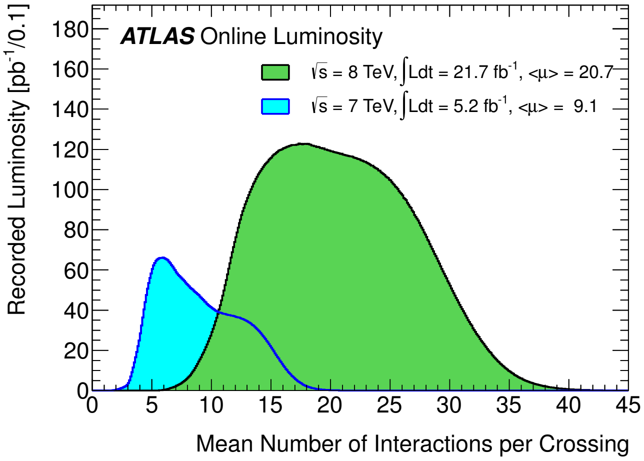

Figure 2.9. *Mean number of interactions per bunch crossing for the* $\sqrt{s} = 7$ *TeV and* $\sqrt{s} = 8$ *TeV data samples [112].*

taking was followed by a heavy ion run in winter 2010/11. A significant increase of the beam intensity allowed to collect 5.25 fb^{-1} of collision data at $\sqrt{s} = 7$ TeV in 2011, again with an outstanding data taking efficiency of ATLAS above 90%. After another heavy ion run, the centre-of-mass energy was further increased to $\sqrt{s} = 8$ TeV at the beginning of 2012, as was the instantaneous luminosity. As a consequence, an integrated luminosity of 23.3 fb^{-1} was delivered by the LHC during 2012, of which ATLAS recorded 21.7 fb^{-1}. In parallel the complexity of the recorded events increased. Due to the larger luminosity, the number of interactions per bunch crossing grew from about 5 in the beginning of 2011 to up to 35. The presence of multiple p-p collisions in a single bunch crossing will be denoted as *pile-up* (PU) in the remainder of this document. Besides the direct impact of pile-up on the event reconstruction, a secondary effect denoted as *out-of-time pile-up* may impact the object reconstruction performance, if collision events in previous bunch-crossings affect the detector signal readout chain. This may happen in sub-detectors, in which the time over which a signal is extracted is longer than the bunch-spacing, like for example in the liquid argon calorimeter system. A measure of the pile-up activity is the mean number of interactions per bunch crossing, which is shown in Figure 2.9 for the 2011 and 2012 data samples analysed for this thesis. The bunch spacing of 50 ns during Run 1 was doubled compared to the design specifications of the LHC, while the achieved peak luminosity of 7.73×10^{33} $\text{cm}^{-2}\text{s}^{-1}$ was close to the design goal of 1×10^{34} $\text{cm}^{-2}\text{s}^{-1}$. This difference was mainly absorbed by a larger number of protons per bunch, so that the average pile-up contribution in 2012 exceeded the design parameters. Reducing the bunch spacing to 25 ns is one major goal for the next data taking period starting in 2015. Figure 2.10 shows the nearly monotonic increase in instantaneous peak luminosity per day as a function of time during the major data taking periods.

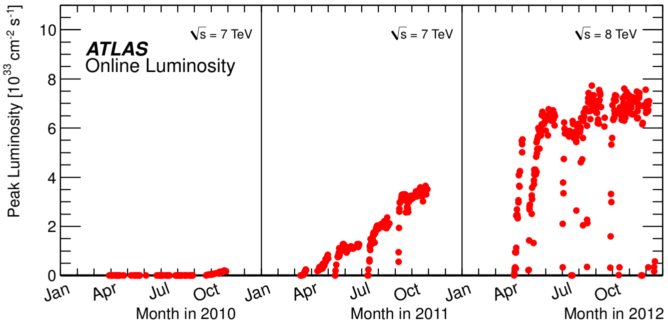

Figure 2.10. *Instantaneous peak luminosity as a function of time as recorded by the ATLAS experiment during data taking between 2010-2012 [112].*

Data Quality

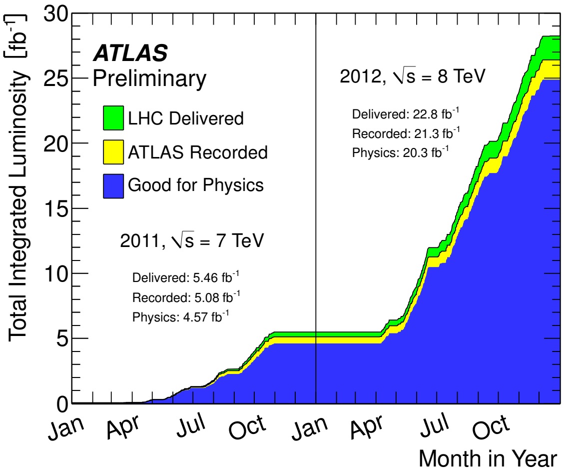

Figure 2.11. *Delivered and recorded integrated luminosity as well as the luminosity after applying basic data quality criteria denoted as "Good for Physics" [112].*

ATLAS data taking is organised in *Runs*, a period defined by the start and stop of the data acquisition system. Each run is subdivided into *luminosity blocks*, the smallest data unit within ATLAS. Each block holds a comparable amount of data, so that its duration is luminosity dependent. All detector subsystems permanently monitor their functionality during data taking. Besides automated online systems, dedicated data quality shifters check the data quality run by run, to ensure that no faulty detector behaviour affects the performance of the experiment. Small defects, like noisy calorimeter cells for instance, are masked before the bulk reconstruction of runs. Larger defects, like offline subsystems, are recorded in a data quality database along with the affected luminosity blocks. This database is used later to create so-called *Good Run Lists*, a collection of run and luminosity blocks which can be used for physics analyses. Masked blocks are simply rejected in the analysis and the total luminosity is calculated based on blocks passing the criteria. Figure 2.11

shows the delivered and recorded luminosity besides the luminosity passing these data quality criteria. Table 2.2 lists the most important parameters of the 2011 and 2012 data samples.

	2011	2012
$\sqrt{s}$ [TeV]	7	8
Peak luminosity [10^{33} cm^{-2}s^{-1}]	3.65	7.73
Mean number of interactions per bunch crossing	9.1	20
Integrated luminosity [fb^{-1}]	4.5	20.3

Table 2.2. *Summary of the run conditions during the proton-proton data taking in 2011 and 2012 [112]. The integrated luminosity corresponds to the sample actually recorded by the ATLAS detector after applying basic quality selection criteria.*

3 Object Reconstruction and Particle Identification

For events passing the online trigger requirements, as well as for simulated events, the raw detector data is stored for further processing and event reconstruction. The full event reconstruction consists of a chain of dedicated algorithms constructing physics objects, particle four-momenta and associated detector-level properties, which can be used for physics analyses. The particle reconstruction and identification algorithms are mostly based on higher-level detector information, as reconstructed tracks instead of single hits in the tracking detectors, or clustered calorimeter deposits instead of single calorimeter cell signals. Besides the reconstructed four-momenta of the particle candidates, additional variables are computed and associated with the respective objects. Among these are for example observables with discriminating power, used to minimise the object misidentification probability.The event and object reconstruction chain is defined and implemented in the Athena software framework [75]. While the same reconstruction chain is used for both data and simulated events, imperfections in the detector simulation will in general lead to potential discrepancies in the particle reconstruction and identification performance. In-depth studies of reference processes like $Z \to l^+l^-$ or QCD dijet events are used to calibrate the identification and reconstruction algorithms in data.In this chapter an overview over the reconstruction and performance of the physics objects used in the search for $H \to \tau^-\tau^+$ decays is given.

The description of the object reconstruction and its performance focuses on the methods and results used for the data taken in 2012. In case of significant differences in the reconstruction of data taken in 2011 this is mentioned explicitly, otherwise the corresponding documentation is cited. In Sections 3.1 and 3.2, tracks and clusters of energy deposits, the most common high-level detector objects, are introduced. They provide the basic ingredients for the reconstruction of jets, leptons and hadronic tau decays as explained in Sections 3.3 to 3.6. As neutrinos cannot be reconstructed within ATLAS due to their small interaction rate with matter, transverse missing energy plays a crucial role in constraining the momentum of escaped neutrinos in the transverse plane. Its reconstruction is described in Section 3.7.

3.1. Tracks and Vertices

Reconstructed tracks, originating from charged particles traversing the inner detector, are one of the most important basic objects for further particle reconstruction and identification. Furthermore, they are used to identify the primary interaction vertex and secondary decay vertices. Tracks are reconstructed by a series of algorithms [113] starting with the conversion of the hit information, recorded in the detector modules, into three dimensional space points. Silicon detector hits are directly translated into space points[1], while the timing information from the TRT is used to construct so-called drift circles around the wires. Primary tracks are emerging from particles produced at the interaction vertex, with sufficiently large lifetimes to travel through the inner detector. An Inside-out algorithm is the baseline track reconstruction algorithm for primary tracks with momenta above $p_T > 400$ MeV. The algorithm builds tracks starting from the Pixel and SCT detectors and extrapolates them to the TRT using the known magnetic field configuration and material geometry in the ID. Track segments of the TRT detector are then merged with these seed tracks, in case of compatibility. An Outside-in algorithm aims at the reconstruction of secondary tracks which emerge from particles created at radii not allowing a reconstruction with the Inside-out algorithm, such as photon conversions and nuclear interactions. It starts with track-segments in the TRT, extrapolates them towards the interaction point and merges them with matching SCT and pixel hits. Both algorithms are finally refitting the tracks, using all associated space points. The transverse and longitudinal impact parameters d_0 and z_0, respectively, are calculated as the closest distance in the transverse and longitudinal planes between the track and the primary vertex at the point of closest approach in the transverse plane. They are used for example in b-tagging algorithms to assess the compatibility of a given track to stem from a given interaction vertex. Track quality criteria, like a minimum number of nine hits in the silicon detectors and the requirement of no missing hit in the pixel detector, are used to reject badly reconstructed tracks. Particle reconstruction algorithms, like the electron or hadronic tau reconstruction, might define slightly different track quality criteria.

Vertices are reconstructed using the distribution of z coordinates of reconstructed tracks at the beamline. A vertex candidate is defined by the maximum in this distribution [114, 115]. Tracks are refitted under the assumption, that they stem from this vertex candidate, and incompatible tracks are removed iteratively, based on a χ^2 measure. The procedure is repeated, taking into account only non-associated tracks, until all tracks are associated to a vertex. Vertices with less than two associated tracks are then discarded. In general, more than one vertex is found per event. The vertex with the largest sum of squared transverse momenta of the associated tracks ($\sum p_T^2$) is chosen as primary vertex of the event, while others are denoted as pile-up vertices. An overview over the tracking and vertex performance in p-p collisions can be found in Ref. [115].

---

[1] In case of the microstrip detector, pairs of hits are needed to reconstruct one space point, see also Section 2.2.2.

3.2. Topological Clustering

Various object reconstruction algorithms in ATLAS, including jet and hadronic-tau decay reconstruction, use topological clusters (TopoClusters) as their main calorimeter input objects. The topological clustering algorithm targets at grouping connected calorimeter deposits, stemming from one particle shower. In addition, it aims at providing an efficient suppression of calorimeter noise. TopoClusters are three dimensional objects, consisting of single calorimeter cells, which are calibrated to the electromagnetic scale (EM-scale). The EM-scale is defined by calibration constants derived in test-beam measurements. To account for the lower energy response of the calorimeter to hadronic showers with respect to electromagnetic deposits, an effect often referred to as non-compensation, TopoClusters might receive cluster specific calibrations and corrections. The clustering involves a cluster making and a cluster splitting step [116], utilising a measure of the significance of the energy deposit in order to suppress noise:

$$\Gamma_i = \frac{E_i}{\sigma_i} \tag{3.1}$$

where E_i is the cell-energy deposit and σ_i the expected noise level of cell i. The noise level is η and calorimeter module dependent and also includes the expected energy deposits from pile-up events. Figure 3.1 shows the expected noise in the different calorimeter systems for two different luminosity levels, corresponding to a low and high pile-up scenario. The topological clustering is seeded by cells exceeding a seed threshold $|\Gamma| > t_{\text{seed}}$. Neighbouring cells are then subsequently added to the TopoCluster if their signal to noise ratio exceeds a threshold level $t_{\text{neighbour}}$. In cases where such a cell is a neighbour to two potential clusters, the clusters

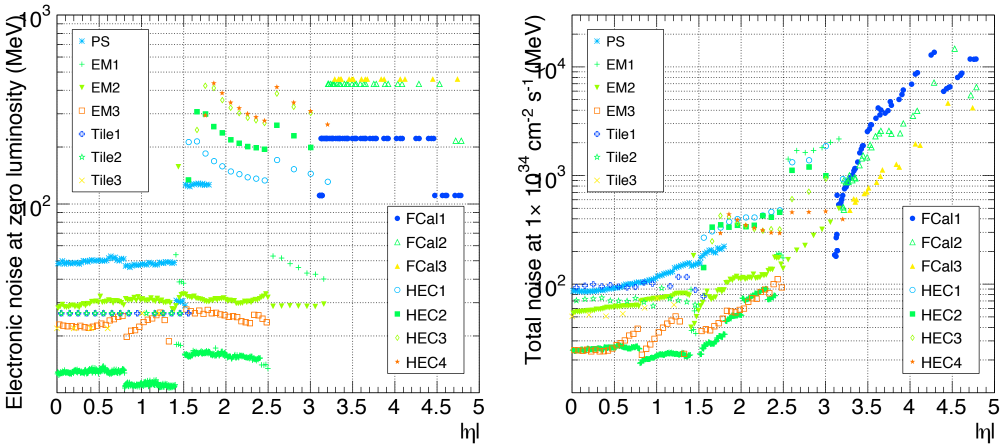

Figure 3.1. *Expected noise level per cell in the different calorimeter subdetectors for two different luminosity profiles. The left plot shows the electronic noise only while the right plot includes energy deposits due to multiple p-p collisions at instantaneous luminosities of* 10^{34} $cm^{-2}s^{-1}$ *[116].*

are merged. Then, all neighbour cells with a signal to noise ratio below $t_{\text{neighbour}}$ but above another threshold level t_{cell} are added to the most significant, adjacent seed cluster. For the jet reconstruction, TopoClusters are built using a threshold set of $\{t_{\text{seed}}, t_{\text{neighbour}}, t_{\text{cell}}\} = \{4, 2, 0\}$, which implies that all adjacent cells to a seed cell are added to the cluster, which improves the energy resolution due to a more complete shower containment. Finally, the cluster splitting step identifies and isolates local energy maxima in the clusters. The algorithm searches seed cells with an energy above 500 MeV, exceeding the energy of all neighbouring cells and having at least four neighbouring cells that belong to the parent cluster of the seed cell. Every local maximum found by this procedure forms a new cluster which is then further grown as described above, where only cells already clustered previously are considered and no cluster merging is performed. In this procedure, cells might be associated to two clusters. Such shared cells are then weighted according to the energy of the two clusters and the geometrical distance between the cell and the cluster centre.

Various cluster properties are calculated, including the energy density and first and second moments of the shower width and depth. Based on these shower shape variables, each cluster is assigned a probability to be of hadronic or electromagnetic origin which is expressed in a measure denoted as p^{EM}. Two copies of each cluster are stored. While the normal cluster collection defines the cluster energy as the sum of the cell energies at EM scale, a second copy is calibrated to the local cluster level (LC)[117, 118]. This calibration scheme is based on comparing the reconstructed energy of simulated charged and neutral pions to their true energy. The corrections account for energy deposits in uninstrumented material, for energy deposits outside the clusters due to the applied noise thresholds and for the non-compensation of the calorimeter. A weighted calibration constant is applied to the cluster and its cells according to the shower classification measure p^{EM}. The cell weights can be defined in a non-ambiguous way by comparing the true energy deposit in a cell, stored in so-called *calibration hits*, to the reconstructed cell energy. For the cluster weights though, a correspondence between nearby calibration hits and the cluster under study needs to be established. In general, jets built from local calibrated clusters have an improved energy resolution with respect to jets built from EM scale clusters, due to these showershape dependent cluster corrections. For the analysis presented in this thesis both jets and hadronic tau decays are reconstructed using calibrated clusters.

3.3. Jets

Collimated sprays of particles originating from the fragmentation of quarks and gluons are referred to as jets. Jets can be used as experimental signatures of quarks and gluons of high transverse momenta (see also Section 1.2). They play a crucial role in many physics analyses including the search for the Higgs boson. Special care needs to be taken in the definition of these objects, to allow a fair comparison between *particle jets* in parton-level calculations and *calorimeter jets* built from reconstructed energy deposits in the experiment's detectors. Jets are reconstructed using a clustering algorithm which operates on three-dimensional calorimeter clusters, described in Section 3.2. The jets are calibrated to the jet-energy scale, which is introduced in Section 3.3.2. Due to the relative long lifetime of b hadrons, jets containing those can be identified as b-jets by so-called b-tagging algorithms, which are briefly introduced in Section 3.3.3.

3.3.1. Jet Reconstruction

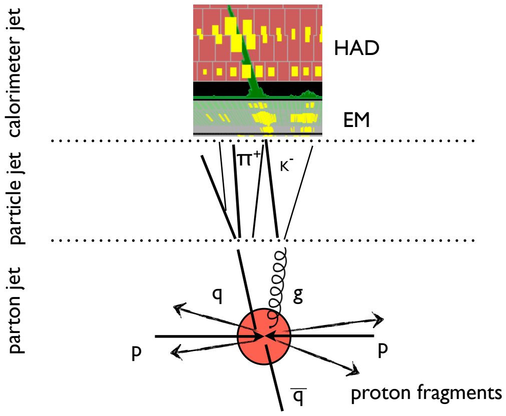

Figure 3.2. *Schematic view of possible definitions of jet levels depending on the input four-momenta to the jet clustering algorithm.*

As discussed above, coloured partons (quarks or gluons) in the final state of a scattering event hadronise at typical scales of the strong interaction. For strongly boosted partons, this will lead to a collimated jet of colour neutral particles, mostly mesons like pions and kaons. Since the hadronisation is a non-perturbative effect, jet properties like the particle multiplicity, their spatial distribution or energy profile cannot be predicted from first principles. To allow a quantitative comparison between the parton level predictions of pQCD and experimentally reconstructed jets, an algorithm needs to define how to build jets. This definition should allow for comparable results of physical observables when working with either coloured partons, stable particles after hadronisation or on reconstructed calorimeter clusters. These different levels are sketched in Fig. 3.2. Comparisons between the different levels allow to study the transition of the jet initiating partons towards particle and detector level jets, for example in order to derive calibration and correction factors. Such jet algorithms should satisfy certain robustness criteria. Namely, they should be stable against additional colinear and infrared radiation of additional partons, be invariant under boost transformations along the z-axis and be independent of the underlying event and other non-perturbative effects. Such stability criteria ensure that cross sections calculated at parton level are comparable to measurements of hadronic jets which necessarily include non-perturbative hadronisation effects. Especially, colinear and infrared safety are important properties to ensure the applicability of the algorithm at parton level, since soft and colinear radiation dominate the parton shower. Different jet algorithms exist and can be classified into *cone* and *clustering* algorithms. While cone algorithms combine objects based on some geometrical measure around the jet axis, clustering algorithms combine objects based on energy and angular variables. The LHC experiments mostly use clustering algorithms. For the analysis presented here, jets are clustered using the anti-k_T algorithm [119] as implemented in the FastJet package [120]. It clusters objects of large transverse momentum first and subsequently moves to softer contributions. The following measures are defined:

$$d_{ij} = \min(p_{T,i}^{-2}, p_{T,j}^{-2}) \frac{\Delta R_{ij}^2}{r^2} \tag{3.2}$$

$$d_{iB} = p_{T,i}^{-2} \tag{3.3}$$

where ΔR_{ij}^2 is the geometrical distance between objects i and j in the $\eta - \phi$ plane and r is a parameter of the algorithm. The algorithm computes the d_{ij} and d_{iB} of all input objects and finds the minimum among these quantities. In case it is of type d_{ij} the objects i and j are combined into a single one, while in case it is of type d_{iB} this object is considered a jet and it is removed from the list of input objects. These steps are repeated until no more input objects are left over. The parameter r controls the geometrical size of the jets. The algorithm produces relative circular jets in the $\eta - \phi$ plane with a stable jet area[2] of πr^2, which is of advantage in the derivation of jet area sensitive corrections, like for example energy subtractions accounting for UE and pile-up activity. It is furthermore colinear and infrared safe and relatively cheap in terms of computing resource consumption. A good overview over different jet algorithms is given in Ref. [121]. In the remainder of this thesis, jets with a distance parameter of $r = 0.4$ are used.

Once reconstructed the jet is subject of a dedicated calibration procedure detailed in Subsection 3.3.2. In addition, auxiliary detector information is stored, including energy fractions in the different calorimeter layers, pulse quality information and information about associated tracks. While jets are reconstructed up to the far forward region ($|\eta| < 4.5$), central jets within the tracker acceptance can be matched to tracks, allowing for a jet-vertex association. The jet vertex-fraction (JVF) [122] of jet_i with respect to the vertex PV_j is defined as:

$$\text{JVF}(\text{jet}_i, \text{PV}_j) = \frac{\sum_k p_\text{T}(\text{track}_k^{\text{jet}_\text{i}}, \text{PV}_j)}{\sum_n \sum_l p_\text{T}(\text{track}_l^{\text{jet}_\text{i}}, \text{PV}_n)}, \tag{3.4}$$

where k runs over all tracks originating from PV_j matched to jet_i, n over all primary vertices in the event and l over all tracks originating from PV_n matched to jet_i. This quantity can be used to suppress jets from PU vertices. In data collected in 2011, a selection criteria of $|\text{JVF}| > 0.75$ is applied for jets within $|\eta| < 2.4$. In data collected in 2012, the cut was loosened in order to ensure a high signal selection efficiency within the denser pile-up environment to $|\text{JVF}| > 0.5$, required for jets

---

[2] Two common definitions of jet areas exist based on counting the number of test-objects of small momentum clustered into the jet. For a detailed introduction see Ref. [121].

with a transverse momentum below $p_T < 50$ GeV and $|\eta| < 2.4$. The selection efficiency was studied in Z+jet events and good agreement in the efficiency between data and simulated samples was found. The systematic uncertainty was estimated to be smaller than ±1% for all jets [122]. To reject jets from beam-gas events, cosmic ray muons or coherent noise in the calorimeters, a set of jet cleaning criteria is applied as detailed in Refs. [123, 124]. The efficiency of genuine jets passing these criteria is larger than 99%.

3.3.2. Jet-Energy Calibration and Resolution

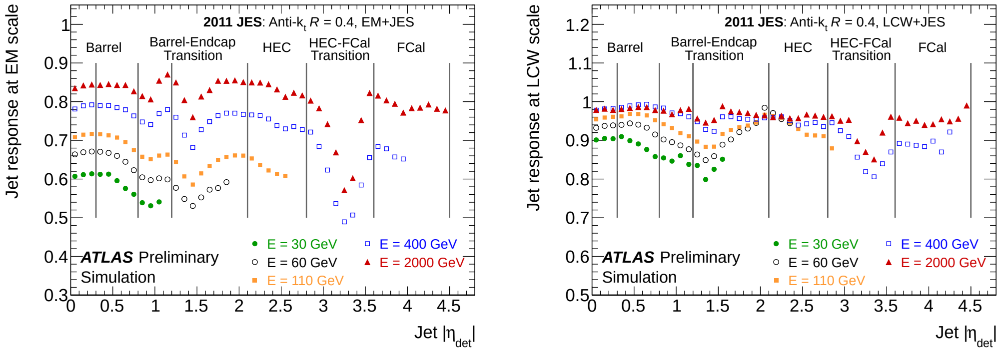

(a) (b)

Figure 3.3. *Jet energy response as extracted from simulated dijet events as a function of the jet pseudorapidity for jets built from TopoClusters at the EM-scale (a) or LCW scale (b). The response of LCW jets is higher due to the calibration applied on the cluster level [125].*

As mentioned above, an additional jet level calibration is applied to correct for effects not accounted for in the local cluster calibration. It is meant to calibrate the jet to the truth particle level, corresponding to the energy of a jet built from the true stable particles after hadronisation. These effects include for example particles not reaching the calorimeter or deposits which are not reconstructed in the calorimeter or not clustered into the jet. The calibration sequence starts with a pile-up correction, subtracting the expected diffuse energy deposition from multiple p-p collisions in the reconstructed jets. While for data taken in 2011 a simple averaged η- and $\langle\mu\rangle$ dependent correction was applied, an improved subtraction scheme, taking into account event-by-event pile-up energy density fluctuations, was employed in 2012. In order to subtract the pile-up contribution, the event p_T density per area is measured, and then applied as jet area dependent correction [122]. The correction reduces the jet energy dependence on the number of primary vertecies from several hundred MeV per vertex to less than 100 MeV for most jets, which is further reduced by a residual correction accounting for out-of-time pile-up effects. The jet direction is corrected by recalculating all four-momenta of the constituents based on the assumption that they originate from the primary reconstructed vertex.

Afterwards, the main calibration constants are applied as a function of the jet energy and its pseudorapidity. The calibration is derived from simulated dijet events [118, 125]. Figure 3.3 shows the ratio between reconstructed and true jet energy as a function of pseudorapidity for jets built from EM-scale or calibrated clusters. The response of the LCW jets is higher due to the cluster level calibration. The corrections are most significant in the transition region between barrel and endcap calorimeters due to the larger amount of uninstrumented material present in this region. Finally, a set of data-driven corrections is applied to correct for small differences in the jet response of the simulated and real calorimeter [125]. These corrections are derived by comparing the jet energy to that of a reference object, as for example a recoiling photon, Z boson or jet system. While the direct balance with respect to electrons, muons and photons is used to infer the absolute scale, dijet balancing allows to reduce uncertainties on the relative scale differences between the central and forward detectors. Various systematic uncertainties on the jet-energy scale[118, 125, 126] arise from these calibration steps and are propagated through the analysis independently.Figure 3.4 shows the combined uncertainty for jets in data taken in 2012 as a function of transverse momentum and pseudorapidity. In total, the jet-energy scale uncertainty (JES uncertainty) is smallest for central jets with a relatively large transverse momentum of hundreds of GeV with uncertainties of about ±1%. Larger uncertainties arise for softer jets in the forward detectors. The jet energy resolution was measured in dijet events and was found to be well modelled in the simulation, with relative uncertainties well below ±10% [127].

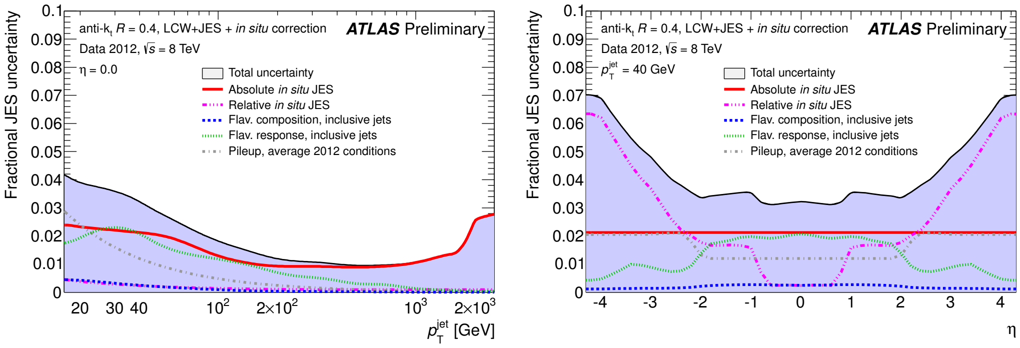

(a) (b)

Figure 3.4. *Combined jet-energy scale uncertainty in data taken in 2012 as a function of the jet transverse momentum (a) and its pseudorapidity (b) [128].*

3.3.3. Identification of b-Jets

The large lifetime of b hadrons leading to decay lengths of the order of $\beta\gamma c\tau \approx 5$ mm for b-hadron energies of about 50 GeV [22], allows to identify jets containing b hadrons. This is referred to as flavour tagging or b-tagging. Flavour tagging is of great interest in many physics analyses, for example due to the large b-jet multiplicity in $t\bar{t}$ decays, or in searches for phenomena beyond the SM of which some predict enhanced contributions in final states containing b-jets. In the search for the Higgs boson, b-tagging is a crucial ingredient in the $H \rightarrow b\bar{b}$ search channel, and is also used to efficiently reduce background contributions from $t\bar{t}$ events in other channels like $H \rightarrow \tau\tau$. In ATLAS, different algorithms exist exploiting the main signatures of b-hadron decays [129].

- The IP3D algorithm is based on the significances of the transverse and longitudinal impact parameters of tracks associated with the jet. The impact parameters are expected to be large for particle tracks originating from a displaced vertex. The algorithm does not rely on the secondary vertex to be actually reconstructed. The expected distributions from simulated light quark and bottom quark jets are used to build a likelihood ratio as discriminant.
- The SV1 algorithm exploits the relative large mass of the b hadrons. It reconstructs the secondary vertex and computes discriminating variables such as the invariant mass of tracks stemming from this secondary vertex and momentum fractions between tracks from the secondary vertex with respect to all the tracks associated with the jet.
- The JETFITTER algorithm reconstructs the decay chain of b hadrons which mostly decay via an intermediate c hadron. Looking for tracks emerging from the estimated b hadron path-of-flight, b and c-decay vertices are reconstructed and a discriminant is built based on similar variables to those used in the SV1 algorithm but adding information about the decay topology.

Given the different approaches, the various algorithms feature different efficiencies and light-jet rejection rates for different kinematic properties of the jets. Combining the approaches leads to a significant improvement in tagging efficiency and a reduction in the mistag rate. One such combination is denoted as MV1, a neural network discriminant based on the discriminant outputs of the SV1,IP3D and combined IP3D+JETFITTER algorithms. The analysis presented in this thesis makes use of the MV1 algorithm, applied to jets within the tracker acceptance at a working point with a selection efficiency of 70%, as measured in simulated $t\bar{t}$ events.

The performance of the b-tagging algorithms, namely the b-tagging and c-tagging efficiencies and the mistag rate are measured in several analyses. The b-tagging efficiency for example, can be measured in jets containing muons from semi-leptonic b-hadron decays [131] and in dileptonic $t\bar{t}$ events [130]. Figure 3.5 shows a comparison between the measured tagging efficiency in $t\bar{t}$ events with respect to a simulated event sample. The ratio between the efficiencies is denoted as *scale-factor* and used to correct the efficiency in the simulation. Systematic uncertainties arise from the choice of a hadronisation model, the PDFs and experimental uncertainties. The uncertainties on the scale factors range from ±6% at low transverse momenta to about ±2% at transverse momenta of $60 - 140$ GeV. The mistag rate of light flavour jets is determined in a inclusive set of jets, with larger systematic uncertainties of the order of ±15% to ±25% depending on p_T and η [132].

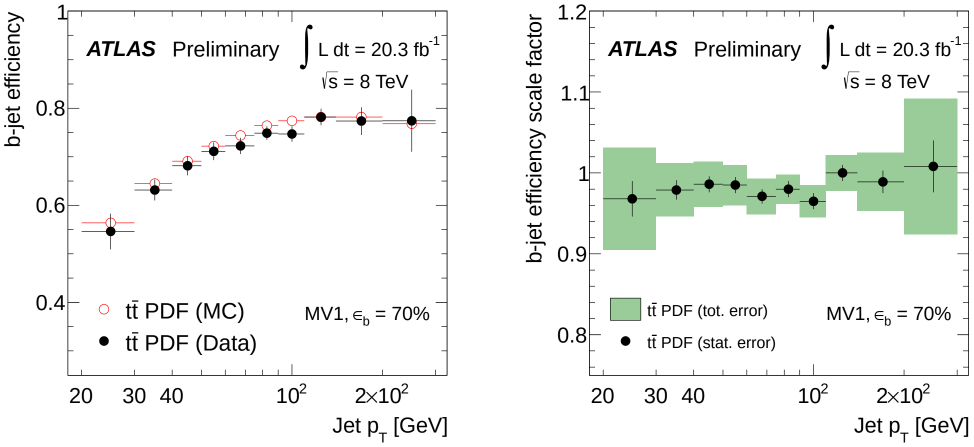

(a) (b)

Figure 3.5. *The b-tagging efficiency as measured in dileptonic $t\bar{t}$ events compared to a simulated event sample (a) and the resulting correction factors and their uncertainties (b) for the MV1 tagging algorithm at its 70% efficiency working point [130].*

3.4. Electrons

Electrons provide an important experimental signature for many physics analyses, due to the ability to precisely measure the electron momentum and energy and to identify them with high purity. This is achieved by combining the measurement of tracking detectors with an energy measurement in the electromagnetic calorimeter (see also Section 2.2.3). The reconstruction of longitudinal and horizontal shower shapes allows to define efficient identification criteria resulting in a relative low misidentification rate of hadronic jets. Electrons also provide a clean signature at trigger level, so that single electron trigger items are used to collect the data sample analysed in the $H \to \tau_e\tau_{\text{had}}$ channel.

3.4.1. Electron Trigger

As discussed in Section 2.2.6, the ATLAS trigger is a three level system, subsequently refining the identification algorithms used at each stage. The L1 regions of interest (ROI) are identified using a sliding window algorithm operating on calorimeter trigger towers with a granularity of $\Delta\eta \times \Delta\phi = 0.1 \times 0.1$. The second trigger level uses the full calorimeter granularity within the ROIs to form clusters and

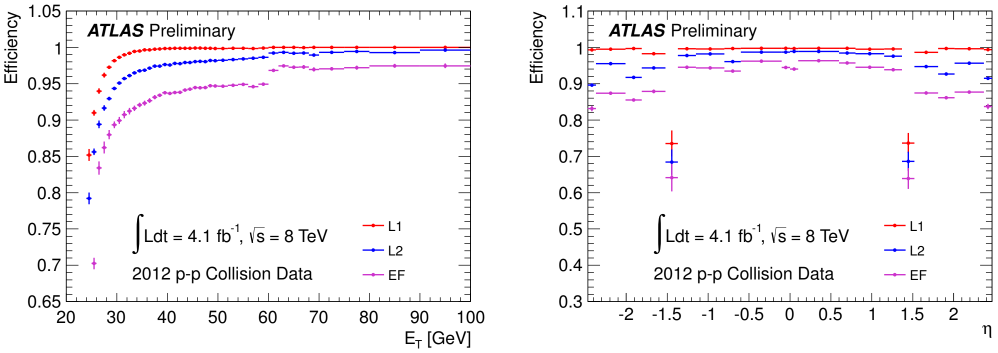

(a) (b)

Figure 3.6. *Single electron trigger efficiencies at the three levels of the ATLAS trigger system as a function of the transverse energy (a) and pseudorapidity (b) of the reconstructed electron. The efficiencies are measured using a tag-and-probe technique in $Z \to ee$ events [133].*

combines them with the result of a fast tracking and track to cluster matching algorithm. At the event filter level, algorithms close to the full offline reconstruction and identification chain are used. Relatively loose identification criteria, eventually combined with isolation requirements, ensure a high selection efficiency. The trigger items used in the analysis are so-called *single-electron trigger* items, requiring the presence of one electron candidate above a certain p_T threshold. The specific triggers are denoted as *e24vhi_medium1* and *e60_medium1* for data collected in 2012 and *e20_medium*,*e22_medium* and *e22vh_medium1* for data recorded in 2011. While the number corresponds to the applied online transverse momentum threshold above which the trigger would accept the electron, the tag *medium* refers to a medium efficient set of identification criteria applied to cluster and track properties. To further reduce the trigger acceptance of misidentified jets, a veto on the activity in the hadronic calorimeter beyond the reconstructed electron cluster can be defined, and is referred to as *vh* in the trigger names. In addition, *e24vhi_medium1* requires that the electron track is isolated with respect to other tracks. The trigger efficiency for real electrons is measured in $Z \to ee$ events, where one electron is required to trigger the event and to pass tight identification criteria and is denoted as *tag-electron*. No identification criteria are required from a second electron candidate in the event. It is denoted as *probe-electron*. If the invariant mass of the di-electron system is close to the Z boson mass, the electron purity in this unbiased sample of electrons is high and can be used to determine the trigger efficiency. Figure 3.6 shows the electron trigger efficiency of a logical or combination of the e24vhi_medium1 and e60_medium1 trigger items, as a function of the reconstructed electron E_T and pseudorapidity, with respect to the offline identification criteria used in the analysis presented in this thesis. The combination of the two trigger items is performed to increase the selection efficiency at large momenta where the isolation and hadronic leakage requirements of the lower threshold trigger are becoming increasingly inefficient, as visible in Fig. 3.6 (a). The measurement is compared to the efficiencies determined in simulated event samples and scale factors are used to correct the simulated efficiencies to the ones observed in data. Systematic uncertainties on these corrections are relatively small and range from ±2% for electrons at large pseudorapidities and low transverse momenta to ±1% for electrons in the central detector region above $E_T > 28$ GeV.

3.4.2. Electron Reconstruction and Identification

In the analysis presented in this thesis, only electrons within the tracker acceptance $|\eta| < 2.47$ are used, therefore the reconstruction of electrons in the forward detectors is not covered in this section. The electron offline reconstruction starts with a sliding window algorithm, identifying clusters of size $\Delta\eta \times \Delta\phi = 0.075 \times 0.125$ [116] with a transverse energy exceeding 1.5 GeV and passing loose shower shape criteria applied on the energy fractions across the calorimeter layers. A dedicated electron track reconstruction is performed in cones of size $\Delta R = 0.3$ around the cluster locations and proceeds in two steps. Firstly, the optimised tracking algorithm attempts to reconstruct tracks under a charged pion hypothesis, and retries to fit them under an electron hypothesis allowing for additional energy loss in case of failure. This approach allows for an improved electron track reconstruction efficiency [107]. Tracks are then associated with the cluster if they pass loose quality criteria, which are applied on the number of hits and on a geometrical matching of their impact point with respect to the calorimeter cluster location. The matched tracks are refitted using a Gaussian Sum Filter algorithm, which accounts for non-linear bremsstrahlung effects [134]. A list of electron candidates is built from clusters with at least one associated track. If multiple tracks are associated, the closest one to the cluster location having at least one hit in the pixel detector is chosen as primary track.

Energy Scale and Resolution

The energy of the electron is determined from the energy deposits inside the cluster and is corrected for the estimated energy deposit in front of the calorimeter, outside the reconstructed cluster and beyond the EM calorimeter [135, 136]. The EM scale of the calorimeter cells is calibrated using testbeam measurements. A refined calibration from fits to the observed di-electron invariant mass spectra from $Z \to ee$ and $J/\Psi \to ee$ decays reduces the uncertainty on the absolute scale calibration significantly. These residual calibration constants are derived as a function of η. In addition, comparisons between the reconstructed energy and the momentum as measured in the inner detector in $W \to e\nu$ events allow to obtain an independent crosscheck of the in situ calibration. Uncertainties on the energy scale arise from limited precision in the modelling of the overall material budget in front of the calorimeter, the energy scale of the presampler calorimeter layer and the background estimation and fit procedures in the data-driven calibration. They are well below

±1% for electrons with transverse energies above $E_T > 20$ GeV in the central barrel calorimeter, and up to ±1% in the endcap region [136].

The lineshape from $Z \to ee$ and $J/\Psi \to ee$ events is also used to determine the energy resolution and the residual difference between data and simulated event samples. Due to imperfections in the detector simulation, the energy resolution in data is about 1% larger than simulated. This effect is corrected for, with relative uncertainties on the correction ranging from ±5% at 20 GeV to ±20% at 100 GeV [136].

Identification Criteria and Efficiencies

Since jets, electrons from heavy flavour hadron decays or electrons from photon conversions[3] present a variety of background processes likely to be reconstructed as electrons, dedicated electron identification criteria are defined to reject background events, while keeping the efficiency for actual electrons high. They are based on a variety of observables, mostly shower shape quantities testing the compatibility of the observed shower development with the expectation from electromagnetic showers. These are combined with track reconstruction quality measures and variables assessing the compatibility of the track cluster matching. Shower shape variables comparing the energy fractions in the core of the cluster to the outer area, or measures of the hadronic energy deposits beyond the electromagnetic calorimeter, are sensitive to the pile-up activity in the event. Therefore, special care was taken to minimise the dependence of the electron identification efficiency on the number of primary vertices in the event. Different criteria are defined and grouped into working points denoted as *loose*, *medium* and *tight*, corresponding to an increasing background rejection rate at signal efficiencies of about 95%, 85% and 75% for reconstructed electron candidates with transverse energies of $E_T = 30$ GeV, respectively. To further increase the background rejection, especially with respect to hadronic jets, two isolation criteria are applied at the analysis level on the relative isolation with respect to either tracks or calorimeter deposits (see Section 5.4.1).

The identification efficiencies are measured in $Z \to ee$ and $J/\Psi \to ee$ events, using a *tag-and-probe* technique as explained above and detailed in Refs. [107, 135, 136]. The total efficiency is factorised into the reconstruction and identification efficiency. While the reconstruction efficiency is about 99% for electrons with a transverse energy above $E_T > 20$ GeV, the identification efficiency shows a strong E_T dependence. Figure 3.7 shows the electron identification efficiency as a function of the transverse energy as measured in data compared to the efficiency found in simulated event samples, as well as their dependence on the number of reconstructed primary vertices. The difference between measured and simulated efficiency is used to correct the simulated event samples. Both reconstruction and identification efficiencies are lower in the transition region between barrel and endcap detectors ($1.37 < |\eta| < 1.52$).

---

[3] While electrons from heavy flavour hadron decays and photon conversions are real electrons, they are nevertheless regarded as background in the reconstruction of primary particles emerging from the hard scatter event.

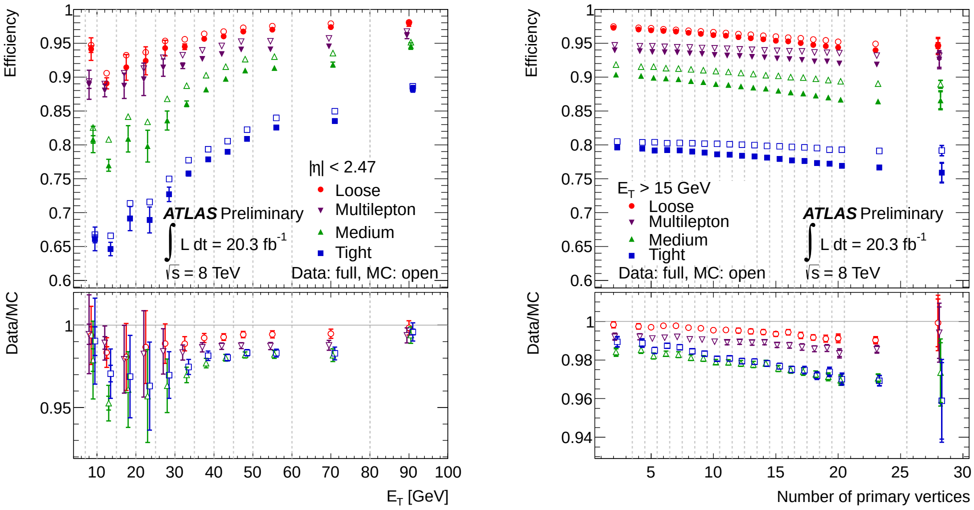

(a) (b)

Figure 3.7. *Electron identification efficiencies for efficiency working points, labelled as loose, multilepton, medium and tight, as a function of the electron transverse energy (a) and the reconstructed vertex multiplicity in the event (b). The efficiencies are measured in $Z \to ee$ events using a tag-and-probe technique. The observed efficiency difference between data and simulated samples, as displayed in the ratio pane, is used to correct simulated event samples [107].*

In the search for $H \to \tau\tau$ events, electrons are therefore only selected outside this region.

3.5. Muons

Muons traversing the ATLAS detector interact so weakly with the material of the calorimeters that they leave the detector with only minimal energy losses. The experimental signature is therefore well distinguishable from jets or electrons. Muons are reconstructed in ATLAS by precisely measuring their path of flight and their deflection by the magnetic field using the inner tracking detectors and the dedicated muon spectrometers located beyond the hadronic calorimeters. The muon spectrometers are located inside a magnetic field of an average field strength of 0.5 T (see also Section 2.2.4) providing the bending power needed to ensure a high momentum resolution for muons up to 1 TeV. Due to the low misidentification rate of backgrounds and the precise momentum measurement, muons are the objects best able to be measured in ATLAS and furthermore provide an excellent trigger signature.

3.5.1. Muon Trigger

The ATLAS muon trigger (see also Section 2.2.6) follows the three-level design of the ATLAS trigger system [137–139]. The L1 trigger takes a decision based on coincident signals in the muon trigger chambers, namely the resistive plate chambers (RPC) within $|\eta| < 1.05$ and the thin gap chambers (TGC) in the endcap region ($1.05 < |\eta| < 2.4$). Regions of interest (ROI) are defined around the hit pattern and used to limit the amount of data to be analysed at the second trigger level L2. A rough estimate of the muon momentum is built from the size of the coincidence window, and is passed together with the geometrical information to the level 2 trigger. The geometrical acceptance of the L1 muon trigger is limited at $\eta = 0$ due to a crack, hosting service structures for the ID and calorimeters. The two software triggers refine the muon reconstruction. L2 adds precision tracking information from the monitored drift tubes (MDT). A first track fit is performed based on the MDT drift times within the ROI. Fast look-up-tables are used to assign an estimate of the muon transverse momentum based on the fit result. In addition, the reconstructed tracks from the ID are combined with the muon spectrometer tracks in order to provide a refined track parameter resolution. To allow for an improved background rejection, isolation variables are computed from reconstructed energy deposits in the calorimeter around the muon track and additional tracks nearby the muon candidate. At event filter level, the full detector information is finally available and algorithms close to the final offline algorithms are used to take the trigger decision. Muon reconstruction using both ID and MS information is performed by two algorithms extrapolating either the ID or the MS tracks towards the spectrometer or the inner detector, respectively. The algorithms are denoted as inside-out and outside-in algorithms. In the analysis presented in this thesis, single muon triggers are used. The corresponding trigger chains are denoted as *mu24i_tight* for the dataset collected in 2012 and *mu18_MG* for data collected in 2011. The name refers to the online transverse momentum threshold applied at trigger level. It is larger for the 2012 data taking period, lowering the trigger rate to allow for an unprescaled operation of the trigger item at the higher instantaneous luminosities achieved in 2012. In addition, isolation criteria were required at trigger level in 2012. During the datataking period in 2011, the inside-out algorithm was used for the event filter level muon reconstruction. In 2012 the inside-out algorithm was only executed in cases where the outside-in algorithm was not able to reconstruct a muon, in order to reduce the computing resource consumption in the dense tracking environment of the high luminosity data taking period [138]. Similar to the procedure with electrons, the trigger efficiency is measured in $Z \to \mu\mu$ events using a tag-and-probe technique which is detailed in Ref. [138]. The tag muon is required to be isolated and to be geometrically matched to the trigger object responsible for the successful triggering of the event. A second muon candidate in the event has to be isolated and of opposite charge. The invariant mass of the dimuon system is required to be compatible with the Z boson mass. The sample of probe muons is expected to be very pure and backgrounds from non-Z events are estimated to contribute at the 1% level at maximum. Figure 3.8 shows the muon

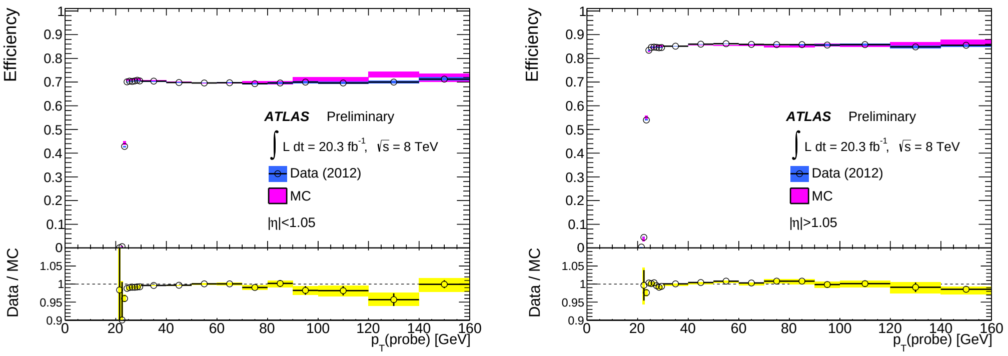

(a) (b)

Figure 3.8. *Single muon trigger efficiency, as measured in $Z \to \mu\mu$ events using a tag-and-probe technique in the central barrel (*$|\eta| < 1.05$*) (a) and the endcap (*$1.05 < |\eta| < 2.5$*) (b) regions, as a function of the muon transverse momentum. The ratio of the measured efficiency and the one found in simulated samples is shown in the lower part and agrees well over the full range of momenta [133, 138].*

trigger efficiency during datataking in 2012 compared to the trigger efficiency in simulated event samples, as a function of the reconstructed transverse momentum. The trigger efficiency shows a sharp *turn-on* behaviour at transverse momenta of approximately $p_T \approx 25$ GeV. Clearly visible is the lower absolute efficiency in the barrel region, due to the poorly instrumented region around $\eta = 0$. The efficiency is well described by the detector simulation with deviations within ±5% over the full momentum range. The measured differences are used to correct the simulated samples in the analysis.

3.5.2. Muon Reconstruction and Identification

Given the clean experimental signature of muons in ATLAS, the reconstruction and identification algorithms focus on a precise momentum measurement, while only minor criteria target the suppression of backgrounds from misidentified muons. Three different muon reconstruction algorithms are defined based on different combinations of sub-detector information [139, 140]:

- Stand-alone (SA) muons are reconstructed from MS information only. The tracks are extrapolated to the interaction point to determine the impact parameters. The expected energy loss in the calorimeter is taken into account.

- Combined (CB) muons are built by combining tracks from the ID with tracks from the MS, where the full covariance matrices of the two track fits are taken into account. Therefore, combined muons provide the highest signal purity and the best momentum resolution among the different muon reconstruction chains.

- Segment-tagged (ST) muons are formed by ID tracks, to which at least one track segment from the MS can be associated.

To reduce backgrounds of muons from heavy flavour hadron decays, additional isolation criteria are applied at analysis level. Both relative calorimeter and tracking isolation criteria are commonly used within ATLAS analyses. The search for $H \to \tau_{\text{lep}}\tau_{\text{had}}$ decays presented in this thesis makes use of combined muons.

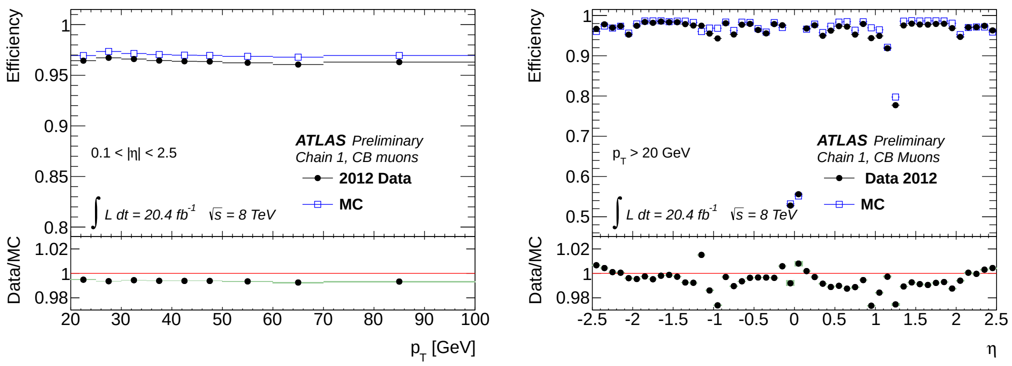

(a) (b)

Figure 3.9. *Muon reconstruction efficiency as a function of the muon transverse momentum (a) and the pseudorapidity (b) from a $Z \to \mu\mu$ tag-and-probe measurement [140]. The ratio between measured and simulated efficiencies shows good agreement over the full momentum and pseudorapidity range.*

While in general the muon reconstruction is performed within the full tracking acceptance up to $|\eta| < 2.5$, two regions show a significantly reduced reconstruction efficiency due to poor instrumentation. At $|\eta| = 0$, the muon spectrometers are only partially available due to service and support structures, while at $1.1 < \eta < 1.3$ some chambers were not installed in time for the data taking up to 2012. Most important for a good description of the muon reconstruction performance in the simulation, is a precise knowledge of the misalignment of the muon chambers. The misalignment can be measured in dedicated studies using cosmic ray events, as well as in special data taking runs in which the toroidal magnetic field was turned off [140].

The reconstruction and identification efficiencies are measured in $Z \to \mu\mu$ events [140], similar to the tag-and-probe measurement used to measure the trigger efficiencies, and are shown in Fig. 3.9 as a function of the muon pseudorapidity and transverse momentum. Clearly visible are the poorly instrumented detector regions, where the reconstruction efficiency drops significantly. The efficiency is well described by the simulation, with relative differences below ±2%. Corresponding scale factors are propagated to other simulated samples to correct for the efficiency difference in the simulation with respect to data. The muon purity in the selected probe-muon sample is of the order of 99.9%, a systematic uncertainty of ±0.2% on the scale factor is assigned to account for uncertainties in this small background component.

3.5.3. Muon-Momentum Scale

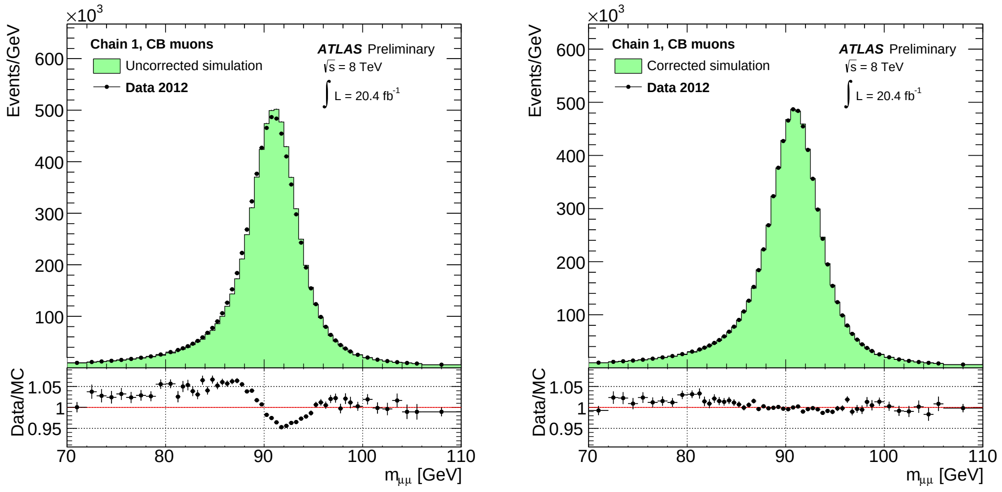

(a) (b)

Figure 3.10. *Invariant dimuon mass spectrum before (a) and after (b) the application of the muon-momentum scale and resolution corrections [140]. A clear improvement in the description of the Z mass distribution is visible.*

The muon-momentum scale and its resolution are studied in $Z \to \mu\mu$, $J/\Psi \to \mu\mu$ and $\Upsilon \to \mu\mu$ events. The fractional momentum resolution can be parametrised by:

$$\sigma(p_T)/p_T \quad = \quad a \oplus b \times p_T \tag{3.5}$$

describing a constant contribution from multiple scattering and a p_T dependent component from the spatial resolution of the detector. Based on this assumption, a template fit can be used to extract corrections to the scale, the multiple scattering and intrinsic resolution parameters from the observed $Z \to \mu\mu$ invariant mass spectrum. This analysis is performed in bins of the reconstructed muon pseudorapidity [140, 141]. The extracted scale corrections are of the order of one per mill and mostly compatible with unity. The corrections to the constant resolution parameter of the ID and the intrinsic resolution parameter of the MS reach up to 2%, depending on the pseudorapidity bin [140]. Figure 3.10 shows the invariant dimuon mass spectrum before and after resolution and scale corrections. A significant improvement in the description is found. The dominant systematic uncertainties arise from the mass window around the Z mass and a potential momentum dependence on the scale correction.

3.6. Hadronic Tau Decays

Tau leptons, as discussed in Section 1.3.3, are the heaviest leptons and decay in either leptons or hadrons with branching ratios summarised in Table 1.4. The leptonic decay modes (τ_{lep}), accounting for 35% of all tau decays, are experimentally effectively indistinguishable from prompt electron or muon production and are therefore not reconstructed or identified by a dedicated algorithm. Instead, the standard electron and muon reconstruction chains are used. The hadronic decays (τ_{had})[4] though, lead to a distinct signature of an odd number of charged hadrons, predominantly pions, eventually accompanied by a small number of neutral hadrons. The neutrino escapes detection but leads to missing transverse energy. Hadronic decays are classified by the number of charged particles into 1-prong and 3-prong decays. Decays with five charged hadrons are rare and not considered in this thesis. The hadronic tau decay products are highly collimated, due to the typically large momenta of the tau leptons produced in electroweak interactions compared to the tau lepton mass. This leads to a more narrow shower profile of the decay products than typically present in jets from quark and gluon hadronisation. Together with the distinct number of charged particles being reconstructed as tracks, this allows to define identification criteria able to differentiate between hadronic jets and hadronic tau decays. Besides jets, electrons provide a signature similar to the one expected from hadronic tau decays, given their narrow shower profile in combination with one single track. A dedicated set of identification criteria is used to suppress electrons being misidentified as τ_{had} objects. The identification algorithms are described in Section 3.6.1. A dedicated energy calibration corrects the reconstructed energy deposits to the true energy of the visible tau decay products. This calibration procedure is described in Section 3.6.2. The determination of the energy scale uncertainty, by propagating different single particle response measurements to the composite tau object, is performed in the course of this thesis and described in Chapter 4.

3.6.1. Reconstruction and Identification of Hadronic Tau Decays

The reconstruction of hadronic tau decays [142–144] is seeded by anti-k_T jets with a distance parameter of $r = 0.4$ built from TopoClusters at the LCW scale, passing loose acceptance criteria of $p_T > 10$ GeV and $|\eta| < 2.5$. An association between each tau candidate and a vertex is performed by choosing such pairs which provide the largest corresponding jet vertex-fraction (see also Section 3.3.1)[144]. All cluster and cell based variables are calculated in coordinate frames with the associated vertex as origin, reducing the impact of pile-up on the reconstruction performance. The four-momentum of the $\tau_{\text{had-vis}}$ candidate is fully determined by E_T, η and ϕ as measured in the calorimeter, while the mass is set to zero. An intermediate direction

---

[4] The symbol τ_{had} is used to denote both a hadronically decaying tau lepton and its reconstructed visible decay products, without the neutrino, since the exact meaning is usually apparent from the context. In cases where special emphasise is put on the fact that only the reconstructed visible decay products are referred to, the symbol $\tau_{\text{had-vis}}$ is used.

is defined by the sum of four-momenta of TopoClusters within $\Delta R < 0.2$ around the barycentre of the seed jet. Afterwards, the four-momentum of each TopoCluster is recalculated with respect to the associated vertex. Due to the collimated topology of hadronic tau decays, a cone of $\Delta R < 0.2$ is wide enough to contain most of the energy deposits of the tau decay products, while reducing the sensitivity to pile-up contributions compared to wider cone sizes. For the tau reconstruction in data taken in 2011 all TopoClusters within $\Delta R < 0.4$ were used. The resulting axis is used as intermediate direction during the calculation of all identification variables and is further refined during the energy calibration. Tracks within a cone of $\Delta R < 0.4$ of the intermediate axis are associated to the $\tau_{\mathrm{had-vis}}$ candidate. Those within a *core-cone* of $\Delta R < 0.2$ are used to determine the number of charged particles, while additional tracks in an *isolation annulus* of $0.2 < \Delta R < 0.4$ are associated to the $\tau_{\mathrm{had-vis}}$ object only for the calculation of certain identification variables. All tracks are required to pass basic tracking quality criteria. The reconstruction steps outlined above provide basically no rejection of backgrounds like hadronic jets, electrons or muons. Various identification variables discriminating real tau decays from these backgrounds are calculated based on calorimeter and tracking information, exploiting basic features of hadronic tau decays:

- Calorimeter shower shapes: Compared to quark and gluon initiated jets, hadronic tau decays feature a low particle multiplicity and a narrow shower profile. The decay products are a distinct mixture of charged and neutral hadrons and variables describing the shower shape, both in the longitudinal and transverse directions, therefore provide good background discrimination. One example is the central energy fraction f_{cent}, which is the ratio of energy depositions within $\Delta R < 0.1$ to energy depositions within $\Delta R < 0.2$ of the tau axis. Energy fractions between the different calorimeter layers, especially between the electromagnetic and hadronic calorimeters, provide a measure of the shower depth and of the relative energy contribution from particles interacting predominantly electromagnetically. This provides a particularly strong discrimination against electrons.

- Tracking information: Hadronic jets, especially gluon initiated ones, usually contain many charged hadrons with a relatively large spread in the $\eta - \phi$ plane. Measuring the p_T weighted track width over the full $\Delta R < 0.4$ cone or building the maximum opening angle between core tracks and the tau axis, allows to exploit this feature for the identification. Especially to improve the identification performance of multi-prong tau decays, variables exploiting the finite life-time of tau leptons can be used. The transverse flight path for example estimates the decay length of a secondary vertex in the transverse plane. To allow a better rejection of electrons, information from the TRT is exploited as well.

- Track-Calorimeter comparison: Variables directly combining the measurements of the tracking detector with calorimeter information, provide powerful variables based on the expected particle composition of hadronic tau decays. The transverse momentum of the leading track divided by the transverse energy of deposits within the core-cone directly relates the charged particle momentum to the total measured energy in the calorimeter.

Due to the tau-vertex association, tracking related variables are relatively stable against pile-up activity. To limit the impact of additional energy deposits by pile-up interactions on calorimeter based variables, pile-up sensitive variables are corrected linearly as a function of the number of reconstructed primary vertices.

An addition to the identification algorithm employed for data taken in 2012, is the use of variables including information from a π^0 cluster identification algorithm [142], attempting to reconstruct the substructure of the hadronic tau decay. This algorithm reconstructs the number of neutral pions within the core cone of the $\tau_{\mathrm{had-vis}}$ candidate, based on strip layer and other calorimeter measurements. Afterwards, the kinematic properties of the reconstructed π^0 clusters are combined with the tracks to form a refined $\tau_{\mathrm{had-vis}}$ four-momentum. Since the tracking detector provides an accurate measurement of the charged particle momenta, a combination of the reconstructed π^0 energy depositions in the calorimeter with the tracks would allow a significant improvement of the $\tau_{\mathrm{had-vis}}$ energy resolution. The π^0 reconstruction algorithm deployed in 2012 though, operates solely on TopoClusters and related shower shape moments. Hence, it cannot exploit the full granularity of the ATLAS calorimeter. Dedicated τ_{had} substructure reconstruction algorithms, operating on cell-level, are being studied and will most likely be used for τ_{had} reconstruction in 2015 and beyond. The TopoCluster based π^0 reconstruction nevertheless provides additional rejection power against hadronic jets in the τ_{had} identification step. The number of reconstructed π^0 clusters, the invariant mass of the tracks and the π^0 clusters as well as the ratio of the $\tau_{\mathrm{had-vis}}$ transverse momentum combining tracks and π^0 clusters with respect to the calorimeter based measurement are used in the identification algorithms for data taken in 2012. A full list of identification variables can be found in Ref. [142].

Discrimination against Jets

A boosted decision tree (BDT) is trained for one- and three-prong tau candidates based on eight and nine variables, respectively, to discriminate real τ_{had} decays from hadronic jets. Simulated samples of tau leptons from from Z, W and Z' decays are used as signal samples, while real collision data collected by jet triggers is used as background sample in the training procedure. Three working points with differing signal selection efficiencies are defined and denoted as *loose*, *medium* and *tight*. The actual BDT score requirements are parametrised as a function of the transverse momentum of the $\tau_{\mathrm{had-vis}}$ candidate to ensure a stable efficiency against p_T. Figure 3.11 shows the signal selection efficiency for one and 3-prong τ_{had} objects as a function of the reconstructed vertex multiplicity, demonstrating the robustness of the identification algorithm against the presence of additional pile-up interactions. For a signal efficiency of about 57% (38%) an inverse background efficiency of roughly 25 (500) is achieved for 1-prong (3-prong) $\tau_{\mathrm{had-vis}}$ objects. It is worth mentioning that the actual number of reconstructed tracks is not used in the $\tau_{\mathrm{had-vis}}$ identification, even though it provides additional discrimination against hadronic jets. A requirement on the number of tracks is instead added at the analysis level, contributing significantly to the rejection power.

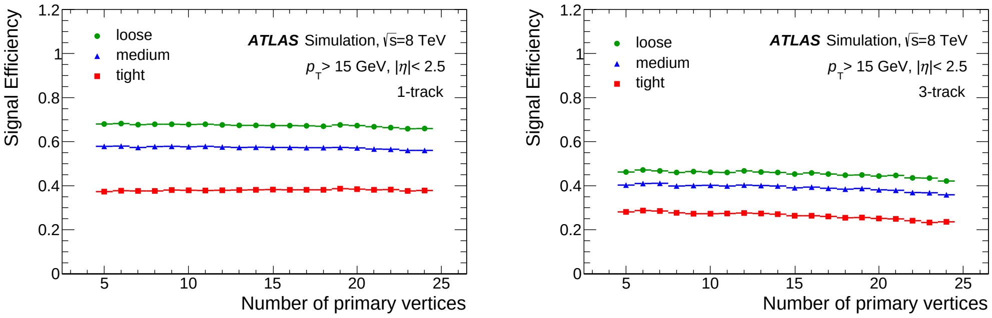

(a) (b)

Figure 3.11. *Signal selection efficiency of the three working points of the* $\tau_{\mathrm{had-vis}}$ *identification algorithm as a function of the number of reconstructed vertices for one- (a) and 3-prong* $\tau_{\mathrm{had-vis}}$ *objects (b). The selection efficiency is stable with respect to additional interaction vertices up to a small efficiency drop at large values of* N_{Vtx} *[142].*

The signal selection efficiencies in data are measured using a $Z \to \tau_{\mathrm{lep}}\tau_{\mathrm{had}}$ tag-and-probe technique. Events are selected using single muon and electron trigger items. The light lepton is required to pass tight quality and identification criteria, while $\tau_{\mathrm{had-vis}}$ candidates with one or three charged tracks, a total charge of unity and not geometrically overlapping with other reconstructed leptons are chosen as *probe*-objects. Only events with exactly one lepton and one $\tau_{\mathrm{had-vis}}$ candidate of opposite electric charge are considered. Additional selection cuts suppress background events from $W \to \ell\nu_\ell$ and $Z \to \ell\ell$ events. In contrast to $Z \to \ell\ell$ tag-and-probe measurements, as discussed above in the context of electron and muon efficiency measurements, the $Z \to \tau_{\mathrm{lep}}\tau_{\mathrm{had}}$ selection is still significantly contaminated with background events. Therefore, a template fit is used to determine the fractional background contribution. This fit is performed on the distribution of the number of tracks within a cone of $\Delta R < 0.6$ of the $\tau_{\mathrm{had-vis}}$ axis. Figure 3.12 shows the track multiplicity spectrum before and after applying the medium $\tau_{\mathrm{had-vis}}$ identification for real τ_{had} objects and the expected background contribution. This distribution shows clear peaks at one and three for real τ_{had} objects while it tends to larger values for hadronic jets and therefore provides excellent discriminating power between signal and background events. The expected shapes can be extracted from a control sample enriched in QCD events by reverting the charge requirement on the probe object, while a control sample enriched in $W \to \ell\nu_\ell +$ jets events can be selected by reverting one of the background suppression selection requirements. Comparing the fit result before and after applying the $\tau_{\mathrm{had-vis}}$ identification criteria allows to extract the signal efficiency. The efficiency ratio between data and simulated $Z \to \tau_{\mathrm{lep}}\tau_{\mathrm{had}}$ events is denoted as scale factor and compatible with one. The systematic uncertainty

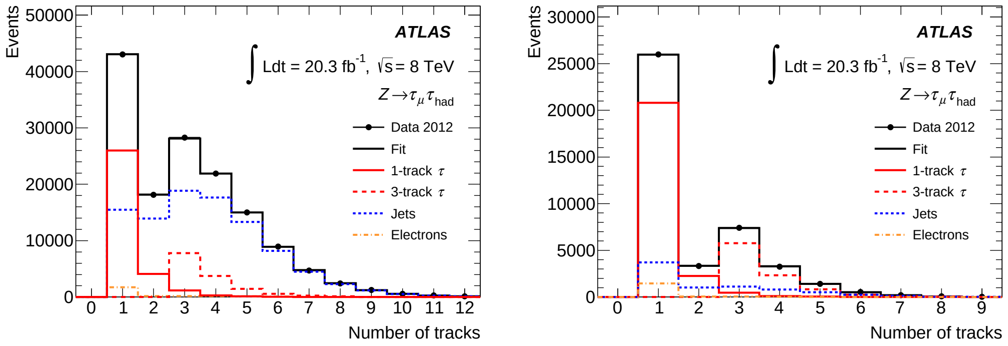

(a) (b)

Figure 3.12. *Number of tracks within a cone of $\Delta R < 0.6$ around the $\tau_{\mathrm{had-vis}}$ axis, for data selected in the $Z \rightarrow \tau_{\mathrm{lep}}\tau_{\mathrm{had}}$ tag-and-probe analysis used to measure the identification efficiency. While (a) shows the fit result of the signal and background contributions compared to the data before applying the τ_{had} identification criteria, (b) shows the same distribution after performing the fit on the sample passing medium τ_{had} identification criteria [142].*

is dominated by the background estimation, namely the jet background fraction and the uncertainty on the background track multiplicity spectrum. The combined systematic uncertainty ranges between $\pm(2-5)\%$, depending on the transverse momentum and pseudorapidity of the τ_{had} decay. The correction factors are applied to simulated τ_{had} objects and the corresponding systematic uncertainty is propagated to the individual analyses.

Discrimination against Electrons and Muons

Electrons, and to a lesser extent also muons, can be misidentified as τ_{had} objects as they feature a single track with narrow energy depositions in the calorimeter. Due to the high reconstruction efficiency of electrons and muons, most of such misidentified τ_{had} decays can be removed by resolving the ambiguity between reconstructed electrons, muons and τ_{had} objects, also referred to as overlap removal. This removal is usually carried out using looser object selection criteria than typically used for final state objects. For example, the $H \rightarrow \tau_{\mathrm{lep}}\tau_{\mathrm{had}}$ analysis presented here selects one electron passing tight identification criteria, while all τ_{had} objects overlapping with electrons passing loose identification criteria are removed. This already ensures a very good rejection of misidentified light leptons. In poorly instrumented detector regions though, where the electron or muon reconstruction and identification efficiency is lower, the overlap removal is not sufficient to reject light leptons from being reconstructed as τ_{had} objects.

A set of BDTs is trained to discriminate between τ_{had} objects and electrons [143]. Depending on the pseudorapidity of the τ_{had} candidate, different input variables are used. Besides information about the number of high threshold TRT hits, variables describing the longitudinal and transverse shower profile, electromagnetic energy fraction and the angular separation between the track and the calorimeter based $\tau_{\mathrm{had-vis}}$ axis are used as discriminating variables in the BDT training. Three working points corresponding to about 75%, 85% and 95% signal efficiency are defined, where the medium working point is used in the $H \to \tau_{\mathrm{lep}}\tau_{\mathrm{had}}$ analysis. While the BDTs are solely trained using one-prong tau decays, the resulting discriminant provides good rejection also for electrons being misidentified as three-prong taus and is used in the analysis. Such misidentified three-prong objects are mostly stemming from electrons undergoing Bremsstrahlung, followed by a photon conversion into a positron-electron pair. The selection efficiency of electrons is measured using a $Z \to ee$ tag-and-probe technique, selecting one isolated electron passing tight identification criteria and a probe τ_{had} candidate. In isolated regions around $|\eta| \approx 0$ and $|\eta| \approx 1$ the selection efficiency in data differs significantly compared to simulated event samples. The measurement is used to extract correction factors, where the precision is limited by the statistical uncertainty and systematic uncertainties on the definition of the tag requirements to up to ±30% [142].

Muons can mimic τ_{had} objects in rare cases in which they are not reconstructed by the muon reconstruction algorithm. This might happen if the muon loses a significant part of its energy during interaction with the calorimeter material, or if it is of such low momentum that it is stopped in the calorimeter and does not reach the muon spectrometer. A muon veto is defined targeting both such cases by placing requirements on the electromagnetic energy fraction and on the ratio between the transverse momentum on the track and the transverse energy deposited in the calorimeter of the τ_{had} candidate. With efficiencies greater than 96% on real τ_{had} decays these criteria remove about 40% of misidentified muons. Given the low misidentification probability of muons, these cuts are not used in the presented analysis.

3.6.2. Tau-Energy Calibration

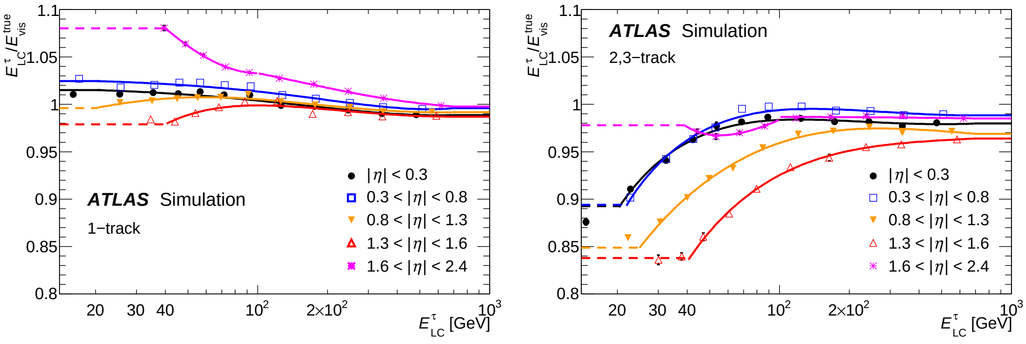

(a) (b)

Figure 3.13. *Tau-energy response of single- (a) and 3-prong (b) $\tau_{\mathrm{had-vis}}$ objects as a function of the reconstructed momentum at the LC scale [142].*

Besides the identification, the calibration of the reconstructed $\tau_{\mathrm{had-vis}}$ objects is crucial for a precise reconstruction of hadronic tau decays. As mentioned above, the τ_{had} reconstruction starts from clusters calibrated at the LC scale (see also Section 3.2). The tau-energy scale (TES) calibration [145, 146] is designed to additionally correct for out-of-cone effects, effects from nearby particles, for particle losses in front of the calorimeter and energy deposits from pile-up events. As starting point, the energy sum of TopoClusters within $\Delta R < 0.2$ around the barycentre of the seed-jet is calculated and compared to the true tau energy in simulated $Z \to \tau\tau$, $W \to \tau\nu$ and $Z' \to \tau\tau$ events. For this purpose, the simulated tau leptons are matched to the reconstructed $\tau_{\mathrm{had-vis}}$ objects, which are required to pass medium identification criteria to ensure an unbiased energy calibration for this set of taus. The energy response, defined as the ratio of reconstructed energy to true energy of the visible decay products, is calculated in bins of the true tau energy, the number of reconstructed tracks and the pseudorapidity. A Gaussian fit to the response distribution is used to determine the mean energy response, which is associated to the average reconstructed energy in each bin. The response as a function of the reconstructed energy is then parametrised by an empirically derived functional form and used as calibration for $\tau_{\mathrm{had-vis}}$ candidates. Figure 3.13 shows these TES response curves for single- and multi-prong τ_{had} objects.

After the main calibration, the pseudorapidity of the reconstructed $\tau_{\mathrm{had-vis}}$ object is refined by applying a linear correction, accounting for a bias due to the lower energy response in poorly instrumented detector regions compared to the average response. This correction is smaller than 0.01 over the full range in $|\eta|$, and is based on the same set of simulated tau decays as used for the energy calibration. By using TopoClusters only within a narrow cone of $\Delta R < 0.2$, the energy dependence on pile-up events is small. Depending on the pseudorapidity of the τ_{had} object, the energy dependence on the number of vertices reaches up to 400 MeV per vertex and is shown in Fig. 3.14 (a). To improve the energy resolution, the pile-up dependence is greatly reduced by applying a linear pile-up correction as a function of the number of primary vertices. It corrects the reconstructed energy to the average pile-up level present in the simulated samples used to derive the calibration. Instead of subtracting the full pile-up energy contribution, this procedure minimises the distance in the number of vertices over which the linear assumption is used for extrapolation. The residual energy response dependence on pile-up after the correction is about $1-3\%$, depending on the transverse momentum and pseudorapidity, and assigned as systematic uncertainty.

The energy resolution as a function of the true visible tau momentum for single- and multi-prong τ_{had} objects is shown in Fig. 3.14 (b) for one pseudorapidity bin. It ranges between 20% for taus of low momentum to less than 10% at higher momenta and is generally smaller for single-prong $\tau_{\mathrm{had-vis}}$ due to the smaller hadronic energy deposits relative to electromagnetic deposits from neutral pion decays. Comparisons of the energy resolutions in simulated event samples with a material budget model varied within the precision of the current best knowledge, two different hadronic shower models and different underlying event tunes revealed differences in the resolution of less than $\pm 1\%$ [145]. Besides the baseline energy calibration, two

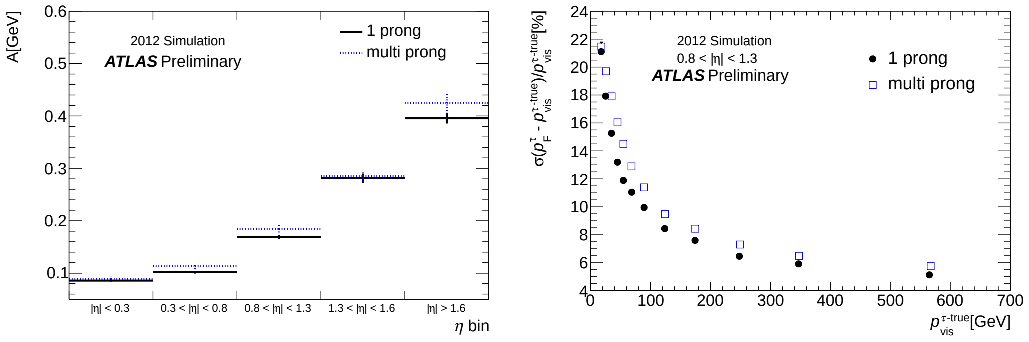

(a) (b)

Figure 3.14. *Average energy deposit from pile-up interactions per additional primary vertex in different pseudorapidity bins (a). The slightly larger pile-up dependence for multi-prong* τ_{had} *objects is due to the larger active area the additional decay particles are causing. Figure (b) shows the relative energy resolution as a function of the true visible tau momentum [145].*

complementary methods are used to probe the calibration with real data, to assess the systematic uncertainty and to assign a data-driven residual correction. Both methods and the resulting systematic uncertainties are discussed in Chapter 4.

3.7. Missing Transverse Energy

In hadron collisions, four-momentum conservation can only be partially used as a constraint during event reconstruction. This is due to the unknown initial momenta of the partons participating in the hard scatter process, leading to an unknown momentum of the final state along the beam axis. For the protons in the LHC beams the transverse momenta of the partons are negligibly small, so that the initial transverse momentum of the scattered partons can be assumed to be zero. An observable denoted as *missing transverse energy* ($\mathbf{E}_T^{\text{miss}}$) is used to quantify the momentum vector in the transverse plane which is missing to achieve a momentum balance equal to a total transverse momentum of zero. A significant amount of missing transverse energy indicates the presence of particles which are not detected by the detector, for example due to their weak interaction with matter, as it is the case for neutrinos. The reconstruction of $\mathbf{E}_T^{\text{miss}}$ is of particular interest for the search for $H \to \tau\tau$ decays, as a significant fraction of the tau momenta is carried by the neutrinos. Reconstructing the sum of their transverse momenta greatly improves the ability to suppress background events or to reconstruct the invariant ditau mass.

The $\mathbf{E}_T^{\text{miss}}$ reconstruction [147–149] in ATLAS makes use of fully reconstructed and calibrated objects, as they are discussed in the previous sections. The x, y components receive contributions from six terms corresponding to electrons, photons, hadronically decaying taus, jets and muons. One additional term denoted as

$\mathbf{E}_T^{\text{miss,SoftTerm}}$ accounts for all contributions not matched to one of these physics objects:

$$\begin{aligned}\mathbf{E}_T^{\text{miss}} &= \mathbf{E}_T^{\text{miss},e} + \mathbf{E}_T^{\text{miss},\gamma} + \mathbf{E}_T^{\text{miss},\tau_{\text{had}}} + \mathbf{E}_T^{\text{miss,jets}} \\ &\quad + \mathbf{E}_T^{\text{miss},\mu} + \mathbf{E}_T^{\text{miss,SoftTerm}} \end{aligned} \tag{3.6}$$

Each term is calculated as the negative sum of the $x(y)$-momentum components of the corresponding objects. Electrons are calibrated to the electron-energy scale as discussed in 3.4, photons contribute at the EM scale and hadronic tau decays are calibrated to the TES as detailed in Section 3.6, including the pile-up correction. The jet term includes jets clustered with the anti-k_T algorithm with $r = 0.4$, fully calibrated and corrected for pile-up energy deposits using the jet-area method detailed in Section 3.3. Only jets with transverse momenta above 20 GeV are included in $\mathbf{E}_T^{\text{miss,jets}}$. To recover contributions from low momentum muons also *tagged* muons (see Section 3.5) are used to form the muon term. Since the standard ATLAS object reconstruction algorithms are optimised on fairly energetic particles, low momentum particles are not covered by these terms. Due to the large particle multiplicity in typical scatter events, the contribution from soft particles can have a significant impact on the missing transverse energy reconstruction performance. A dedicated soft term $\mathbf{E}_T^{\text{miss,SoftTerm}}$ accounts for these particles, and makes use of energy deposits and tracks. To reduce the impact of noise, only energy deposits clustered in calibrated TopoClusters (see Section 3.2) are used, while tracks are only added in case they are not matched to either a physics object or a TopoCluster. In addition, to avoid double counting, the expected energy loss of muons along their flight path is subtracted from the soft term. Pile-up events degrade the $\mathbf{E}_T^{\text{miss}}$ reconstruction performance, mainly the resolution. Most affected by pile-up events are the jets and the soft term. To suppress the impact on the jet term, jets with $p_T < 50$ GeV and within $|\eta| < 2.4$ are required to pass a cut on the jet-vertex-fraction (see also Section 3.3.1) of $|\text{JVF}| > 0$.

The soft term receives a correction based on the soft term vertex fraction [150], defined, similarly as JVF, as the momentum fraction of tracks matched to the primary vertex and a soft term cluster with respect to the sum of all track momenta matched to the soft term clusters:

$$\text{STVF} = \sum_{\text{tracks}_{\text{SoftTerm}},\text{PV}} p_T \Big/ \sum_{\text{tracks}_{\text{SoftTerm}}} p_T \tag{3.7}$$

The $\mathbf{E}_T^{\text{miss,SoftTerm}}$ is scaled by the STVF to compute the pile-up corrected $\mathbf{E}_T^{\text{miss}}$.

Figure 3.15 shows two quantities describing the performance of the $\mathbf{E}_T^{\text{miss}}$ reconstruction. Figure 3.15 (a) shows the E_T^{miss} resolution as a function of the scalar sum of all contributions to the E_T^{miss} calculation ($\sum E_T$) before (black) and after applying pile-up corrections to the jet and soft terms (red) in simulated VBF $H \to \tau_{\text{lep}}\tau_{\text{had}}$ events. The event topology of VBF $H \to \tau\tau$ events is special in the sense, that genuine E_T^{miss} is expected from the presence of neutrinos and that at least two high energetic jets are present in the event. Therefore, the soft term contributes

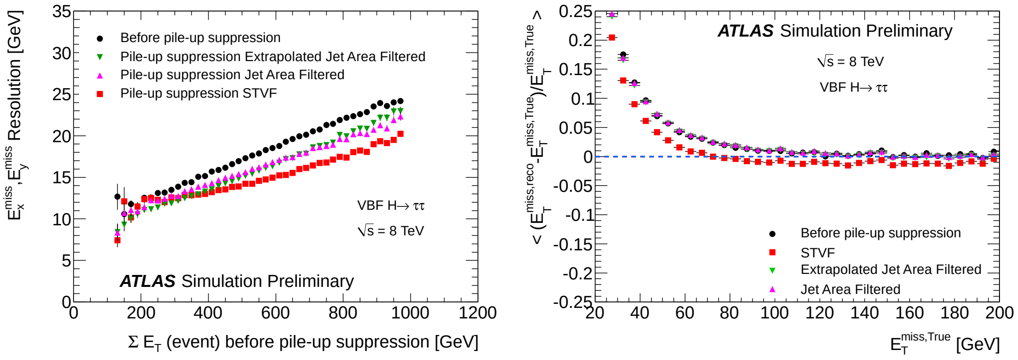

(a) (b)

Figure 3.15. *Resolution of E_T^{miss} as a function of $\sum E_T$ (a) as well as the linearity as a function of $E_T^{miss,\,True}$ (b) for simulated VBF $H \to \tau_{\text{lep}}\tau_{\text{had}}$ events before (black) and after (red) applying the pile-up correction to the soft term. Taken from Ref. [148].*

to a smaller extent than for example in events without any jets. Nevertheless, the soft term pile-up correction significantly improves the E_T^{miss} resolution. Figure 3.15 (b) shows the linearity, a measure of the bias between reconstructed and true E_T^{miss}, as a function of the true missing energy. At low $E_T^{\text{miss,True}}$ a positive bias is present which is due to resolution effects and the strictly positive definition of E_T^{miss}. Over a wide range of true E_T^{miss}, the pile-up correction improves the linearity significantly. At large values of E_T^{miss} exceeding 80 GeV, the pile-up correction is slightly overcorrecting the missing transverse energy.

As $\mathbf{E}_T^{\text{miss}}$ receives contributions from all physics objects, the systematic uncertainty on the $\mathbf{E}_T^{\text{miss}}$ reconstruction and performance also depends highly on the systematic uncertainties of the individual energy scales and resolutions. In addition to those, a systematic uncertainty on the soft term resolution and scale is studied in $Z \to \mu^+\mu^-$ events without jets. In such events, only the muon and the soft term are expected to contribute to the $\mathbf{E}_T^{\text{miss}}$ reconstruction and are therefore well suited to study the modelling of the soft term in the ATLAS simulation. For the $\mathbf{E}_T^{\text{miss}}$ reconstruction in 2012, using the STVF pile-up correction of the soft term, systematic uncertainties of about ±8% on the scale and about ±5% on the resolution of the soft term are found [148].

4 Determination of the Tau-Energy Scale Uncertainty

Hadrons traversing the calorimeter of ATLAS interact with the material and create hadronic showers. Compared to electromagnetic showers, mostly a cascade of pair-creation and bremsstrahlung events, hadronic showers are of a much more complex structure. Their spatial width and depth fluctuates to a larger extent on an event-by-event basis and neutron emission, the breakup of nuclei and leptonic hadron decays to neutrinos and muons lead to a reduced energy response by the ATLAS sampling calorimeter compared to electromagnetic showers. All these effects lead to a worse energy resolution in the reconstruction of hadronic energy deposits. The complexity of strong interactions leads to a significantly larger systematic uncertainty in the modelling of the response compared to typical electromagnetic deposits by photons or electrons. For a precise reconstruction of hadronic tau decays it is therefore crucial to validate the calibration and to reliably assess the systematic uncertainty on the energy scale in simulated event samples.

The dominant source of systematic uncertainty is the modelling of the hadronic shower. Early assessments of the tau-energy scale uncertainty in 2011 [151] were based on comparing the energy response in simulated event samples, using the nominal hadronic shower model QGSP_BERT [152–154] to the response using an alternate model denoted as FTFP_BERT [155]. These comparisons resulted in estimates of the energy scale uncertainty of the order of $3-6\%$. While the QGSP_BERT model includes a quark-gluon string model at high energy and combines it with the Bertini intra-nuclear cascade at low energy, the FTFP_BERT model uses the Fritjof model at high energy together with the Bertini intra-nuclear cascade at low energy. To reduce this uncertainty, a direct comparison of the calibration performance in data to the simulated energy response is necessary. In contrast to the calibration of the electron energy based on the reconstructed invariant mass spectrum in $Z \to ee$ events, or the calibration of the jet energy based on $\gamma+\text{jets}$ and $Z+\text{jets}$ balancing outlined in Sections 3.4 and 3.3, the tau-energy scale is harder to assess due to the neutrino escaping detection. Two different methods are pursued to tackle this issue. The *decomposition method* is based on propagating response measurements of the individual tau decay products to the composite tau object. It makes use of measurements of the charged pion response in collision data as well as in testbeam measurements done prior to the ATLAS data taking. This analysis was performed within the course of this thesis and is described in Section 4.1. It was used to estimate the TES uncertainty for 2011 data as well as for 2012 data. Only the latter is explained in detail. The second method reconstructs the *visible mass* (m_{vis}) in $Z \to \tau_\mu \tau_{\text{had}}$ events. Even though ignoring the neutrinos in the final state, the peak position depends approximately linearly on the energy scale and can be used to assess the response in data. This is described in Section 4.2. Both methods are available for data taken in 2012 and yield compatible results. Since the more direct approach of fitting the $Z \to \tau_\mu \tau_{\text{had}}$ visible mass peak only has sensitivity in a limited kinematic phase-space, it is combined with the decomposition method where necessary. This is explained in Section 4.3.

4.1. Tau-Energy Scale Uncertainty from Single Particle Response Measurements

The TES uncertainty receives contributions from the general calorimeter energy response to the τ_{had} decay products, the underlying event model used in the chosen event generator, the general detector model in the ATLAS simulation and additionally from calibration method inherent uncertainties, which are referred to as *non-closure*. To assess the calorimeter-response uncertainty in τ_{had} decays, dedicated response measurements of the individual decay products can be performed and propagated to the level of the $\tau_{\text{had-vis}}$ object. This methodology was used to assess the TES uncertainty for 2011 and 2012 [142, 145, 146] as well as the jet-energy scale uncertainty for data taken in 2010 [156–158].

As summarised in Table 1.4, τ_{had} decays result in a mixture of charged and neutral hadrons, mostly pions, as well as one neutrino. The ATLAS simulation framework [76] links simulated energy deposits in the detector material to the initiating particle. This allows to decompose the reconstructed $\tau_{\text{had-vis}}$ object and to build a correspondence between each tau decay product and its reconstructed energy deposits. That way the results of single particle response measurements can be propagated on a particle-by-particle basis.

Each decay product is classified into one of the following three classes determining which energy response measurement is to be used in the propagation procedure:

- Low momentum charged hadrons. In the momentum range between 2 GeV $\leq p \leq$ 20 GeV and within the tracking detector acceptance, the energy response of charged hadrons is directly assessed using a $\langle E/p \rangle$ measurement. For this measurement the momentum (p) of isolated tracks is compared to geometrically matched reconstructed energy deposits (E) in the calorimeter. The $\langle E/p \rangle$ measurement is described in Section 4.1.2.

- High momentum charged hadrons. As the statistical power of the $\langle E/p \rangle$ response measurement is limited for large particle momenta, the energy response uncertainty for charged hadrons with momenta above $p >$ 20 GeV is estimated by test-beam measurements performed in 2004. During these measurements, a full slice of the ATLAS detector, corresponding to the

$|\eta| < 0.8$ region, was exposed to a pion beam with momenta between 20 GeV and 350 GeV.

- Neutral pions. Energy deposits from neutral pions decaying into a pair of photons are subject to the calorimeter-response uncertainty to electromagnetic showers. The EM scale is studied in detail using the reconstructed mass of $Z \to ee$ decays and minimum ionising muons in the hadronic tile calorimeter. The absolute energy scale is considered well described by the simulation and the corresponding uncertainties are propagated to the τ_{had} scale.

Figure 4.1 shows the fractional contribution to the total energy deposit within reconstructed $\tau_{\mathrm{had-vis}}$ objects, by particles whose response is constrained by the $\langle E/p \rangle$, the test-beam measurement and the global EM scale uncertainty. As expected, the energy scale uncertainty determination is dominated by the $\langle E/p \rangle$ measurement for low τ_{had} momenta, while the test-beam measurement dominates for larger momenta. Particles subject to the global EM scale uncertainty, mostly photons from neutral pion decays, contribute independently of the tau momentum. The fraction of energy carried by charged hadrons is of the order of 60% for $\tau_{\mathrm{1-prong}}$ and of the order of 85% for $\tau_{\mathrm{multi-prong}}$ decays.

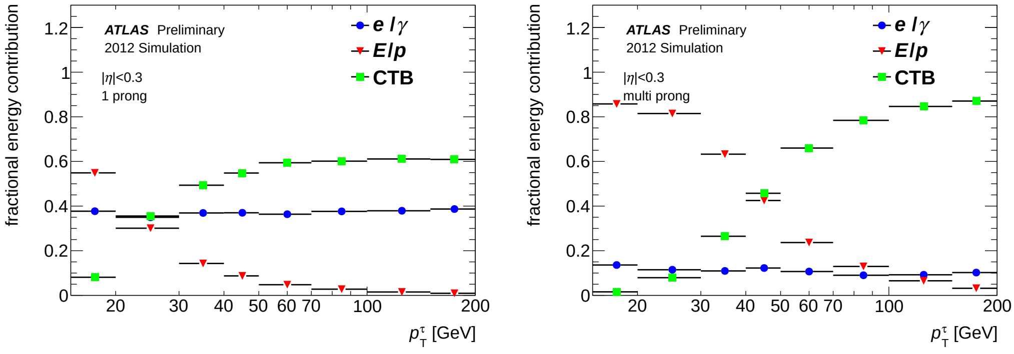

(a) (b)

Figure 4.1. *Fractional energy contributions to reconstructed single (a) and multi-prong (b) $\tau_{\mathrm{had-vis}}$ objects by particles inside of one of the three classes used to determine the single particle response measurement to be used in the uncertainty determination.*

4.1.1. Particle Decomposition

To propagate the single particle uncertainties to the τ_{had} object, pseudo-experiments are performed, which effectively sample over the various uncertainty dimensions. Each pseudo-experiment corresponds to a slightly varied reconstruction performance. For each pseudo-experiment (t), particle type, momentum (i) and pseudorapidity bin (j) a random factor f_t is sampled from a Gaussian (G) probability-density function (PDF) with a mean given by the measured response ratio r between data and simulated events and its width given by the statistical uncertainties $\Delta r^{(i,j)}$ of the corresponding energy response measurement.

$$f_t^{(i,j)} = \mathrm{N}(r^{(i,j)}, \Delta r^{(i,j)}) \tag{4.1}$$

Systematic uncertainties (δ) of the response measurements are included as additional multiplicative scale factors $u_{t,\delta}^{(i,j)}$, which are again sampled from Gaussian PDFs centred at 1, where their widths are given by the corresponding systematic uncertainty, which may depend on particle type, momentum and pseudorapidity.

In every pseudo-experiment t, the reconstructed $\tau_{\mathrm{had-vis}}$ energy is recalculated, using the varied response values, by summing all energy deposits E_k of the reconstructed $\tau_{\mathrm{had-vis}}$ objects' constituents:

$$E_t^{\tau_{\mathrm{had-vis}}} = \sum_k \big(f_t^{(i_k,j_k)} \cdot \prod_\delta u_{t,\delta}^{(i_k,j_k)}\big) \cdot E_k \tag{4.2}$$

This energy is compared to the reconstructed energy without any response variations applied, in order to assess the impact on the TES of this specific choice of parameters and $\tau_{\mathrm{had-vis}}$ object.

For each toy experiment a large sample of simulated tau decays is evaluated. These simulated event samples contain $Z \to \tau\tau$ and $Z' \to \tau\tau$ events generated with the PYTHIA 8 event generator. The events are simulated without additional pile-up interactions to allow a pure calorimeter-response uncertainty evaluation. Only reconstructed $\tau_{\mathrm{had-vis}}$ objects being geometrically matched to a true τ lepton and passing medium identification criteria are used, following the same selection criteria as applied during the TES calibration. The mean value $\mu_t := \langle E_t^{\tau_{\mathrm{had-vis}}} / E^{\tau_{\mathrm{had-vis}}} \rangle$, within one momentum and pseudorapidity bin, over this sample yields the relative TES shift for a specific pseudo-experiment t. The distribution of μ_t values over a set of 1000 pseudo-experiments is then fitted with a Gaussian to extract a width and a central value. While the width corresponds to the calorimeter-response uncertainty of the TES, the central value corresponds to the expected TES shift between data and simulation, given the measured scale differences in single particle response measurements.

In the following, the response measurements to be applied to the three particle classes are summarised.

4.1.2. Response of Low Momentum Charged Hadrons

The mean energy response to charged hadrons is measured by comparing the momentum measurement of the inner detector to the calorimeter energy deposits. For well isolated tracks the momentum measurement offers a precise reference scale with uncertainties well below the typical calorimeter-response uncertainties. Such a measurement was performed using 2010 data [126] and updated using data taken in 2011 and 2012 in the course of this thesis [145, 146]. While pion production in p-p collisions occurs frequently, the ATLAS trigger system rejects most of these events at low momentum scale. In addition, the large instantaneous luminosity during nominal data taking in 2011 and 2012 limits the number of well isolated particles. An unbiased sample of such events was collected during a dedicated low pile-up run in 2012, where the average number of interactions per bunch-crossing corresponded to 0.01. Therefore the data is compared to simulated event samples not including any pile-up events. In contrast to the nominal 2012 reconstruction settings, the average noise level in the topological clustering algorithm is configured to match these non-PU conditions.

Tracks are required to pass quality criteria, ensuring a high signal purity and to be well isolated. Tracks accompanied by other reconstructed track candidates within a cone of $\Delta R < 0.4$ are rejected. The measured track momentum p is compared to reconstructed energy deposits in TopoClusters within a $\Delta R < 0.2$ cone around the calorimeter impact point of the track, where the cone size was chosen to contain more than 90% of all energy deposits of the charged hadron while keeping neutral background contributions small. While the isolation requirement rejects backgrounds emerging from charged particles, neutral particles still contribute to the reconstructed energy. Such a background component depends strongly on the modelling of non-perturbative QCD effects, like the underlying event, and it is likely not well described in simulated events. Any mismodelling might bias the response measurement and the background component is therefore subtracted on average. Neutral particles are expected to deposit their energy predominantly in the electromagnetic calorimeter. To estimate their energy deposit, a sample of particles needs to be selected which start their hadronic shower development late enough, so that the energy deposits in the electromagnetic calorimeter are dominated by the background contribution. Such a sample is selected by requiring that the charged particle is compatible with being a minimum ionising particle showering mainly in the hadronic calorimeter. Particle candidates compatible with minimum ionising particles are selected by requiring an energy deposit of at least 1.1 GeV in the EM calorimeter within a narrow cone of $\Delta R < 0.1$ around the impact point of the track, and that a fraction of at least 40% of their track momentum was deposited in the hadronic calorimeter within the same cone size. This selection ensures that the actual hadronic shower starts late enough to enable a valid background energy density estimate inside an annulus of $0.1 < \Delta R < 0.2$ in the EM calorimeter. This background energy measurement is scaled by a geometrical factor of 4/3 and used to correct the measured $\langle E/p\rangle$ value on average in every pseudorapidity and track momentum bin independently:

$$\langle E/p\rangle_{\mathrm{corr.}} = \langle E/p\rangle - \langle E/p\rangle_{\mathrm{BG}} \tag{4.3}$$

Figure 4.2 (a) shows the E/p distribution in one pseudorapidity and track momentum bin, while Fig. 4.2 (b) shows the corresponding $(E/p)_{\mathrm{BG}}$ background distribution, both using reconstructed energy deposits at the EM scale. The data is compared to simulated Minimum Bias event samples using the PYTHIA8 event generator [62] with the A2 tune [159]. The samples were passed through the ATLAS Geant4 model, using the QGSP_BERT hadronic physics model. While the peak region is generally well described, large discrepancies are found for large and small values of E/p. The region with $E/p > 1$ is dominated by energy deposits from neutral particles close to the selected track. This contribution is not well modelled in the simulated event samples as can be seen from the background distribution. The region of small E/p values is dominated by negative energy contributions from cells in the Liquid Argon calorimeter. Such negative cell energies occur from the long lasting bipolar pulse-shape of the Liquid Argon calorimeter in case of energy deposits in the cell during previous bunch-crossings. Even though the studied data sample features a generally low level of pile-up in each bunch-crossing, neighbouring bunch-crossings still affect this low-end tail. The background-subtraction method is capable of also removing these effects on average. Figure 4.3 shows the corrected $\langle E/p\rangle_{\text{corr.}}$ distribution as a function of the track momentum in four different pseudorapidity regions. After subtracting the neutral background component, the mean value of the E/p distributions is very well described by the simulation with deviations smaller than 5%.

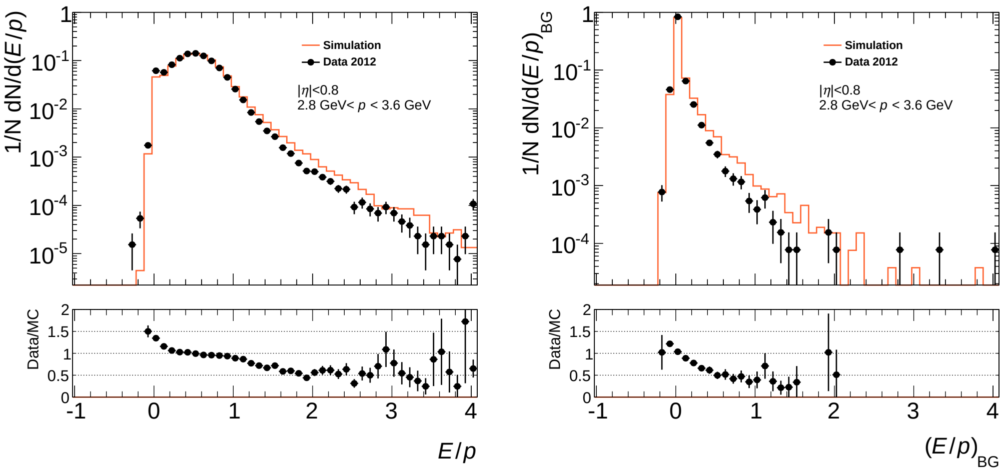

(a)

(b)

Figure 4.2. *Distribution of E/p for tracks within a momentum range of 2.8 GeV $<$ $p < 3.6$ GeV in the central detector region. While Figure (a) shows the nominal track selection, Figure (b) shows the distribution for tracks passing the minimal ionising particle track selection, used to estimate the neutral background component in the EM calorimeter. Therefore, only EM calorimeter deposits are included in Figure (b).*

Systematic Uncertainties

The average energy deposit from pile-up interactions is taken into account in the noise suppression during the topological clustering for nominal data reconstruction, while no pile-up noise suppression was performed during reconstruction of the dedicated low pile-up run. To ensure the applicability of the obtained results to τ_{had} objects in 2012 data, the impact of the noise suppression on the $\langle E/p\rangle$ result

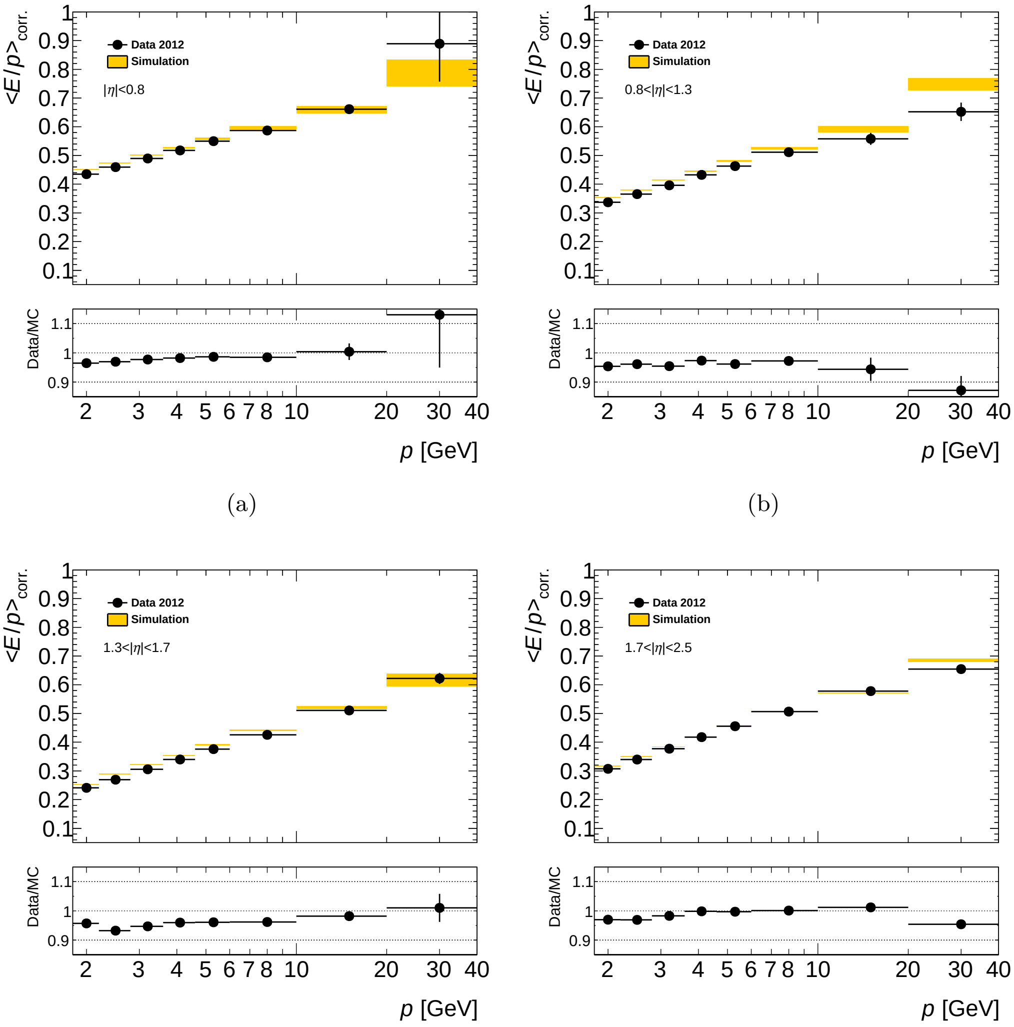

(a)

(b)

(c)

(d)

Figure 4.3. *Background subtracted* $\langle E/p \rangle_{corr.}$ *distributions as a function of the track momentum in pseudorapidity regions corresponding to* $|\eta| < 0.8$ *(a),* $0.8 < |\eta| < 1.3$ *(b),* $1.3 < |\eta| < 1.7$ *(c),* $1.7 < |\eta| < 2.5$ *(d). The yellow band corresponds to the statistical uncertainty of the simulated event sample.*

was evaluated. Comparisons between the agreement of data and simulated event samples using different noise suppression settings were carried out. In addition, a comparison between the agreement of data and simulated event samples using a cell-based $\langle E/p \rangle$ measurement and the nominal cluster-based measurement probes the total effect of noise suppression. For the cell-level measurement, all energy deposits in calorimeter cells within the cone are used, while the cluster-based measurement is based on clustered energy deposits only. Within $|\eta| < 1.5$ both comparisons showed no significant deviations within uncertainties of up to ±2%. Therefore, an uncertainty of ±2% is assigned to energy deposits within this region. For larger pseudorapidities, in the acceptance of the hadronic endcap calorimeter, larger deviations are observed, as the average noise level is larger. Here uncertainties of up to ±10% for track momenta of 2 GeV to ±2% for momenta of 8 GeV are assigned. These uncertainties are conservative since the performance of the clustering noise suppression depends heavily on the energy density surrounding the particle under study. The energy density in the $\Delta R < 0.2$ cone considered for τ_{had} reconstruction is expected to be larger than in the surroundings of isolated tracks. In general, two effects might impact the performance of the noise suppression in data compared to the simulated event samples. Of major interest in the application to τ_{had} objects is the description of the hadronic shower of the charged pion itself. A second effect may arise from the neutral background component, which especially at low track momenta contributes significantly to the total reconstructed energy. The difference between cell-level and cluster-based $\langle E/p \rangle$ measurements is found to be larger for the background measurement than for the nominal track sample. Furthermore a radial dependence in the modelling of the ratio between reconstructed cluster to cell energies is observed. While the energy deposit profile of the charged particle is expected to fall off rapidly as a function of the radius, the background contribution is expected to have only a small dependence on the radius, giving rise to larger fractional background contributions in outer annuli compared to inner cones. In addition, studies comparing two simulated event samples from the PYTHIA6 and PYTHIA8 event generators showed a different background level of the order of ±10%, directly impacting the number of formed TopoClusters. Since the pion shower itself is purely simulated by GEANT4 this difference is directly related to the actual background from non-perturbative QCD effects.

Additional systematic uncertainties account for the track selection, the tracking momentum scale uncertainty and E/p acceptance effects.

4.1.3. Response of High Momentum Charged Hadrons

In 2004 a slice of the ATLAS detector was exposed to a test beam of charged pions with energies between 20 and 350 GeV at fixed pseudorapidities between 0.2 and 0.65 [160]. The combined test beam data (CTB) is used to constrain the calorimeter response for high momentum charged pions, which are not covered by the in situ E/p analysis. The response was found to be generally well described with deviations of the order of a few percent.

To account for all changes in the calorimeter simulation and calibration method since the test beam data analysis, like the Geant 4 version used during the simulation or changes to the detector model within the simulation framework, single pions with energies and pseudorapidities corresponding to the test beam setup are simulated using the latest simulation release and conditions configurations. The difference in the pion response between the two simulation releases was found to be within ±0.5%. Therefore the test beam results are included in the response uncertainty determination with an additional ±0.5% systematic uncertainty to cover possible response changes in the simulation. Other systematic uncertainties are included to account for the fact that the experimental setup and alignment in the test beam might differ slightly from the final ATLAS setup. These include uncertainties for the LAr (±0.4%) and Tile (±1.5%) uniformity for all energies measured at the same pseudorapidity point, as well as scale uncertainties in the LAr (±0.7%) and Tile calorimeter (±0.5%) [157].

4.1.4. Global Electromagnetic Energy Scale

The electromagnetic energy scale is precisely measured in $Z \to ee$ decays for the electromagnetic calorimeters, as well as from studying the energy loss of minimal ionising muons in the hadronic Tile calorimeter. As these studies mostly focus on reconstructed electron or muon objects, the uncertainties on the energy scale are based on the reconstruction performance in calorimeter clusters. The uncertainties applicable to cell-energy measurements are slightly larger than the corresponding uncertainties of the reconstructed objects energy or momentum scale. For the electromagnetic barrel calorimeter a ±1.5% uncertainty on the cell energy measurement is propagated to the τ_{had} object, while energy deposits within the hadronic tile calorimeter are subject of a ±3% uncertainty. These absolute scale uncertainties are applied to EM energy deposits like photons from neutral pion decays, as well as to deposits emerging from particles outside the phase space covered by the in situ $\langle E/p \rangle$ analysis.

4.1.5. Impact of Shower-Shape Modelling on the LC Cluster Calibration

Imperfections in the hadronic shower model might impact the energy density profile of the shower, and hence also the way cells are clustered during the TopoCluster reconstruction. Any such effect is neglected in the pseudo-experiment approach outlined above, as only cells included in the TopoClusters of the reconstructed $\tau_{\mathrm{had-vis}}$ object are considered. The impact of the response uncertainty on the clustering algorithm is studied by re-applying the clustering algorithm after changing the various energy scales in each pseudo-experiment. This effect is negligible, as is the difference on clustering performance between different hadronic shower models. Since the $\tau_{\mathrm{had-vis}}$ energy reconstruction is based on calibrated LC clusters, an additional uncertainty arises from a potential dependence of the LC calibration

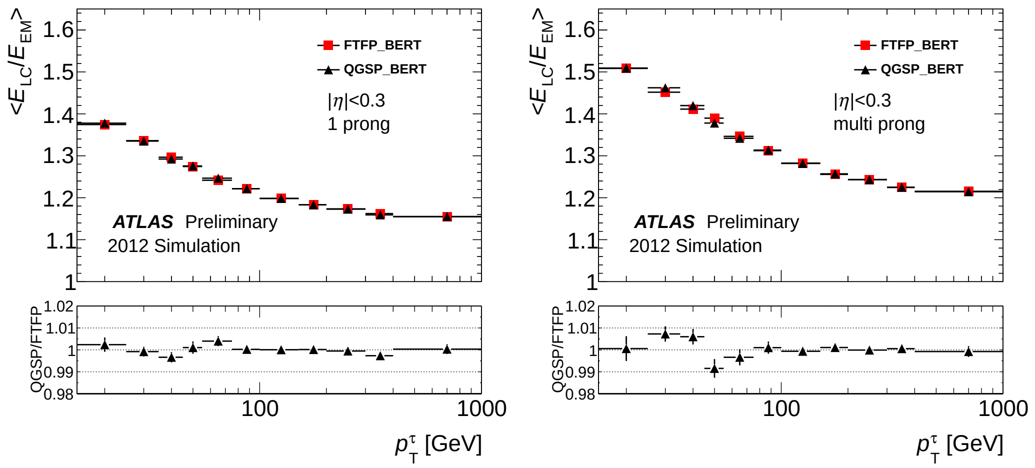

(a) (b)

Figure 4.4. *Effective LC-cluster calibration weights $\langle E_{LC}/E_{EM}\rangle$ for clusters associated to single (a) and multi-prong (b) $\tau_{\text{had-vis}}$ objects, as a function of the reconstructed $\tau_{\text{had-vis}}$ transverse momentum. Compared are simulated event samples using two different hadronic shower models.*

weights on the hadronic shower model. Two different hadronic shower models, the QGSP_BERT and FTFP_BERT physics models, are studied with respect to differences in the LC calibration. Since an absolute energy-response difference is well expected, the effective calibration weight $\langle E_{\text{LC}}/E_{\text{EM}}\rangle$ is used to assess this effect. Figure 4.4 shows the effective cluster-calibration weight for single and multi-prong $\tau_{\text{had-vis}}$ objects for the most central pseudorapidity bin. For multi-prong τ_{had} decays, deviations less than 1% are observed, while the differences are even smaller for single-prong τ_{had} decays. In addition, the multiplicity of clusters classified as likely being of hadronic origin (see also Section 3.2) was studied and also found to show deviations of 1% or less.

An alternative and simulation-independent way to assess this uncertainty is to compare the agreement between data and simulation in $\langle E/p\rangle$ measurements performed on EM scale and LC-calibrated TopoClusters, respectively. Again, these comparisons show deviations below ±1%. Therefore, an additional uncertainty of ±1% for $\tau_{\text{multi-prong}}$ and ±0.5% for $\tau_{\text{1-prong}}$ is assigned to account for the dependence of the LC calibration scheme on imperfections in the hadronic shower model.

4.1.6. Calorimeter-Response Uncertainty Results

For pseudorapidities of $|\eta| < 0.8$, all single particle energy-response uncertainties are available. Figure 4.5 shows the expected shift of the TES and the corresponding uncertainty due to the calorimeter response in this region. The error bars reflect the width of the Gaussian distribution fitted to the distributions of μ_t as explained in Section 4.1.1, while the dots represent the central value. Overall, low momentum hadrons show a lower response in data than in simulation in the $\langle E/p \rangle$ and CTB analyses. This translates into an expected TES shift of the order of 1% for $p_T^\tau =$ 15 GeV. The response uncertainty is of the order of $\pm 1.5 - 2\%$ for $\tau_{1-\text{prong}}$, while it is about $\pm 2 - 2.5\%$ for $\tau_{\text{multi}-\text{prong}}$. The expected scale shift is smaller than its uncertainty, hence no calibration correction is extracted. To avoid double-counting of systematic uncertainties, the maximum deviation from unity among the uncertainty value and the scale bias is taken as the uncertainty on the calorimeter response.

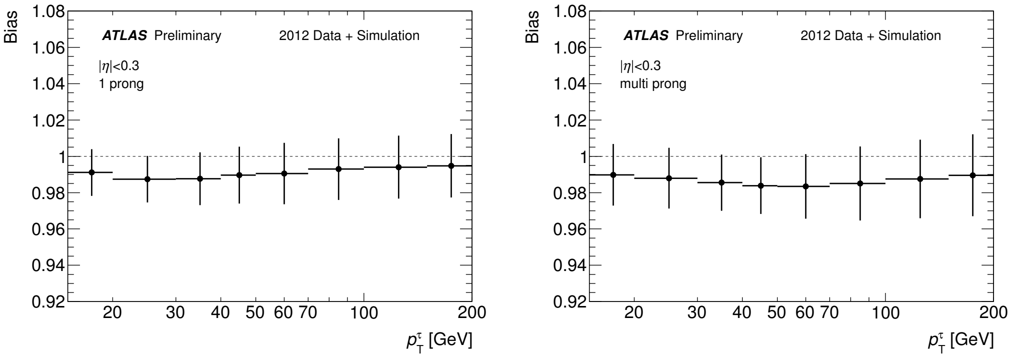

(a) $\tau_{1-\text{prong}}$ (b) $\tau_{\text{multi}-\text{prong}}$

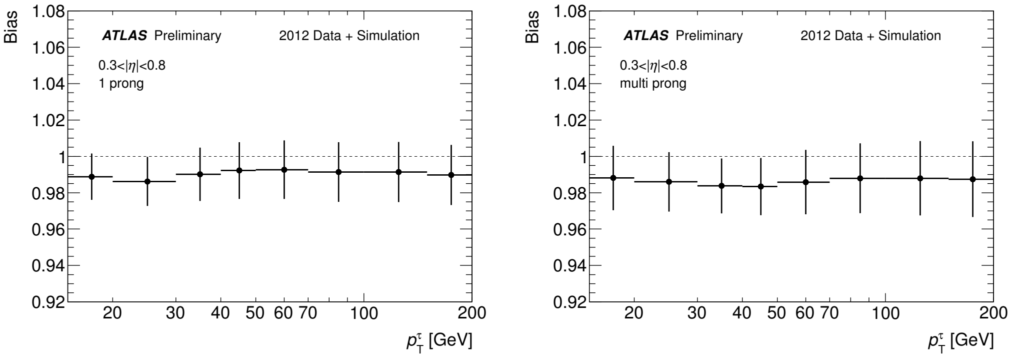

(c) $\tau_{1-\text{prong}}$ (d) $\tau_{\text{multi}-\text{prong}}$

Figure 4.5. *TES bias and uncertainty for single (left) and multi-prong (right) $\tau_{\text{had}-\text{vis}}$ objects as a function of the transverse momentum of the reconstructed $\tau_{\text{had}-\text{vis}}$ in the central pseudorapidity region. The scale shifts and uncertainties are the result of the propagation of single particle response measurements to the composite $\tau_{\text{had}-\text{vis}}$ level.*

For pseudorapidities beyond $|\eta| > 0.8$ no data-driven response uncertainty for high momentum charged hadrons is available. The pseudo-experiment based propagation of the uncertainties is therefore performed only on energy deposits covered by the global EM scale uncertainties or the $\langle E/p \rangle$ measurement. The response uncertainty of high momentum charged hadrons is instead estimated by comparing the energy response in simulated event samples using the QGSP_BERT and FTFP_BERT physics models. While the response difference in $\tau_{\text{had}-\text{vis}}$ objects between the two models ranges from ±0.5% – 1% for one-prong τ_{had} decays, it reaches up to ±3% for multi-prong τ_{had} objects. These uncertainties are then scaled by the average fractional energy contribution carried by high momentum charged hadrons within reconstructed $\tau_{\text{had-vis}}$ objects and combined in quadrature with the response uncertainty estimate for neutral and low momentum charged hadrons.

4.1.7. Tau-Energy Scale Uncertainty

Besides the calorimeter response, four additional uncertainty sources are considered for the total uncertainty on the TES: knowledge of the dead material in front of the calorimeters, underlying event model, the non-closure of the calibration method and the pile-up correction. These additional sources of uncertainty and their estimation is detailed in Ref. [145, 146].

While any mismodelling of the uninstrumented material (*dead material*) budget in front of the calorimeters is already reflected in the in situ $\langle E/p \rangle$ measurement, an additional dead material uncertainty is applied to the energy deposits outside the scope of the $\langle E/p \rangle$ measurement. It is estimated by comparing the tau energy response between simulated event samples in which the amount of material in the detector model is systematically varied within the uncertainties on the knowledge of the material budget. The dead material contribution to the TES uncertainty is scaled by the energy fraction carried by particles outside the phase-space region of the $\langle E/p \rangle$ measurement and contributes between ±1% and ±2% to the TES uncertainty.

The uncertainty due to the specific underlying event model chosen in the simulated event samples used to derive the calibration constants is estimated by evaluating the TES difference in a simulated event sample generated with a varied UE tune [73]. This uncertainty contributes about ±1% to the TES uncertainty. The non-closure of the calibration procedure contributes about ±0.5% to the TES uncertainty in most phase-space areas, with larger uncertainties for low momentum multi-prong τ_{had}. The pile-up uncertainty accounts for the remaining dependence of the TES on the number of primary vertices after the pile-up correction. It contributes between ±3% for low momenta 15 GeV $< p_T <$ 20 GeV and less than ±2% elsewhere.

Figure 4.6 shows the combined TES uncertainty as a function of p_T for single and multi-prong $\tau_{\text{had-vis}}$ objects passing medium particle identification criteria. The uncertainty is smallest for $\tau_{\text{1-prong}}$ objects in the central region, while the largest uncertainties are present in the transition region between barrel and endcap ($1.3 < |\eta^{\tau}| < 1.6$), mainly due to the large amount of dead material in front of the calorimeter. The analysis was repeated for objects passing tight particle identification criteria and uncertainties larger by about ±0.5% were found [145]. All in all, including single-particle response measurements into the estimation of the TES uncertainty allowed to significantly reduce the uncertainty to the level of ±3% in large areas of the phase-space.

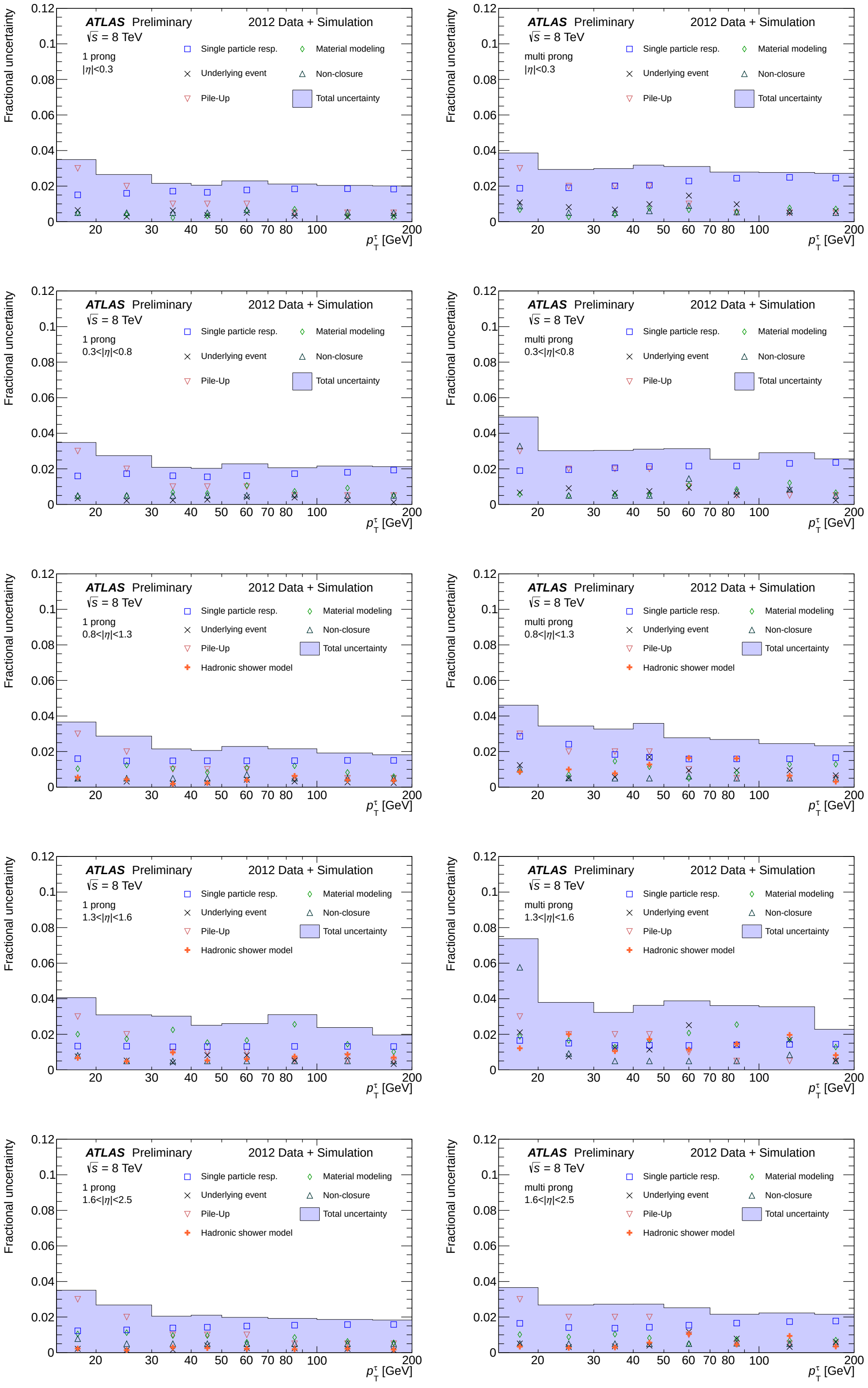

Figure 4.6. *Summary of the combined TES uncertainty for single (left) and multi-prong (right) $\tau_{\mathrm{had-vis}}$ objects as a function of the transverse momentum of the reconstructed $\tau_{\mathrm{had-vis}}$ in different pseudorapidity regions $|\eta| < 0.3$ up to $1.6 < |\eta| < 2.5$.*

4.2. Tau-Energy Scale Calibration with $Z \rightarrow \tau_\mu \tau_{\text{had}}$ Events

The large data sample collected in 2012 allows to perform an independent measurement of the TES by reconstructing the visible mass peak in $Z \rightarrow \tau_{\text{had}}\tau_\mu$ events and comparing it to simulated event samples. This can be used to directly constrain the energy response to all tau decay products at once, rather than to propagate single particle uncertainties as discussed above. In addition, this analysis is able to cover the full pseudorapidity range and therefore offers the only data-driven response measurement for τ_{had} objects beyond $|\eta| > 0.8$. Due to the hadronic tau identification criteria and the additional background suppression cuts, this measurement is statistically limited and covers only a limited kinematic phase-space.

The data used for this analysis was collected using a single muon trigger. A single muon and a single τ_{had} candidate of opposite electrical charge are required to suppress $Z \rightarrow \ell\ell$ background events. The muon is required to be well isolated and to exceed $p_T > 26$ GeV to lie inside the trigger efficiency plateau region. The tau is required to pass medium identification criteria as in the calibration procedure and to have a transverse momentum greater than 20 GeV. Additional selection cuts on variables separating between background and $Z \rightarrow \tau_{\text{had}}\tau_\mu$ events are applied in order to ensure a high purity of real $Z \rightarrow \tau_{\text{had}}\tau_\mu$ events. The major background after all selection cuts comes from $W+$jets and QCD multijet events, where a hadronic jet is misidentified as a τ_{had} object. These backgrounds are modelled using a data sample after reverting the charge correlation requirement to select only events where the muon and the τ_{had} objects have same sign charge. The contribution from events with real taus is very small in this control region, while it is enhanced in QCD multijet and $W+$jets events. Since the charge correlation between the reconstructed muon and the reconstructed τ_{had} is expected to be small in QCD processes, this sample can be used as a data-driven estimate of the QCD background contribution in the opposite sign region. Since the first jet in $W+$jets events exhibits a charge correlation to the muon from the W decay, an additional contribution accounting for the larger opposite sign event yield needs to be taken into account and is denoted as (OS-SS) contribution. Its kinematic distributions are estimated from simulated event samples using the ALPGEN event generator, while the overall normalisation is extracted from a data-driven control region enriched in $W+$jets events. This background estimation method is discussed in more detail in Section 5.5.

The TES is parametrised by $E_T \rightarrow (1+\alpha)E_T$ and the expected $Z \rightarrow \tau_{\text{had}}\tau_\mu$ distributions are generated with shifted scale values α between (-10%) to $(+10\%)$ in steps of 1%. These are further referred to as *templates*. The peak position in data as well as in the templates is extracted by using a fit of a fifth order polynomial. The peak positions of the templates as a function of the applied TES shift α are compared to the peak position in data to determine the TES shift offering the best match to data.

The systematic uncertainties are propagated using a pseudo-experiment approach. Dominant systematic uncertainties are due to the chosen fit model (0.5%), the missing transverse energy resolution and soft term contribution (0.2%), the muon momentum resolution and scale ($0.1 - 0.3\%$) and the normalisation of the multijet background ($0.1 - 0.3\%$). The measured TES shift in data with respect to simulated τ_{had} decays is $\alpha = 0.8 \pm 1.3\%$ (stat.) $\pm\, 0.6\%$ (syst.) and $\alpha = 1.1 \pm 1.4\%$ (stat.) $\pm\, 0.7\%$ (syst.) for single and 3-prong τ_{had}, respectively [142]. This is very well compatible with the expected scale shift from single particle response measurements discussed above. Within the statistical uncertainties, no significant dependence of the scale on the pseudorapidity or the number of primary vertices is observed. Figure 4.7 shows the visible mass distributions used to extract this measurement before applying the scale correction. This procedure is sensitive only to relative response differences, but not to absolute scale uncertainties. The TES uncertainties are therefore combined with the non-closure and pile-up uncertainties outlined above, to arrive at the combined TES uncertainty.

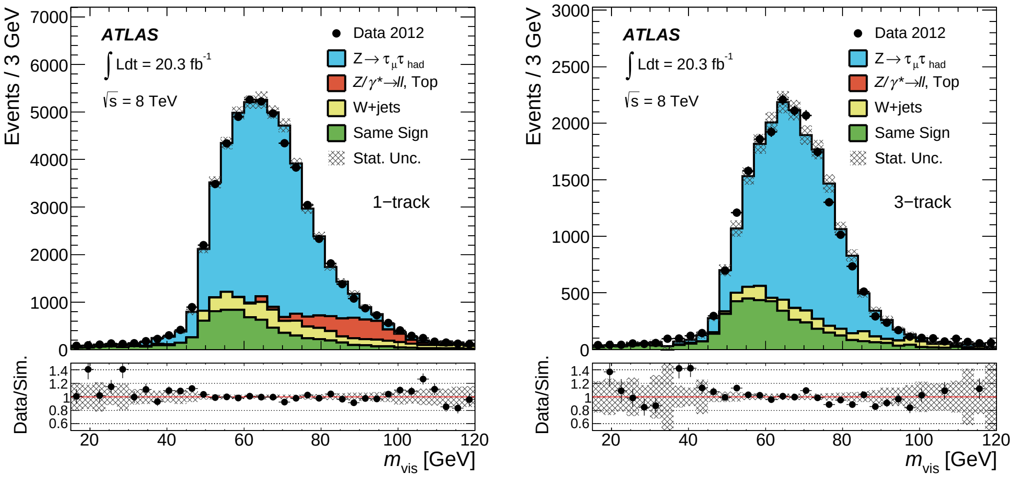

(a) $\tau_{1-\mathrm{prong}}$

(b) $\tau_{3-\mathrm{prong}}$

Figure 4.7. *Visible mass distribution for single (a) and 3-prong (b)* $\tau_{\mathrm{had-vis}}$ *objects in events used to correct the tau-energy scale calibration [142].*

4.3. Combined Tau-Energy Scale Uncertainty

The determination of the TES using the peak position of the visible mass spectrum in $Z \to \tau_{\mu}\tau_{\mathrm{had}}$ events offers a direct assessment of the TES, and is therefore used to correct the central scale value in data. Nevertheless, it is statistically limited and covers a restricted phase-space only. The τ_{had} objects used in this analysis cover a transverse momentum regime up to 50 GeV, while the τ_{had} transverse momentum spectrum in the search for Higgs boson decays can be considerably harder. Therefore, the results of the direct TES measurement are interpolated in the momentum range $50\ \mathrm{GeV} < p_T < 70\ \mathrm{GeV}$ to match the results of the decomposition method at high momentum. This interpolation is performed linearly in the central scale value and the squared energy response uncertainty. Since the two methods feature uncertainties originating from different sources, they are treated as uncorrelated in the analysis.

5 Search for the Higgs Boson in the $\tau_{\mathrm{lep}}\tau_{\mathrm{had}}$ Final State

The search for the Higgs boson was one of the major experimental challenges in high energy physics of the past years. Increasingly precise measurements of electroweak parameters allowed to put theoretical bounds on the Higgs boson mass (see Section 1.1.7), but direct searches provide the only way to discover or rule out the existence of the particle. The LHC experiments ATLAS and CMS offer the possibility to finally solve this question. Given the high centre-of-mass energy and the high instantaneous luminosity of the LHC, sensitivity studies of searches for the Higgs boson revealed, that either the Higgs boson hypothesis would be experimentally ruled out over the full mass range allowed by theoretical considerations or the discovery of the particle would be possible within the first years of running [106]. Indeed, the ATLAS and CMS experiments discovered the Higgs boson in the ZZ^* and $\gamma\gamma$ final states in 2012 in the third year of data taking (see Section 1.4). Higgs bosons at the LHC are produced predominantly via the gluon fusion (ggF) and vector-boson-fusion (VBF) as well as via the Higgs-strahlung (VH) process as discussed in Section 1.3. The decay branching ratios depend heavily on the Higgs boson mass. At a mass of $m_H = 125$ GeV the decay into a pair of b-quarks dominates (BR $\approx 58\%$) followed by the decay into W bosons (BR $\approx 22\%$). Decays into pairs of tau leptons contribute with a branching ratio of about 6.3%. After the discovery in the bosonic final states mentioned above, the search for fermionic decay modes plays a crucial role in the identification of this particle as the Higgs boson of the Standard Model, especially because of the direct sensitivity towards the Yukawa couplings of the Higgs boson to leptons. As discussed in Section 1.3.3, the search for $H \to \tau\tau$ decays is in addition the most sensitive search for Higgs bosons produced in the VBF process. This is of particular interest, since measuring the Higgs boson event rates separately in different production mechanisms allows to extract information about the underlying coupling parameters in the electroweak symmetry breaking sector.

This chapter discusses the search for $H \to \tau\tau$ decays in the $\tau_{\mathrm{lep}}\tau_{\mathrm{had}}$ final state, which was in large parts developed, implemented and performed in the course of this thesis. It is based on a multivariate classification algorithm denoted as *Boosted Decision Tree classification* (BDT) to discriminate signal from background events. Two event categories are defined, optimised for ggF and VBF signal production mechanisms. In each category, separate BDTs are trained and their outputs are then used as discriminant variables. A maximum-likelihood fit to the BDT output distributions and to additional control regions is performed to estimate the parameters of the combined signal and background model and to extract a measurement of the product of signal cross section and decay branching ratio. The ratio between the fitted signal cross section and the SM expectation will be referred to as the signal-strength modifier $\mu = \sigma/\sigma_{\rm SM}$.

Section 5.1 introduces the experimental signature of the signal processes and compares it to the main background processes. The analysed data samples, as well as simulated event samples used in the analysis are detailed in Sections 5.2 and 5.3, respectively. Section 5.4 describes the event selection and introduces the concept of analysis categories. To establish a potential excess of data over the expected SM backgrounds a reliable model of the background processes has to be built. This model is described in Section 5.5 and comparisons between the observed data and the background expectations are made. Section 5.6 finally discusses ways of isolating signal sensitive phase-space areas, introduces relevant discriminating variables which are exploited in this search and explains the BDT training and optimisation procedure. A careful validation of the background model with respect to the BDT score distributions is performed. This search was performed *blinded* to avoid biasing analysis design decisions due to the observed data, and the blinding strategy is discussed in Section 5.6. Systematic uncertainties and their propagation to the final observable are described in Section 5.7. An important step of the analysis is the construction the profiled likelihood model, used to estimate the signal strength and background model related parameters. The statistical analysis is described in Chapter 6.

5.1. Experimental Signature of $H \to \tau_{\rm lep}\tau_{\rm had}$ Decays

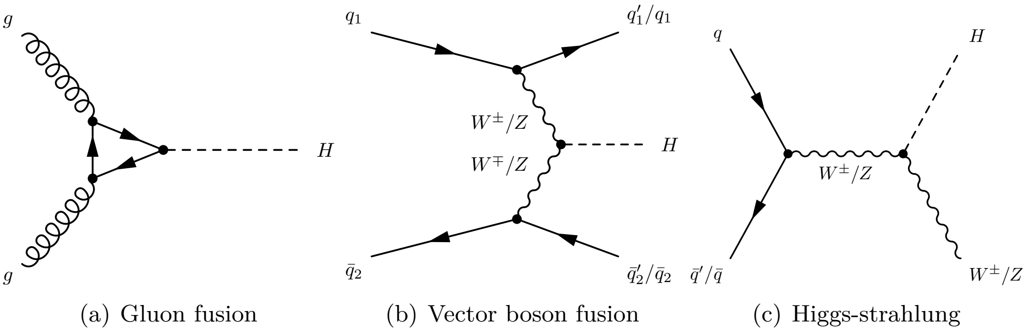

(a) Gluon fusion (b) Vector boson fusion (c) Higgs-strahlung

Figure 5.1. *Feynman diagrams of the three main production mechanisms of Higgs bosons at the LHC. Only the leading order diagram is shown for each process.*

The experimental signature of $H \to \tau\tau$ events depends on the decays of the τ leptons, as well as on the Higgs boson production mechanism. As discussed in Section 1.3.3, the $\tau_{\rm lep}\tau_{\rm had}$ final state is statistically dominant across the possible ditau decay combinations. This final state consists of a single electron or muon, denoted as ℓ, two neutrinos from the leptonic τ decay, one reconstructed $\tau_{\rm had}$ object and one neutrino from the hadronically decaying tau lepton. The light lepton and the τ_{had} object carry opposite electric charge. Neutrinos, which escape direct detection, lead to a significant amount of missing transverse energy which can be used to complement the information from the reconstructed decay products. Dependent on the Higgs boson production mechanism additional jets can be present in the event. The event selection criteria discussed in Section 5.4 are constructed based on these final state objects. In the following, the kinematic properties of the signal processes as well as of the dominant background processes are described, in order to motivate these selection criteria and the specific discriminating variables discussed in Section 5.6.

5.1.1. Signal Processes

Figure 5.1 shows the leading order Feynman diagrams of the three main Higgs boson production mechanisms considered in this search, all featuring slightly different kinematic event properties. Since Higgs bosons produced in association with a top-quark pair are not expected to contribute significantly to the signal regions deployed in the analysis discussed here, this production mechanism is neglected. As discussed in Section 1.3, the ggF process contributes with the largest cross section. At leading order it has no additional partons in the final state, but due to the heavy quark loop and the coloured initial state higher order QCD corrections are large. Therefore, processes with additional partons contribute significantly to the total ggF cross section. In the presence of additional jets, the Higgs boson recoils against this jet system and is boosted with respect to the centre-of-mass frame. As the kinematic properties of such additional emissions differ between the signal and background processes, events with jets in the final state can be useful to differentiate between ggF signal and background events. In the VBF process, two jets are present already at tree-level. It is a purely electroweak process and therefore higher order QCD corrections are in general smaller than in the ggF case. The two outgoing quarks hadronise and can be reconstructed as jets. They tend to be well separated in pseudorapidity and as no colour charge is exchanged between them, the hadronic activity in the region between the two jets is expected to be small. This distinct event topology differs significantly from the main background processes discussed below and can be exploited to define signal enriched phase-space regions. The final state of the VH process is rather complex due to the vector boson, of which the Higgs boson is radiated. In principle, the selection of one light lepton and one τ_{had} object covers a variety of possible decays of the VH final state. In practice though, after applying the event selection criteria discussed below, the dominant contribution from VH events to the analysis stems from $H \to \tau_{\text{lep}}\tau_{\text{had}}$ decays and a hadronic decay of the vector boson.

Since the ditau system originates from the intermediate resonant state, combining the four-vectors of the decay products allows to reconstruct information about the Higgs boson four-momentum. Due to the three neutrinos though, the event cannot be reconstructed fully. Instead, magnitude and angular information of the missing transverse energy is used to complement the information from the visible decay products. The missing transverse energy provides valuable information, especially to distinguish between resonant ditau processes, like the signal, and non-resonant processes with misidentified τ_{had} objects, like QCD multijet events. A crucial property of the ditau system is the invariant ditau mass $m_{\tau\tau}$. As the most important background process, $Z \to \tau_{\text{lep}}\tau_{\text{had}}$ features kinematic properties nearly identical to the signal process. The mass difference between the Z and H bosons provides a powerful discriminating property between these two processes. To estimate $m_{\tau\tau}$, assumptions about the neutrino momenta have to be made, as the four-momenta of the two tau leptons cannot be reconstructed. Different mass reconstruction methods are used and range from the *visible mass*, m_{vis}, where the neutrino four-momenta are simply neglected, to complex fits, in which the most likely neutrino four-momenta are estimated based on the kinematic tau lepton decay properties. Subsection 5.1.3 gives a brief overview of these observable definitions.

5.1.2. Dominant Background Processes

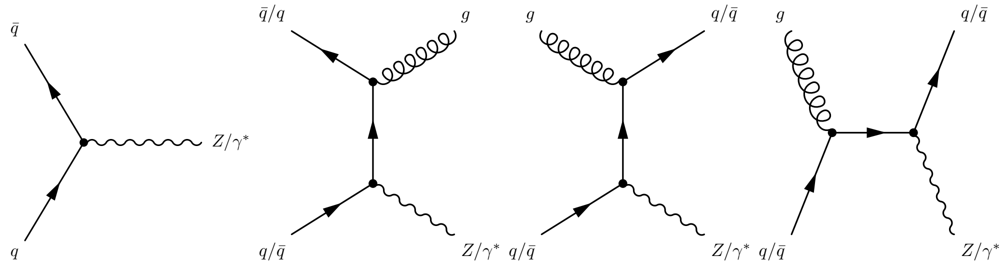

Figure 5.2. *Feynman diagrams of processes leading to Z/γ^* + jets events. Only tree-level diagrams with up to one additional parton are shown.*

Background processes contributing to the final state discussed above can be grouped into processes with a real hadronically decaying tau lepton and one light lepton and processes in which either a hadronic jet or a lepton is misidentified as a τ_{had} object, also referred to as *fake* τ_{had} events. While the first group is in principle harder to distinguish from the signal process, the event yields of the second group are complicated to assess, due to the τ_{had} misidentification probability, which is not well reproduced in the simulation.

The major background with real τ_{had} decays stems from Z boson decays into tau leptons produced in association with jets, which will be denoted as $Z/\gamma^* \to \tau_{\text{lep}}\tau_{\text{had}} + \text{jets}$ events in the remainder of this thesis. This process features the same final state objects as $H \to \tau_{\text{lep}}\tau_{\text{had}}$ events. In Figure 5.2 the tree-level Feynman diagrams of Z/γ^* production with up to one additional parton are shown. In general, two features can be used to differentiate between signal and the $Z/\gamma^* \to \tau_{\text{lep}}\tau_{\text{had}} + \text{jets}$ process. The invariant ditau mass is in principle capable of separating the two processes. The separation power depends crucially on the mass resolution, which itself can vary significantly between the mass reconstruction methods. In practice, the resolution is dominated by the large $\mathbf{E}_T^{\text{miss}}$ resolution, limiting the separation power. The ditau mass spectrum of the signal peaks on the upper tail of the $Z/\gamma^* \to \tau_{\text{lep}}\tau_{\text{had}}$ distribution and due to the large cross-section difference between signal and background processes, further background rejection is needed in general. The second handle on the $Z/\gamma^* \to \tau_{\text{lep}}\tau_{\text{had}}$ background is offered by the kinematic properties of additional jets in the final state. Focussing on either ggF or VBF production, selection criteria can be optimised to exploit the different event topologies in events with jets to further suppress $Z/\gamma^* \to \tau_{\text{lep}}\tau_{\text{had}}$ events. In Figure 5.3 the distributions of the invariant ditau mass, the pseudorapidity difference of the two highest p_T jets in the event ($\Delta\eta_{jj}$), as well as the transverse momentum of the ditau system in $H \to \tau\tau$ and $Z/\gamma^* \to \tau\tau$ events are shown. The variables are defined at truth level, based on the tau lepton four-momenta as well as on anti-k_T jets built from stable particles in the final state after parton showering and hadronisation. No event selection criteria are applied. As can be seen, the ditau mass spectrum can be used to separate $Z/\gamma^* \to \tau\tau$ from signal events. The event selection criteria applied in the analysis strongly suppress the contribution from low mass Drell-Yan events. Furthermore, the reconstruction of the invariant ditau mass is complicated by the presence of the neutrinos and is further discussed below. The low mass tail in the signal distribution stems from electromagnetic final state radiation and is suppressed by the event selection criteria applied in the analysis.

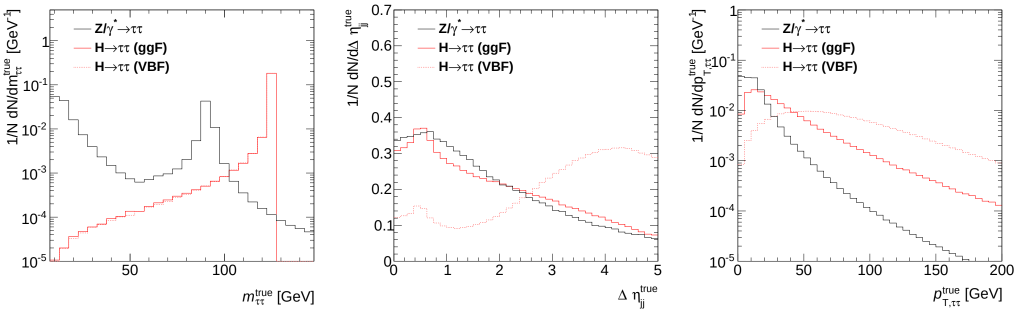

(a) (b) (c)

Figure 5.3. *Distributions of the invariant mass of the ditau system (a), the pseudorapidity difference between the two leading jets in the event (b) and the transverse momentum of the ditau system (c) in ggF and VBF $H \to \tau\tau$ events as well as in $Z/\gamma^* \to \tau\tau$ events. The observables are obtained at truth-level, using the four-momenta of the tau leptons and anti-k_T jets built from stable particles in the final state after parton showering and hadronisation. While the invariant ditau mass offers separation between the dominant background process and signal events, the $\Delta\eta_{jj}$ distribution allows to differentiate between ggF and VBF signal events.*

Two additional quantities can be used to further differentiate between signal and the dominant background process. The pseudorapidity difference between the two leading jets in an event is a powerful observable to isolate VBF signal events from both background and ggF signal events. Besides the invariant ditau mass, this observable plays a major role in defining a VBF signal sensitive phase space region. If additional partons are emitted in ggF or Drell-Yan events, the ditau system will recoil against them, leading to a larger transverse momentum. In Fig. 5.3 (c) it is shown, that the kinematic properties of these emissions differ significantly between $Z/\gamma^* \to \tau\tau$ and ggF events. The $p_{T,\tau\tau}$ spectrum tends to be harder for signal events. The large difference between VBF and ggF events arise from the intrinsic difference in the jet multiplicity between the two processes. Both observables, $p_{T,\tau\tau}$ and $\Delta\eta_{jj}$, will play a key role in the definition of the analysis categories discussed in Section 5.4.

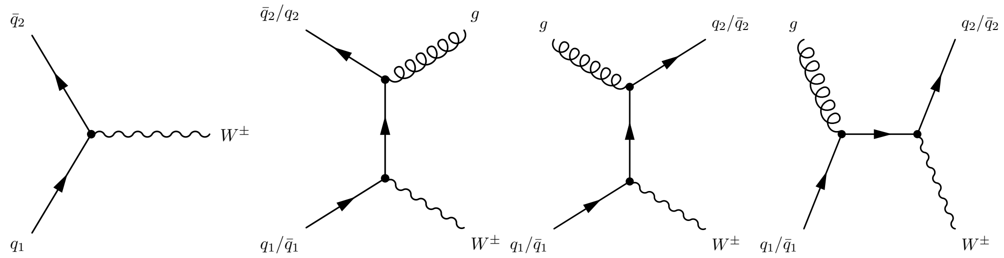

Figure 5.4. *Feynman diagrams of processes leading to $W+$jets events. Only tree-level diagrams with up to one additional parton are shown.*

Different SM processes with misidentified τ_{had} objects contribute to the considered final state. The dominant one is $W+$ jets production, where the W boson decays leptonically to either an electron or muon and a neutrino, while a hadronic jet is misidentified as τ_{had} object. Due the presence of one neutrino, such events also lead to genuine missing transverse energy, mimicking the signal signature. In Figure 5.4 the tree-level Feynman diagrams contributing to $W+$ jets production with up to one additional parton are shown. In the majority of $W+$ jets events, due to the large numerical value of the gluon PDF at low x, the hardest emitted parton is a quark. It exhibits a direct electric-charge correlation to the charge of the W boson, leading to the opposite sign (OS) signature between light lepton and τ_{had}, as present in signal events. In a sizeable fraction of events though, the misidentified τ_{had} object is reconstructed with the same electric charge as the light lepton (SS). The ratio between these events yields will be referred to as the *OS/SS* ratio. The background event rate depends directly on the power of the τ_{had} identification criteria, namely the misidentification probability. In addition, various discriminating variables offer separation power to further suppress fake τ_{had} events. A powerful variable to suppress $W+$ jets events is the transverse mass. As the neutrino from the W decay escapes detection, the mass of the W cannot be fully reconstructed. Instead the transverse mass can be used as an estimate, which exploits the $\mathbf{E}_T^{\text{miss}}$ as a proxy for the neutrino momentum in the transverse plane:

$$m_T = \sqrt{2p_T^\ell E_T^{\text{miss}}(1 - \cos\Delta\phi_{\ell,\mathbf{E}_T^{\text{miss}}})} \tag{5.1}$$

The transverse mass in $W+$ jets events peaks close the physical W mass, and falls off rapidly above.

Apart from this, various angular variables can be exploited to suppress such events. Since the lepton and the τ_{had} object do not originate from the same particle, the kinematic properties differ significantly from resonant $H \to \tau_{\text{lep}}\tau_{\text{had}}$ decays. Figure 5.5 shows a schematic view of the angular orientation of the decay products in the transverse plane in typical resonant $H \to \tau_{\text{lep}}\tau_{\text{had}}$ decays and $W+$ jets events. On the one hand, the angular separation between the lepton and the $\tau_{\text{had-vis}}$ object will depend on the boost of the Higgs boson in $H \to \tau\tau$ events. In the presence of a high p_T jet, this opening angle will tend to be significantly smaller than in $W+$ jets events, where the leptonically decaying W boson recoils against a jet, which eventually is misidentified as τ_{had} object. On the other hand, the angular orientation of the $\mathbf{E}_T^{\text{miss}}$ is highly correlated to the angular orientation of the visible tau decay products. As two neutrinos originate from the leptonic tau decay, and one neutrino stems from the τ_{had} decay, the reconstructed $\mathbf{E}_T^{\text{miss}}$ vector will in most cases be oriented in-between the angle spanned by the light lepton and the reconstructed $\tau_{\text{had-vis}}$. In backgrounds with misidentified τ_{had} objects, the $\mathbf{E}_T^{\text{miss}}$ direction is oriented differently.

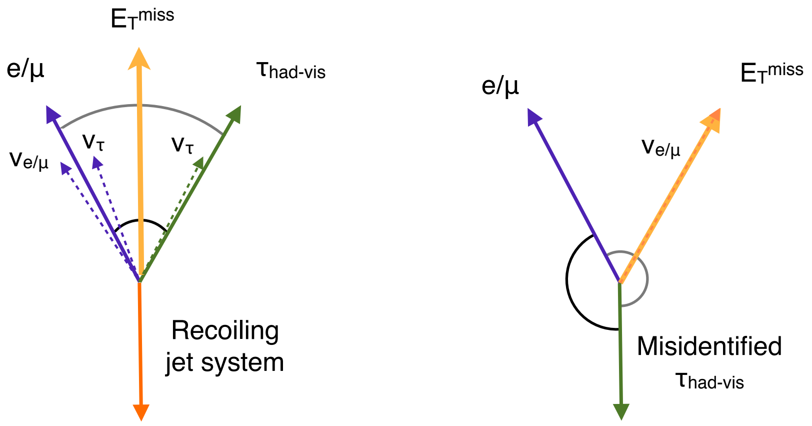

(a) (b)

Figure 5.5. *Schematic drawing of the angular orientation of the decay products in the transverse plane in $H \to \tau_{\text{lep}}\tau_{\text{had}}$ or $Z/\gamma^* \to \tau_{\text{lep}}\tau_{\text{had}}$ events (a) and in events with misidentified τ_{had} objects, like in $W+$ jets events (b). While for $H \to \tau_{\text{lep}}\tau_{\text{had}}$ events, the $\mathbf{E}_T^{\text{miss}}$ is oriented in between the two tau lepton candidates, the angular separation between $\mathbf{E}_T^{\text{miss}}$ and the τ_{lep} and $\tau_{\text{had-vis}}$ objects is large in $W+$ jets events. The opening angle of the ditau system tends to be smaller in $H \to \tau_{\text{lep}}\tau_{\text{had}}$ events where the ditau system recoils against additional jets than in events with misidentified τ_{had} objects.*

A variety of other SM processes contribute to the background with misidentified τ_{had} objects. The major ones are listed below. Section 5.6 will discuss observables capable of separating such background events from the signal processes in more detail.

- The production of multijet events via QCD processes is an important background due to its large cross section at the LHC. In such events, two jets need to be misidentified as an electron or muon and a τ_{had} object. Tight lepton selection and identification criteria can reduce the contribution from this background.

- $Z/\gamma^* \to \ell\ell +$ jets events can be selected if either a lepton is misidentified as the τ_{had} object or one lepton escapes reconstruction, while a jet is misidentified as τ_{had}. The former type of events is a minor background, as the misidentification probability for electrons or muons is small in general. The latter one provides a sizeable fraction of background events with misidentified τ_{had} decays. Such events can be suppressed by maximising the light lepton acceptance and rejecting all events with more than one lepton.
- $t\bar{t}$ events and single-top production feature event topologies with multiple jets and genuine $\mathbf{E}_T^{\mathrm{miss}}$ in the final state, as top-quarks decay to a bottom quark and a W boson with a branching ratio of nearly 1. Both events with real and misidentified τ_{had} objects contribute as a background to the analysis. The fraction of events with misidentified τ_{had} decays ranges from 40% to 60%, depending on the kinematic phase space. The event yields of top-quark events can be significantly reduced by exploiting flavour-tagging information and rejecting events with identified b-jets.

5.1.3. Ditau Mass Reconstruction

The invariant mass of the ditau system is one of the most important event properties in the search for $H \to \tau\tau$ decays. It offers a direct handle to differentiate between $Z/\gamma^* \to \tau\tau$ and $H \to \tau\tau$ events and allows, if observed, to assess the mass of the Higgs boson. The mass reconstruction requires some approximations to be made due to the neutrinos in the final state. In the following, the main mass reconstruction methods are summarised.

Visible Mass

To reconstruct the visible mass, the neutrinos are neglected and m_{vis} is built as the invariant mass of the visible decay products

$$m_{\mathrm{vis}} = \sqrt{(E_\ell + E_{\tau_{\mathrm{had-vis}}})^2 - (\vec{p}_\ell + \vec{p}_{\tau_{\mathrm{had-vis}}})^2} \tag{5.2}$$

As the neutrinos carry a significant fraction of the tau lepton momenta, the visible mass spectrum of $Z/\gamma^* \to \tau_{\mathrm{lep}}\tau_{\mathrm{had}}$ events is shifted to lower values with respect to the Z mass and the separation between the reconstructed Higgs and Z boson mass peaks is small. This variable is not used as discriminating variable to isolate signal processes, but can be used to validate the background model of $Z/\gamma^* \to \tau_{\mathrm{lep}}\tau_{\mathrm{had}}$ events.

Colinear Mass Approximation

In the colinear mass approximation, the neutrino four-momenta are estimated based on the assumption, that all the missing transverse energy stems from the neutrinos and that the neutrinos are emitted along the direction of flight of the respective visible tau decay products. This approximation is valid in the limit of highly boosted tau leptons, as it is expected if the mass of the intermediate resonant state is large compared to the tau mass. Under these assumptions, the colinear mass can be written as [139]

$$m_{\text{col.}} = \frac{m_{\text{vis}}}{\sqrt{x_\ell x_{\tau_{\text{had}}}}} \tag{5.3}$$

where $x_\ell, x_{\tau_{\text{had}}}$ are the momentum fractions carried by the visible tau decay products of the leptonic and hadronic tau decay, respectively. These can be reconstructed in the colinear approximation using the measured $\mathbf{E}_T^{\text{miss}}$ vector

$$x_\ell = \frac{p^x_{\tau_{\text{had}}} p^y_\ell - p^y_{\tau_{\text{had}}} p^x_\ell}{p^x_{\tau_{\text{had}}} p^y_\ell + E_T^{\text{miss},x} p^y_\ell - p^y_{\tau_{\text{had}}} p^x_\ell - E_T^{\text{miss},y} p^x_\ell} \tag{5.4}$$

$$x_{\tau_{\text{had}}} = \frac{p^x_{\tau_{\text{had}}} p^y_\ell - p^y_{\tau_{\text{had}}} p^x_\ell}{p^x_{\tau_{\text{had}}} p^y_\ell - E_T^{\text{miss},x} p^y_{\tau_{\text{had}}} - p^y_{\tau_{\text{had}}} p^x_\ell + E_T^{\text{miss},y} p^x_{\tau_{\text{had}}}} \tag{5.5}$$

In cases where the tau leptons are emitted back-to-back in the laboratory frame, the two equations become linearly dependent and cannot be solved. Therefore, if the colinear mass approximation is used, selection criteria are typically applied to ensure that the opening angle is small enough. As the missing transverse energy has a coarse resolution, unphysical solutions ($x < 0$ or $x > 1$) of these equations can occur and such events are typically discarded.

Missing Mass Calculator

The missing mass calculator (MMC) [161] attempts to overcome two limitations of the colinear approximation. It releases the assumption of the vanishing opening angle between the visible decay products and the neutrinos and it considers the experimental $\mathbf{E}_T^{\text{miss}}$ resolution to maximise the efficiency of the mass reconstruction method. The MMC algorithm estimates the momenta of the ν_τ from the hadronic tau decay and the $\nu_\ell\nu_\tau$ system from the leptonic tau decay by determining the most likely momentum configuration, given the probability densities of the tau decay kinematic properties. In case of the lepton-hadron final state, seven unknown variables describe the neutrino system. Namely, two three-vectors of the ν_τ and the $\nu_\ell\nu_\tau$ neutrino systems and one opening angle between the ν_ℓ and ν_τ neutrino. The reconstructed $\mathbf{E}_T^{\text{miss}}$ provides two constraints, as does the known tau lepton mass. To reconstruct the ditau mass in a given event, the parameter space of the unknown variables is scanned. For each phase-space point, the mass solution is weighted with the probability density of the decay kinematic properties of this chosen point. Figure 5.6 shows as an example the PDFs of the opening angle between the neutrino system and the visible tau decay products for leptonic and hadronic tau decays. The PDFs are obtained from samples of simulated tau decays. To reduce the dependence on the $\mathbf{E}_T^{\text{miss}}$ reconstruction performance, the two components $E_T^{\text{miss},x}$ and $E_T^{\text{miss},y}$ are added to the list of unknown variables and scanned within three standard deviations around the measured values. Each solution is weighted by a Gaussian resolution term, parametrised as a function of $\sum E_T$ in the event. In $\tau_{\text{lep}}\tau_{\text{had}}$ events, five variables are scanned using a Markov-chain method. In total about 10^5 different points are considered. After the scan, the weighted distribution of solutions is used to find the maximum value, which is used as final reconstructed mass in this event. This procedure allows to find a solution in nearly all signal events and therefore has a larger efficiency compared to the colinear mass approximation. It further improves the mass resolution due to the consideration of finite neutrino opening angles and by taking $\mathbf{E}_T^{\text{miss}}$ resolution effects into account on an event by event basis. In case of background events with misidentified τ_{had} objects the efficiency can be significantly lower, as no true ditau system can be reconstructed.

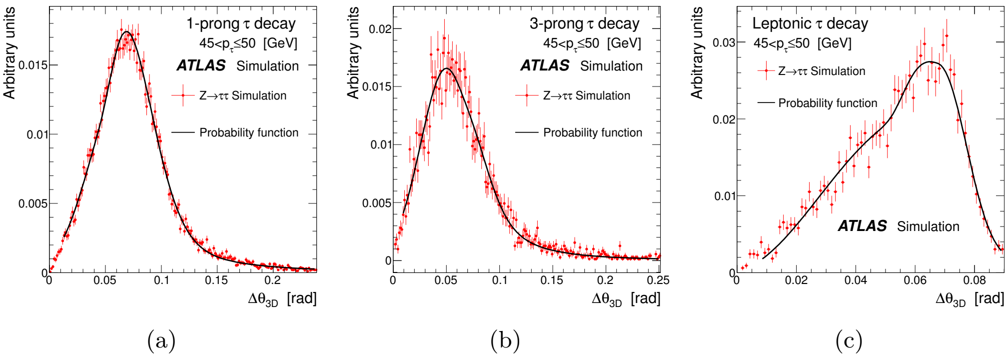

(a) (b) (c)

Figure 5.6. *Probability-density functions of the opening angle between the neutrino system and the visible tau decay products in one- (a) and three-prong (b) hadronic tau decays and leptonic tau decays (c) in the p_T range of 45 GeV < p_T < 50 GeV. The distributions are obtained from simulated tau decays and used in the missing mass calculator algorithm to estimate the momenta of the neutrino system. Taken from Ref. [162].*

In Figure 5.7 the performance of the three mass reconstruction methods in samples of simulated $Z/\gamma^* \to \tau_{\text{lep}}\tau_{\text{had}}$ and $H \to \tau_{\text{lep}}\tau_{\text{had}}$ events with at least one hadronic jet, passing basic preselection criteria discussed below is compared. For the colinear mass approximation and the MMC algorithm, additional selection criteria ensure a physical solution of the method or the convergence of the algorithm. As the efficiency of these criteria depends on the kinematic event topology and therefore on the selection criteria applied, a requirement of at least one jet with a transverse momentum of $p_T > 30$ GeV is applied. In general, the colinear mass approximation is expected to perform better in events where the Higgs or Z boson has larger transverse momenta. As expected, both the MMC and the colinear mass reconstruction methods are able to correctly estimate the peak position, but differ significantly in the mass resolution and efficiency. The visible mass has a smaller resolution as it neglects the neutrino momenta completely, but fails to reconstruct the mean true ditau mass. The analysis presented here used the MMC algorithm to estimate the ditau mass. The observable will be denoted as $m_{\tau\tau}$.

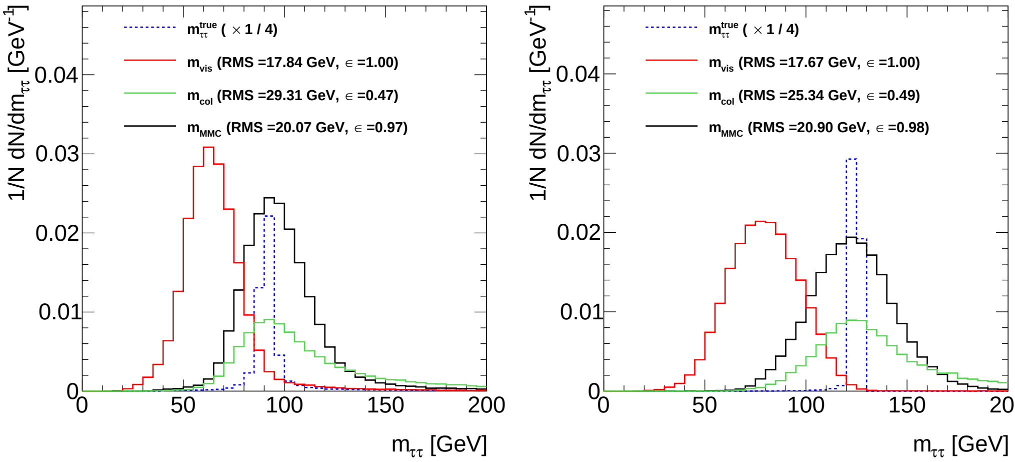

(a) (b)

Figure 5.7. *Distributions of the invariant ditau mass using different reconstruction methods in simulated* $Z/\gamma^* \to \tau_{\text{lep}}\tau_{\text{had}}$ *(a) and* $H \to \tau_{\text{lep}}\tau_{\text{had}}$ *(b) events. The performance of the different methods is compared to the true invariant mass distribution (dashed blue line). The events are required to pass basic preselection criteria and to have at least one hadronic jet of* $p_T > 30$ *GeV. Both the colinear mass and the MMC mass are able to reconstruct the mean value of the true ditau mass spectrum but differ significantly in their mass resolution and efficiency parameters.*

5.2. Data Samples and Trigger Selection

The data sample analysed in this search was recorded during the data taking periods in 2011 and 2012 and a general overview of the data taking conditions is given in Section 2.3. During that time, the LHC was operated at centre-of-mass energies of $\sqrt{s} = 7$ TeV and $\sqrt{s} = 8$ TeV, respectively. Basic data quality criteria are applied to ensure that the detector was functioning well (see Section 2.3). Passing these criteria, integrated luminosities of 4.5 fb^{-1} at $\sqrt{s} = 7$ TeV and 20.3 fb^{-1} at $\sqrt{s} = 8$ TeV are available for data analysis. The luminosity calibration is obtained from van der Meer scans with uncertainties of ±1.8% for the 2011 data taking period and ±2.8% for 2012 (see Section 2.2.5). The peak instantaneous luminosity increased significantly to 7.7×10^{33} cm^{-2} s^{-1} in the 2012 data taking period compared to 3.7×10^{33} cm^{-2} s^{-1} in 2011. As a consequence, the mean number of interactions per bunch crossings reached a value of 20 in 2012, while on average only 9.1 interactions per bunch crossing took place in 2011.

Events are selected using single electron and muon triggers. As the instantaneous luminosity varied over the data taking period, the online p_T thresholds of these single lepton trigger items were adjusted several times to cope with the limited bandwidth available for data storage. Four different electron trigger items, with p_T thresholds between $20 - 22$ GeV and increasingly tight online identification criteria (see also Section 3.4.1) are used for the 2011 data sample, while a single electron trigger item with a p_T threshold of 24 GeV is used for data taken in 2012. Similarly, two muon trigger items with a p_T threshold of 18 GeV and increasingly tight identification algorithms are employed for 2011 data and a single item with $p_T > 24$ GeV is used for 2012 data (see also Section 3.5.1). The selection criteria on the transverse momentum of the reconstructed leptons applied at trigger level are referred to as *online* requirements, in contrast to the criteria applied in the analysis, which are denoted as *offline* criteria. The offline lepton p_T thresholds are chosen such, that the trigger efficiency, of the trigger item in use, reaches a stable plateau region as a function of the lepton p_T. In this plateau region, systematic uncertainties on the simulated trigger efficiency are typically smaller than in the *turn-on* region, where the efficiency depends strongly on the lepton transverse momentum. The offline thresholds are summarised, together with the full event selection criteria, in Section 5.4.1.

5.3. Simulated Event Samples

Various simulated event samples are used throughout the analysis to model differential distributions of signal and background processes. Different event generators are available to simulate events with differing accuracy. Even though the background estimation in the analysis is in large parts data-driven, simulated event samples of background processes are used in the design and validation of such methods, as well as in the development of background-suppression strategies. Simulated signal event-samples are an integral part of the analysis, as they are used as the SM reference and the measurement is interpreted with respect to this expectation. In the following, an overview of the various simulated event samples of signal and background processes used in this search is given.

5.3.1. Signal Processes

All simulated signal event-samples are normalised to the cross sections provided by the Higgs cross-section working group [77–79]. These are summarised in Section 1.3. As the analysis makes extensive use of kinematic event properties, the precision of the event generator used to simulate the event samples is of special importance. Therefore, differential correction factors are applied in some cases to correct distributions to more accurate theoretical predictions.

The ggF event sample is generated at next-to-leading order in QCD using the POWHEG event generator [163] interfaced to PYTHIA [61, 62] for the simulation of the underlying event, parton showering and hadronisation. While the samples for $\sqrt{s} = 7$ TeV use PYTHIA 6, PYTHIA 8 is used in the generation of the $\sqrt{s} = 8$ TeV samples. The latter one also includes the effect from finite bottom and top-quark masses in the quark loop. In both cases, the CT10 [55] parton distribution function is used. The transverse momentum spectrum of the Higgs boson (p_T^H) is corrected to match the spectrum obtained from HRES2.1 [164, 165]. This programme provides

NNLO accuracy for the differential cross section, takes into account effects from finite bottom and top-quark masses and their interference. Furthermore, a dynamic renormalisation and factorisation scale is used, $\mu = \sqrt{m_H^2 + p_H^2}$, in order to reflect the larger energy scale in events with energetic jets. As the Powheg generator implements the ME at NLO in QCD, events with two jets only occur due to contributions from the parton showering. Such events with two jets though are of special interest in the analysis and therefore the differential cross section $d\sigma/dp_T^H$ in events with at least two jets is in parallel corrected to match the spectrum obtained from Minlo Hjj [166]. Minlo Hjj calculates the $H+\geq$ 2 jets process at NLO accuracy and can be interfaced to parton-shower programs. This procedure ensures an accurate prediction of the inclusive p_T^H spectrum, as well as an NLO accuracy in the $H+\geq$ 2 jets phase space.

A sample of VBF events is generated, like the ggF sample, using Powheg [167] interfaced to Pythia at NLO in QCD, and the CT10 [55] PDF set. Electroweak corrections are sizeable for this process and included in the absolute cross-section normalisation. Therefore, the p_T^H spectrum is corrected to match the differential distribution as obtained from Hawk [168–170], which includes the full NLO electroweak contributions. The size of the correction ranges from a percent level effect at low values of p_T^H, to about 20% at $p_T^H = 300$ GeV. Event samples of the WH and ZH processes are generated at LO only using the Pythia event generator.

For all signal processes, multiple event samples are generated for various values of the Higgs boson mass m_H. In total, ten mass points between 100 GeV and 150 GeV in steps of 5 GeV are considered. The sample size ranges from 30×10^3 events for the associated production samples at $\sqrt{s} = 7$ TeV to 2×10^6 for the ggF and VBF samples at $\sqrt{s} = 8$ TeV.

5.3.2. Background Processes

Apart from QCD multijet events, simulated event samples are generated for all major background processes. Simulated QCD events are not used due to two reasons. One the one hand, QCD processes with multiple final-state partons are in general complex to simulate and depend to a large extent on non-perturbative effects. On the other hand, the strong fake τ_{had} suppression achieved by the tau identification algorithms would require the simulated events samples to be too large in size. Samples of $Z/\gamma^* +$ jets and $W+$ jets events are generated with Alpgen [59] interfaced to either Pythia [62] or Herwig [63] and Jimmy [171] for the simulation of the underlying event, parton shower and hadronisation. It implements the LO matrix elements for W and Z production with up to five additional partons in the final state and makes use of a matching scheme [172] between the matrix element contributions and the parton shower algorithm (see also Section 1.2). The Cteq61l PDF set [55, 56] is used. The samples are normalised to the cross section of corresponding NNLO calculations [173–175] as implemented in Fewz [176] making use of the MSTW2008 [57] PDF set. Uncertainties arise from the chosen PDF and missing higher order corrections and are of the order of ±5%, for inclusive event selection criteria. $Z/\gamma^* +$ jets event samples are generated separately for low and high values of the invariant dilepton mass $m_{ll}^{\text{true}} \lessgtr 40$ GeV and combined by weighting the inclusive cross section by the corresponding event-filter efficiency. While the low-mass samples are interfaced to Herwig and Jimmy for the modelling of non-perturbative QCD effects, the high-mass samples use Pythia. Since these processes account for a large fraction of the total background in signal enriched phase-space regions, a high statistical power is desirable for the optimisation of the classification algorithms. Therefore a filter algorithm is used to generate dedicated event samples in the VBF like phase-space regions. This filtering is performed on the generated particles, before detector simulation and allows to simulate a larger amount of events in the phase-space region sensitive to the presence of signal. The samples are then combined with the inclusive samples, by weighting the actual cross sections with the filtering efficiency and by rejecting events passing the filter requirements in the inclusive samples. A loose and a tight filter is employed for the generation of $Z/\gamma^* +$ jets samples, while only the loose filter is used to generate filtered $W +$ jets samples. The loose (tight) filter requires that the two highest p_T jets in the event are separated by $\Delta\eta_{jj} > 2(4)$ and exceed an invariant mass of the dijet system of $m_{jj} > 200$ GeV(400 GeV). The considered jets are built from stable particles in the final state. After detector simulation, the overlay of PU events and event reconstruction, additional jets might be present in the event. This is the reason why the filtering thresholds appear smeared out at reconstructed level. Figure 5.8 shows the $\Delta\eta_{jj}$ distribution for $Z/\gamma^* +$ jets and $W +$ jets events after combining the event samples. At large values of $\Delta\eta_{jj}$, the statistical uncertainty on the combined sample remains small due to the high statistical power of the filtered samples.

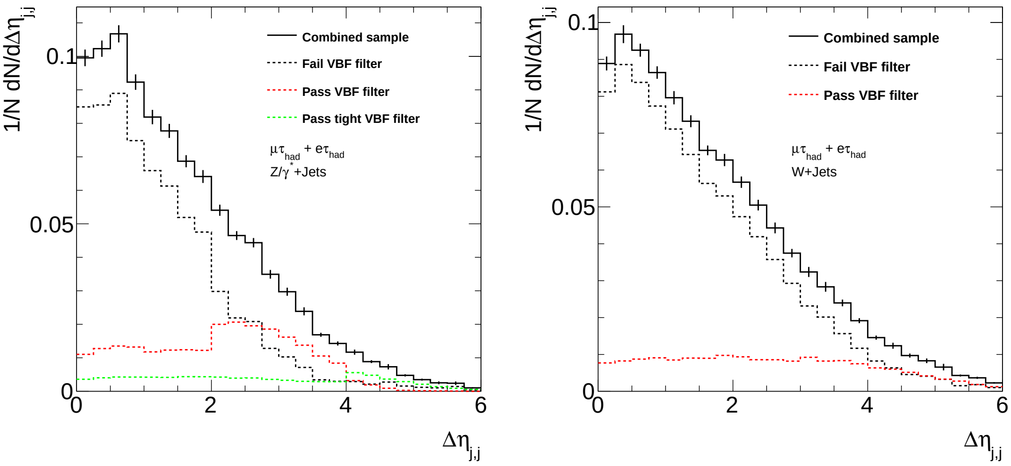

(a) (b)

Figure 5.8. *Distribution of $\Delta\eta_{jj}$ for $Z/\gamma^* +$ jets (a) and $W +$ jets (b) events for the different filtered event samples. The solid line shows the combination of the filtered samples (dashed lines) after removing the overlap.*

Process	$\sigma_{\text{pp, 8 TeV}} \pm \delta_{\text{PDF},\alpha_s} \pm \delta_{\text{QCD}}$	$\sigma_{\text{pp, 7 TeV}} \pm \delta_{\text{PDF},\alpha_s} \pm \delta_{\text{QCD}}$
$Z/\gamma^* \to \tau\tau$	$5.50 \pm 0.22 \pm 0.05$ nb	$4.97 \pm 0.20 \pm 0.05$ nb
$Z/\gamma^* \to \ell\ell$	$10.99 \pm 0.44 \pm 0.11$ nb	$9.93 \pm 0.40 \pm 0.10$ nb
$W \to \ell\nu_\ell$	$24.53 \pm 0.98 \pm 0.25$ nb	$20.97 \pm 0.84 \pm 0.21$ nb
$W \to \tau\nu_\tau$	$12.27 \pm 0.49 \pm 0.12$ nb	$10.48 \pm 0.42 \pm 0.10$ nb
$t\bar{t}$	$0.25 \pm 0.02 \pm 0.02$ nb	$0.18 \pm 0.01 \pm 0.01$ nb
single-top	$0.053 \pm 0.004 \pm 0.003$ nb	$0.038 \pm 0.003 \pm 0.002$ nb
WW	$0.029 \pm 0.001 \pm 0.001$ nb	$0.045 \pm 0.002 \pm 0.002$ nb
WZ	$0.022 \pm 0.001 \pm 0.001$ nb	$0.018 \pm 0.001 \pm 0.001$ nb
ZZ	$0.007 \pm 0.001 \pm 0.001$ nb	$0.006 \pm 0.001 \pm 0.001$ nb
$H \to \tau\tau$ (VBF)	$0.100 \pm 0.003 \pm 0.001$ pb	$0.077 \pm 0.002 \pm 0.001$ pb
$H \to \tau\tau$ (ggF)	$1.218 \pm 0.093 \pm 0.095$ pb	$0.956 \pm 0.073 \pm 0.075$ pb
$H \to \tau\tau$ (WH)	$0.045 \pm 0.001 \pm 0.001$ pb	$0.037 \pm 0.001 \pm 0.001$ pb
$H \to \tau\tau$ (ZH)	$0.026 \pm 0.001 \pm 0.001$ pb	$0.021 \pm 0.001 \pm 0.001$ pb

Table 5.1. *Cross-section predictions for the most important background and signal processes for centre-of-mass energies of* 7 *TeV and* 8 *TeV at the LHC. The accuracy of each calculation is detailed in the text. The quoted uncertainties refer to inclusive cross-section and differ from those in the exclusive analysis categories which are discussed in Section 5.7.*

An event sample of $t\bar{t}$ events is generated at NLO in QCD, using the Powheg [66, 67] event generator interfaced to Pythia for the simulation of the UE, parton shower and hadronisation. The Cteq61l PDF set is used. The events are normalised to the cross section at NNLO in QCD, including the resummation of next-to-next-to-leading logarithmic soft gluon contributions [177–183] and assuming a top mass of $m_{\text{top}} = 172.5$ GeV. Single-top events are generated using Powheg interfaced to Pythia for the s-channel and Wt processes, while AcerMC [184, 185] interfaced to Pythia is used to generate the t-channel processes. The single-top event samples are normalised to cross sections at NLO accuracy taking into account NNLL contributions from soft gluon emission [186–189].

Diboson production is simulated using Herwig for samples of WZ and ZZ events, while Alpgen interfaced to Herwig is used to generate the WW event sample. Event samples of the loop-induced $gg \to WW$ processes are generated using gg2WW [190] interfaced to Herwig [63] and Jimmy [171] for the modelling of the non-perturbative QCD effects. While Alpgen gives a more precise description of the jet topology in diboson events than a LO generator, it does not include off-shell Z contributions in WZ and ZZ events, which is why Herwig is used instead. The samples are normalised to the corresponding cross sections at NLO accuracy as implemented in Mcfm[191].

Table 5.1 lists the cross sections for the most important background and signal processes with the corresponding uncertainties on the inclusive cross section due to the PDF set and α_s ($\delta_{\mathrm{PDF},\alpha_s}$) and due to missing higher order corrections (δ_{QCD}). All simulated samples are weighted with various correction factors discussed in Chapter 3 to account for differences in the object reconstruction performance between the simulated event samples and data.

5.4. Event Selection and Categorisation

Several event selection criteria are used to define phase-space regions of special interest. Basic *preselection* requirements are applied to select events with the final state objects expected in the signal process. Two event *categories* are defined, based on the signal process event topology discussed above, and targeted to be enriched in either VBF or ggF signal events. For each category, several *control regions* (CR) are constructed, with kinematic event properties as similar as possible to the actual *signal region* (SR). Each of these control regions is aimed to be enriched in one specific background process, in order to validate the background model which is discussed in Section 5.5.

5.4.1. Analysis Preselection and Object Definitions

After passing trigger and basic data quality requirements (see Section 5.2) the reconstructed physics objects are defined. These definitions include identification criteria detailed in Chapter 3, transverse momentum thresholds and so-called *overlap removal* (OLR) prescriptions, which are meant to resolve potential ambiguities in the object reconstruction.

As outlined above, jets are used as an important ingredient to define a VBF signal enriched category. Jets are reconstructed from local calibrated clusters using the anti-k_T algorithm with a distance parameter of $r = 0.4$ (see Section 3.3). They are used in the analysis if they lie within $|\eta| < 4.5$ and exceed $p_T > 30$ GeV. To reject jets from PU events, jets within the ID acceptance $|\eta| < 2.4$ are required to pass jet vertex-fraction criteria of $|\mathrm{JVF}| > 0.5$, if they have a transverse momentum below $p_T < 50$ GeV, while for the analysis of 7 TeV data a slightly tighter criteria of $|\mathrm{JVF}| > 0.75$ is used. The use of flavour-tagging information is able to greatly reduce background from $t\bar{t}$ events. The Mv1 algorithm is used to identify jets originating from bottom quarks within a pseudorapidity region of $|\eta| < 2.5$. The tagging algorithm employs a working point at a b-jet selection efficiency of 70% (see also Section 3.3.3).

Hadronic taus are reconstructed as detailed in Section 3.6 and required to pass medium identification criteria, to have a transverse momentum above $p_T > 20$ GeV and to be within $|\eta| < 2.47$. The number of associated charged tracks in the core cone is required to be either one or three and their reconstructed electric charges must add up to an absolute value of 1. In addition, in the $\tau_e\tau_{\mathrm{had}}$ channel, the τ_{had} object is required to pass the medium electron veto.

Object	Criteria
Muons (Preselection)	Combined or segmented-tagged
	$p_{\mathrm{T}} > 10$ GeV (2 GeV for OLR with τ_{had})
	$\lvert\eta\rvert < 2.5$
	ID quality criteria
Muons (Selection)	Combined
	$p_{\mathrm{T}} > 26$ GeV
	($p_{\mathrm{T}} > 22$ GeV for 7 TeV data)
	$I_{0.4}^{p_T} < 0.06$
	$I_{0.2}^{E_T} < 0.06$
Electrons (Preselection)	Medium identification
	$p_{\mathrm{T}} > 15$ GeV
	$\lvert\eta\rvert < 2.47$
	not within $1.37 < \lvert\eta\rvert < 1.52$
Electrons (Selection)	Tight identification
	$p_{\mathrm{T}} > 26$ GeV
	($p_{\mathrm{T}} > 25$ GeV for 7 TeV data)
	$I_{0.4}^{p_T} < 0.06$
	$I_{0.2}^{E_T} < 0.06$
Hadronic tau decays	Medium identification
	$p_{\mathrm{T}} > 20$ GeV
	$\lvert\eta\rvert < 2.47$
	Charge $= \pm 1$
	Medium electron veto (only in $\tau_e\tau_{\mathrm{had}}$ channel)
	1 or 3 tracks
Jets	Built from LC TopoClusters
	$p_{\mathrm{T}} > 30$ GeV
	$\lvert\eta\rvert < 4.5$
	JVF requirement
	Jet cleaning criteria

Table 5.2. *Overview over the object-selection criteria. The light-lepton criteria are separated into preselection and selection criteria. The former are used to perform the object overlap removal and the dilepton veto, while the latter ones are used in the event selection criteria.*

As crucial part of the signal signature, light leptons are selected if they pass tight identification criteria. In order to suppress $Z \to \ell\ell$ events or events in which leptons are misidentified as τ_{had} in general, looser lepton identification requirements would allow a better lepton veto performance. Therefore, the lepton selection is performed in two steps. Initially, muons are required to be either combined or segmented-tagged muons (see also Section 3.5), to exceed a transverse momentum of $p_T > 10$ GeV and to lie within $|\eta| < 2.5$. Electrons are identified as clusters in the electromagnetic calorimeter which are geometrically matched to reconstructed tracks in the inner detector. The electron is required to pass loose identification criteria (see also Section 3.4), to exceed $p_T > 15$ GeV and to have a pseudorapidity of $|\eta| < 2.47$. In addition, electrons in the transition region between the barrel and endcap calorimeter ($1.37 < |\eta| < 1.52$) are discarded due to the poor identification and reconstruction performance. These loose object definitions are used to resolve object ambiguities. If identified objects overlap within $\Delta R < 0.2$, only one of them is used in the analysis. As muons provide the highest reconstruction purity, an identified muon is always kept and prioritised over electrons, τ_{had} objects and hadronic jets. The overlap removal of the other objects is performed following this order which is based on the reconstruction purities. For the overlap removal between muons and τ_{had} decays, the muon p_T threshold is further lowered to 2 GeV to remove nearly all muons which are misidentified as τ_{had}.

After the overlap removal, the such defined lepton objects are also used to perform a dilepton veto in order to suppress events from $Z \to \ell\ell$ decays. Only events with exactly one light lepton and exactly one τ_{had} object are kept. In addition, this ensures orthogonality to the $\tau_{\mathrm{had}}\tau_{\mathrm{had}}$ and $\tau_{\mathrm{lep}}\tau_{\mathrm{lep}}$ analyses. The second step of the lepton object definition is used to enhance the lepton purity, by tightening the identification criteria. Muons are required to be reconstructed as combined ID and MS objects, while electrons must pass tight identification criteria. Furthermore, cuts on isolation variables are used to further reduce backgrounds from hadronic jets. Two different isolation variables are used. The track isolation $I_{0.4}^{p_T}$ is build as the ratio between the sum of all transverse momenta of additional tracks within a cone of $\Delta R < 0.4$ around the reconstructed lepton and the p_T of the lepton itself. As it makes use of tracks associated to the primary vertex of the event, this quantity is rather robust against the presence of PU events. The calorimeter isolation $I_{0.2}^{E_T}$ instead, is defined as the ratio between the sum of transverse energy deposited in cells within a cone of $\Delta R < 0.2$ around the object and the transverse energy of the lepton itself. Depositions close to the barycentre of the electron or muon are not considered and in case of electrons the expected leakage of the electron shower into the isolation cone is subtracted. As the calorimeter isolation depends on the number of PU events it is corrected for this effect as a function of the number of vertices. Electrons and muons are required to pass isolation criteria of $I_{0.4}^{p_T} < 0.06$ and $I_{0.2}^{E_T} < 0.06$.

As single lepton triggers are used to record the events, the light lepton momentum threshold is chosen to ensure a high trigger selection efficiency according to the trigger item in use. In data taken in 2011, electron trigger items with online p_T thresholds of $20 - 22$ GeV were used, while the muon trigger required an online

p_T threshold of 18 GeV. The reconstructed electrons and muons in the analysis are required to exceed a transverse momentum of $p_T > 25$ GeV and $p_T > 22$ GeV, respectively. For data taken in 2012, both lepton triggers used online requirements of $p_T > 24$ GeV. An offline criteria of $p_T > 26$ GeV is therefore applied for electrons and muons in the 8 TeV analysis.

Finally, events are discarded if the MMC algorithm described above does not converge. As the MMC efficiency is close to 100% for signal events this requirement discards nearly only background events, but ensures a valid ditau mass estimate for all events in the analysis. Tables 5.2 and 5.3 summarise the object and preselection requirements. The chosen trigger selection features selection efficiencies between 26 − 33% for signal events and about 40% for $W+$ jets events as one of the major fake backgrounds and depends crucially on the transverse momentum spectrum of the light lepton. The full preselection features a selection efficiency of about 7 − 9% for signal events and about 0.01% $W+$ jets events. Despite this strong rejection of events with misidentified τ_{had} objects, such events provide one of the major backgrounds due to their large cross section.

Event preselection criteria
Positive single lepton trigger decision
Basic data quality criteria
Exactly one electron or muon
Exactly one τ_{had} object
MMC convergence

Table 5.3. *Summary of the event preselection-criteria used to define the data sample entering the analysis.*

5.4.2. Event Categorisation

The event categorisation splits the phase space into two categories, targeted to be sensitive to the presence of either VBF or ggF and VH signal events. As these signal processes have different kinematic event properties the categorisation allows to optimise the signal extraction procedure separately. The categories are defined in a fully exclusive way:

- **VBF category:** The defining property of the VBF category is the presence of two jets which are well separated in pseudorapidity. The leading jet is required to have a transverse momentum larger than $p_T > 50$ GeV, while the subleading jet has to exceed $p_T > 30$ GeV. Their pseudorapidity separation $\Delta\eta_{jj}$ has to be greater than 3. This selection enhances the VBF signal process over ggF and VH processes. Due to the larger cross section of the ggF process, a non negligible contribution remains. In total, the VBF process contributes about 64% to the total expected signal yield, while the gluon fusion process accounts for about 35%. The composition of the expected signal yields differs though in the most sensitive bins of the BDT output distribution, as the background suppression in this category is optimised solely based on the event topology of VBF events. Events with an extremely low visible ditau mass of $m_{\text{vis}} < 40$ GeV are discarded.

- **Boosted category:** The Boosted category targets ggF events with a large transverse momentum of the Higgs boson. The defining quantity is the reconstructed transverse momentum of the ditau system p_T^H which is required to exceed 100 GeV. It is calculated as the vectorial sum of lepton, τ_{had} and $\mathbf{E}_T^{\text{miss}}$ momentum vectors in the transverse plane. To ensure orthogonality to the VBF category, events passing the VBF category selection are not considered. A sizeable fraction of VBF and VH events contribute as well to this category, and the signal extraction procedure is optimised for this specific mixture of signal processes. The ggF process accounts for about 66% of the expected signal yield, while the VBF process contributes with approximately 19%. One advantage of defining this category based on the reconstructed lepton, τ_{had} and $\mathbf{E}_T^{\text{miss}}$ objects instead of using jets to describe the boosted topology is that systematic uncertainties on the jet-energy scale only enter indirectly via the $\mathbf{E}_T^{\text{miss}}$ reconstruction. The overall acceptance uncertainty is significantly reduced in this approach.

As discussed in Section 5.1, p_T^H and $\Delta\eta_{jj}$ are powerful discriminating variables against the dominant $Z/\gamma^* \to \tau\tau$ background and are therefore chosen as the defining quantities for the categorisation. While the categorisation itself already provides some background discrimination, this is not the primary goal of this analysis step. The main background suppression is achieved by boosted decision trees as described in Section 5.6. In general, events not categorised in one of the two classes above could be used in additional categories. In fact two additional categories, denoted as 0- and 1-jet categories, were studied. These categories were selecting events not categorised in either the VBF or Boosted category, and yielding zero and one or more jets in the final state, respectively. They were found to provide only a very small increase of the analysis sensitivity and were therefore discarded. Besides the discriminating power of the p_T^H distribution, the Boosted category exploits a second aspect of highly boosted ditau systems. The relative mass resolution gets improved with larger values of p_T^H. This increases the separation power of the ditau mass distribution between signal and $Z/\gamma^* \to \tau\tau$ events. This effect is due to the relative decrease in the E_T^{miss} resolution with rising $\sum E_T$, as the MMC resolution is dominated by the E_T^{miss} reconstruction performance. Figure 5.9 shows the MMC distributions of $Z/\gamma^* \to \tau\tau$ and $H \to \tau\tau$ events after preselection and after categorisation. While the $Z/\gamma^* \to \tau\tau$ distributions are normalised to unit area, the signal is scaled with the same scale factor and enhanced by an additional factor 50. This allows to compare the increase in the signal-to-background ratio after categorisation. The mass resolution improves in both, Boosted and VBF categories, with respect to the preselection.

Region	VBF category	Boosted category
Signal region	≥ 2 jets ($p_{\mathrm{T}} > 50/30$ GeV) $\Delta\eta_{jj} > 3.0$ • $m_T < 70$ GeV • b-jet veto • $m_{\mathrm{vis}} > 40$ GeV Opposite sign	Not in VBF cat. $p_T^H > 100$ GeV $m_T < 70$ GeV b-jet veto Opposite sign
$Z \to \tau\tau$ CR	As SR, and $m_T < 40$ GeV $m_{\tau\tau} < 110$ GeV	As SR, and $m_T < 40$ GeV $m_{\tau\tau} < 110$ GeV
W+jets CR	As SR, but $m_T > 70$ GeV	As SR, but $m_T > 70$ GeV
Top CR	As SR, but ≥ 1 b-tagged jet $m_T > 70$ GeV	As SR, but ≥ 1 b-tagged jet $m_T > 70$ GeV
Fake τ_{had} CR	As SR, but Same sign	As SR, but Same sign

Table 5.4. *Summary of the selection criteria used to define the VBF and Boosted analysis categories and the corresponding control regions. Events passing all other selection cuts for the VBF category but failing requirements marked with a bullet (•) are discarded, and not considered for the Boosted category.*

For both categories, one signal and multiple control regions are defined. While the signal region is targeted to provide the signal sensitivity, the control regions are enriched in background processes in order to validate the background model or to extract parameters of the background model. The following regions are used:

- **Signal region:** The signal region is defined by requiring that the electric charges of the reconstructed lepton and τ_{had} are of opposite sign and that no identified b-jet is present. To allow the definition of an orthogonal control region enriched in $W +$ jets events, events are further required to have a transverse mass of $m_T < 70$ GeV.
- ***W* control region:** The signal region selection is used, while the cut on the transverse mass is inverted to $m_T > 70$ GeV.
- **Top control region:** Two different top control regions are defined. While both invert the b-tag requirement of the signal selection, two transverse mass selections are used. One region is defined with $m_T < 70$ GeV, while a second region is defined as $m_T > 70$ GeV. The first control region is used in the measurement of the τ_{had} misidentification probability of jets in $t\bar{t}$ events (see

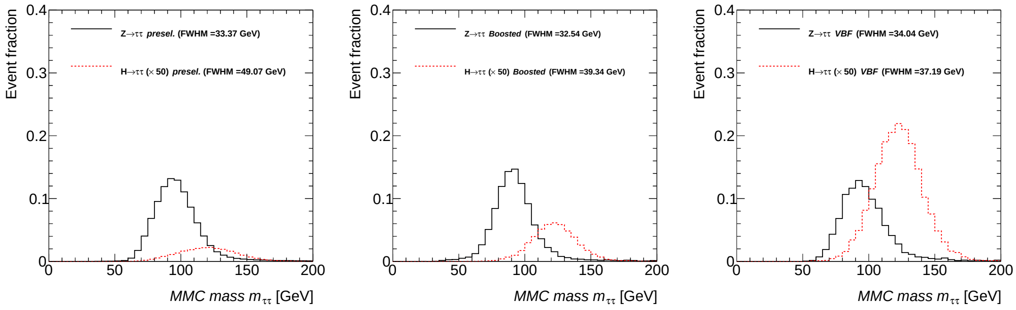

(a) (b) (c)

Figure 5.9. *Distribution of the reconstructed ditau mass in simulated $Z \to \tau\tau$ and $H \to \tau\tau$ events after preselection (a), in the Boosted (b) and VBF category (c). The $Z/\gamma^* \to \tau\tau$ distributions are normalised to unity and the signal is scaled by the same factor and enhanced by a factor 50, to visualise the signal-to-background ratio at preselection and after categorisation. The full width of the distributions at half maximum (FWHM) are given as a measure of the mass resolution.*

Section 5.5), while the second control region is used to validate and correct the normalisation of $t\bar{t}$ events with real τ_{had} decays, which are modelled by simulated event samples.

- **$Z/\gamma^* \to \tau\tau$ control region:** As the $Z/\gamma^* \to \tau\tau$ background behaves kinematically very similar to the signal processes, it is hard to define a pure and signal depleted control region for this process. The $Z/\gamma^* \to \tau\tau$ control region is defined by $m_{\tau\tau} < 110$ GeV to ensure a negligible signal contamination and $m_T < 40$ GeV to suppress fake events.
- **Fake control region:** By inverting the charge correlation requirement a region enriched in events with misidentified τ_{had} objects is defined.

Table 5.4 summarises the event categorisation and the selection criteria of the control and signal regions.

5.5. Background Model

In order to establish the potential existence of $H \to \tau\tau$ decays, the background processes contributing to the final state under study must be well understood and their event yields estimated with the best possible accuracy. The background estimation in this analysis is built in multiple steps. This section describes the methodology used to model the different background processes, while the fit to estimate the background model parameters for the final result is described in Section 6. As multiple observables are used to suppress background events, not only an estimate of the event rate is needed, but also a reliable model of the differential distributions of these observables. Wherever possible, the background model is based on data-driven estimates, so that the dependence of the result on simulated event samples and their systematic uncertainties is minimised. Two different methods to model the complicated fake τ_{had} background are outlined in Section 5.5.2. While the first method, denoted as (OS-SS) estimate, is used to estimate the contribution of misidentified τ_{had} objects after preselection, a more refined estimate is constructed in the two main analysis categories, denoted as *fake factor* method. As the Higgs boson signal is expected to manifest itself as an excess on the falling tail of the $Z/\gamma^* \to \tau\tau$ mass distribution, a reliable estimate of the reconstructed Z boson mass distribution is crucial. This is achieved using a sample of *embedded* $Z \to \tau\tau$ events, which is explained in Section 5.5.1. Section 5.5.5 finally shows first comparisons between observed data events and the expected background yields. In general, all background estimates are subjects to uncertainties. Their dependence on these uncertainties are parametrised. In parallel, some models might depend on additional parameters, of which some are apriori unconstrained. All these parameters of the background model will finally be estimated in a combined likelihood fit, taking into account all correlations between the various parameters across all regions. To allow comparisons between data and background estimates also before performing the fit, all these parameters are set to initial estimates which will be denoted as their *prefit* values in the following.

5.5.1. Background Model for $Z \to \tau\tau$ Events

$Z/\gamma^* \to \tau\tau$ decays are modelled using a technique denotes as *embedding* [192]. A modified data sample of $Z \to \mu\mu$ events is constructed by replacing the reconstructed muons by simulated tau decays. The initial sample of $Z \to \mu\mu$ events is selected by single muon triggers and events are required to have at least two combined, well isolated muons of opposite electric charge with $m_{\mu\mu} > 40$ GeV and passing p_T thresholds of 20/15 GeV for the leading and subleading muon, respectively. If more than one such muon pair exists in an event, the pair with an invariant mass closest to the Z boson mass is chosen. The selected reconstructed muons determine the four-momenta of two tau leptons. Their four-momenta are corrected for the different tau lepton mass by setting the absolute momentum value to $p_\tau = \sqrt{E_\mu^2 - m_\tau^2}$. The decay of these two tau leptons is simulated using Tauola [71] and final state radiation is simulated using Photos [193]. This event is then processed by the ATLAS simulation. Before merging the simulated tau decays with the data event, the original muon tracks are removed. To account for energy deposits of the initial muons, two muons are simulated using the kinematic event properties of the reconstructed event. The energy deposits in calorimeter cells in this simulated dimuon event are subtracted from the data event. Afterwards, the simulated tau decays are added to the data event, including the tracks and calorimeter deposits. To provide a larger statistical power of the embedded event sample, Tauola is required to decay one tau lepton leptonically and the second one hadronically. Furthermore, in the 2012 embedded samples the decay products are required to have transverse momenta exceeding 15 GeV and 24 GeV for the lepton and τ_{had} decay, respectively, otherwise the simulation of the tau decay is repeated. The bias introduced by this requirement is corrected by applying the filtering efficiency as an additional event weight.

The such prepared sample offers several advantages over simulated event samples of $Z/\gamma^* \to \tau\tau$ events. As the expected signal contribution in dimuon final states is negligibly small due to the low branching ratio of $H \to \mu\mu$ decays, $Z \to \mu\mu$ events offer a basically signal free control sample to extract the event topology and mass spectrum of Z boson decays at identical LHC data taking conditions as present in the analysed data sample. Muons are the experimentally most precise reconstructed objects in ATLAS and therefore their momenta are measured with negligible uncertainties with respect to the uncertainties present in the $H \to \tau\tau$ analysis. The effect of the muon momentum resolution is found to have negligible impact as well. While the embedded, simulated tau decays are of course subject to experimental uncertainties, key features of the events are taken directly from data. Of especial relevance are the kinematic properties of additional jets in the events as these are used to define the signal sensitive VBF region as well as the kinematic properties of the Z boson, like its mass and p_T spectrum. Furthermore, the underlying event and pile-up activity are additional aspects in the embedded samples which all do not rely on simulation, making the embedded sample a powerful tool to model $Z/\gamma^* \to \tau\tau$ events accurately.

The systematic uncertainties of this method account for the muon energy subtraction procedure and the isolation requirement in the initial event selection. The cell energy in the simulated dimuon events which are used to subtract the energy deposits of the initial muons is varied by 20%(30%) for data taken in 2012 (2011). The uncertainty of the isolation requirement is estimated by varying the selection criteria from the nominal isolation requirement of $I_{0.2}^{p_T} < 0.2$ to either no isolation requirement at all or to a tight requirement of $I_{0.4}^{p_T} < 0.06$ and $I_{0.2}^{E_T} < 0.04$.

The initial sample of dimuon events has a large purity in $Z \to \mu\mu$ events. Nevertheless a small fraction of $t\bar{t}$ and diboson events is present. This overlap is accounted for in the analysis by removing events passing the embedding selection criteria in the corresponding $t\bar{t}$ and diboson event samples, with negligible impact on the final analysis result. The embedded sample is used to model the event topology. The absolute normalisation of the sample is determined in a fit to the observed data, and the prefit estimate of this normalisation is determined after preselection in a visible mass window of $40\ \text{GeV} < m_{\text{vis}} < 70\ \text{GeV}$. To account for the initial dimuon selection criteria, which reject low mass events, a small amount of $Z/\gamma^* \to \tau\tau$ events from simulated event samples is added for true ditau masses below 40 GeV. The finite trigger efficiency of the single muon trigger used in the data selection is corrected for, as it is done for the muon reconstruction efficiency. As no simulated trigger response is available for the embedded event sample, the trigger efficiency of the single lepton trigger items used in the analysis event selection is applied as event weight to account for the finite selection efficiency.

5.5.2. Estimation of Background Events with Misidentified τ_{had} Objects

Background events with jets misidentified as τ_{had} objects are hard to simulate due to several reasons. The identification algorithms deployed to suppress fake τ_{had} decays rely on various kind of shower shape variables describing the evolution of the hadronic and electromagnetic showers of the charged and neutral pions. As hadronic showers are subject to large event-by-event fluctuations they are naturally hard to simulate. Furthermore, to simulate misidentified hadronic τ_{had} it is not the shower of a hadronically decaying tau which needs to be well simulated, but the experimental signature of hadronic jets originating from quark or gluon hadronisation. While the simulation of jets and the calibration of the jet-energy scale is rather accurate, the strict tau identification criteria select a subset of jets which are complex and deviate significantly from the bulk of hadronic jets in terms of shower shape, track multiplicity, and charged particle content. Besides this, another crucial aspect in a correct simulation of τ_{had} misidentifaction probabilities is the modelling of the quark and gluon fraction within the sample of jets. As gluons tend to hadronise into wider jets with larger particle multiplicities due to their larger effective colour charge, the shower shapes and therefore also the τ_{had} misidentification probability differs significantly. To achieve the correct quark and gluon fractions within an inclusive sample of jets, for example from $W+$ jets events, is complicated and subject to large uncertainties. Besides these complications, no reliable and statistically sufficiently large simulated event samples of multijet events from strong interactions exist. All these points clearly motivate the need for data-driven estimation techniques.

The (OS-SS) Method

The (OS-SS) method [194, 195] exploits the different charge correlation in backgrounds with fake τ_{had} objects than present in real ditau events. If the ratio between OS and SS events in QCD multijet events is denoted as r_{QCD}, the expected event yield for events with opposite charge can be extracted from the event yield with same-sign charge. For differential distributions, this holds individually in bins of observables, if the shape of the spectrum is independent of the reconstructed charge product. This assumption has been checked in a control region enriched in QCD events, which is defined by a low amount of E_T^{miss}, low m_T, a reversed calorimeter isolation requirement on the reconstructed lepton and a looser τ_{had} ID requirement. Contamination from electroweak processes in this region ranges between $1-27\%$ depending on the charge product and lepton flavour, and is subtracted using simulated event samples. Even though the charge reconstruction efficiency in misidentified τ_{had} objects is not well-defined, especially in the case of gluon initiated jets, r_{QCD} might be slightly larger than one, due to remaining charge correlation effects from processes as $q_1\bar{q}_2 \to q_1\bar{q}_2$ or $gg \to q\bar{q}$. Therefore the ratio r_{QCD} is measured in the same QCD control region mentioned above and found to be $r_{\text{QCD}} = 1.00 \pm 0.05(\text{stat.}) \pm 0.12(\text{syst.})$ for $e + \tau_{\text{had}}$ events and

$r_{\mathrm{QCD}} = 1.10 \pm 0.06(\mathrm{stat.}) \pm 0.13(\mathrm{syst.})$ for $\mu + \tau_{\mathrm{had}}$ events. The systematic uncertainty arise from the exact definition of the control region and a small dependence of r_{QCD} on the calorimeter isolation requirement. Defining a SS control region with the exact same selection criteria as in the signal region but an inverted requirement on the charge product, so that both reconstructed lepton and τ_{had} objects feature same-sign electric charge, the combined background can be estimated as:

$$N_{\mathrm{OS}}^{\mathrm{bkd}} = r_{\mathrm{QCD}} \cdot N_{\mathrm{SS}}^{\mathrm{data}} + N_{add-on}^{Z\to\tau\tau} + N_{add-on}^{Z\to\ell\ell} \tag{5.6}$$

$$+N_{add-on}^{W+\text{ jets}} + N_{add-on}^{\mathrm{top}} + N_{add-on}^{VV} \tag{5.7}$$

where $N_{\mathrm{SS}}^{\mathrm{data}}$ is the full event yield observed in data in the SS control region. As it contains contributions from all sort of background processes, only the expected difference between OS and SS event yields for additional processes needs to be added to the SS data yield in order to estimate the full background expectation in the OS region. These terms are denoted as add-on terms:

$$N_{add-on}^{X} = N_{\mathrm{OS}}^{X} - r_{\mathrm{QCD}} \cdot N_{\mathrm{SS}}^{X} \tag{5.8}$$

where r_{QCD} accounts for the overestimation when scaling the total observed SS event yield with r_{QCD}, instead of only the fraction stemming from QCD multijet events. While the shape of the add-on terms is taken from simulated event samples, normalisation corrections are used for those where misidentified τ_{had} objects contribute. Namely, for $W+$ jets, $Z \to \ell\ell +$ jets($\to \tau_{\mathrm{had}}$) events where a jet is misidentified as τ_{had} and top events. These correction factors are determined in background enriched control regions, in order to not rely on the simulation for the misidentification probability. The definition of these regions follows the Table 5.4 apart from the $Z \to \ell\ell +$ jets($\to \tau_{\mathrm{had}}$) CR, which is defined by requiring two same flavour leptons with an invariant mass compatible with the Z boson mass 61 GeV $< m_{\ell\ell} <$ 121 GeV in addition to the τ_{had} object. The correction factors are obtained separately for OS and SS events and the add-on terms are built as:

$$N_{add-on}^{W+\text{ jets}} = k_{\mathrm{OS}} \cdot N_{\mathrm{OS}}^{W+\text{ jets}} - r_{\mathrm{QCD}} \cdot k_{\mathrm{SS}} \cdot N_{\mathrm{SS}}^{W+\text{ jets}} \tag{5.9}$$

Table 5.5 lists these factors, determined at preselection level for both the 7 and 8 TeV analysis. The large differences in the correction factors between the 7 TeV and 8 TeV analyses is mainly due to differences in the chosen event generators. For example, PYTHIA is used for showering and hadronisation of the $W+$ jets samples in the 8 TeV analysis, while HERWIG is used in the 7 TeV samples. This choice majorly affects the τ_{had} misidentification probabilities. Figures 5.10 and 5.11 show some kinematic distributions after preselection, comparing the observed data with the background estimation. Figure 5.10 (e) and (f) show the transverse momentum distributions of the reconstructed hadronic τ_{had} decay. The observed discrepancy between data and background model is due to the neglected p_T dependence of the τ_{had} misidentification probability in the extraction of the normalisation correction-factors. As the OS-SS method is not used in the final signal regions, this effect is not accounted for in these plots, but was shown to be responsible for the observed bias. This background estimation technique is not used in the final analysis, but

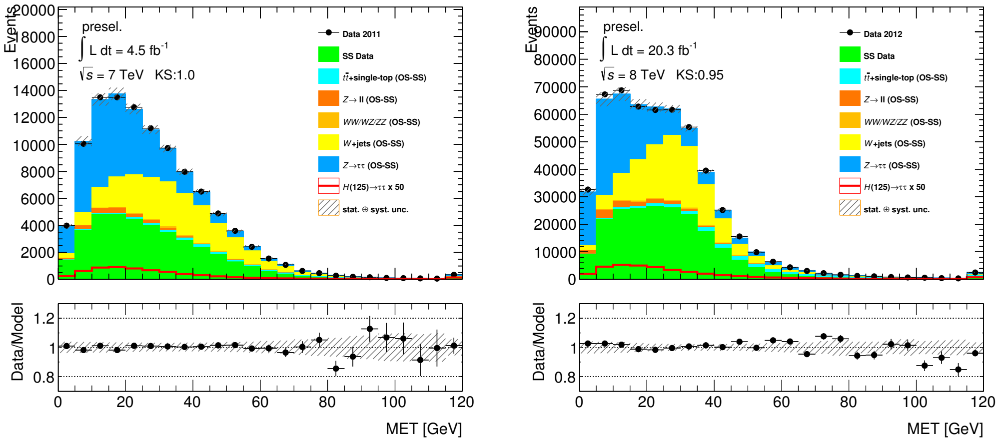

(a) 7 TeV - $E_{\mathrm{T}}^{\mathrm{miss}}$ (b) 8 TeV - $E_{\mathrm{T}}^{\mathrm{miss}}$

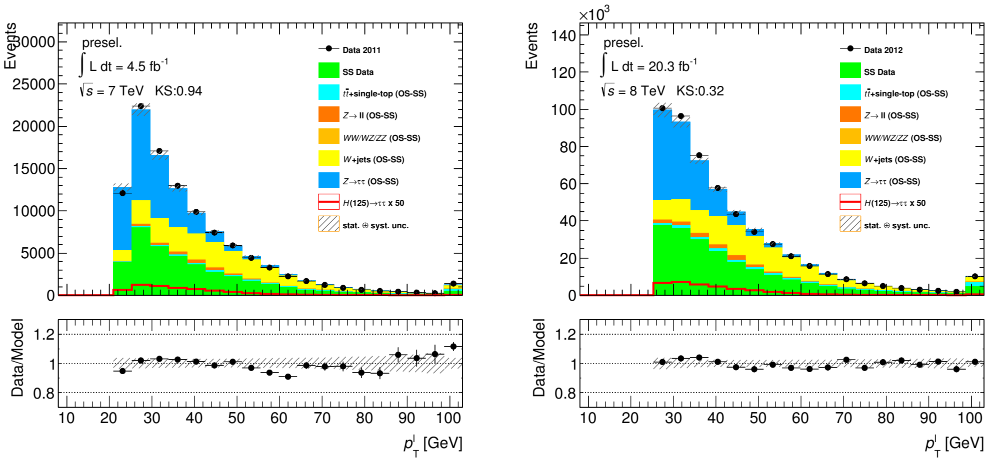

(c) 7 TeV - p_{T}^{ℓ} (d) 8 TeV - p_{T}^{ℓ}

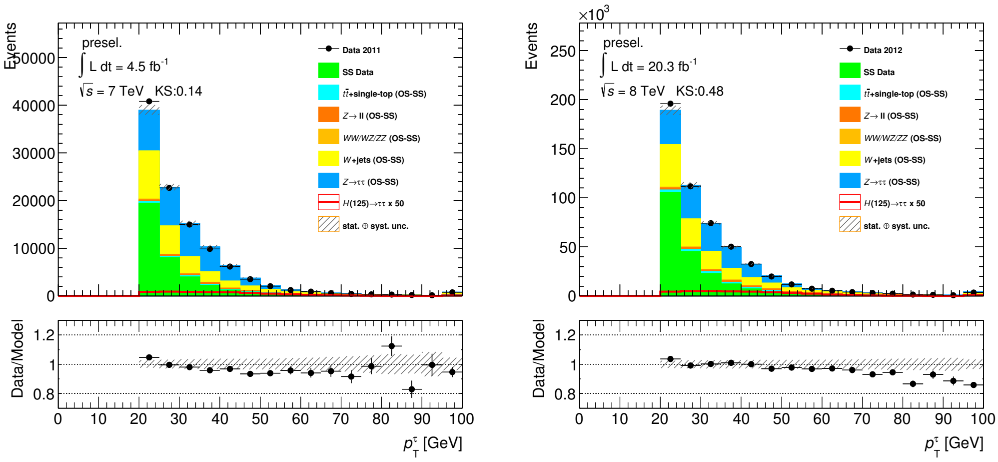

(e) 7 TeV - p_{T}^{τ} (f) 8 TeV - p_{T}^{τ}

Figure 5.10. *Distribution of E_T^{miss} (a, b), p_T^{ℓ} (c, d) and $p_T^{\tau_{\mathrm{had}}}$ (e, f) at preselection level of the 7 TeV (left) and 8 TeV (right) analysis. The hatched band includes systematic and statistical uncertainties of the background estimate. (OS-SS) denotes the add-on term of the corresponding process. The last bin includes the event yields beyond the displayed range.*

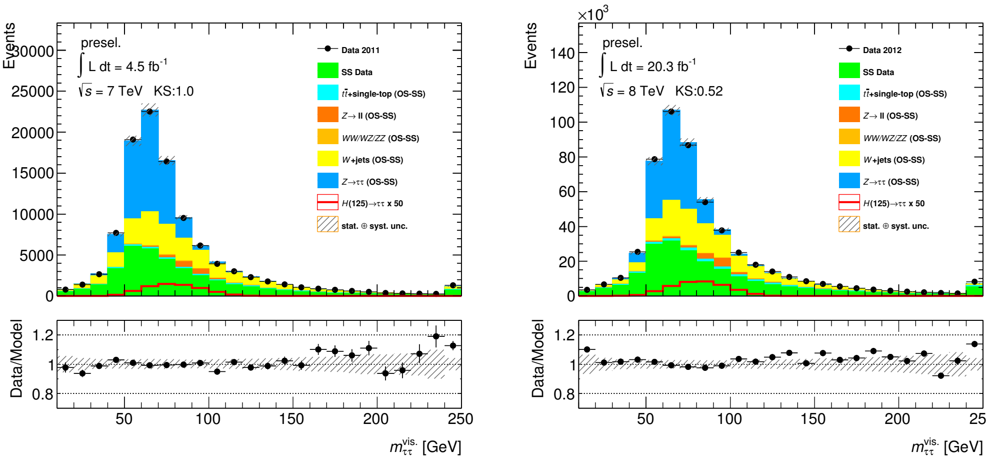

(a) 7 TeV - $m_{\tau\tau}^{vis}$ (b) 8 TeV - $m_{\tau\tau}^{vis}$

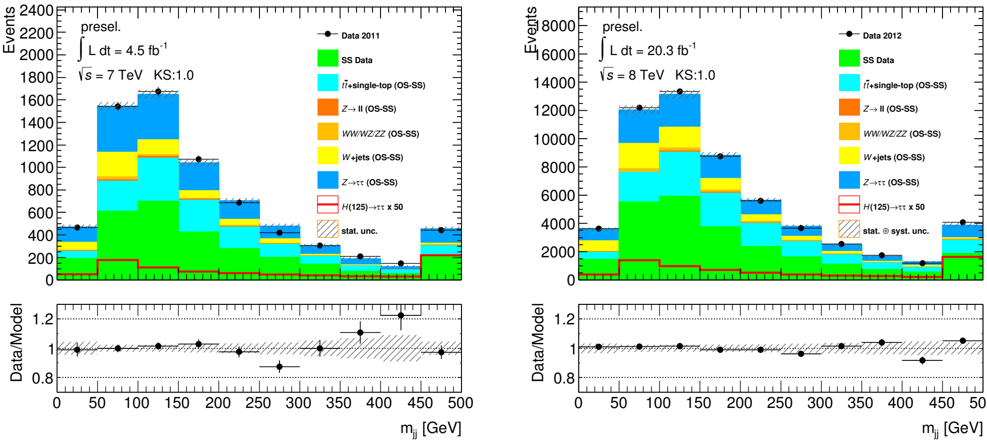

(c) 7 TeV - m_{jj} (d) 8 TeV - m_{jj}

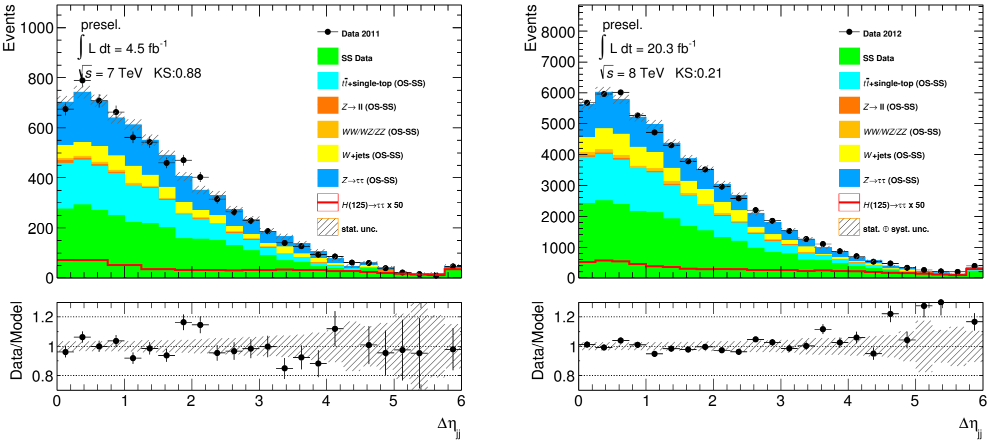

(e) 7 TeV - $\Delta\eta_{jj}$ (f) 8 TeV - $\Delta\eta_{jj}$

Figure 5.11. *Distribution of $m_{\tau\tau}^{vis}$ (a, b), m_{jj} (c, d) and $\Delta\eta_{jj}$ (e, f) at preselection level of the 7 TeV (left) and 8 TeV (right) analysis. The hatched band includes systematic and statistical uncertainties of the background estimate. (OS-SS) denotes the add-on term of the corresponding process. The last bin includes the event yields beyond the displayed range.*

Bkd. process	$e + \tau_{\text{had}}$ (8 TeV)	$\mu + \tau_{\text{had}}$ (8 TeV)
W+jets (OS)	0.94 ± 0.01	0.86 ± 0.01
W+jets (SS)	1.22 ± 0.02	1.03 ± 0.02
$t\bar{t}$ and single-top (OS)	1.07 ± 0.01	1.07 ± 0.01
$t\bar{t}$ and single-top (SS)	1.43 ± 0.05	1.43 ± 0.05
$Z \to \ell\ell +$ jets ($\to \tau_{\text{had}}$)	0.85 ± 0.01	0.85 ± 0.01
	$e + \tau_{\text{had}}$ (7 TeV)	$\mu + \tau_{\text{had}}$ (7 TeV)
W+jets (OS)	0.60 ± 0.01	0.59 ± 0.01
W+jets (SS)	0.89 ± 0.02	0.76 ± 0.02
$t\bar{t}$ and single-top (OS)	1.49 ± 0.05	1.49 ± 0.05
$t\bar{t}$ and single-top (SS)	2.08 ± 0.20	2.08 ± 0.20
$Z \to \ell\ell +$ jets ($\to \tau_{\text{had}}$)	0.61 ± 0.01	0.61 ± 0.01

Table 5.5. *Normalisation correction-factors used at preselection in combination with the OS-SS background estimation. The factors are extracted in background enriched control regions and the uncertainties are statistical only. The differences across the 7 TeV and 8 TeV analysis is mainly due to differences in the chosen event generators.*

only to visualise the background composition at preselection and to optimise the background suppression strategy. The reason for that is, that the OS-SS method is statistically limited by the amount of data events observed in the SS control region, especially after applying tight background suppression criteria. Therefore another, statistical more powerful, background model is used to estimate the background with fake τ_{had} objects in the actual signal regions, denoted as *Fake Factor method.*

The Fake Factor Method

The fake factor (FF) method [196] is based on a control region defined by inverting the τ_{had} identification criteria. Such τ_{had} candidates are referred to as $anti - \tau_{\text{had}}$ objects. This inversion makes the control region of much higher statistical power than the actual signal region. It is used to model all background processes where a jet is misidentified as τ_{had}, apart from diboson events. The extrapolation factor, used to estimate the signal region yield based on the observed number of events in the control region, is denoted as fake factor. It is defined as:

$$N^{\tau}_{Bkg.} = \left(N^{\text{anti}-\tau}_{\text{data,SR}} - N^{\text{anti}-\tau}_{\text{others,SR}}\right) \times \text{FF}_{\text{CR}} \tag{5.10}$$

$$\text{FF}_{\text{CR}} \equiv \frac{N^{\text{identified}-\tau}_{\text{CR}}}{N^{\text{anti}-\tau}_{\text{CR}}} \tag{5.11}$$

where $N^{\text{anti}-\tau}_{\text{others,SR}}$ is the number of events in which real τ_{had} decays or light leptons reconstructed as τ_{had} objects fail the identification criteria, and which stem from

	Boosted (8 TeV)	VBF (8 TeV)	Boosted (7 TeV)	VBF (7 TeV)
R_W	0.62	0.46	0.75	0.60
R_{QCD}	0.26	0.40	0.13	0.24
R_Z	0.05	0.11	0.06	0.13
R_{Top}	0.07	0.03	0.06	0.03

Table 5.6. *Fractional fake background contributions by the various processes estimated with the fake factor method.*

processes modelled differently like $Z \to \tau\tau$, $Z \to \ell\ell(\to \tau_{\text{had}})$, top or diboson events. These subtraction terms are taken from simulated event samples and correct the final fake estimate by less than 10%. The fake factors are measured separately in different control regions, enriched in the various background processes. $N_{\text{CR}}^{\text{identified}-\tau}$ denotes the number of events with exactly one identified τ_{had} object in one of these CRs, while several anti-τ_{had} objects can contribute to $N_{\text{CR}}^{\text{anti}-\tau}$ and $N_{\text{data,SR}}^{\text{anti}-\tau}$. As the fake factors are applied to data, no distinction between the different physics processes can be made. Instead the fake factors measured in the CRs are combined into an effective fake factor, based on the expected background composition in the SR. The fake factors are determined as a function of $p_T^{\tau_{\text{had}}}$, the number of reconstructed tracks of the τ_{had} candidate and the event category, so that the effective fake factor is determined as:

$$\text{FF}(p_T, n_{\text{prong}}, \text{cat}) = \sum_{i \in \text{processes}} R_i \, \text{FF}_i(p_T, n_{\text{prong}}, \text{cat}) \tag{5.12}$$

The background composition is estimated using simulated event samples, with a normalisation correction-factor applied to $W+$ jets events, as explained for the OS-SS method above.The fractional contribution of QCD multijet events is determined as $R_{\text{QCD}} = 1 - R_{\text{W}} - R_{\text{top}} - R_{Z\to\ell\ell}$. The fractional contributions are listed in Table 5.6. The following CRs are used to determine the fake factors:

- **W+jets:** As SR, but m_T selection inverted.
- **QCD:** As SR, but inverted track isolation and loosened calorimeter isolation requirement.
- **Top($j \to \tau$):** As SR, but at least one b-jet and $m_T < 70$ GeV.
- **$Z \to \ell\ell(j \to \tau)$:** As SR, but requiring two same flavour leptons with an invariant mass compatible with the Z boson mass 61 GeV $< m_{\ell\ell} <$ 121 GeV.

These definitions follow closely the CR definitions in Table 5.4 and those used in the OS-SS method. The top CR though differs in the applied m_T selection, where $m_T < 70$ GeV is used to define the region used in the FF derivation and $m_T > 70$ GeV is used to define the analysis CR which has a larger purity in top events with real τ_{had} decays, while the low m_T region is enriched in events with misidentified τ_{had}. The effective fake factors range from 0.15 for one-prong τ_{had}

objects with low p_T in the Boosted category, to 0.03 for three-prong τ_{had} of large transverse momentum.

Missing Transverse Energy in anti-τ_{had} Events

One complication in the use of anti-τ_{had} events to model the fake background in the SR arises due to the $\mathbf{E}_T^{\text{miss}}$ reconstruction algorithms, which are executed prior to the analysis. In this algorithm, the $\mathbf{E}_T^{\text{miss}}$ is computed based on the nominal identification criteria, and therefore anti-τ_{had} objects are entering the computation as hadronic jets, calibrated to the jet-energy scale. To avoid a bias from this wrong calibration, the $\mathbf{E}_T^{\text{miss}}$ reconstruction is rerun in the 8 TeV data samples, forcing the chosen anti-τ_{had} object to enter at the tau-energy scale instead. This majorly improves the modelling of $\mathbf{E}_T^{\text{miss}}$ related observables. This recomputation is not performed for the 7 TeV data samples, and instead a correction as a function of the projection of $\mathbf{E}_T^{\text{miss}}$ onto the three-momentum of the anti-τ_{had} candidate is performed. This variable offers a good sensitivity towards the impact of the energy scale of the anti-τ_{had} object which enters the $\mathbf{E}_T^{\text{miss}}$ computation. The correction weights are obtained from the $W+$ jets CR, as it is offering a high purity of fake backgrounds. As this correction is only performed in one-dimension and derived only based on a $W+$ jets enriched CR, a conservative symmetric ±100% systematic uncertainty is assigned to these weights. Figure 5.12 shows the resulting event weights in the two analysis categories. Figure 5.13 shows the projection of $\mathbf{E}_T^{\text{miss}}$ onto the three-momentum of the anti-τ_{had} candidate in units of the transverse tau

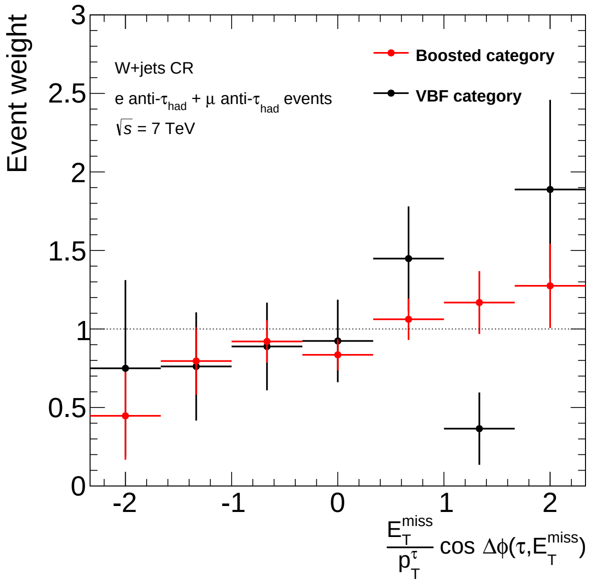

Figure 5.12. *Event weights as a function of the projection of $\mathbf{E}_T^{\text{miss}}$ onto the three-momentum of the anti-τ_{had} candidate. The weights are used to reweight anti-τ_{had} events in the fake background estimation in the 7 TeV VBF and Boosted analysis categories. The displayed uncertainties are of statistical origin only.*

momentum for both, the 7 TeV and 8 TeV analyses in the same-sign charge control region for both categories. In general, a good agreement is observed after the $\mathbf{E}_T^{\mathrm{miss}}$ recomputation or the application of the correction weights. In the 7 TeV sample, a small bias of the background estimate might remain due to the correlations between the τ_{had} identification BDT scores and the $\mathbf{E}_T^{\mathrm{miss}}$ projection. As the τ_{had} identification exploits shower shapes and fractional energy density information, directly impacting the calorimeter response, a small impact especially on $\mathbf{E}_T^{\mathrm{miss}}$ related observables is inevitable. As the fake factors are derived in bins of p_T^{τ} though, these correlations are extremely small for all discriminating observables used in the analysis. As outlined below, it is verified that no significant bias is present in the final discriminating variable.

Systematic Uncertainties

Several sources for systematic uncertainties on the fake background estimate are considered. The statistical uncertainty on the effective fake factor is ±4% (±2.3%) in the 8 TeV VBF (Boosted) category and about ±22% (±11%) in the 7 TeV VBF (Boosted) category, respectively. The dominant systematic uncertainty on the methodology itself arises from the composition of the combined fake background (W+jets, Z+jets, multijet, and $t\bar{t}$ fractions), which is in large parts estimated based on simulated event samples as explained above. The uncertainty is estimated by varying each fractional contribution by ±50%, which affects the effective fake factor by ±3% (±6%) in the 8 TeV VBF (Boosted) category and by ±10% (±15%) in the 7 TeV VBF (Boosted) category. To verify the background estimation procedure, and to detect potential biases originating from the method itself, a closure test is performed using simulated event samples. In this test, anti-τ_{had} objects from the simulated events are used to estimate the number of events from the same simulated event sample in the SR. This procedure allows to assess potential biases due to neglected correlations between the fake factors and observables. The closure test is performed using simulated event samples of $W+$ jets, top and $Z \to \ell\ell$ events. A small discrepancy of the order of ±10% in the Boosted category of the 7 TeV analysis is observed and a systematic uncertainty assigned to cover for a potential systematic effect. This bias originates most likely from to the imperfections of the $\mathbf{E}_T^{\mathrm{miss}}$ correction explained above. In all other analysis categories, no bias is found in any discriminating variable.

5.5.3. Estimation of Background Events with Top Quarks

Approximately 50% of $t\bar{t}$ and single-top events are modelled by the fake factor method explained above. The subset of top events in which the τ_{had} object stems from either a real τ_{had} decay or from a misidentified lepton is modelled using simulated event samples. A control region enriched in such events is used to measure a normalisation correction-factor and to minimise the dependence on theoretical uncertainties of the estimated background yield. As summarised in Table 5.4, the CR is built from

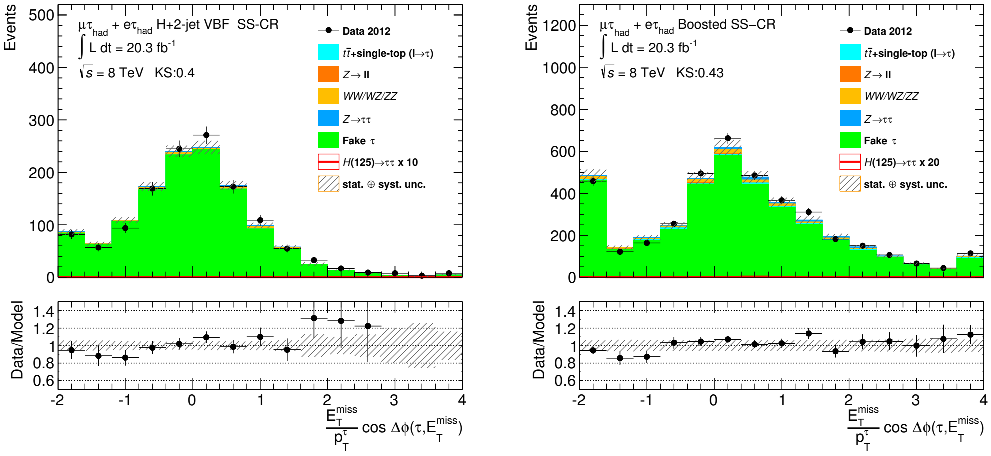

(a) 8 TeV - VBF

(b) 8 TeV - Boosted

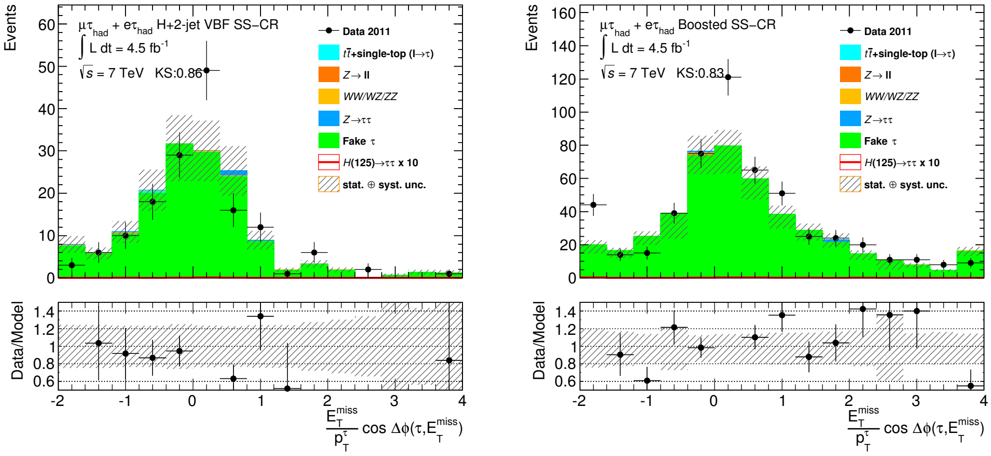

(c) 7 TeV - VBF

(d) 7 TeV - Boosted

Figure 5.13. *Projection of* $\mathbf{E}_T^{\text{miss}}$ *onto the three-momentum of the anti-*τ_{had} *candidate in units of the transverse tau momentum in the SS CR of the VBF (left) and Boosted (right) categories of the 8 TeV (top) and 7 TeV (bottom) analyses.*

the SR selection by reverting the b-jet veto and the m_T requirement. This choice of control region, allows to make use of two statistically independent regions to extract the fake factor ($m_T < 70$ GeV) and the normalisation correction ($m_T > 70$ GeV) for events with real τ_{had} objects.

Naturally, events with real τ_{had} decays contribute as well to the FF CR and are subtracted based on the simulated event samples, assuming no additional normalisation correction. This treatment introduces an ambiguity between the top normalisation correction and the fake factor. A deviation of the correction factor from unity would affect the fake factor in an anti-correlated manner. The impact of this anti-correlation was tested by parametrising the effect of a varying normalisation correction on the combined fake background in the likelihood fit. The impact on both, the top background yield as well as on the final analysis result was found to be negligible.

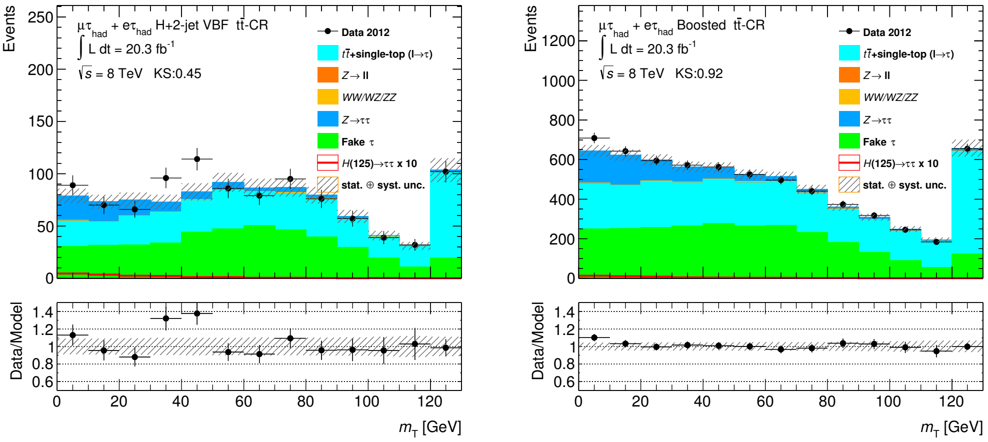

(a) 8 TeV - VBF

(b) 8 TeV - Boosted

Figure 5.14. *Transverse mass distribution in the VBF (a) and Boosted (b) category after requiring the presence of at least one b-tagged jet.*

Figure 5.14 shows the inclusive m_T distribution in the Boosted and VBF categories with inverted b-jet veto. While the low m_T region is dominated by events with misidentified τ_{had}, the high m_T has larger contributions by top events with real τ_{had} decays, motivating the choice of the CR. The prefit estimates of this normalisation correction are listed in Table 5.7.

Two systematic extrapolation uncertainties account for potential biases due to the application of correction factors determined in a CR of slightly different kinematic properties than present in the SR. One uncertainty arises from the b-tagging efficiency calibration and is directly propagated from the corresponding calibration measurements described in Chapter 3.3.3. The dominant b-tagging uncertainties arise from to the light-flavour jet mistag rate in the top-CR, with uncertainties of the order of $\pm(10-15)\%$, and the b-jet veto efficiency in the signal region with

	VBF	Boosted
8 TeV	0.84 ± 0.08	0.96 ± 0.04
7 TeV	1.44 ± 0.36	1.12 ± 0.14

Table 5.7. *Prefit values of the normalisation correction-factors for top events with τ_{had} objects stemming from real τ_{had} decays or misidentified leptons for the VBF and Boosted categories of the 8 TeV and 7 TeV analyses.*

uncertainties of the order of $\pm(8-10)\%$. To account for the different m_T requirement across CR and SR, the extrapolation behaviour was compared between the nominal event samples generated using POWHEG [66, 67] interfaced to PYTHIA [61] and an alternative event sample generated using MC@NLO [65] interfaced to HERWIG [63] for the simulation of the parton shower and hadronisation model. Differences in the extrapolation factor of up to 6% are found and therefore an additional extrapolation uncertainty of ±6% is assigned to the normalisation of the simulated top sample in the SR.

5.5.4. Modelling of Additional Background Processes

Diboson events are modelled using the simulated event samples summarised in Section 5.3.2. As the cross section of diboson processes is small, no corresponding control region can be defined. Instead, systematic uncertainties account for the theoretical cross-section uncertainties and the luminosity measurement of the data sample. Similarly, $Z \to \ell\ell +$ jets events in which a lepton is misidentified as τ_{had} decay, are modelled by simulated event samples. As the kinematic topology of the additional jets in the event is known to be not well reproduced in the simulation, an additional correction is applied to reweight the $\Delta\eta_{jj}$ spectrum of the simulated events to data, based on a control region. This control region is defined by requiring exactly two leptons of same flavour and opposite charge with a mass compatible with the Z-boson mass $|m_{\ell\ell} - m_Z| < 15$ GeV. After the correction, also other kinematic properties like the dijet mass m_{jj} are well described. Comparing the cut efficiency of tight VBF topology selection criteria between data and the background model, a maximum deviation of ±10% is observed and assigned as a systematic uncertainty on the correction.

5.5.5. Comparison of the Combined Background Model to Data

In this section, the full background model as described in the preceding sections is compared to data. Tables 5.8 and 5.9 list the observed and expected event yields in the VBF and Boosted categories of the 7 TeV and 8 TeV analyses, respectively. The uncertainties correspond to the statistical and systematic components. Figures 5.15 and 5.16 show some basic kinematic distributions in the two signal regions and their respective control regions enhanced in $W +$ jets and $Z/\gamma^* \to \tau\tau$ events.

Process	7 TeV VBF category	7 TeV Boosted category
Fake backgrounds	$197 \pm 3^{+51}_{-52}$	$829 \pm 7 \pm 203$
$Z/\gamma^* \to \tau\tau$	$136 \pm 7^{+22}_{-21}$	$1228 \pm 25^{+144}_{-139}$
Top	$10 \pm 1 \pm 2$	$52 \pm 2^{+6}_{-5}$
Diboson	$6.5 \pm 0.4 \pm 1.6$	$40 \pm 1 \pm 5$
$Z \to \ell\ell$	$4.6 \pm 0.7^{+2.2}_{-1.2}$	$30 \pm 3^{+8}_{-7}$
$ggF : H \to \tau\tau$ ($m_H = 125$ GeV)	$1.5 \pm 0.1^{+0.6}_{-0.5}$	$6.4 \pm 0.2^{+2.2}_{-1.8}$
$VBF : H \to \tau\tau$	$3.3 \pm 0.1 \pm 0.4$	$2.1 \pm 0.1 \pm 0.2$
$WH : H \to \tau\tau$	$0.03 \pm 0.01^{+0.41}_{-0.39}$	$1 \pm 0.05 \pm 0.12$
$ZH : H \to \tau\tau$	$0.02 \pm 0.01 \pm 0.01$	$0.50 \pm 0.03^{+0.36}_{-0.05}$
Total background	$354 \pm 8^{+56}_{-56}$	$2180 \pm 26^{+249}_{-246}$
Total signal	$4.9 \pm 0.1^{+0.7}_{-0.6}$	$10.0 \pm 0.2^{+2.2}_{-1.8}$
Data	349	2199

Table 5.8. *Predicted event yields in the 7 TeV VBF and Boosted categories compared to the observed events in data. The uncertainties correspond to the statistical and systematic uncertainties, respectively. The expected background events are estimated based on the methods described above using the prefit estimates of normalisation corrections and other parameters.*

Good agreement is observed in all categories within the uncertainties. The fake background accounts for about 60% of the total background in the VBF category and about 43% in the Boosted category of the 8 TeV analysis. In the 7 TeV analysis its fractional contribution is slightly lower and contributes about 55% and 38%, respectively, of the total background yield. While the fake background presents the dominant background in the VBF SR, $Z/\gamma^* \to \tau\tau$ events are the dominant source of background events in the Boosted category.

As can be seen, the signal expectation is extremely small compared to the overwhelmingly large background. Therefore, additional background suppression is needed to achieve sensitivity towards a potential signal, and strategies to achieve this are presented in the following section.

5.6. Background Suppression

The categorisation as presented above is not intended to provide sizeable background suppression, but separates phase space areas dominated by VBF and ggF signal processes. In this section, ways to suppress background events are discussed. Firstly, in Section 5.6.1 different discriminating variables against the various background processes are introduced. They can be exploited in several ways. So called cut-based

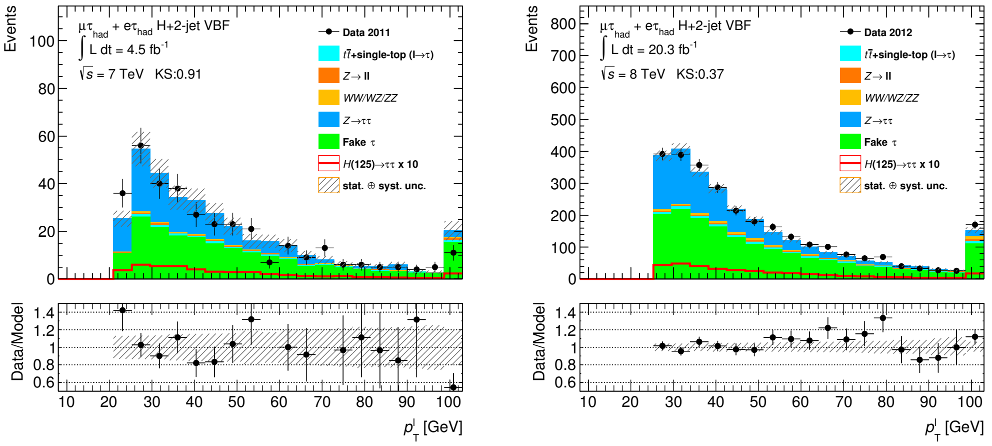

(a) 7 TeV SR - p_T^ℓ

(b) 8 TeV SR - p_T^ℓ

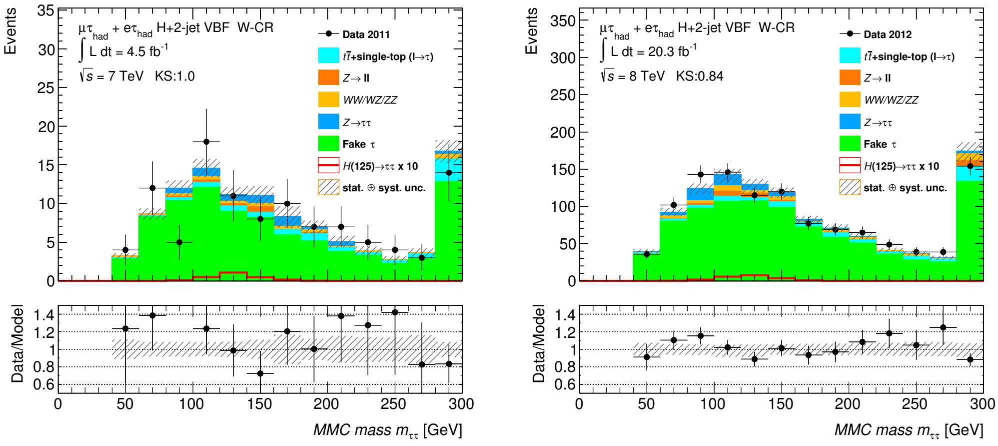

(c) 7 TeV W-CR - $m_{\tau\tau}$

(d) 8 TeV W-CR - $m_{\tau\tau}$

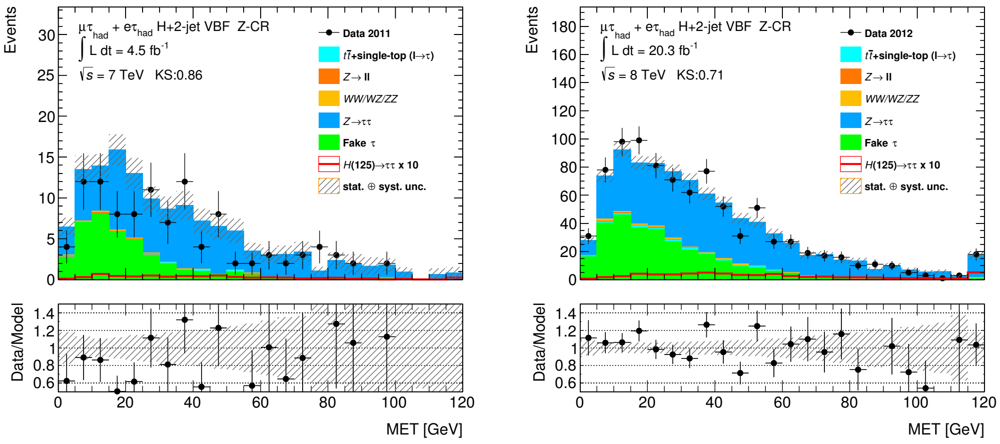

(e) 7 TeV Z-CR - E_T^{miss}

(f) 8 TeV Z-CR - E_T^{miss}

Figure 5.15. *Distribution of p_T^ℓ in the SR (a, b), $m_{\tau\tau}$ in the $W+$ jets control region (c, d) and E_T^{miss} in the Z enriched control region (e, f) of the 7 TeV (left) and 8 TeV (right) VBF categories. The observed data is compared to the background expectation. The hatched band corresponds to the statistical and systematic uncertainty of the background estimate. The last bin includes the event yields beyond the displayed range.*

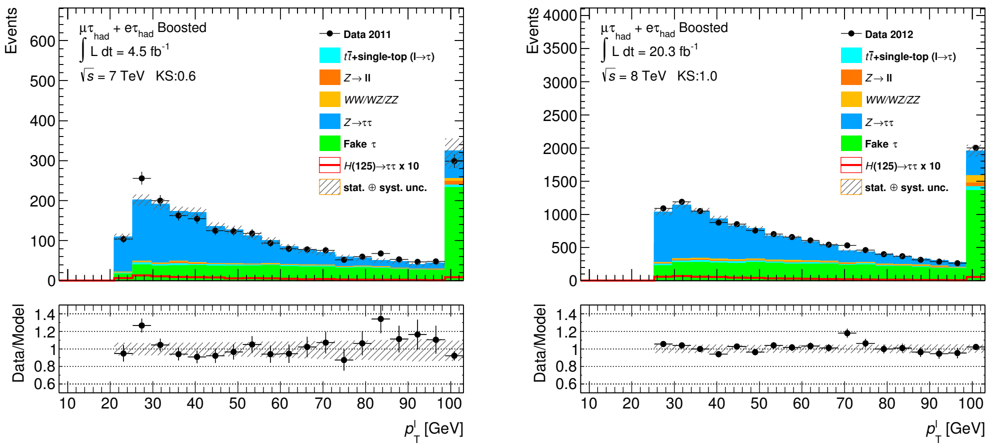

(a) 7 TeV SR - p_{T}^{ℓ} (b) 8 TeV SR - p_{T}^{ℓ}

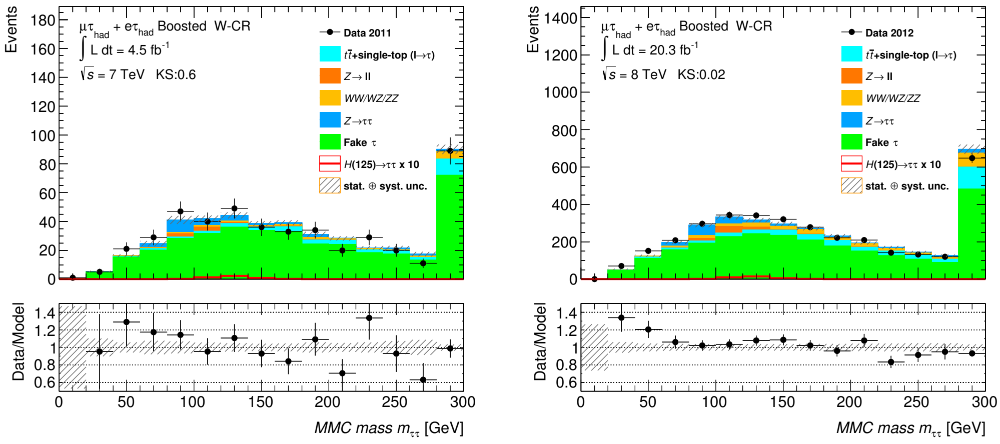

(c) 7 TeV W-CR - $m_{\tau\tau}$ (d) 8 TeV W-CR - $m_{\tau\tau}$

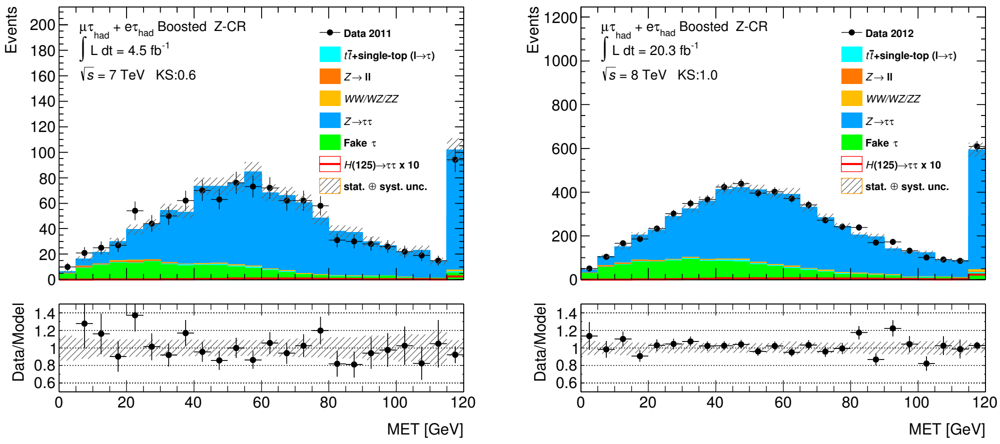

(e) 7 TeV Z-CR - E_T^{miss} (f) 8 TeV Z-CR - E_T^{miss}

Figure 5.16. *Distribution of p_{T}^{ℓ} in the SR (a, b), $m_{\tau\tau}$ in the $W+$ jets control region (c, d) and E_T^{miss} in the Z enriched control region (e, f) of the 7 TeV (left) and 8 TeV (right) Boosted categories. The observed data is compared to the background expectation. The hatched band corresponds to the statistical and systematic uncertainty of the background estimate. The last bin includes the event yields beyond the displayed range.*

Process	8 TeV VBF category	8 TeV Boosted category
Fake backgrounds	$1637 \pm 13 \pm 72$	$5425 \pm 26^{+337}_{-335}$
$Z/\gamma^* \to \tau\tau$	$900 \pm 17^{+62}_{-59}$	$6323 \pm 57^{+282}_{-281}$
Top	$85 \pm 5^{+11}_{-12}$	$398 \pm 11^{+50}_{-48}$
Diboson	$64 \pm 5 \pm 13$	$421 \pm 12 \pm 48$
$Z \to \ell\ell$	$56 \pm 3^{+30}_{-27}$	$213 \pm 11^{+59}_{-60}$
$ggF : H \to \tau\tau$ ($m_H = 125$ GeV)	$12 \pm 1 \pm 4$	$40 \pm 1^{+13}_{-11}$
$VBF : H \to \tau\tau$	$22 \pm 0.2^{+2}_{-3}$	$11.0 \pm 0.1 \pm 1.1$
$WH : H \to \tau\tau$	$0.36 \pm 0.02^{+0.30}_{-0.08}$	$6.5 \pm 0.1 \pm 0.7$
$ZH : H \to \tau\tau$	$0.11 \pm 0.01^{+0.12}_{-0.02}$	$3.2 \pm 0.1 \pm 0.3$
Total background	$2740 \pm 23^{+101}_{-98}$	$12779 \pm 65^{+448}_{-446}$
Total signal	$34 \pm 1^{+5}_{-4}$	$61 \pm 1^{+13}_{-11}$
Data	2830	12952

Table 5.9. *Predicted event yields in the 8 TeV VBF and Boosted categories compared to the observed events in data. The uncertainties correspond to the statistical and systematic uncertainties, respectively. The expected background events are estimated based on the methods described above using the prefit estimates of normalisation corrections and other parameters.*

selection criteria are summarised in Section 5.6.2, while a multivariate approach based on BDTs is detailed in Sections 5.6.3 and following.

5.6.1. Discriminating Variables

To distinguish between signal events and events with misidentified τ_{had} objects it is useful to reconstruct main features of resonant ditau final states. As such, the opening angle between the visible tau decay products in the $\eta - \phi$ plane ΔR, the ditau mass $m_{\tau\tau}$, estimated using the MMC algorithm, and the $\mathbf{E}_T^{\text{miss}}$ orientation with respect to the visible tau decay products in the $x - y$ plane, $\mathbf{E}_T^{\text{miss}}$ *centrality*, are used. The $\mathbf{E}_T^{\text{miss}}$ centrality expresses, in a continuous manner, how central the $\mathbf{E}_T^{\text{miss}}$ vector is oriented between the lepton and the τ_{had} object. It is defined as:

$$E_T^{\text{miss}} \text{ centrality} \quad = \quad \frac{A+B}{\sqrt{A^2+B^2}} \tag{5.13}$$

where

$$A \;=\frac{\sin\left(\phi_{E_T^{\text{miss}}} - \phi_{\tau_{\text{had}}}\right)}{\sin\left(\phi_{\ell} - \phi_{\tau_{\text{had}}}\right)}, \qquad B \;= \frac{\sin\left(\phi_{\ell} - \phi_{E_T^{\text{miss}}}\right)}{\sin\left(\phi_{\ell} - \phi_{\tau_{\text{had}}}\right)} \tag{5.14}$$

It will take the value $\sqrt{2}$ if $\mathbf{E}_T^{\text{miss}}$ is perfectly central between the lepton and the τ_{had} object, and $-\sqrt{2}$ if it is directly opposite to this position. While ΔR and $\mathbf{E}_T^{\text{miss}}$

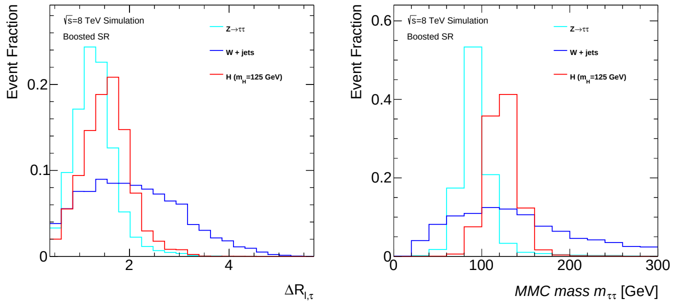

(a) ΔR (b) $m_{\tau\tau}$

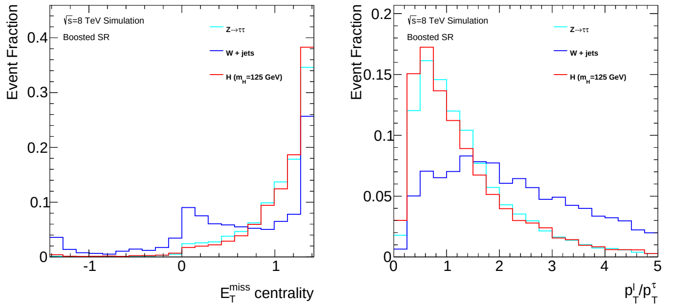

(c) $\mathbf{E}_T^{\mathrm{miss}}$ centrality (d) $p_T^{\ell}/p_T^{\tau_{\mathrm{had}}}$

Figure 5.17. *Kinematic distributions of discriminating variables, describing key features of ditau final states, for signal and* $Z/\gamma^* \to \tau\tau$ *and fake background events.*

centrality provide good separation against fake backgrounds, the ditau mass is also a powerful quantity to suppress $Z/\gamma^* \to \tau\tau$ events. A specific feature of $\tau_{\mathrm{lep}}\tau_{\mathrm{had}}$ decays is the difference in the p_T spectra of the visible tau decay products, due to the different number of neutrinos in leptonic and hadronic tau decays. On average, the visible hadronic tau decay products carry more momentum than the leptonic ones. An asymmetry which is absent in events with misidentified τ_{had} objects. The ratio between the transverse momenta of the lepton and the τ_{had} can therefore be exploited to suppress fake backgrounds. Figure 5.17 shows the distributions of these observables in the signal region of the Boosted category and compares them between signal, $Z/\gamma^* \to \tau\tau$ and $W+$ jets events.

As discussed in Section 5.1, to separate $Z/\gamma^* \to \tau\tau$ from $H \to \tau\tau$ events, two features are used. The mass difference between the Z and H boson offers a direct assessment, while the topology of additional jets in the events offers an indirect way to suppress $Z/\gamma^* \to \tau\tau$ events. While in the Boosted category, the main feature of the different jet topology is already exploited by the p_T^H selection cut, the two jets present in VBF-like events can be used to construct various observables. All of these rely on the same basic properties of the two jets in VBF events. The jets are well separated, of high momentum, and as no colour charge is exchanged in the VBF process, additional hadronic activity in the event is expected to be small. The following observables are used to describe these specific features:

- m_{jj}: The invariant dijet mass. Combining information about the momentum of the jets with their angular separation. The signal process provides a much harder m_{jj} distribution than present in both $Z/\gamma^* \to \tau\tau$ and fake background events.
- $\Delta\eta_{j_1 j_2}$: The pseudorapidity separation between the two jets, which is also used to define the VBF category.
- $\eta_{j_1} \cdot \eta_{j_2}$: The product of the pseudorapidities of the two jets, providing another measure of their separation. The signal process features a long tail into large negative values, indicating well separated jets in the two opposite hemispheres.
- ℓ–η centrality: A measure of the orientation of the lepton in the pseudorapidity plane with respect to the two jets. In the majority of VBF signal events, the lepton is located inside the angle spanned by the two jets. A feature, much less distinguished in $Z/\gamma^* \to \tau\tau$ or fake background events. The ℓ–η centrality is computed as:

  $$\ell\ \eta \text{ centrality} \quad = \exp\left[\tfrac{-4}{(\eta_{j_1}-\eta_{j_2})^2}\left(\eta_\ell - \tfrac{\eta_{j_1}+\eta_{j_2}}{2}\right)^2\right] \tag{5.15}$$

  It takes a value of 1 if the lepton is central between the two jets and smaller than $1/e$ if located outside the range spanned by the two jets.
- p_T^{tot}: The vectorial sum of the visible tau decay products, the $\mathbf{E}_T^{\text{miss}}$ and the two jets. As no additional radiation is present in most VBF events, this variable serves as a measure of additional activity in the event. In the limit of no additional final state objects, p_T^{tot} vanishes.

Figure 5.18 shows the corresponding distributions for signal and background events in the VBF signal region. The signal distribution includes contributions from all signal processes.

Two more variables are used in the following Sections. The transverse mass m_T, between the lepton and $\mathbf{E}_T^{\text{miss}}$, as defined and discussed in Section 5.1, provides excellent discrimination against $W+$ jets events. In addition, a measure of the total activity in the event is useful to quantify for example additional initial or final state radiation. The scalar sum of the transverse momenta of the lepton, the τ_{had} object and the jets in the event is denoted as $\sum p_T$. The distribution of m_T and $\sum p_T$ are shown for signal and background processes in Fig. 5.19.

In general, correlations are present between all variables described here. For example, the opening angle ΔR is strongly correlated with the momentum of the ditau system. A feature which can be further exploited by either placing p_T^H depended selection criteria on ΔR, or indirectly, in multivariate analysis approaches. If signal and background processes show different correlation properties across discriminating variables this offers additional discriminating power in the combination of these variables. Figure 5.20 shows the linear correlation coefficients between selected variables, evaluated in a sample of background (a) and signal events (b). As expected, the ditau mass shows a strong correlation with ΔR. The size of the correlation

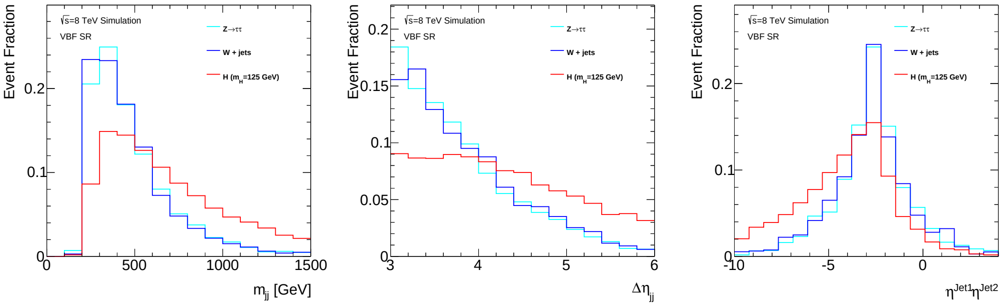

(a) $m_{j_1,j-2}$ (b) $\Delta\eta_{j_1,j_2}$ (c) $\eta_{j_1} \cdot \eta_{j_2}$

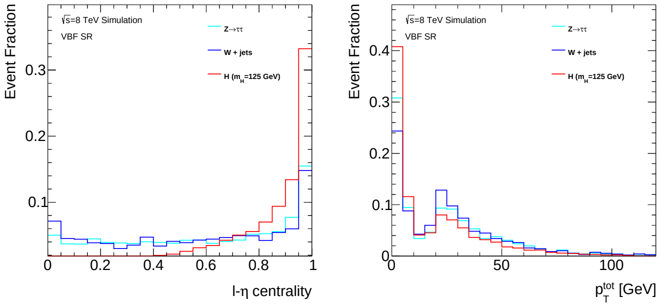

(d) ℓ–η centrality (e) p_T^{tot}

Figure 5.18. *Kinematic distributions of discriminating variables, describing key features of the VBF topology, for signal and $Z/\gamma^* \rightarrow \tau\tau$ and fake background events.*

though, differs significantly between background and signal events. This different correlation pattern can be exploited to achieve a greater background suppression while keeping the signal acceptance constant. In analyses based on plain selection cuts, this can be achieved by splitting the phase space further into e.g. low and high mass events and applying distinct ΔR cuts in such subcategories. Figure 5.20 (c) shows the difference between the linear correlation coefficients between background and signal events, but also between fake backgrounds and signal as well as between $Z/\gamma^* \rightarrow \tau\tau$ and signal events. The largest differences are present between events with fake τ_{had} objects and signal events.

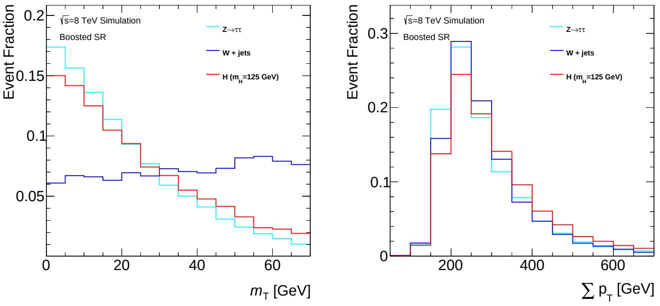

(a) m_T (b) $\sum p_T$

Figure 5.19. *Kinematic distributions of discriminating variables for signal and* $Z/\gamma^* \to \tau\tau$ *and fake background events.*

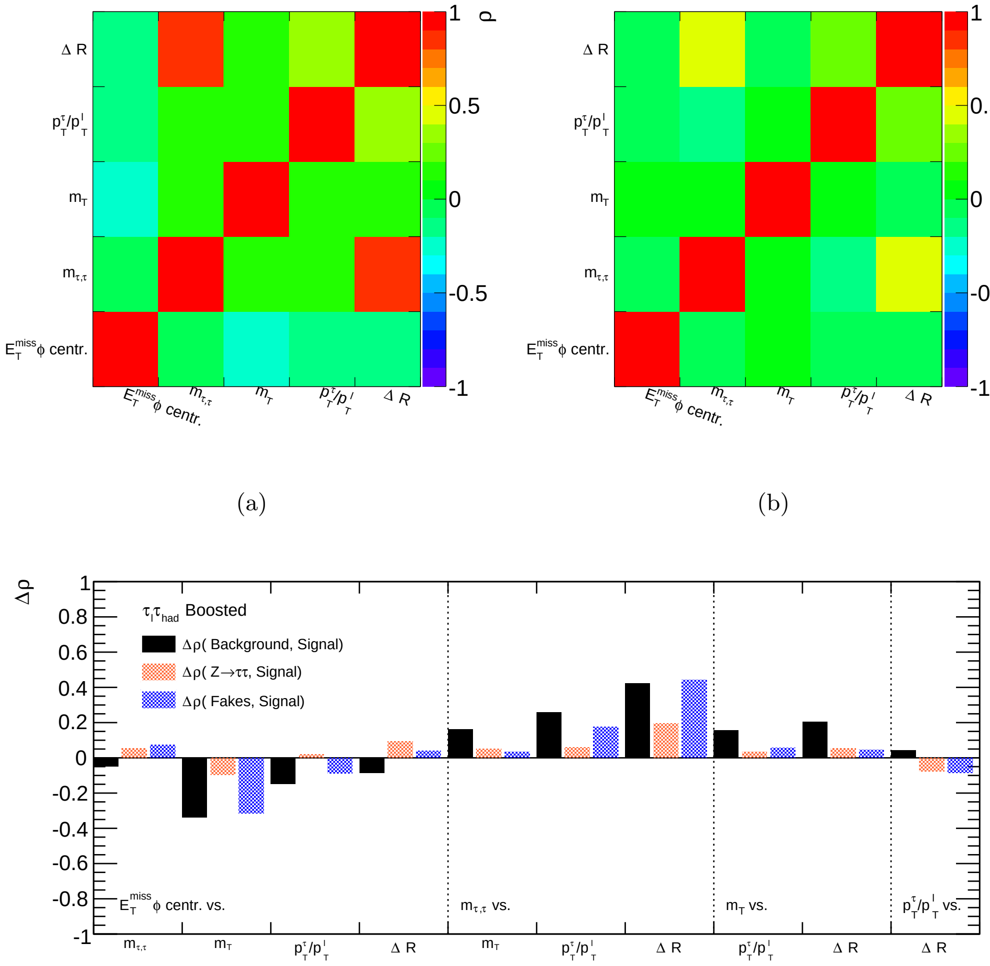

(a)

(b)

(c)

Figure 5.20. *Linear correlation coefficients between discriminating variables evaluated in a representative sample of background events (a) and a signal event sample (b). Figure (c) shows the difference between the linear correlation coefficients in background and signal events.*

5.6.2. Background Suppression using Selection Cuts

To suppress background events, subsequent selection criteria based on discriminating variables can be defined in different analysis categories. Such a chain of selection cuts leads to signal enriched event classes, so that the signal contribution can be estimated by comparing the observed event yield to the background expectation. Additional sensitivity can be achieved by exploiting the differential distribution of a discriminating variable in the fit used to extract the signal. In $H \to \tau\tau$ searches, often the reconstructed ditau mass is used for this purpose. ATLAS published a first result on the search for $H \to \tau\tau$ decays in 2012, based on the 7 TeV dataset [195]. In total, seven analysis categories were used. One VBF category, one 1-jet category and two 0-jet categories for events with low and high E_T^{miss}. The 1- and 0-jet categories were further split into an electron and muon category. To suppress background events, only a small set of selection criteria were applied. Events with $m_T > 30$ GeV were discarded and in categories with jets, $E_T^{\text{miss}} > 20$ GeV was required. Especially no information about the angular orientation of $\mathbf{E}_T^{\text{miss}}$ was exploited. The VBF categorisation was based on the kinematic properties of the two highest p_T jets in the events, which were required to fulfil $\Delta\eta_{jj} > 3$, $m_{jj} > 300$ GeV and $\eta_{j_1} \cdot \eta_{j_1} < 0$. In all categories, a fit to the $m_{\tau\tau}$ spectrum of events passing all selection criteria was used to estimate the signal contribution. In the $\tau_{\text{lep}}\tau_{\text{had}}$ channel an upper limit on the signal strength modifier $\mu = \sigma/\sigma_{SM}$ of about 6 at a Higgs boson mass hypothesis of $m_H = 125$GeV was set at 95% confidence level (CL). Combining all $H \to \tau\tau$ decay channels, an upper limit on μ of about 4 was set at the same mass hypothesis.

This analysis was used as a baseline, to re-optimise the selection criteria and to review the categorisation strategy towards the first ATLAS results [194] using a preliminary sample of 8 TeV data, corresponding to 13 fb^{-1}. Within the course of this thesis, a Boosted category was introduced in order to exploit the harder Higgs boson p_T spectrum with respect to the $Z/\gamma^* \to \tau\tau$ background and the improved mass resolution in boosted event topologies. Furthermore, the selection criteria in the VBF category were tightened significantly. In order to cope with the low event yields in the VBF category of this re-analysis, the fake factor background estimation was established. Besides the VBF and Boosted categories, a 1-jet and a 0-jet category were included, selecting events failing both, the VBF and Boosted topology cuts. In these rest categories, the $e\tau_{\text{had}}$ and $\mu\tau_{\text{had}}$ final states were considered separately. The analysis introduced many discriminating variables also exploited in the multivariate analysis presented in this thesis. It further exploited the correlation between $\mathbf{p}_T^{\tau_{\text{had}}\ell} = \mathbf{p}_T^{\tau_{\text{had}}} + \mathbf{p}_T^{\ell}$ and ΔR, by parametrising the mean ΔR in signal events as a function of $p_T^{\tau_{\text{had}}\ell}$. This parametrisation is used to define a variable denoted as $\Delta(\Delta R)(p_T^{\tau_{\text{had}}\ell})$. It corresponds to the deviation of ΔR from it's expected value, under the signal process assumption, and the value of $p_T^{\tau_{\text{had}}\ell}$ in the event. Another variable used in this analysis is $\sum \Delta\phi = |\phi_\ell - \phi_{E_{\text{T}}^{\text{miss}}}| + |\phi_\tau - \phi_{E_{\text{T}}^{\text{miss}}}|$, the sum of the angular separation in the transverse plane between the missing transverse energy and the visible tau decay products. A variable closely related to the $\mathbf{E}_T^{\text{miss}}$ centrality discussed above. Table 5.10 lists all selection criteria in the $\tau_{\text{lep}}\tau_{\text{had}}$

VBF Category	Boosted Category	1 Jet Category	0 Jet Category
≥ 2 jets		≥ 1 jet	0 jets
$E_{\text{T}}^{\text{miss}}$ >20 GeV	$E_{\text{T}}^{\text{miss}}$ >20 GeV	$E_{\text{T}}^{\text{miss}}$ >20 GeV	$E_{\text{T}}^{\text{miss}}$ >20 GeV
$p_{\text{T}}^{\tau_{\text{had}}}$ >30 GeV	$p_{\text{T}}^{\text{H}} > 100$ GeV		
$p_{\text{T}}^{j1}, p_{\text{T}}^{j2} > 40$ GeV	$0 < x_{\ell} < 1$		
$\Delta\eta_{jj} > 3.0$	$0.2 < x_{\tau_{\text{had}}} < 1.2$		
$m_{jj} > 500$ GeV	Fails VBF	Fails VBF	
centrality req.		Fails Boosted	Fails Boosted
$\eta_{j1} \times \eta_{j2} < 0$			
$p_{\text{T}}^{\text{tot}} < 40$ GeV			
• m_T <50 GeV	• m_T <50 GeV	• m_T <50 GeV	• m_T <30 GeV
• $\Delta(\Delta R) < 0.8$	• $\Delta(\Delta R) < 0.8$	• $\Delta(\Delta R) < 0.6$	• $\Delta(\Delta R) < 0.5$
• $\sum \Delta\phi < 3.5$	• $\sum \Delta\phi < 1.6$	• $\sum \Delta\phi < 3.5$	• $\sum \Delta\phi < 3.5$
			• $p_{\text{T}}^{\ell} - p_{\text{T}}^{\tau} < 0$

Table 5.10. *Event requirements applied in the categories of the re-analysis of the 7 TeV dataset in the $H \to \tau_{\text{lep}}\tau_{\text{had}}$ channel. The first set of selection criteria are used for categorisation, events failing such criteria are reconsidered in the other categories. Requirements marked with a bullet (•) are only applied to events passing all other requirements of a category, and events failing such cuts are discarded [194].*

channel of this re-analysis of the 7 TeV data. The selection thresholds used are the result of a dedicated optimisation procedure, based on the expected upper limit on the signal strength modifier using statistical uncertainties only. Beside the sheer analysis sensitivity, considerations about the robustness with respect to certain systematic effects are taken into account, as for example systematic uncertainties on the differential Higgs production cross-section as a function of p_T^H. Figure 5.21 shows the $m_{\tau\tau}$ spectrum in the VBF and Boosted categories of the 7 TeV analysis. The sensitivity of the combined 7 TeV and 8 TeV $H \to \tau_{\text{lep}}\tau_{\text{had}}$ analysis is best expressed in the expected upper limit on μ of 1.72 at 95% CL and $m_H = 125$ GeV. For the 7 TeV analysis alone, a limit of 3.12 was expected. This presents a significant improvement of over 40% with respect to the first analysis on the same dataset, where a limit on μ of about 6 was expected. Combining the results of all $H \to \tau\tau$ final states and the 7 TeV and 8 TeV datasets, an expected upper limit on μ of 1.2 was achieved, while a limit of 1.9 was observed, both at a Higgs boson mass hypothesis of $m_H = 125$ GeV. This corresponds to an expected significance of 1.7 standard deviations (σ).

Projecting this intermediate result to the complete available dataset at 8 TeV, corresponding to a integrated luminosity of 20.3 fb^{-1}, taking into account no additional improvements of either the analysis, nor the precision of systematic uncertainties, yields an expected discovery significance of about 2.1σ. This presents a strong moti-

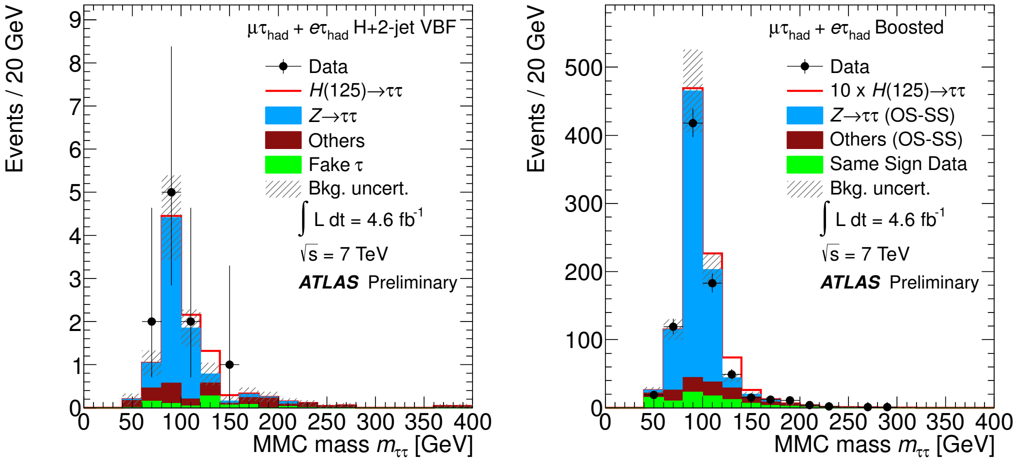

(a) (b)

Figure 5.21. *Distribution of the reconstructed ditau mass in the VBF (a) and Boosted category (b) of the re-analysis of the 7 TeV dataset in the* $\tau_{\mathrm{lep}}\tau_{\mathrm{had}}$ *final state.*

vation to study more sophisticated analysis techniques, like the BDT based analysis presented in the next sections, to allow for a 3σ evidence of $H \to \tau\tau$ decays using the Run 1 data sample of the LHC. Nevertheless, improvements to the cut-based analysis were made which slightly enhanced its sensitivity. As selection cuts do not exploit different correlation pattern between signal and background events, the sensitivity of the cut-based analysis can be improved by further categorising the signal regions, in order to allow for separately optimised selection criteria in the different phase space areas. Following this idea, the improved cut-based analysis features a Boosted category, as well as one tight and one loose VBF category. The tight VBF categorisation applies an additional requirement of $p_T^H > 100$ GeV on top of the VBF selection criteria. The loose VBF category applies a slightly less stringent cut on m_{jj}, which is required to exceed 300 GeV instead of 500 GeV. This allows to extend the signal acceptance for VBF events, while ensuring a high signal-to-background ratio in the tight VBF category. All other selection criteria and the definition of the Boosted category still follow closely the re-analysis discussed above. This results into an expected discovery significance of 1.7σ. Combining it with the improved cut-based analyses in the other final states which followed a similar strategy of further subdividing the categories, a discovery significance of 2.5σ is expected.

5.6.3. Background Suppression using Boosted Decision Trees

Background suppression based on a set of discriminating variables is a problem usually denoted as *classification problem*. A *classifier* is a function $F(\mathbf{x}) = \hat{y}$, mapping the input variables $\mathbf{x}$ on an estimate $\hat{y}$ of the true category y. In the context of background suppression, the target categories are of a binary form, either an event is classified to be signal like or background like. In contrast to this, in *regression* problems one tries to estimate the value of a continuous variable based on the input variable set. The cut-based analysis approach, as discussed above, implements such a classifier in terms of selection criteria. Events passing all criteria can be interpreted as being classified as signal like. The classifier is usually optimised, also referred to as *trained*, on a given set of *training events* for which the true categories are known. It is then used to predict the category of *testing events* whose true categories are unknown. In general, the dimension of the input variable space, usually denoted as *feature space*, is large and the correlation patterns across the various input variables complicated. The construction of powerful classifiers is therefore a complex problem and statistical methods can be used to exploit feature spaces of high dimensionality and those exhibiting strong correlations. The field of statistical learning in computer science studies such methods. A variety of algorithms targeting classification problems exist. Reference [197] offers a detailed introduction into this interesting topic. In the context of this thesis, boosted decision trees (BDT), as implemented in the *Toolkit for MultiVariate Data Analysis* (TMVA) package [198], are used to define a classifier which is deployed in the $H \to \tau_{\text{lep}}\tau_{\text{had}}$ analysis. This section briefly introduces the general idea and concepts of BDTs. The actual training procedure of the BDTs used in the analysis is then summarised in Section 5.6.4.

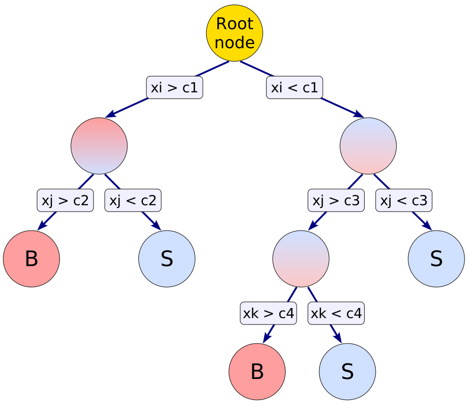

Figure 5.22. *General structure of a single decision tree. Subsequent node splittings classify each event into a background or signal-like leaf node. Figure taken from Ref. [198].*

A cut-based analysis involving categories as discussed above can be regarded as a *decision tree*. They implement a subsequent series of binary splits, based on the input variables, ending up in a series of *leaf nodes*, labelled as being signal or background like depending on the fractional contribution of the two categories. Figure 5.22 shows a schematic view of such a decision tree. The actual numerical values used to define the splits, and the variable being exploited at each step, can be optimised once a metric defining the separation power is specified. A typical choice is the so-called *Gini Index* defined by $G = p \cdot (1 - p)$, where p is the signal purity in a given node. Each splitting can then be optimised by choosing the variable and corresponding cut value which yields the largest increase of the Gini index when comparing the index value of the parent node to the sum of the index values of the two resulting daughter nodes weighted by their relative event fractions. The resulting decision tree features a given depth, which describes the maximum number of subsequent splits, and each leaf features a leaf size, describing the number of training events ending up in the leaf node. In principle, a decision tree could grow to such high depths, that each leaf node contains exactly one training event. Such a tree would offer perfect signal purity on the training event sample, but the performance on an independent testing set would be drastically worse. Such cases, in which statistical fluctuations of the training sample are exploited to define the classifier, are usually denoted as *overtraining*. To avoid biases in such situations, every event used to train a classifier in this thesis is discarded afterwards and never used to either evaluate the performance of the classifier, nor in any background estimation in later analysis steps. To prevent overtraining to occur, the decision tree is usually only grown until specific criteria are met. Two commonly used criteria are restrictions on the maximum tree depth and the minimum leaf size. The maximum tree depth also controls the dimension of variable correlations which can be exploited. While single node trees can only assess one variable at a time, each node splitting opens the possibility to exploit a certain correlation feature. For this reason, usually higher level input variables, like an invariant mass, yield better performance compared to large sets of low level variables, like the combined set of particle four-momenta. Given the two stopping criteria defined above, the number of training events directly impacts whether a tree is allowed to grow to its full complexity or whether the construction is aborted before the maximum depth is reached. Therefore, the size of the training sample impacts the BDT performance crucially.

Such decision trees are rather weak classifiers. Their performance can be significantly enhanced by combining them with a series of additional trees. The general concept is based on training each tree on a slightly reweighted training sample, allowing the set of trees to focus on different aspects of the feature space. This procedure is denoted as *boosting*. One prominent boosting algorithm is *AdaBoost* [199], which is based on simply increasing the relative weights of events which were misclassified in the previous tree. Following this approach, in each tree-training iteration the focus is shifted towards events which were hard to classify in previous iterations. The final classification result is then no longer a binary information, but instead a function of the response of the individual trees, which is denoted as *classification output*.

The BDTs for this analysis were trained using a slightly different boosting algorithm, known as *Gradient Boosting* [200]. The training procedure is a minimisation problem in which the *loss function*, quantifying the quality of the classifier, should be minimised. AdaBoost makes use of an exponential loss function $L(F, y) = \exp\{F(\mathbf{x})y\}$, where y denotes the true category value of the event with input variables $\mathbf{x}$. Gradient Boosting tries to minimise a slightly different loss function defined by $L(F, y) = \ln(1 + \exp\{-2F(\mathbf{x})y\})$. To achieve this, the gradient of this loss function is estimated and the classifier built by subsequently following the steepest descent towards the minimum and adding corresponding terms to the classifier. The final classifier is a linear combination of all iteration steps

$$f(\mathbf{x}) = \sum_{a=0}^{N} w_a f_a(\mathbf{x}) \tag{5.16}$$

A transformation of the form $S(\mathbf{x}) = (2)/(1 + \exp\{-2f(\mathbf{x})\}) - 1$ finally maps the combined classification function on a score value within the range $(-1, 1)$.

Complications arise since the gradient of the loss function with respect to the current classifier is only defined at points in the input variable space for which the true category is known, namely at the training events $(\mathbf{x}, y)$. Since the result must be applicable for arbitrary values of the input variables though, this limitation is overcome by fitting a regression tree to estimate the gradient value for any point in the feature space. To stabilise the result with respect to statistical fluctuations in the training sample, the learning rate during the iterative procedure can be artificially lowered, scaling down the relative weights w_a of each term in 5.16 by a factor β. Requiring a larger number of iterations, this procedure known as *shrinkage* can improve the classification power significantly, especially for scenarios of complex correlation patterns within the feature space.

5.6.4. Boosted Decision Tree Training Procedure and Optimisation

Using boosted decision trees based on gradient boosting, two BDTs are trained for the VBF and Boosted categories of the $H \to \tau_{\mathrm{lep}}\tau_{\mathrm{had}}$ analysis. In this section, the training procedure is described. Given the discovery of a Higgs boson with a measured mass of $m_H \approx 125$ GeV, simulated signal samples with the Higgs boson mass set to $m_H = 125$ GeV are used to train the main BDTs. BDTs for which alternative mass hypotheses were used in the training were studied, but the presentation in the following focuses on the baseline BDTs at $m_H = 125$ GeV.

Input Variables

In general, BDTs can be trained using an arbitrarily large number of input variables. The decision tree training procedure always chooses optimal node splittings. While from this perspective no limitation on the number of input variables is given, experimental considerations suggest to keep the number of input variables at a minimum. With growing dimensionality of the feature space, it becomes increasingly difficult to identify the patterns and aspects of the feature space exploited by the BDTs. To accurately model the BDT output distribution, the background model further needs to describe the correlations between the input variables. With larger input variable sets, this requirement becomes more and more complicated to verify. Therefore, an optimisation on the input variables to be used in the training is performed.

Variable	Definition	Boosted	VBF
$\Delta R_{\tau\ell}$	Separation of the τ and the isolated lepton	•	•
m_T	Transverse mass of $\ell + E_T^{miss}$	•	•
$\mathbf{E}_T^{\mathrm{miss}}\phi$ centrality	See text	•	•
$m_{\tau\tau}$	See text	•	•
$\sum p_T$	Sum of p_T of $\tau + \ell$+jets	•	
$p_T(\tau)/p_T(\ell)$	Ratio of p_T for τ_{had} and ℓ	•	
m_{j_1,j_2}	Invariant mass of the 2 leading jets		•
$\eta_{j1} \times \eta_{j2}$	Product of the ηs of the two leading jets		•
$\lvert\eta_{j2} - \eta_{j1}\rvert$	Absolute difference ηs of the two leading jets		•
ℓ–η centrality	See text		•
p_T^{tot}	$\lvert\mathbf{p}_T^{\ell} + \mathbf{p}_T^{\tau_{\mathrm{had}}} + \mathbf{p}_T^{\mathrm{j1}} + \mathbf{p}_T^{\mathrm{j2}} + \mathbf{E}_T^{\mathrm{miss}}\rvert$		•

Table 5.11. *Discriminating variables used for the BDT training in the two categories.*

The optimisation starts by identifying well suited discriminating variables, where the focus is put on variables describing physically motivated features of signal and background processes. These variables are required to be well modelled and to be either only weakly correlated to other input variables, or to feature well understood correlation patterns which differ between signal and background processes. Based on these prerequisites, a list of variables is created of which various subsets are tested as BDT input variable sets. The relative importance of each input variable can be quantified by determining the number of times each variable is used to define a node splitting. Weighting each occurrence by the squared gain of the Gini-Index and the number of events present in that node, a variable importance ranking is established. Such a ranking can be used to identify variables which do not contribute significantly to the classification power of the BDT. Since the discovery significance is the final measure the analysis aims to optimise, tests are performed which compare the significance between different input variable sets, taking into account statistical uncertainties only. Given that adding additional variables can never degrade the performance of a BDT, personal judgement enters in the definition on a minimal but still powerful set of input variables. These studies result in a list of input variables summarised in Table 5.11. In total, six variables are used in the Boosted category, while nine variables are used in the VBF category. Both sets include the ditau mass. This presents a crucial difference with respect to the cut-based analysis approaches summarised above. There, the selection criteria defined a signal enriched phase space area in which the mass spectrum was used as the final discriminating variable, exploited in a likelihood fit. In contrast to this, the BDT output involves the mass as input variable and is used itself as discriminant variable in the likelihood fit. This procedure is the most simple approach towards an optimal sensitivity at a given Higgs boson mass.

(a) VBF cat.

Variable	Ranking Index
$\lvert\eta_{j2} - \eta_{j1}\rvert$	0.129
$m_{\tau\tau}$	0.120
m_T	0.116
$\mathbf{E}_T^{\text{miss}}\phi$ centrality	0.112
p_T^{tot}	0.112
m_{j_1,j_2}	0.106
$\Delta R_{\tau\ell}$	0.104
ℓ–η centrality	0.103
$\eta_{j1} \times \eta_{j2}$	0.098

(b) Boosted cat.

Variable	Ranking Index
$m_{\tau\tau}$	0.245
$\Delta R_{\tau\ell}$	0.189
$p_T(\tau)/p_T(\ell)$	0.163
$\mathbf{E}_T^{\text{miss}}\phi$ centrality	0.146
m_T	0.138
$\sum p_T$	0.119

Table 5.12. *Importance ranking of the input variables used in the BDT training in the VBF (a) and Boosted category (b).*

Table 5.12 shows the variable importance rankings for the two categories. As expected, the ditau mass is ranked high in both categories. The relative importance though is much larger in the Boosted category, since the topology of the dijet system in the VBF category adds substantial discriminating power against $Z \to \tau\tau$ events. All variables yield very comparable importance scores, indicating that they contribute in a similar way to the classification power. In this sense, the set of variables is minimal, even though the impact of removing single variables from the set on the BDT performance can not be deducted from such importance rankings alone. Figure 5.23 shows the linear correlation coefficients between the input variables and the BDT output for signal and background events in the two categories. While a rather strong linear correlation is present between the BDT output and $m_{\tau\tau}$ for signal events in the Boosted category, this correlation is much weaker in the VBF category, indicating the larger relative importance of the ditau mass in the Boosted category. As discussed previously, different correlations are present for signal and background events, especially between variables describing the resonant ditau system.

Training Samples and Cross-Evaluation

To achieve an optimal performance, the BDT training samples should reflect as accurately as possible the actual signal and background composition in the signal regions. While in principle the full background model as detailed in Section 5.5 could be used for this purpose, the samples used to train the BDTs deviate from this model in some points. As discussed above, the event sample used to train the BDTs should be as large as possible to optimise their classification power. To increase the number of training events, the VBF SR definition is loosened by dropping the

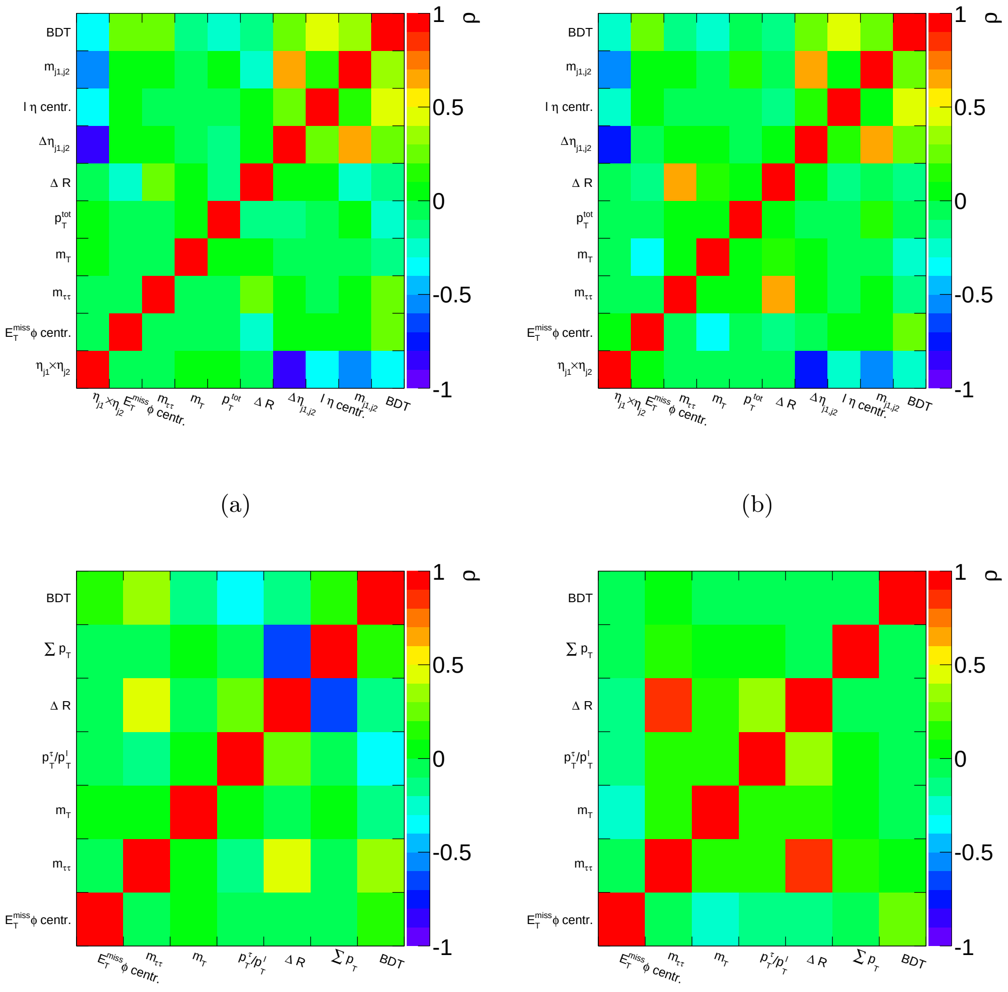

(a) (b)

(c) (d)

Figure 5.23. *Linear correlation coefficients between input variables and the BDT output for signal (a, c) and background (b, d) events, in the VBF (a, b) and Boosted (c, d) category.*

$\Delta\eta_{jj}$ requirement. By doing so, the Boosted and VBF category definitions used for the BDT training are no longer perfectly disjoint. As the training procedure simply defines a prescription to calculate a new variable, the BDT score, this overlap in the training procedure does not harm the statistical analysis. Similarly, the m_T requirements in the Boosted and VBF category definitions are dropped. Since simulated event samples of the $Z/\gamma^* \to \tau\tau$ process employing the VBF filter described in Section 5.3.2, offer a large number of events in the signal sensitive VBF like phase space, these samples are used instead of the embedded $Z \to \tau\tau$ samples in the training procedure. While systematic uncertainties guide the choice of the background model, the number of available events guides the choice of the training samples. Finally, the (OS-SS) background estimation technique, as explained in Section 5.5.2, is used to model events with misidentified τ_{had} objects. Using the Fake Factor approach instead to define the training sample was tested and found to not yield a significantly different performance in terms of the expected discovery significance. To define the add-on terms of the (OS-SS) method, only events with oppositely charged lepton and τ_{had} objects are used and weighted to match the expected add-on term event yield.

One complication in the analysis arises from the limited number of events to construct the background model and the training events. For the reasons mentioned above, every event used in the training procedure is discarded for any further use. Nevertheless, also the background model benefits from larger event counts, since the statistical uncertainties in the signal-sensitive phase space areas are sizeable. A technique denoted as cross-evaluation is used to overcome these concurrent needs. All event samples are split into two classes, denoted **A** and **B**, on a random basis. While event samples **A** are used to train a BDT denoted BDT1, event samples **B** are used to train a BDT denoted as BDT2. As the event samples **A** are statistically independent of the samples **B**, they can be used as independent *test-samples* for BDT2, and vice versa. The final discriminant is then built by simply summing the score distributions of BDT1 and BDT2. Since the splitting to define training samples **A** and **B** is performed randomly, the two BDTs feature the same output shape and score within the statistical uncertainties, and no discrimination power is lost by adding their respective classification scores. In that way, the fully available statistical power can be used to built the final background estimate.

One exception to this scheme is made for the signal samples. As a large amount of simulated signal events, for example about 2 million ggF events at $m_H = 125$ GeV, is available, the training samples **A** and **B** make use of 75% of the available simulated signal events. This leaves $2 \cdot 25\%$ of the simulated signal events to construct the standard model expectation to be used in the statistical interpretation. In the VBF category, only the VBF signal is considered during the training to enhance the VBF process purity in the high BDT output region. All signal processes are considered in the Boosted category though, to optimise the overall sensitivity. Table 5.13 lists the number of events available in the event samples used for the training of a single BDT in the two categories.

Data events are split on a random basis into two samples of equal size which are

Category	VBF	Boosted
Signal ($m_H = 125$ GeV)	53978	39166
Top	8024	3773
$Z \to \ell\ell$	1934	868
Diboson	2376	1388
W+jets	16336	7260
$Z \to \tau\tau$	34588	20728
SS Data	7051	2867
Background Training Events Sum	70309	36884

Table 5.13. *Number of events used for the training of the BDTs in the VBF and Boosted categories. In the VBF category, the signal sample includes only the VBF process, while all production mechanisms are used in the Boosted category.*

then classified by the two BDTs. The final data distribution is again obtained by summing the two individual distributions. It is validated, that swapping the sample-BDT association for data events does not affect the result of the analysis.

BDT Training Parameter Optimisation

The BDT training procedure depends on parameters which control certain aspects in the construction of either single decision trees or the boosting procedure. The three main parameters affecting the classification power of the BDT are the maximum tree depth d_{max}, defining how complex each tree may grow, the shrinkage parameter β, which defines the learning rate in each boosting iteration, and the total number of trees to be grown N. All three parameters depend on each other, as a slower learning rate or shallow trees will in general lead to a preference towards more boosting iteration steps. Besides the maximum tree depth, a second parameter controls the complexity of the tree, the minimum leaf size. As the performance evaluation is solely determined on events, statistically independent from the training sample, the minimum leaf size does not play a crucial role. Instead, it is set to a small value and the tree depth is used to control the tree complexity. Values of 0.1% and 0.17% of the total training sample size were chosen as minimum leaf size in the VBF and Boosted categories, respectively.

To determine a point in this parameter space which offers close to optimal performance, an optimisation is performed based on a measure of the relative separation between the signal and background distributions:

$$S = \frac{\langle s \rangle - \langle b \rangle}{\sqrt{(\sigma_s^{\mathrm{RMS}})^2 + (\sigma_b^{\mathrm{RMS}})^2}} \tag{5.17}$$

where s and b denote the BDT output distributions of the signal and background testing samples, respectively. Other metrics can be used to quantify the separation power of a classifier. A common one is the so-called *Receiver Operating Characteristic* (ROC) curve, which shows the background rejection as a function of the signal efficiency when placing subsequent cuts on the BDT output and integrating the background and signal distributions towards higher score values. As the ROC curve is independent of the actual shape of the BDT output distributions, it is a well defined performance measure also to compare different classification approaches. Integrating the area under the ROC curve offers a single valued metric of the BDT performance. The parameter scans presented below are repeated for such other measures, to ensure that the outcome of the optimisation is independent of a specific choice of the metric.

Scanning a sizeable volume of the three dimensional parameter space is computationally expensive due to the large number of BDTs to train. Instead, a two-dimensional scan in the $d_{\mathrm{max}} - N$ plane, using a shrinkage parameter of 0.2 and 0.3 in the VBF and Boosted categories, is performed. These shrinkage parameters were determined in initial coarser scans. The optimal point in the $d_{\mathrm{max}} - N$ plane is then chosen in order to perform a one-dimensional scan in β, to determine the final set of parameters to be used. Figure 5.24 shows these parameter scans. A strong dependence between N and d_{max} is present, as expected. A similar separation power is achieved for either a small number of deep trees, or a large number of shallow trees. As the BDT behaviour is more stable with respect to statistical fluctuations in the training sample for larger number of boosting iterations, a configuration is chosen featuring a large number of total trees at a medium tree depth. In the VBF category a configuration of $N = 400, d_{\mathrm{max}} = 5$ is chosen, while in the Boosted category $N = 600, d_{\mathrm{max}} = 4$ is used. The remaining separation power dependence on β is small for this parameter settings and shrinkage parameters of $\beta = 0.2$ and $\beta = 0.1$ are used for the VBF and Boosted category BDT training.

BDT Performance

The BDTs are trained solely on $\sqrt{s} = 8$ TeV event samples, offering a significantly larger sample size compared to the respective $\sqrt{s} = 7$ TeV samples. The BDTs obtained from this training step are then directly applied to the 7 TeV samples as well. Figures 5.25 (a,b) show distributions of the BDT discriminants for signal and background models in the two categories of the 8 TeV analysis. Both BDTs provide a powerful separation between signal and background processes. In the distributions of the VBF and ggF processes in the VBF category, the effect of training this BDT on VBF signal samples only manifests itself in the better separation of VBF signal against the background compared to ggF events. This results in a higher VBF process purity in the high score region. Figures 5.25 (c,d) show the corresponding ROC curves of the BDT output distributions. In each category, the ROC curves for the 7 TeV and 8 TeV analyses are compared to each other, showing compatible discriminating power of the BDTs, independent of the event sample they are applied to. This supports the choice of applying the BDTs trained on 8 TeV samples to the 7 TeV analysis as well. The reason for this behaviour is mostly that the background

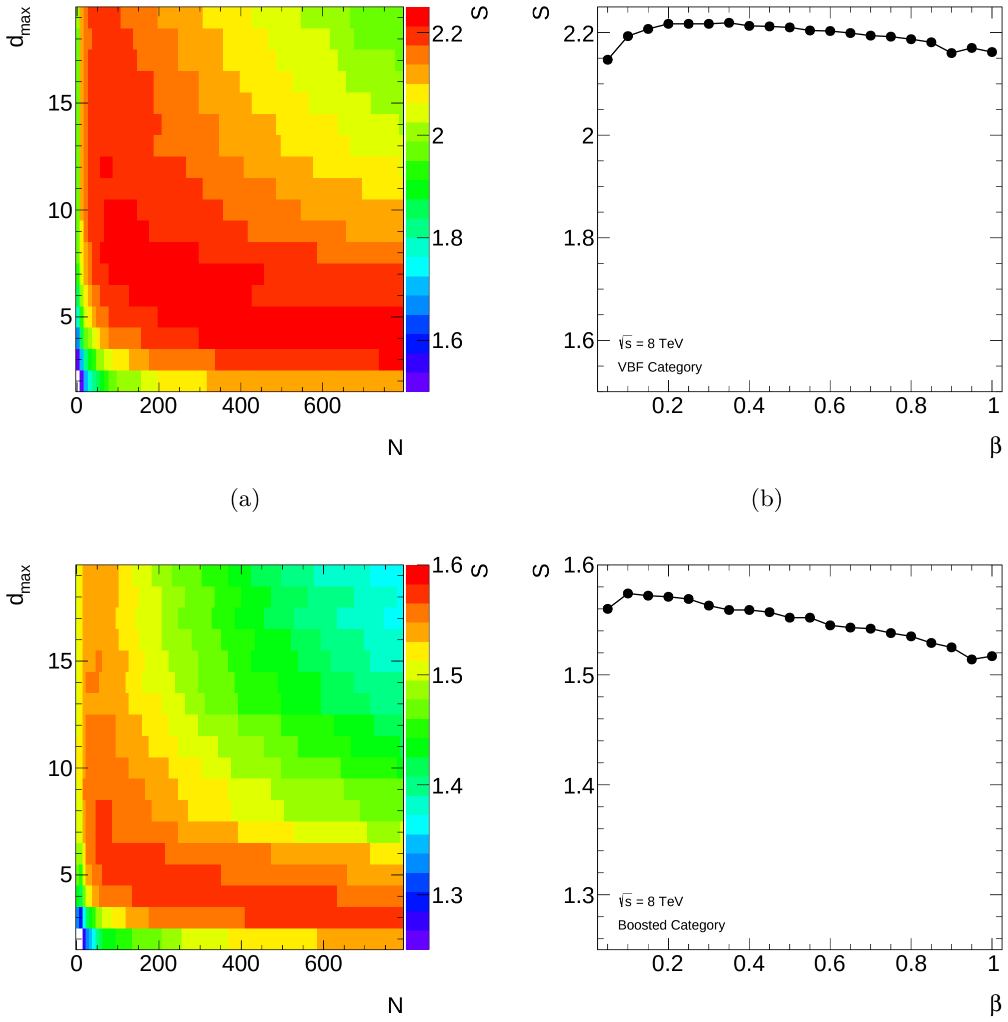

(a) (b)

(c) (d)

Figure 5.24. *BDT training parameter optimisation for the VBF (a, b) and Boosted (c, d) categories. Shown are two-dimensional scans in the* $d_{max} - N$ *plane (a, c) and one-dimensional scans in* β *(b, d), where the other two parameters were fixed to their optimal values from the two-dimensional optimisation.*

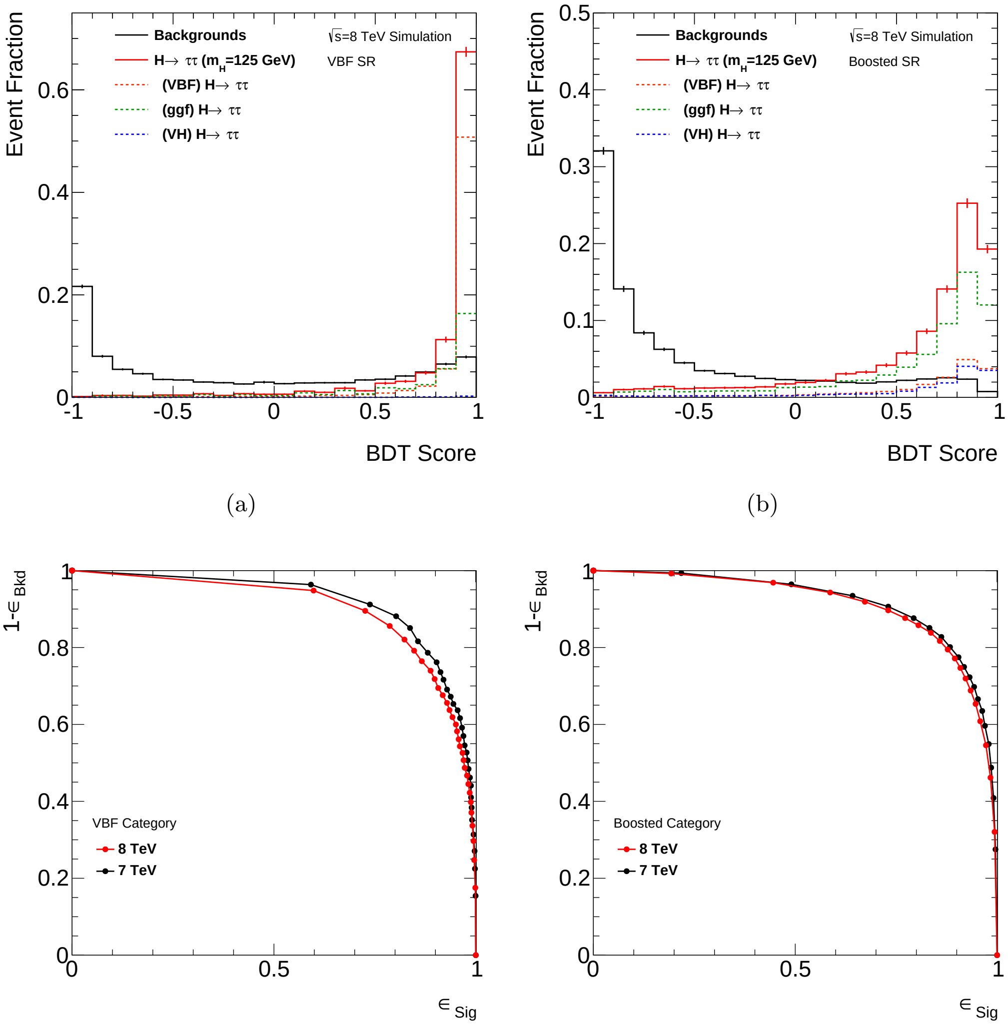

(a) (b)

(c) (d)

Figure 5.25. *Distributions of the BDT output of background and signal events in the VBF (a) and Boosted (b) categories of the 8 TeV analysis, as well as the corresponding ROC curves (c,d) in the 7 TeV and 8 TeV analyses.*

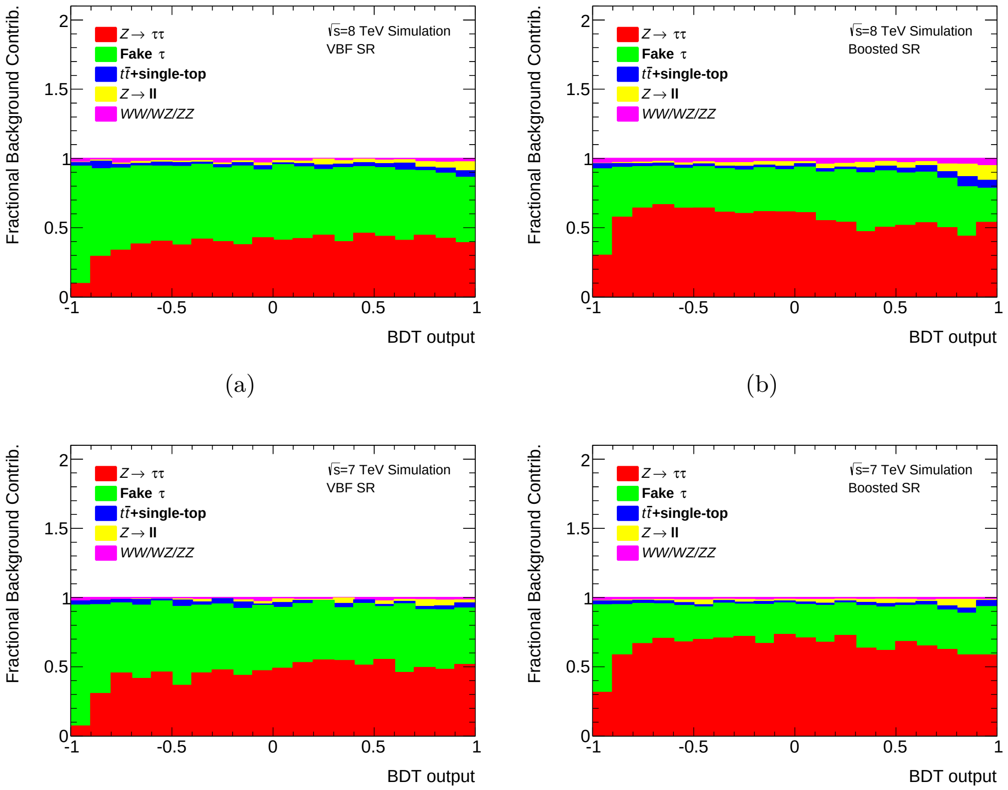

(a) (b)

(c) (d)

Figure 5.26. *Fractional contributions to the total background by different processes, as a function of the BDT output, in the VBF (a, c) and Boosted (b, d) categories of the 7 TeV and 8 TeV analyses.*

composition is relatively independent of the centre-of-mass energy. Figure 5.26 shows the fractional background contributions as a function of the BDT output for the VBF and Boosted categories in the 7 TeV and 8 TeV analyses, respectively. Besides small increases in the contributions from backgrounds with misidentified τ_{had} objects and from top-quark production in 8 TeV, the composition remains roughly unchanged. In general, the backgrounds with misidentified τ_{had} objects are most strongly separated from the signal and dominate the low BDT score region. This also results in a good separation between $Z \to \tau\tau$ and fake events, allowing to determine the $Z \to \tau\tau$ normalisation parameter in the likelihood fit relatively independent of systematic uncertainties on the fake background yield.

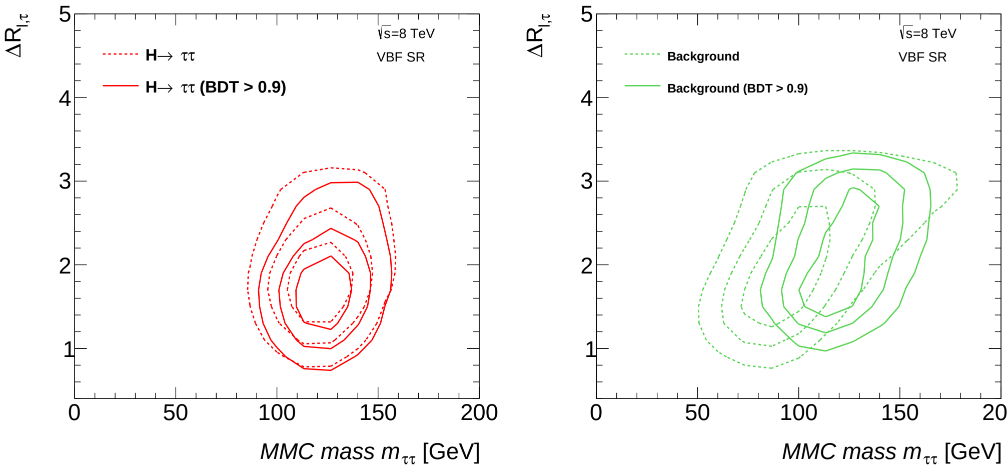

(a) (b)

Figure 5.27. *Contour lines of constant event fractions of signal (a) and background (b) distributions in the* $(\Delta R, m_{\tau\tau})$*-plane in the inclusive (dashed lines) and high BDT score region (solid lines) of the VBF category. The contour lines are placed in equidistant spacing of the normalised event distributions.*

To visualise the phase space region selected by the BDTs, it is instructive to compare signal and background distributions in inclusive and high BDT score regions. Figure 5.27 shows such a comparison in the $\Delta R - m_{\tau\tau}$ plane for the VBF category. The high score region is defined by selecting events with a BDT output greater than 0.9. In the inclusive samples, the different correlation between the two variables in signal and background events is clearly visible. Applying the BDT score requirement, the signal distribution remains nearly unbiased, reflecting the capability of the BDT to single out a highly non-trivial phase-space area. The background distribution for high BDT score values though, gets strongly biased towards the corresponding signal distribution, indicating that the rest of the phase space is strongly suppressed. Studying such two-dimensional distributions allows to gain insight in how variables and correlations are exploited by the BDTs. One of the most important features is the difference in the impact of the ditau mass spectrum between the Boosted and VBF categories. While in the VBF category a rather broad $m_{\tau\tau}$ window is selected in the high score region, a much more stringent selection is present in the high score region of the Boosted category. This is directly connected to the presence of other discriminating variables against the $Z \to \tau\tau$ background in the VBF category, allowing for a looser $m_{\tau\tau}$ selection. This impacts the dependence of the two BDT output distributions on systematic uncertainties of the tau-energy scale as well.

5.6.5. Validation of the Background Model

Before comparing data yields to the background model in the high score region, a careful validation of the background model is performed. This step builds the foundation to rely on the background expectation in signal-sensitive regions. The following validation steps are performed:

- Input variable validation: The differential background model is compared to data for all BDT input variables, in the background process enriched control regions as well as in the SR categories. Since the SR definitions feature only a low signal-to-background ratio, the background model is expected to describe data well.
- Input variable correlation: Since the modelling of correlation is important for a reliable background estimate of the BDT score as discussed above, the correlation patterns between all input variables are compared between the background model and data in the signal regions. To do so, two-dimensional profiles are prepared, showing the mean value and its error of variable y in bins of variable x. By creating such profiles for all variable pairs a complete comparison of the mean values in data and the background model can be performed.
- BDT score validation: The BDT score distributions of the background model are compared to the data in the background enriched control regions. Furthermore the SR BDT score distributions are validated in the low score region, where only a negligible signal contribution is expected. This *blinded* validation ensures that any decision on the analysis strategy is not based on observations made in signal-sensitive regions. The *unblinded* part of the signal region BDT score distribution is defined by the BDT score value, at which 30% of the expected signal event yield is reached when integrating from the low score region.

Since the number of plots is large, only some representative examples are presented in this chapter. The complete set of validation plots is shown in Appendix A instead.

Input Variables

Figure 5.28 shows distributions of the dijet mass and the ℓ–η centrality variables in the signal region and in control regions enriched in fake τ_{had} and $Z \to \tau\tau$ events in

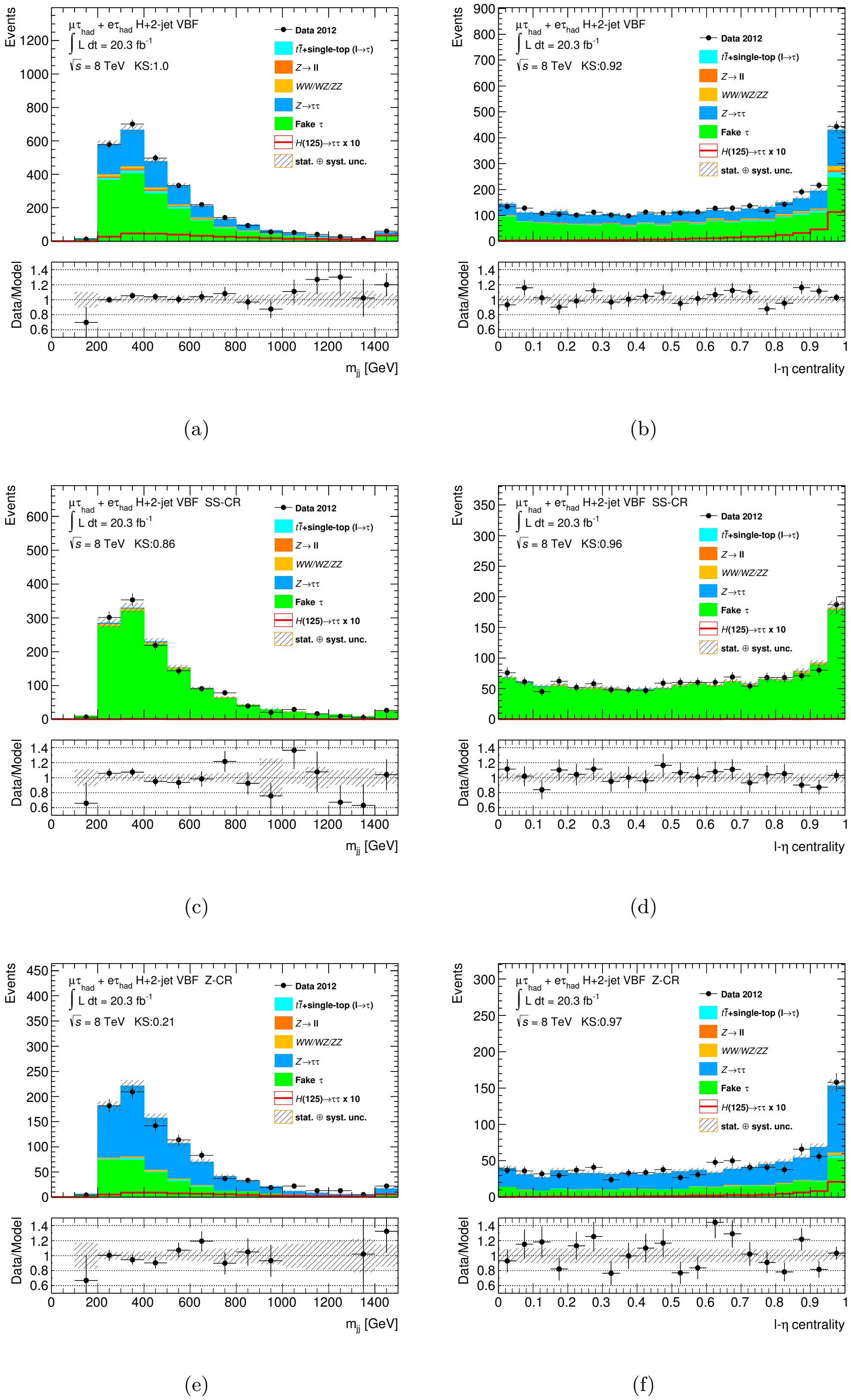

(a) (b)

(c) (d)

(e) (f)

Figure 5.28. *Distributions of the dijet mass (a, c, e) and ℓ–η centrality (b, d, f) in the SR (a, b), the fake τ_{had} (c, d) and the $Z \to \tau\tau$ CR (e, f) of the VBF category in the 8 TeV analysis. The last bin includes all contributions beyond the displayed axis range.*

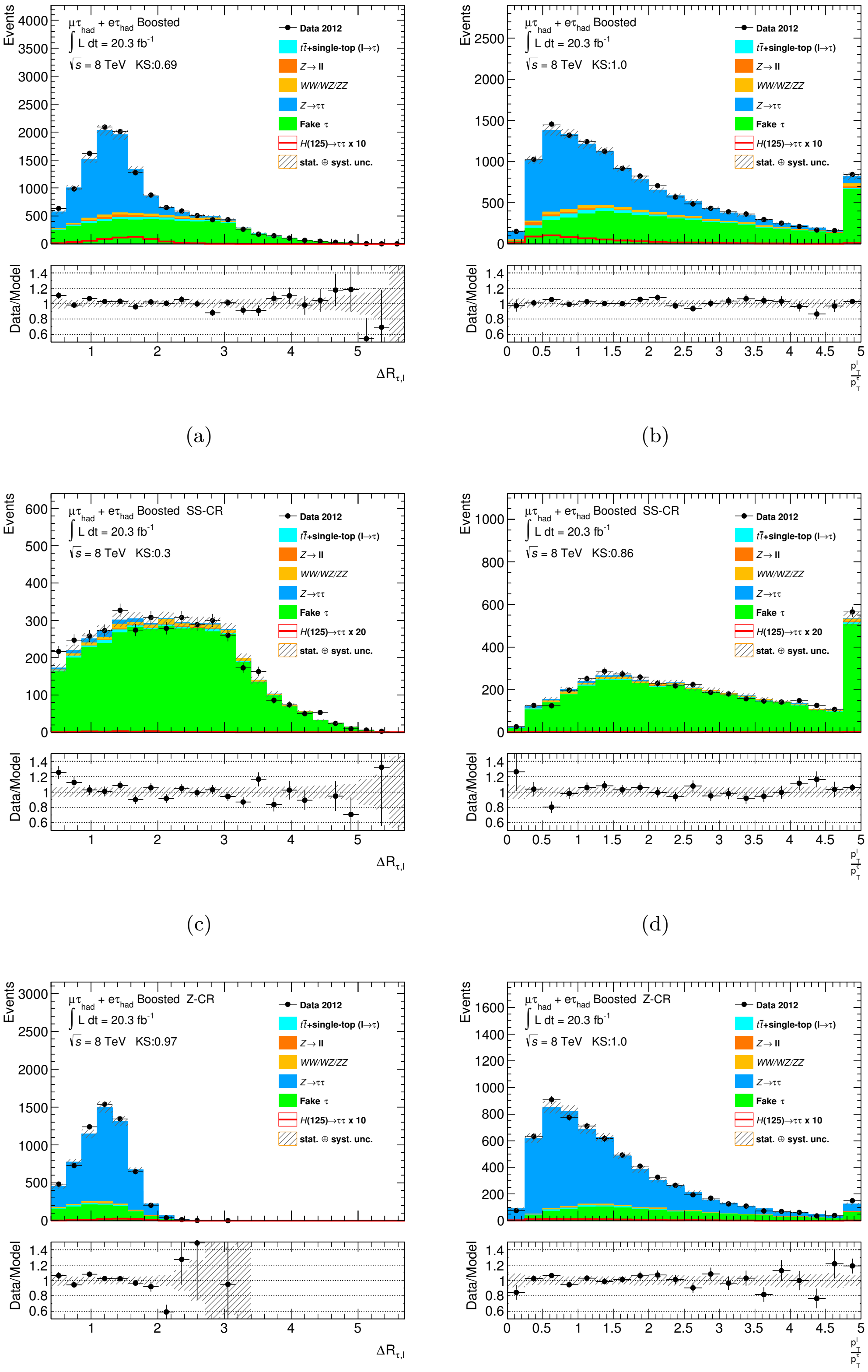

(a) (b)

(c) (d)

(e) (f)

Figure 5.29. *Distributions of the angular separation between the visible tau decay products (a, c, e) and the ratio of lepton and* τ_{had} *transverse momenta (b, d, f) in the SR (a, b), the fake* τ_{had} *(c, d) and the* $Z \to \tau\tau$ *CR (e, f) of the Boosted category in the 8 TeV analysis. The last bin includes all contributions beyond the displayed axis range.*

the 8 TeV VBF category. The control region definitions follow Table 5.4. Figure 5.29 shows the $\Delta R_{\tau\ell}$ and $p_T(\tau)/p_T(\ell)$ in the respective control regions of the Boosted category. All input variables are well described by the background model. Since the ditau mass offers a larger signal sensitivity than all other input variables, the mass distribution in the signal region is only studied in the unblinded, low BDT score region. The two mass distributions in the VBF and Boosted categories of the 8 TeV analysis are shown in Fig. 5.30 and a good description of this observable is found as well. All input variables in all control regions are shown in Figs. A.1 to A.10 in Appendix A.

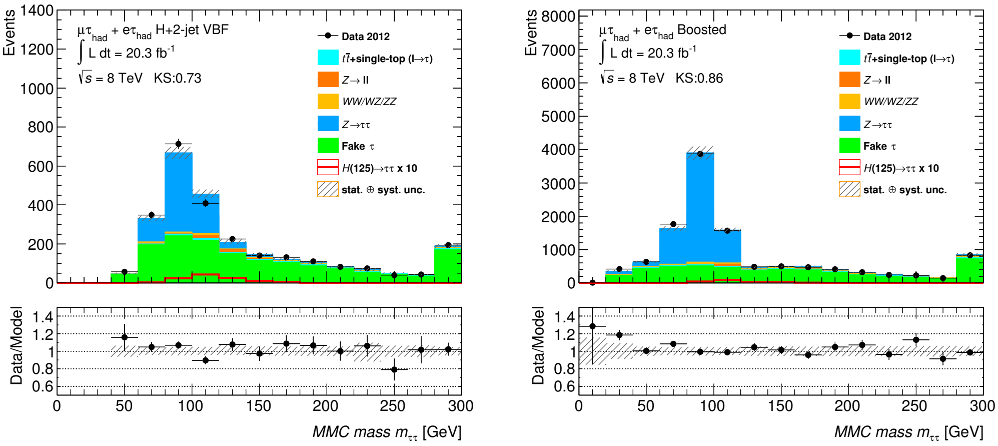

(a) (b)

Figure 5.30. *Ditau mass distribution in the low BDT score region of the VBF (a) and Boosted (b) category of the 8 TeV analysis.*

Input Variable Correlation Profiles

To validate the modelling of correlations across the input variables, a set of profile distributions is prepared for both data, and the background model. A profile distribution shows the mean value of one variable in slices of a second variable. All possible variable pairs are validated for the VBF and Boosted category of the 8 TeV analysis. The background model is found to describe all input variable correlations well. Two examples are shown in Fig. 5.31, the profile of $\Delta\eta_{jj}$ in bins of m_{jj} in the VBF category and the profile of $\Delta R_{\tau\ell}$ as a function of $m_{\tau\tau}$ in the Boosted category. The displayed uncertainty corresponds to the standard error of the mean value, systematic uncertainties are not included. The profiles of all other variable combinations are shown in Figs. A.11, A.12 of Appendix A.

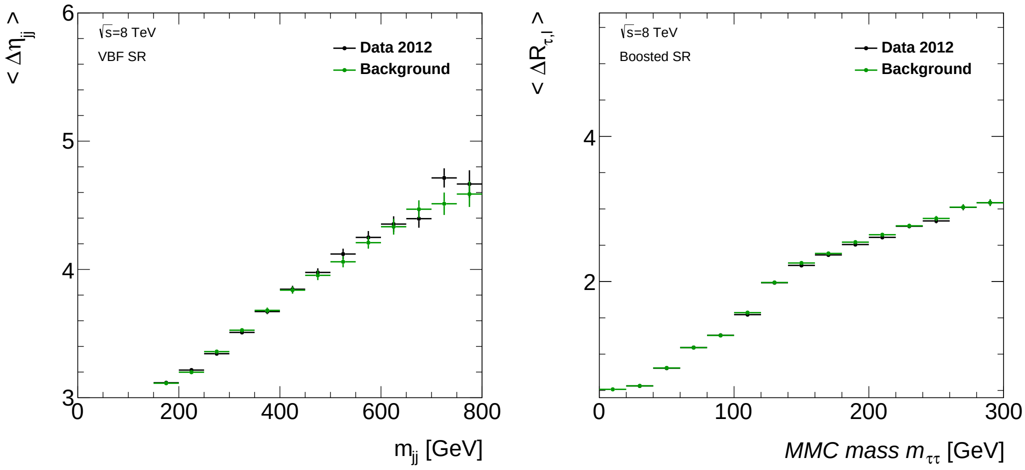

(a) (b)

Figure 5.31. *Profile plots displaying the mean values of $\Delta\eta_{jj}$ in bins of m_{jj} in the VBF category (a) and the profile of $\Delta R_{\tau\ell}$ as a function of $m_{\tau\tau}$ in the Boosted category (b) of the 8 TeV analysis.*

BDT Output Validation

The final step in the validation of the background model is to examine the agreement between data and background expectation in the actual BDT output distributions. Since the BDTs achieve a strong separation between background and signal events, it is possible to do so in a wide BDT score range without any sensitivity to a potential signal. These partially blinded signal region distributions are shown in Fig. 5.32 for both categories and datasets. In the VBF category, the data is shown for nearly the full BDT score range up to score values of 0.9, while in the Boosted categories the threshold of 30% signal efficiency is reached at score values of 0.6 and 0.7 in the 8 TeV and 7 TeV analyses, respectively. The data agrees well with the background expectation, and no sign for any systematic mismodelling is observed. In addition, the BDT score distributions in control regions allow to validate the background model of individual processes. Figures 5.33 and 5.34 show such distributions for the VBF and Boosted category, respectively. In general, the data is well described by the model up to the high BDT score region in all control regions. A small deviation is observed in the $Z/\gamma^* \to \tau\tau$ control region of the 7 TeV VBF category, where the model overestimates the number of data events by about 20%. Extensive checks of individual input variables and correlations revealed no apparent origin of this discrepancy. Especially, no mass dependence of the discrepancy is evident, even though the Z control region is a subset of the corresponding signal region, shown in Fig. 5.32 (b), in which very good agreement between the model and the data is found. The systematic uncertainties of the background model cover the observed deviation.

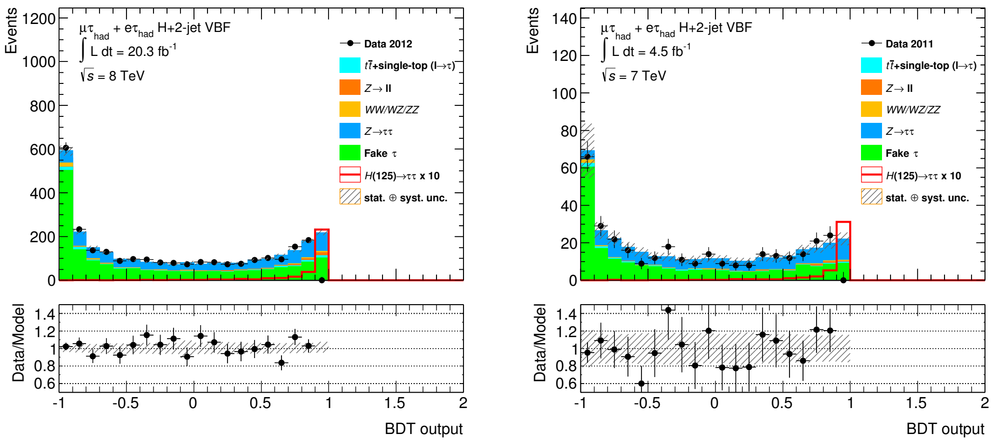

(a) 8 TeV - VBF SR (b) 7 TeV - VBF SR

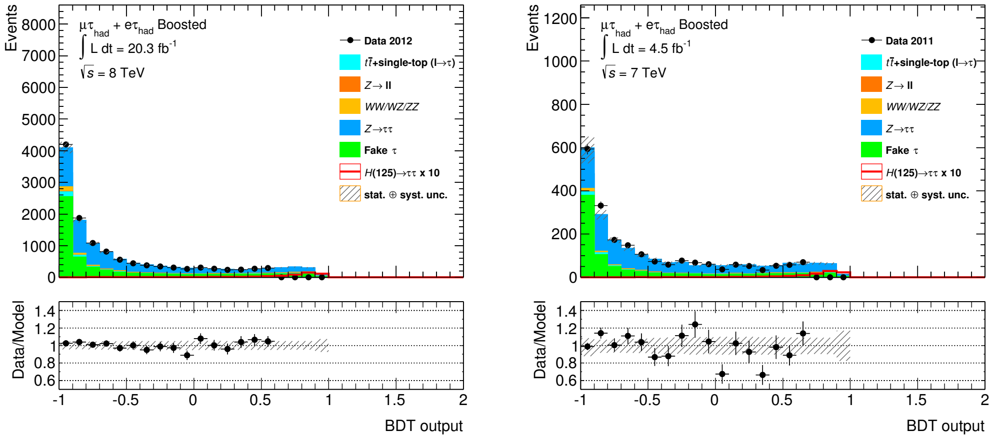

(c) 8 TeV - Boosted SR (d) 7 TeV - Boosted SR

Figure 5.32. *Distributions of the BDT output in the signal region in the VBF (top) and Boosted (bottom) category of the* 8 *TeV (left) and* 7 *TeV (right) analysis. Data is only shown in the low score region, up to a signal efficiency of* 30%.

5.7. Systematic Uncertainties

Various systematic uncertainties on the physics object reconstruction and calibration, the theoretical modelling of signal and background processes, as well as on background modelling techniques do affect the number of expected signal and background events in the various analysis regions. These effects will be referred to as *acceptance* uncertainties. Besides the uncertainties on the acceptance, the differential distributions of BDT input variables are subject to the same uncertainties. These *shape* uncertainties need to be propagated to the BDT score distribution to be taken

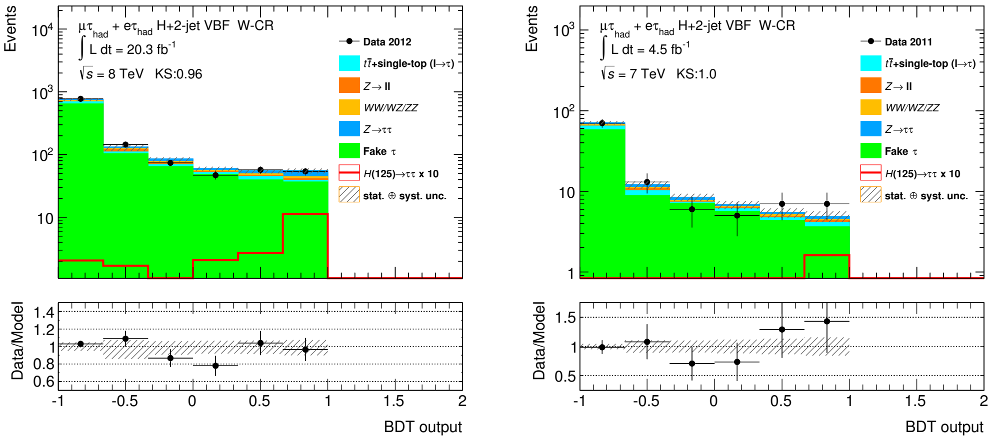

(a) 8 TeV - W-CR (b) 7 TeV - W-CR

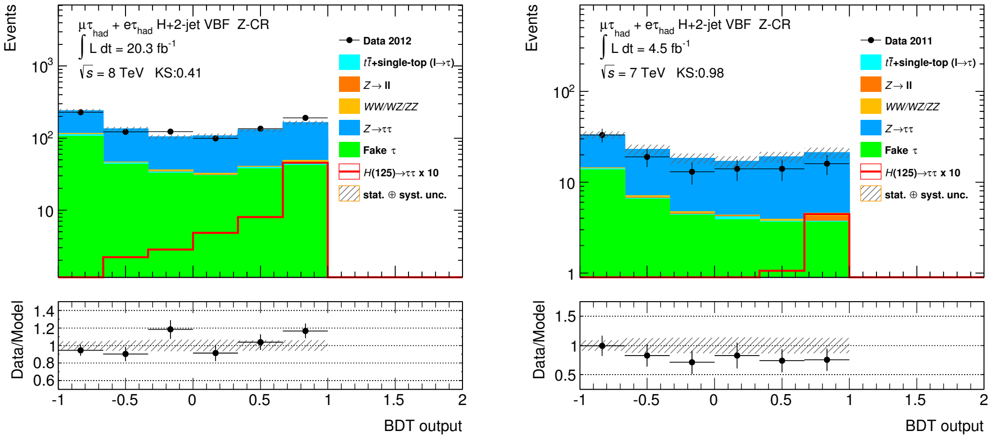

(c) 8 TeV - Z-CR (d) 7 TeV - Z-CR

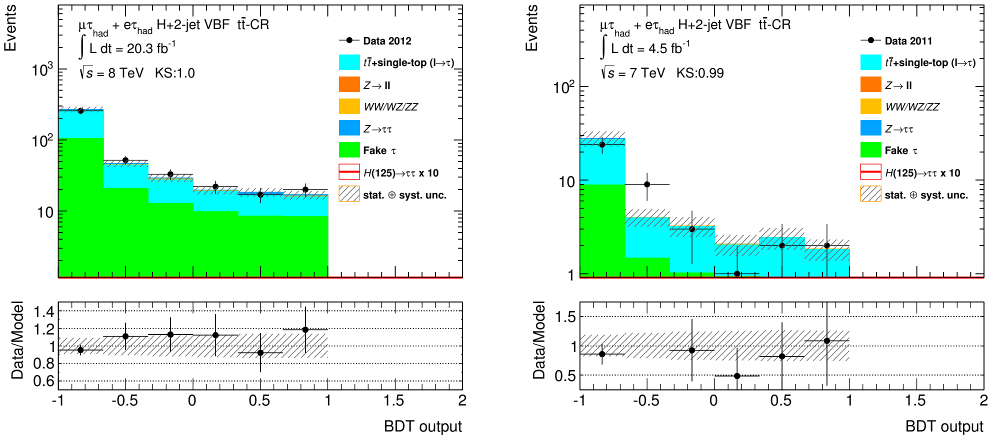

(e) 8 TeV - top-CR (f) 7 TeV - top-CR

Figure 5.33. *Distributions of the BDT output in W, Z and top-quark control regions of the VBF category of the 7 TeV (right) and 8 TeV (left) analysis.*

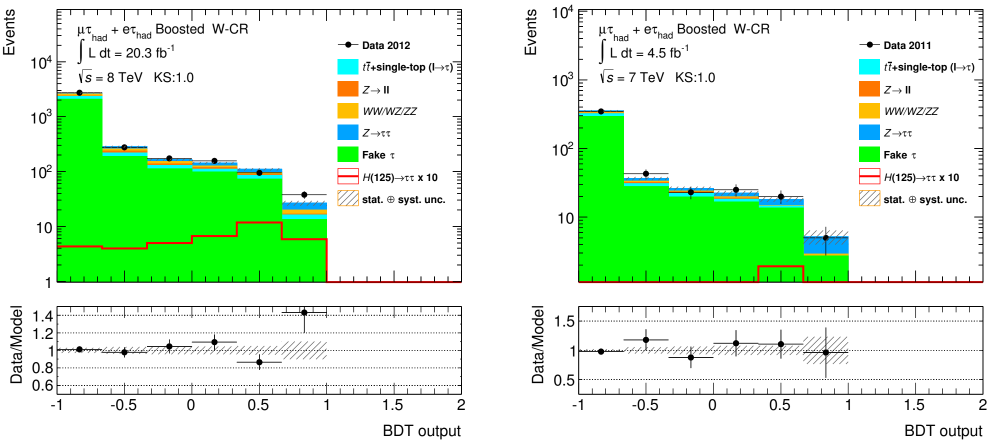

(a) 8 TeV - W-CR (b) 7 TeV - W-CR

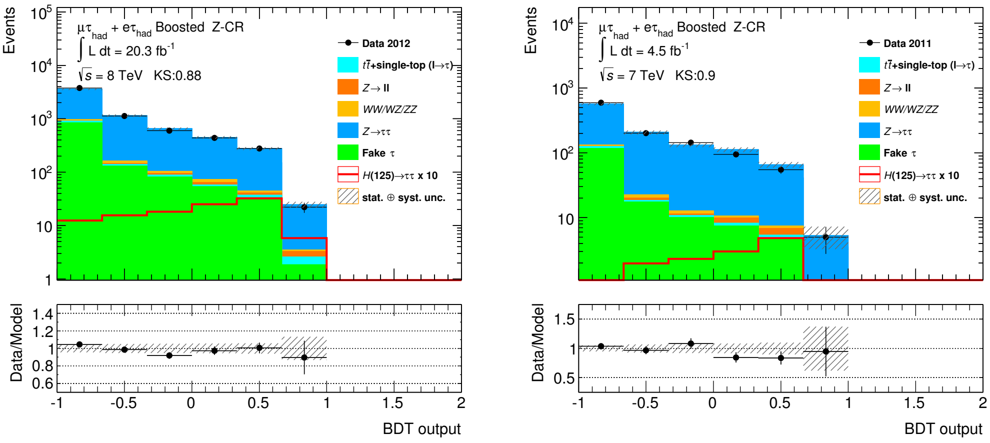

(c) 8 TeV - Z-CR (d) 7 TeV - Z-CR

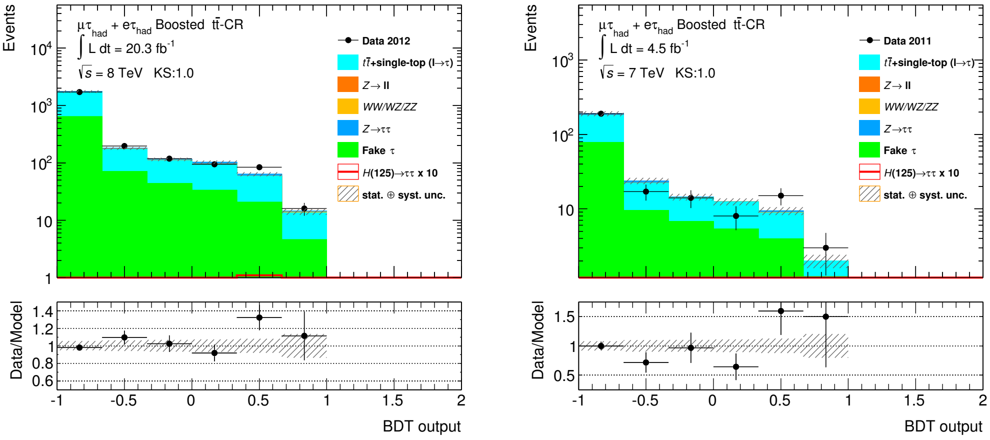

(e) 8 TeV - top-CR (f) 7 TeV - top-CR

Figure 5.34. *Distributions of the BDT output in W, Z and top-quark control regions of the Boosted category of the 7 TeV (right) and 8 TeV (left) analysis.*

into account in the signal extraction procedure. The different systematic uncertainties are grouped into experimental and theoretical uncertainties and discussed in Sections 5.7.1 and 5.7.2, respectively. While this section intends to summarise the various uncertainties, their inclusion into the combined likelihood fit and their impact on the final analysis result is discussed in Section 6.2.1.

5.7.1. Experimental Uncertainties

Experimental systematic uncertainties arise from imperfections in the energy and momentum calibration of jets, τ_{had} objects and leptons, from the $\mathbf{E}_T^{\text{miss}}$ reconstruction as well as from efficiency uncertainties on the trigger simulation and particle reconstruction and identification procedures. Furthermore, the uncertainty on the luminosity measurement affects the overall expected event rate and is summarised in Section 2.2.5. The performance of the particle reconstruction and calibration, as well as the trigger performance is mostly measured in data and the respective uncertainties are briefly discussed in Chapter 3. These uncertainties are propagated to the analysis categories by varying the corresponding parameters in the event reconstruction and repeating the full analysis. The resulting event yields and their differential distributions can then be compared to the central values obtained with nominal event reconstruction settings, in order to get an estimate of the effect of the systematic uncertainty. While such uncertainties affect simulated events only, other uncertainties account for limitations in the data driven background modelling techniques explained above.

Efficiencies

Trigger, reconstruction and identification efficiencies on both leptons and hadronic tau decays are determined using tag-and-probe techniques as outlined in Sections 3.4, 3.5 and 3.6. The simulated event samples are corrected for differences in the performance between simulation and data. Uncertainties on the single lepton trigger efficiencies dominate to overall efficiency uncertainties for light leptons and are of the order of $\pm(1-2)\%$.

The τ_{had} identification efficiency is determined in $Z \to \tau_\mu \tau_{\text{had}}$ decays with uncertainties of the order of $\pm(2-5)\%$ depending on the number of tracks, the pseudorapidity and transverse momentum of the τ_{had} object. These measurements receive uncertainty contributions of statistical and systematic origin and these components are propagated uncorrelated to the $H \to \tau_{\text{lep}}\tau_{\text{had}}$ analysis. A conservative uncertainty of $\pm 15\%$ on the τ_{had} misidentification probability of muons is assigned based on a comparison between data and simulated events in a control region, while the fake electron rate is measured in a tag-and-probe analysis as discussed in Section 3.6.

The b-tagging efficiency uncertainty affects the analysis due to the b-jet veto in the SR and the b-jet requirement in the top CR. It is measured in data, using dileptonic $t\bar{t}$ events and inclusive jet samples as summarised in Section 3.3.3. The uncertainty on the mistag rate of light-flavour jets is of the order of ±15%, while the tagging efficiency of b-jets is measured with a precision of the order of ±2%. The efficiency uncertainties on light-flavour jets and b-jets are treated as uncorrelated in the analysis by a total of 26 uncorrelated uncertainty components identified by a diagonalisation of the the full covariance matrix.

An uncertainty on the selection efficiency of the JVF criteria applied on jets within the geometrical tracker acceptance is propagated to the analysis and found to be well below ±1% for all processes and analysis categories.

Table 5.14 summarises the effect of these efficiency uncertainties on the acceptance of signal and background events.

Source	VBF category					
	ggF	VBF	$Z \to \tau\tau$	$t\bar{t}$ *	$Z \to \ell\ell$ *	VV
τ_{had}	±3.3%	±3.3%	±3.3%	±3.2%	±21%	±2%
e	±1%	±1%	$< 1\%$	$< 1\%$	±1%	±1%
μ	±1%	±1%	±1%	±1%	$< 1\%$	±1%
b-jets	$< 1\%$	$< 1\%$	-	±7.3%	$< 1\%$	$< 1\%$
	Boosted category					
τ_{had}	±3.3%	±3.3%	±3.3%	±3.1%	±20%	±2%
e	$< 1\%$	$< 1\%$	$< 1\%$	$< 1\%$	±1%	±1%
μ	±1%	±1%	$< 1\%$	±1%	$< 1\%$	±1%
b-jets	$< 1\%$	$< 1\%$	-	±9.2%	$< 1\%$	±1%

Table 5.14. *Systematic uncertainties on the signal-region acceptance of major signal and background processes in the $\sqrt{s} = 8$ TeV analysis, arising from different object efficiencies including effects from triggering, reconstruction and identification.*
**: For the $t\bar{t}$ and $Z \to \ell\ell$ processes, only events in which the τ_{had} object is not faked by a jet are considered.*

Energy Scales and Resolutions

Important uncertainties arise from the calibration of jets, τ_{had} objects and leptons. The jet-energy scale uncertainty (JES) is grouped into several components accounting for response uncertainties due to the pile-up subtraction method, the η intercalibration, the jet flavour composition and other effects. In total eleven different components are considered and are treated as uncorrelated. The combined uncertainties range from $\pm(1-2)\%$ for central jets to $\pm(3-7)\%$ in the forward region (see also Section 3.3.2). The jet energy resolution is measured in dijet events with uncertainties well below ±10%. To propagate the uncertainty in the description of the jet energy resolution, the energy response is smeared by an additional Gaussian term. Since the simulated resolution cannot be reduced easily, the uncertainty corresponding to a larger resolution is symmetrised to estimate the full uncertainty due to the jet energy resolution. As the jets in both, the $Z \to \tau\tau$ and the fake τ_{had} background model are directly determined from data, the JES uncertainty affects the analysis mainly via the simulated signal samples.

The τ_{had} energy scale (TES) is determined from a fit to the visible mass spectrum of $Z \to \tau_\mu \tau_{\text{had}}$ events as discussed in Chapter 4. Uncertainties are of the order of $\pm(2-4)\%$ and are treated uncorrelated for real and fake τ_{had} candidates. Furthermore three uncorrelated uncertainty components are considered for data taken in 2012, associated to the systematic uncertainties in the $Z \to \tau_\mu \tau_{\text{had}}$ fit and the single particle response propagation. The tau energy resolution is studied in simulated event samples and uncertainties are estimated to be below $\pm 1\%$ (see also Section 3.6.2). The uncertainty on the acceptance due to this effect is found to be negligible.

The energy and momentum scales of electrons (EES) and muons (MMS) are determined to a much higher precision than those of hadronic energy deposits. Their impact on the analysis is therefore small. The uncertainties on the energy scales are propagated also to the E_T^{miss} reconstruction. In addition to that, an uncertainty on the energy scale and resolution of $E_T^{\text{miss,SoftTerm}}$ is determined in $Z \to \mu^+\mu^-$ events without jets and of the order of $\pm 8\%$ and $\pm 5\%$, respectively. Table 5.15 summarises the effect of these uncertainties on the acceptance of signal and $Z \to \tau\tau$ events.

Background Modelling Uncertainties

Background model uncertainties inherent to the embedding and fake factor methods are discussed in Section 5.5. Two systematic uncertainties account for the cell-energy subtraction and the isolation requirement on the muon selection within the embedding procedure. The cell-energy scale in the subtraction of energy deposits of the initial muons is varied by $\pm 20\%(30\%)$ for data taken in 2012 (2011). The uncertainty due to the isolation requirement is estimated by tightening or dropping this selection cut. Due to the normalisation of the embedded sample to data, the effect on the total number of events at preselection is vanishing by construction. The relative effect of these uncertainties on the category selection efficiencies though, is accounted for by repeating the analysis using the modified embedded samples. These relative acceptance uncertainties are found to be of the order of $\pm(1-4)\%$.

Uncertainties on the fake factor method account for the background composition and the statistical uncertainty on the fake factors. These uncertainties are treated uncorrelated, where up to five statistical independent uncertainties per category are used to reflect the statistical uncertainty of the fake factors (see also Section 5.5.2). In total, the combined uncertainty is of the order of $\pm 5\%$ in the VBF category and $\pm 6\%$ in the Boosted category of the $\sqrt{s} = 8$ TeV analysis. An additional uncertainty arises from the E_T^{miss} correction applied in the fake estimate of the $\sqrt{s} = 7$ TeV analysis (see Section 5.5.2). The overall normalisation of the $Z \to \tau\tau$ and $t\bar{t}$ background are freely floating in the likelihood fit. Since the determination of the normalisation parameter of the $t\bar{t}$ background is dominated by the top CR

Source	VBF category					
	ggF	VBF	$Z \to \tau\tau$	$t\bar{t}$ *	$Z \to \ell\ell$ *	VV
JES	±17%	±6%	-	±8.5%	±25%	±16%
JER	±1%	< 1%	-	< 1%	±20%	±10%
TES	±4%	±2%	±3.5%	±4%	±20%	±5%
EES	< 1%	< 1%	< 1%	< 1%	±10%	±1%
$E_T^{\mathrm{miss,SoftTerm}}$	±1%	±1%	-	±1%	±10%	±3%
	Boosted category					
JES	±5%	±1%	-	±1.5%	±12%	±7%
JER	±1%	< 1%	-	±2.5%	±1%	±1%
TES	±3%	±2%	±2%	±3.5%	±3.5%	±5%
EES	< 1%	< 1%	< 1%	< 1%	1%	< 1%
$E_T^{\mathrm{miss,SoftTerm}}$	±1%	< 1%	-	< 1%	1%	< 1%

Table 5.15. *Impact of systematic uncertainties of the different energy scales and resolutions on the signal-region acceptance of the major signal and background processes in the $\sqrt{s} = 8$ TeV analysis. The large uncertainties on the $Z \to \ell\ell$ and diboson processes arise from statistical fluctuations and category migration effects when repeating the analysis with varied energy scales. The simulated samples used to estimate the number of events from these processes are of relatively low statistical power and yield single events of large weights. The quoted uncertainties therefore represent conservative upper bounds on the uncertainty.*
**: For the $t\bar{t}$ and $Z \to \ell\ell$ processes, only events in which the τ_{had} object is not a misidentified jet are considered.*

included in the fit, an additional ±6% extrapolation uncertainty accounts for the different kinematic properties in the signal and control regions (see Section 5.5.3). The background from $Z \to \ell\ell$ events, modelled by simulation, is corrected for a known deficit in the description of the kinematic properties of additional jets in the event. The correction is performed as a function of $\Delta\eta_{jj}$ as discussed in Section 5.5.4, with an additional systematic uncertainty of ±10% on the acceptance in the VBF category.

5.7.2. Theoretical Uncertainties

Background and signal estimates based on simulated event samples like diboson and $Z \to \ell\ell$ processes where a lepton is misidentified as τ_{had} object are further subject to theoretical uncertainties. These arise from missing higher order corrections in the cross-section calculations, from the precision of the PDF and the modelling of the underlying event and parton shower. The uncertainties of the diboson and $Z \to \ell\ell$ cross sections, summarised in Table 5.1, are estimated by varying the renormalisation and factorisation scale and by propagating uncertainties on the

PDF sets. The QCD and PDF uncertainties are of the order of ±5% and ±4% for the diboson processes and about ±1% and ±4%, respectively for the $Z \to \ell\ell$ processes. Their overall impact on the analysis result is small.

Theoretical uncertainties on the signal prediction due to missing higher order corrections are estimated similarly. For the VBF and VH production cross-sections, a nominal scale choice of $\mu_{F,R} = m_W$ is used and variations by a factor of two yield uncertainties of the order of $\pm(2-5)\%$. To account for missing higher order electroweak corrections, an additional uncertainty of ±2% is assigned to the VBF cross section. The QCD scale uncertainties on the gluon-fusion process are generally larger. Here, a nominal value of the renormalisation and factorisation scale of $\mu_{F,R} = \sqrt{m_H^2 + p_H^2}$ is used. Selection criteria mimicking the category definitions are implemented at parton level and the uncertainties on the exclusive cross section in the Boosted and VBF categories are estimated following Ref. [201], taking category migration effects into account. Since events which pass the selection criteria of the Boosted and VBF categories are solely considered in the latter one, two uncertainty components are considered. One corresponding to the uncertainty on the inclusive cross section of events with $p_T^H > 100$ GeV and a second one corresponding to the uncertainty of the cross section of events which pass both selection criteria of the VBF and Boosted categories. While the latter uncertainty is large, the absolute contribution of ggF events with $p_T^H > 100$ GeV to the VBF category is very small, so that the impact of this uncertainty on the result is small as well. In total, this results in a relative uncertainty of the order of ±30% in the Boosted category and ±25% in the VBF category. The uncertainty on the ggF cross section in the VBF category is treated anti-correlated to the second uncertainty component of the ggF production in the Boosted category, to account for the migration effects due to the exclusive category definition.

The BDT in the VBF category makes use of input variables carrying information about the jet activity in the events, as for example p_T^{tot}. While no explicit jet veto is applied, these input variables provide enough information to suppress contributions from events with a third jet in the high BDT output region. This effective suppression introduces an additional uncertainty on the shape of the BDT output distribution. It is expected to be sizeable, given that the cross section of gluon fusion events accompanied by three jets is only described at LO precision. The opening angle between the Higgs boson and the dijet system in the transverse plane $\Delta\phi(H, jj)$ can be used to parametrise additional jet activity. In case of no additional jet, a value of $\Delta\phi(H, jj) = \pi$ is expected. Evaluating the impact of scale variations on the production cross-section of events with $(\Delta\phi(H, jj) - \pi) > 0.2$ indeed yields large uncertainties of the order of ±80%. The uncertainty on such events is propagated to the BDT score distribution and considered as an uncertainty on the shape, resulting in an uncertainty of the order of ±30% in the highest BDT score bin. This is shown in Fig. 5.35, where the left plot shows the enhancement of the low $\Delta\phi(H, jj)$ region in events with high BDT score values, while the right plot shows the resulting systematic uncertainty. As in general the sensitivity of the VBF category is dominated by VBF signal events, the impact of this additional

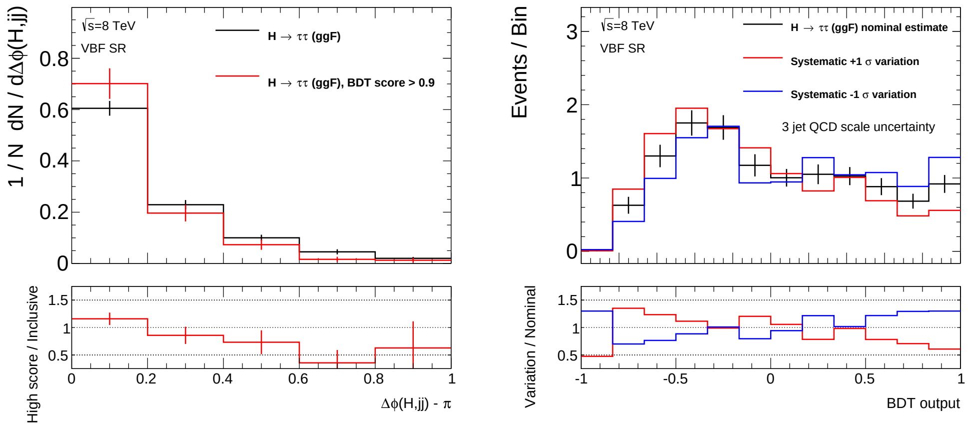

(a) (b)

Figure 5.35. *Figure (a) shows the distribution of the opening angle between the Higgs boson momentum and the dijet system in the transverse plane for ggF events in the VBF category. The distribution shows a significant enhancement around $\Delta\phi(H, jj) \approx \pi$, once a lower cut on the BDT output is applied. This enhancement corresponds to an effective suppression of additional radiation in the high BDT output region. Figure (b) shows the BDT output distribution of ggF events in the VBF category and the systematic uncertainty applied to account for the large cross-section uncertainty for ggF events with three jets.*

uncertainty on the sensitivity on the analysis is less than 1%.

The uncertainty due to the underlying event and parton shower model is estimated by comparing the signal-region acceptance in event samples generated with Powheg [163, 167] interfaced to Pythia 8 [62] to samples where Powheg was interfaced to Herwig [63] and Jimmy [171] instead. This comparison results in an uncertainty estimate of the order of $\pm(4-8)\%$, depending on the process and analysis category. The PDF uncertainties on the inclusive cross section are calculated by the LHC Higgs cross-section working group [77–79] and are of the order of ±8% for the gluon fusion process and about ±3% for the VBF production cross-section. Additional uncertainties arise from the effect of PDF uncertainties on the signal-region acceptance and are evaluated by comparing different PDF sets, as well as by propagating the PDF uncertainties of the nominal PDF set to the signal-region acceptance. Resulting acceptance uncertainties are of the order of $\pm(5-6)\%$ for the gluon fusion process and about ±1% for VBF production.

To account for a potential uncertainty on the signal region acceptance arising from the choice of a specific NLO Monte Carlo event generator, the acceptance of ggF events in the Boosted category is compared between samples generated with either Powheg interfaced to Herwig or Mc@nlo interfaced to Herwig. Differences of the order of ±1.9% are found and assigned as systematic uncertainty. A similar comparison is performed for the acceptance of VBF events in a VBF enhanced signal region in the context of the search for $H \to WW^*$ decays [91], resulting in a systematic uncertainty of ±4.2%. Since the category definition used in this analysis is tighter than the one used in the analysis presented here, the uncertainty estimate is expected to cover the uncertainty also in the search for $H \to \tau\tau$ decays. The impact on the analysis result is found to be negligible. Table 5.16 summarises the different theoretical uncertainties on the signal predictions.

Source	VBF category			Boosted category		
	ggF	VBF	VH	ggF	VBF	VH
QCD scale	$^{+27\%}_{-21\%}$	±2.1%	±1%	$^{+29.2\%}_{-22.2\%}$	±1.4%	±4%
PDF	±9.2%	±3.2%	±3.2%	±9.9%	±3.2%	±3.2%
UE/PS	±8%	±4%	±4%	±4%	±6%	±6%
ME-PS matching	-	±4.2%	-	±1.9%	-	-

Table 5.16. *Theoretical uncertainties on the signal cross sections in the VBF and Boosted analysis categories. The combined uncertainties from QCD scale variations in the Boosted category are quoted. In the likelihood fit, two nuisance parameters are associated to the scale uncertainty on ggF events in the Boosted category in order to reflect the anti-correlation with the corresponding uncertainty in the VBF category, as detailed above.*

6 Statistical Analysis of the Search for $H \to \tau_{\mathrm{lep}}\tau_{\mathrm{had}}$ Decays

This chapter describes the combined likelihood fit to the BDT output distributions of the VBF and Boosted categories which is used to estimate the signal event yield. The general concept of maximum-likelihood fits and the likelihood function is introduced in Section 6.2. A summary of the categories included in the fit, as well as a description of the BDT output binning optimisation is presented in Section 6.1. This optimisation aims to find a compromise between the concurring needs to exploit the differential BDT output information and to bin the distributions in a way that avoids large statistical fluctuations of the background model. The likelihood function needs to reflect the various statistical and systematic uncertainties of the background and signal expectation. The parametrisation of these effects is described in Sections 6.2.2 and 6.2.1. Besides a measurement of the signal-event rate, the compatibility of the data with the *background-only hypothesis* is quantified using a hypothesis test described in Section 6.3. Finally, the results are presented in Section 6.4 along with validation checks of the fitting procedure.

6.1. Binning Optimisation

As stated before, a simultaneous fit to the signal and top control regions is performed in order to estimate all parameters of the signal and background model. While the control regions are meant to provide a handle on the top-normalisation factors, the signal regions provide the discriminating power between background and signal events via the BDT output distributions presented in Chapter 5. Therefore, the shape of the BDT output distributions needs to be exploited in the fit, while it suffices to include the sheer event counts in the control regions. As the probability-density functions of signal and background events are unknown, the signal and background models as introduced above are used to estimate them in a binned form. The specific binning to be used in the fit should on one hand be fine enough to provide as much shape information as possible, but on the other hand it should as well be coarse enough to allow for a sensible background estimate, which is affected by statistical fluctuations in case of too finely segmented histograms. In principle, a binning optimisation based on the expected discovery significance as figure of merit could be performed. As the full statistical analysis is computationally expensive, a slightly different approach is chosen. Firstly, a bin width is determined at which single events of the background model are resolved in the high BDT output region. By construction, bin widths of even higher granularity cannot provide additional shape information. For both categories this limit is reached at widths of about 0.001 units. Afterwards, different bin widths are tested for the expected discovery significance, neglecting systematic uncertainties but taking into account the statistical uncertainties on the background model. As expected, this test reveals that the expected significance is maximised if the smallest allowed bin width is chosen. Therefore, the finest possible binning which still provides a robust background estimate should be chosen. In order to avoid complications in the estimation of systematic uncertainties, and to not optimise the binning based on statistical fluctuations, robustness criteria are required for the relative statistical uncertainty on each component of the background model. Namely, the relative statistical uncertainty of the $Z \to \tau\tau$ and fake τ_{had} background model is required to be smaller than 30% and 50%, respectively, and to be smaller than 100% for all other backgrounds. While not being based on first principles, these robustness criteria ensure that statistical fluctuations in the background estimates cannot mimic an artificially high or low expected discovery significance. Alternative background estimation techniques, like simulated samples of $Z \to \tau\tau$ events, yield comparable estimates of the main background components in the highest BDT score bins.

The signal sensitivity of the BDT score distribution is located at high score values. The lower BDT output region instead provides valuable information about the normalisation of the different background processes. Since the computational resources needed to perform the likelihood fit grow extensively with the number of bins, a coarser bin width is desirable in the low score region. The following algorithm is used to determine the final binning. Starting from histograms with constant bin widths of 0.001 units, bins are merged starting from the high BDT score end until the following criteria are met:

- The total expected background in the new bin exceeds the total expected background in the previous bin.
- The relative statistical uncertainty of each background component is smaller than the defined threshold.
- Either the signal-to-background ratio is at most 10% smaller than in the previous bin or the ratio between the expected $Z \to \tau\tau$ and fake τ_{had} background changed by more than 50% with respect to the previous bin or the total expected background exceeds the one in the previous bin by more than 50%.

The first criteria simply ensures a monotonic falling background shape while the second criteria ensures that the robustness criteria defined above are met. The third criteria states that a new bin should be created in case the new bin would offer a high signal sensitivity. If that is not the case, a new bin should be created anyway in case it offers a different background composition than the previous one. This feature ensures the possibility to disentangle systematic effects and normalisation factors of the various background components. In general, the resulting binning features non-uniform bin widths. The algorithm is run on both the VBF and Boosted categories of the 7 TeV and 8 TeV to determine the binning used in the fitting procedure. The last bins are chosen as $[0.988, 1]$ ($[0.97, 1]$) and $[0.904, 1]$ ($[0.926, 1]$) in the VBF and Boosted categories of the 8(7) TeV analyses, respectively.

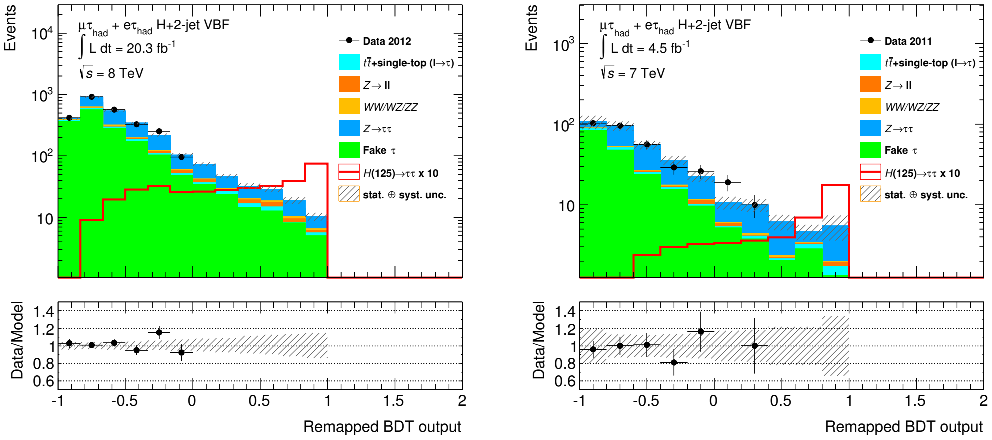

(a) 8 TeV - VBF SR (b) 7 TeV - VBF SR

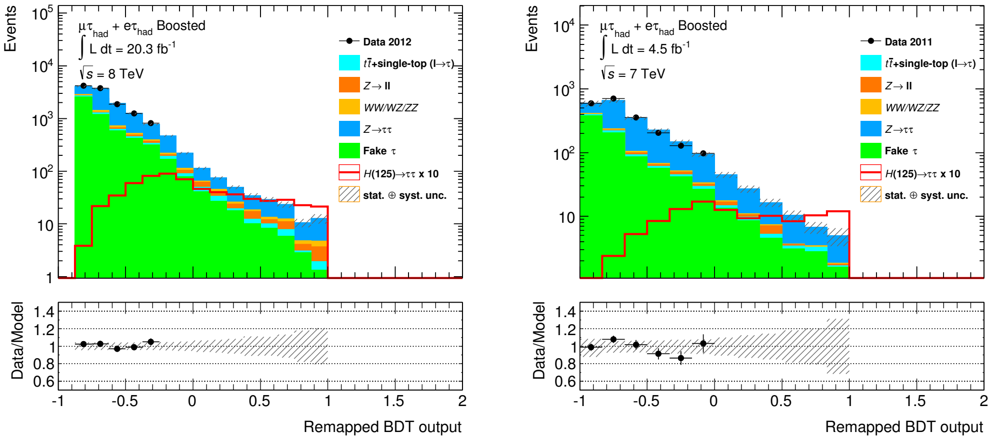

(c) 8 TeV - Boosted SR (d) 7 TeV - Boosted SR

Figure 6.1. *Distributions of the BDT discriminants in the signal region in the VBF (top) and Boosted (bottom) category of the 8 TeV (left) and 7 TeV (right) analysis. Data is only shown in the low BDT output region, up to a signal efficiency of* 30%. *The BDT output axis was transformed to display the optimised binning in bins of equal width. The expected signal distribution is enhanced by a factor 10.*

Since the BDT output itself does not carry physical information, BDT output distributions are shown on a transformed axis in the remainder of this thesis. This transformation simply remaps the optimised, non-uniform bins, onto bins of equal bin width. This serves a purely visual purpose. Figure 6.1 shows the expected background and signal BDT output distributions using this optimised binning. In comparison to Fig. 5.32, these distributions reflect a much higher resolution of the high BDT score region and therefore provide more shape information in the signal sensitive part of the distribution, while the overall number of bins is kept small.

6.2. The Likelihood Function

An extended maximum-likelihood fit [202] to the observed data is used to estimate the parameters of the combined signal and background model, including the signal strength parameter μ. The probability-density functions (PDFs) of the background and signal models are denoted as $f_B(x;\boldsymbol{\theta})$ and $f_S(x;\boldsymbol{\theta})$, respectively. They are functions of an observable x, for example of the BDT score, and normalised to unity. Furthermore, they might depend on a set of parameters $\boldsymbol{\theta}$. In the following, such parameters will be denoted as *nuisance parameters* (NP), as their measurement is not the primary goal of the analysis. In general, both PDFs will consist of several contributions from various physics processes as discussed above. If S and B are the expected number of signal and background events, where their dependence on the nuisance parameters is suppressed, the probability to observe N events in data can be written as

$$\mathcal{P}(\boldsymbol{x};\mu,\boldsymbol{\theta}) = \frac{e^{-(\mu S+B)}(\mu S+B)^N}{N!}\left[\prod_e^N \frac{\mu S f_S(x_e;\boldsymbol{\theta}) + B f_B(x_e;\boldsymbol{\theta})}{\mu S+B}\right] \tag{6.1}$$

The first term describes the Poisson probability to observe N events while expecting $(\mu S+B)$. The second term describes the probability to observe the N events at values x_e of the observable x, given the combined signal plus background PDF taking into account the relative background and signal contributions at a signal strength of μ. Considering the data as being constant, this probability can be regarded as function of the parameters and is usually denoted as likelihood function $L(\mu,\boldsymbol{\theta}|\boldsymbol{x})$. A maximum-likelihood fit estimates the parameter values of the model by maximising the likelihood function, given the observed data. Combining several analysis categories can be incorporated by simply multiplying the likelihood functions of each category. In the case of binned distributions, as in this analysis, Eq. (6.1) can be rewritten as

$$\mathcal{P}'(\boldsymbol{n_i};\mu,\boldsymbol{\theta}) = C\prod_{i\in\text{Bins}} \frac{e^{-(\mu s_i(\boldsymbol{\theta})+b_i(\boldsymbol{\theta}))}(\mu s_i(\boldsymbol{\theta})+b_i(\boldsymbol{\theta}))^{n_i}}{n_i!} \tag{6.2}$$

where n_i denotes the number of data events in bin i, $s_i(\boldsymbol{\theta})$ and $b_i(\boldsymbol{\theta})$ the expected number of signal and background events in this bin and C a combinatorial constant which can be neglected in the maximisation procedure as it is constant. In this form it becomes evident that the various bins in the combined likelihood function may describe very different categories, including those which consider the shape of an observable and others which just consider the event count. The product can run over all bins of several binned BDT output distributions and in addition contain single binned categories, as the top control regions.

To simplify the maximisation procedure, it is convenient to consider the logarithm of the likelihood function, since the product then decouples into a sum, and to consider the negative logarithm of the likelihood function (NLL) instead, since common and fast computer codes as MINUIT [203] exist to solve minimisation problems. In the following, the values of the parameters $(\mu, \boldsymbol{\theta})$ which minimise the NLL are denoted as the estimators $(\hat{\mu}, \hat{\boldsymbol{\theta}})$, or best-fit values:

$$\min\{-\ln L(\mu, \boldsymbol{\theta})\} = -\ln L(\hat{\mu}, \hat{\boldsymbol{\theta}}) \tag{6.3}$$

The variance of the estimators can be estimated by considering the change in the *profile* of the likelihood function. The likelihood profile

$$\Delta(-\ln L(\theta_0, \hat{\hat{\theta}}'))\tag{6.4}$$

describes the absolute change of the likelihood as a function of a variable θ_0, while the likelihood is minimised with respect to all other dependencies θ' pointwise[1].

Especially in the case of a Gaussian likelihood it is clear that the uncertainty of a parameter θ_0 can be obtained by searching the parameter value for which the NLL profile differs from its minimum by 1/2. Considering a simple likelihood depending on one parameter, one finds:

$$\begin{aligned} L(\theta_0) &= L_{\max} e^{-\frac{(\theta_0-\hat{\theta}_0)^2}{2\sigma^2}} & (6.5)\\ -\ln L(\theta_0) &= -\ln L_{\max} + \frac{(\theta_0-\hat{\theta}_0)^2}{2\sigma^2} & (6.6)\\ \Delta\text{NLL} &= \ln L_{\max} - \ln L(\hat{\theta}_0 + \sigma) = \frac{1}{2} & (6.7)\end{aligned}$$

The same construction holds for likelihood functions of a non-Gaussian form, as demonstrated for example in Ref. [204], even though the likelihood will approach a Gaussian asymptotically. The procedure can also be generalised towards multidimensional likelihood functions in a straight forward manner.

6.2.1. Integration of Systematic Uncertainties

The signal and background expectations $s_i(\boldsymbol{\theta}), b_i(\boldsymbol{\theta})$ depend on the nuisance parameter values $\boldsymbol{\theta}$. A good example for such a nuisance parameter is the freely floating normalisation of the $Z \to \tau\tau$ background, similar to the signal strength modifier μ which linearly affects the normalisation of the signal contribution. A second type of nuisance parameters is used to parametrise the impact of systematic uncertainties. The qualitative difference of a nuisance parameter describing a systematic uncertainty and a parameter describing a normalisation constant which is to be estimated in the fit, is that a prior knowledge exists about the value of the nuisance parameter. Systematic uncertainties reflect the precision of a calibration measurement which

---

[1] The notation $L(\theta_0, \hat{\hat{\theta}}')$ refers to the conditional minimum of the likelihood with respect to θ' and fixed parameter θ_0.

was performed prior to the analysis. To incorporate the result of such additional measurements into the likelihood function, an important extension to Eq. (6.2) need to be considered. The likelihood function is modified by terms, usually denoted as *subsidiary measurements*, describing this information. In principle, these terms should reflect the full likelihood of the calibration measurement. This way correlations between the various systematic uncertainties could be reflected in the combined likelihood function. For practical reasons, and due to the complexity of each of these calibration measurements, the subsidiary measurements are implemented as an effective likelihood $P_i^{sub.}(\theta_i)$ depending solely on one nuisance parameter θ_i. Motivated by the central limit theorem, the form of $P^{sub.}$ is often chosen to be a Gaussian $P_i^{sub.}(\theta_i) = G(\theta_i|c_i, \sigma_i)$, centred around the result of the calibration measurement c_i and its width given by the associated systematic uncertainty σ_i. It is convenient to parametrise the effect of the systematic uncertainties on the signal and background expectations relative to the nominal estimate and the ones corresponding to $\pm 1\sigma$ shifts, so that instead the subsidiary measurement terms take the form of Gaussian distributions centred around zero with a width of one.

$$P_i^{sub.}(\theta_i) = G(\theta_i|0, 1) \tag{6.8}$$

A nuisance parameter value of one then corresponds to a shift of the uncertain parameter of one standard deviation.

Usually, systematic uncertainties are propagated to the analysis by performing the analysis after shifting the corresponding parameter in the event reconstruction by one standard deviation. Following this straight forward approach, estimates of the impact of 1σ up- and downward shifts of the parameter in question are obtained. For the systematic uncertainty to be incorporated into the likelihood function though, a continuous, smooth parametrisation of the systematic uncertainty must be constructed. This is done using interpolation approaches, which interpolate and extrapolate in a linear or exponential way between the given estimates at the nominal parameter value and the corresponding 1σ up- and downward shifts.

Systematic uncertainties can have an impact on both the absolute normalisation of a background or signal component and on its differential distribution. Slightly different interpolation procedures are chosen for the parametrisation of these two effects, and therefore the impact on the shape is considered after normalising the corresponding histograms to the nominal expected event yields. Considering a single process p, the number of expected events in bin j in channel c can be written as:

$$n_j^p = \phi_{pc}(\boldsymbol{\theta})\eta_{pc}(\boldsymbol{\theta})\nu_{j,pc}(\boldsymbol{\theta}) \tag{6.9}$$

where $\phi_{pc}(\boldsymbol{\theta})$ denotes the product of unconstrained normalisation factors, $\eta_{pc}(\boldsymbol{\theta})$ the product of the normalisation factors corresponding to nuisance parameters reflecting systematic uncertainties and $\nu_{j,pc}(\boldsymbol{\theta})$ denotes the number of events in bin j of the parametrised histogram of the process p in channel c. The impact of nuisance parameters on the shape of the distribution is modelled in the histogram $\nu_{j,pc}$, which uses a piecewise linear interpolation to incorporate the systematic uncertainties:

$$\nu_{j,pc}(\boldsymbol{\theta}) = \nu^0_{j,pc} + \sum_{k\in\mathrm{Syst.}} I_{\mathrm{lin.}}(\theta_k, \nu^0_{j,pc}, \nu^+_{j,pc,k}, \nu^-_{j,pc,k}) \tag{6.10}$$

$$I_{\mathrm{lin.}}(\theta_k, \nu^0_{j,pc}, \nu^+_{j,pc,k}, \nu^-_{j,pc,k}) = \begin{cases} \theta_k(\nu^+_{j,pc,k} - \nu^0_{j,pc}) & \text{for } \theta_k \geq 0 \\ \theta_k(\nu^0_{j,pc,k} - \nu^-_{j,pc,k}) & \text{for } \theta_k < 0 \end{cases} \tag{6.11}$$

where $\nu^0_{j,pc}$ denotes the nominal histogram and $\nu^\pm_{j,pc,k}$ the corresponding histograms where the systematic uncertainty on parameter k was shifted by $\pm 1\sigma$. The normalisation effect is encoded in $\eta_{pc}(\boldsymbol{\theta})$, making use of a piecewise exponential interpolation:

$$\eta_{pc}(\boldsymbol{\theta}) = \prod_{k\in\mathrm{Syst.}} I_{\mathrm{exp.}}(\theta_k, \eta^+_{pc,k}, \eta^-_{pc,k}) \tag{6.12}$$

$$I_{\mathrm{exp.}}(\theta_k, \eta^+_{pc,k}, \eta^-_{pc,k}) = \begin{cases} (\eta^+_{pc,k})^{\theta_k} & \text{for } \theta_k \geq 0 \\ (\eta^-_{pc,k})^{-\theta_k} & \text{for } \theta_k < 0 \end{cases} \tag{6.13}$$

where $\eta^\pm_{pc,k}$ denote the relative impact on the normalisation of process p in channel c by $\pm 1\sigma$ shifts of the parameter k. While the piecewise linear interpolation is the most easy interpolation option, it might lead to a negative number of expected events in case of large values of the nuisance parameters. This nonphysical feature cannot occur in the piecewise exponential interpolation. Since the shape deviations are usually of smaller size than the impact of systematic uncertainties on the normalisation, the piecewise linear interpolation is chosen to parametrise shape effects, while the exponential method is chosen to parametrise normalisation effects. A comparison of the two methods is shown in Fig. 6.2 for one nuisance parameter with its $\pm 1\sigma$ estimates given by $\eta^+ = 1.5$ and $\eta^- = 0.5$.

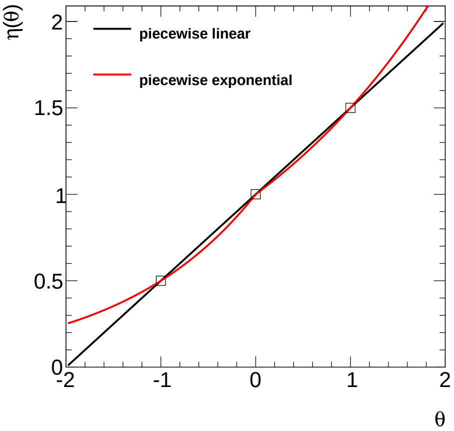

Figure 6.2. *Comparison of the piecewise linear (black line) and piecewise exponential (red line) interpolation of a normalisation factor depending on a single nuisance parameter with its* $\pm 1\sigma$ *shifts given by* $\eta^+ = 1.5$ *and* $\eta^- = 0.5$.

The likelihood function for this analysis is built using the HISTFACTORY [205] and ROOFIT/ROOSTATS [206, 207] software packages. HISTFACTORY constructs the likelihood function based on histograms of expected event yields for all background and signal processes and for all systematic variations. The number of systematic variations is large, and as different aspects of the calibration procedures affect the corresponding physics objects in different ways, various nuisance parameters are assigned to single calibrations. For the description of the jet-energy scale uncertainty for example, eleven different nuisance parameters are used to parametrise uncorrelated effects across different phase-space regions, as detailed in Section 5.7.

Many systematic variations lead to only small variations in the BDT output distributions. Due to bin migration effects the estimates of the systematic variations are subject to statistical fluctuations. To cope with these, three additional modelling steps are performed before using the systematically varied histograms to build the likelihood function. These are summarised in the following.

Smoothing & Symmetrisation

Systematic variations which are estimated by changing parameters in the event reconstruction followed by a repetition of the whole analysis chain suffer from statistical fluctuations with respect to the nominal histogram, occurring due to event migration effects between bins and analysis categories. The actual statistical correlation between the nominal expected event yield per bin and the systematically varied one is hard to estimate without keeping track of an exact identifier of events present in each individual bin in the nominal and varied histograms. These statistical fluctuations complicate the estimation, especially of systematic shape variations. Therefore a smoothing algorithm is exploited to flatten statistical fluctuations in the systematically varied histograms. As the shape of the BDT score distribution for single background components might react in a non-smooth manner to systematic variations, the smoothing algorithm is applied to the ratio between the varied and nominal histograms, which is expected to change more smoothly under a shift in reconstruction and calibration parameters. The smoothed ratio is then used to correct the actual varied histogram by multiplying the ratio with the nominal histogram bin contents.

The smoothing algorithm is denoted as 353QH algorithm [208] and is based on a computation of subsequent medians of the bin contents. In detail, it computes running medians of the bin contents of three bins, which are themselves used as input to compute the median of five such values, serving as starting point to compute the median of three such medians of medians. This is followed by corrections dealing with specific shortcomings of the smoothing based on medians, like for example a flattening of peaks. The algorithm is a standard smoothing algorithm for histograms and implemented within the Root [209] framework. It does not rely on a correct estimate of the statistical uncertainty on the bin content, and instead is based solely on the assumption that the shape of the histogram should change smoothly and not too abrupt.

While the smoothing algorithm is capable to cure most extreme fluctuations, in some cases and in single bins, the up- and downward variations deviate from the nominal expectation in the same direction. In special scenarios, systematic uncertainties might lead to such situations. If for example some strict criteria are used to select the peak position of a reconstructed mass, an up- or downward shift in the energy scale of the reconstructed objects might lead to a decrease in the expected event yields within this mass window. In most cases though such bins with one-sided systematic variations are due to statistical fluctuations in the nominal or systematically varied histograms. In the likelihood minimisation procedure, such bins might lead to ambiguities since two nuisance parameter configurations correspond to the same likelihood value. In extreme cases this might lead to multiple minima in the likelihood function and disturb the minimisation. Therefore, such bins are symmetrised, so that the larger variation is left unchanged while the other variation is set to reflect a variation of the same size but of opposite direction than the first one. This effectively increases the size of the uncertainty compared to the case where no such symmetrisation is applied.

This treatment affects the shape variations only. As mentioned above, the effect on the normalisation of each systematic uncertainty is factorised and treated separately. Figure 6.3 shows six examples out of the most important shape uncertainties, of how the smoothing and symmetrisation affects systematic variations. Figure 6.3 (a) displays the impact of varying one jet-energy scale parameter, which reflects the uncertainty on the η-intercalibration between the central and forward calorimeter, on the VBF $H \to \tau\tau$ BDT output distribution in the VBF category. While the solid lines correspond to the nominal and varied estimates, the dashed lines show the varied histograms after applying the smoothing and symmetrisation algorithms. In the ratio pane, the solid black line indicates the statistical uncertainty on the nominal expectation. Especially in the BDT output range between 0 and 0.7 the impact of the smoothing algorithm can clearly be seen. Figure 6.3 (d) shows the impact of shifting the parameter of the tau-energy scale which corresponds to the in situ calibration based on a fit to the $Z \to \tau_\mu \tau_{\text{had}}$ mass spectrum, on the distribution of $Z/\gamma^* \to \tau\tau$ events in the Boosted category. Here, the last bin in this distribution gives a good example of the effect of the symmetrisation procedure. The same variation for the VBF category is shown in Fig. 6.3 (c). The statistical fluctuations are larger compared to the Boosted category due to the smaller sample size. Figures 6.3 (e) and (f) show the variation of statistical uncertainties on the fake factors of high p_T τ_{had} objects, with $p_T^{\tau_{\text{had}}} > 40$ GeV and $p_T^{\tau_{\text{had}}} > 80$ GeV for the VBF and Boosted categories, respectively. This uncertainty only affects the weights of events entering the background estimate. In such cases, no statistical fluctuations can occur because the events present in the nominal and varied histograms are perfectly correlated. It can be seen that the impact of the smoothing and symmetrisation procedure is negligible on these distributions. The uncertainty on τ_{had} objects of large momentum affects mostly the high BDT output region in the Boosted category, indicating that the BDT selects a phase-space area of large $p_T^{\tau_{\text{had}}}$. Additional plots of some of the most significant systematic shape uncertainties can be found in Figs. B.1 and B.2 of the Appendix.

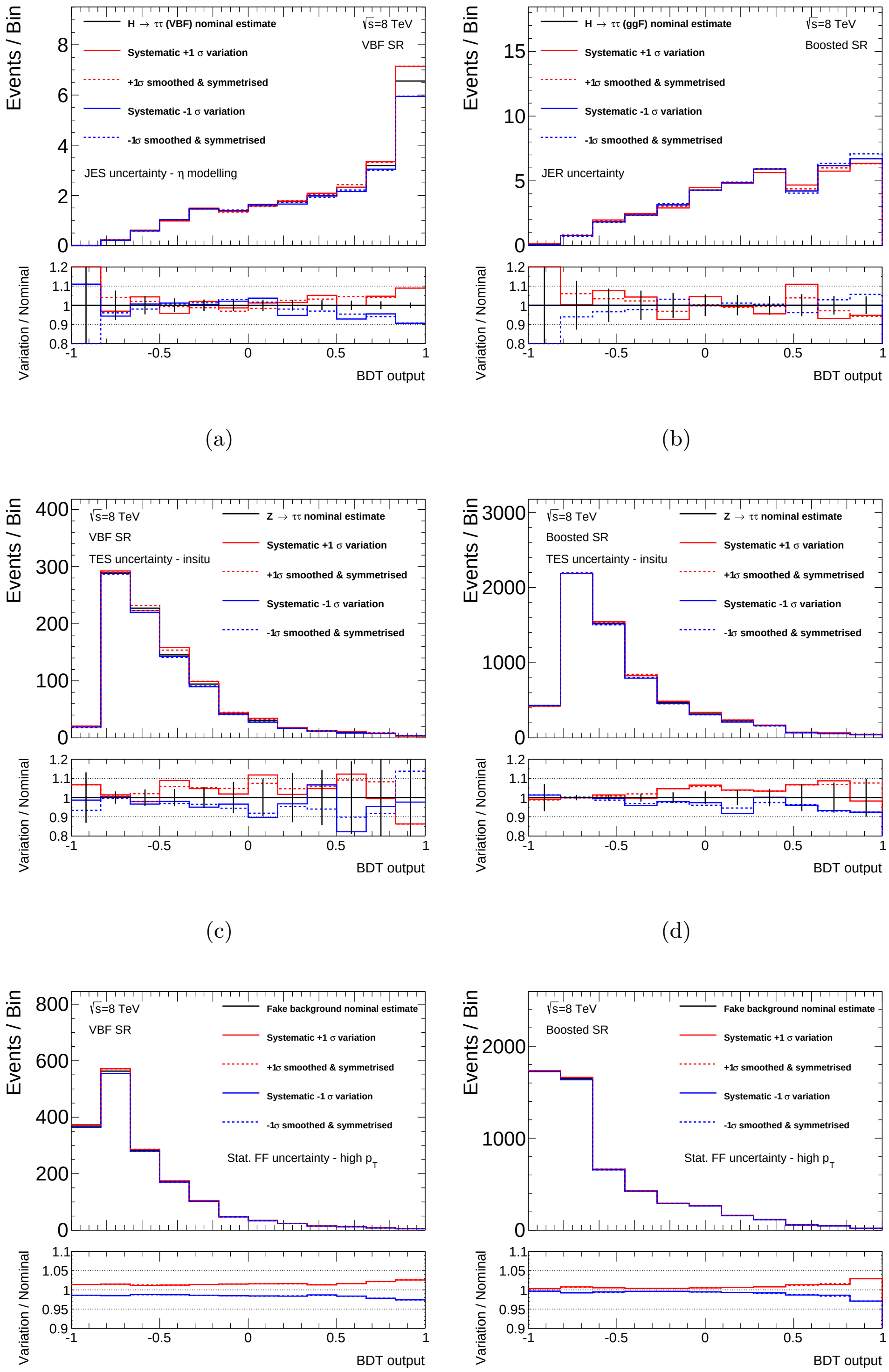

(a) (b)

(c) (d)

(e) (f)

Figure 6.3. *BDT output distributions of signal and background components and the impact of systematic uncertainties on them in the VBF (left) and Boosted (right) categories. The solid black line shows the nominal expected distribution, the solid blue and red lines show the distributions after shifting the corresponding parameter. The dashed lines indicate the impact of the applied smoothing and symmetrisation procedures. Figures (a, b) show uncertainties on the JES η modelling and JER parameters, (c, d) correspond to the TES in situ parameter and (e, f) to the statistical uncertainty on the fake factors.*

Pruning

Many systematic variations are well compatible with the nominal expectation, either because the systematic uncertainty does not affect the shape of the BDT output distribution, or because the limited sample size prevents to resolve the systematic variation. As the complexity of the likelihood function grows rapidly with the number of shape degrees of freedom, it is desirable to reduce their number in cases, where they do not reflect a significant systematic uncertainty. Therefore, a number of tests is applied to each systematic variation in order to decide whether it is implemented as an uncertainty on the shape or as an uncertainty on the normalisation only. They are generally performed before applying any smoothing and symmetrisation corrections, as these might artificially decrease the compatibility between the nominal and varied histograms. These tests are denoted as *pruning* criteria in the following.

- The compatibility between the nominal and varied distributions is tested using the following measure:

  $$\chi_v^2 = \sum_{i \in \text{bins}} \frac{(n_i - v_i)^2}{\max\{\sigma_i^n, \sigma_i^v\}} \tag{6.14}$$

  where n_i and v_i refer to the bin content of the nominal and varied histogram. In the denominator, the maximum among the two statistical uncertainties of the bin contents is chosen instead of their quadrature sum. Due to the unknown correlation between the two bin contents, only the larger uncertainty of the two is considered. Two $\chi_{u/d}^2$ values are obtained for the up- and downward variation respectively. The p-values under a χ^2 distribution with the degrees of freedom given by the number of bins are computed, and the minimal value among the up- and downward variations is used as compatibility measure between the nominal and systematically varied distribution:

  $$p = \min\{p(\chi_u^2), p(\chi_d^2)\} \tag{6.15}$$

  As the statistical correlation between the histograms is not known, this p-value does not reflect an actual probability, but is rather used as an ad hoc measure of compatibility without rigour statistical interpretation. If the value of this measure is below 0.98 the systematic variation is considered as an uncertainty on the shape of the distribution, otherwise it is considered solely as normalisation uncertainty. The threshold of 0.98 was chosen by studying the behaviour of the likelihood fit, and requiring that no double minima are present in the function, that the projections of the likelihood function onto each parameter is sufficiently parabolic and that the expected sensitivity is not artificially increased by removing important systematic shape uncertainties. Pruning criteria based on a *Kolmogorov-Smirnov* compatibility test were considered as well and found to yield comparable results.

- If the maximal relative deviation of the varied distribution among all bins is smaller than 0.5%, the shape degree of freedom is not considered.

- If the maximal deviation of the varied distribution among all bins is smaller than 10% of the statistical uncertainty of the combined background in this bin, the shape degree of freedom is not considered. This pruning criteria is only applied on background processes, in order to reduce the number of shape uncertainties on small background components without significant impact on the uncertainty of the combined background expectation.

In general, no pruning is applied to systematic variations which correspond to variations of the event weights only.

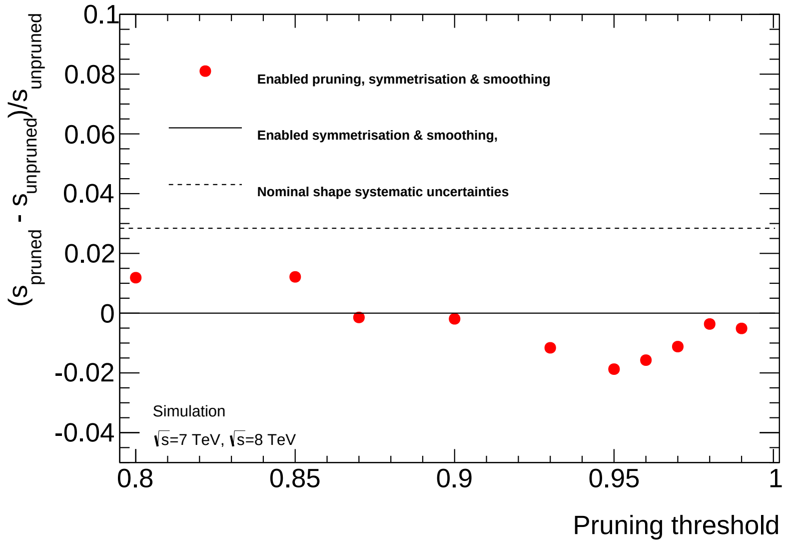

Figure 6.4. *Relative difference in the expected discovery significance of the analysis when applying the pruning criteria to systematic shape variations (red dots) with respect to the expected significance if no such criteria are applied (solid black line). In addition, the dashed line indicates the difference in the expected significance if neither pruning, smoothing nor symmetrisation algorithms are applied to the systematic shape variations. While the symmetrisation procedure lowers the expected significance by about* 3%*, the pruning criteria with a threshold of* 0.98 *do not alter the sensitivity significantly.*

Figure 6.4 shows the impact of the pruning and symmetrisation algorithms on the expected discovery significance of the analysis, as defined below in Section 6.3. The symmetrisation procedure effectively increases the systematic uncertainties and therefore lowers the expected significance by about 3%. Applying pruning criteria with a threshold of 0.98 has negligible impact on the sensitivity, while tighter pruning thresholds would lead to larger differences of up to 2%. Interestingly, the sensitivity is lowered for values of the pruning threshold above 0.95 with respect to the case were no pruning is applied, while pruning thresholds below 0.95 lead to an increase in the sensitivity. To understand this behaviour, it is important to keep in mind that one single nuisance parameter corresponds to shape and normalisation effects, while only the shape effects are subject to the pruning criteria. Reducing the number of systematic shape uncertainties with large statistical fluctuations, and which are highly compatible with the nominal expectations, can lead to an effectively less constrained background estimate, since normalisation uncertainties get decoupled from fluctuating shape variations. The total number of systematic shape variations across all samples in the VBF category of the $\sqrt{s} = 8$ TeV analysis gets reduced from 159 to 90 by applying the chosen pruning criteria, reducing the computation time for a single likelihood fit by about 35%.

6.2.2. Integration of Statistical Uncertainties

Statistical uncertainties on the background expectation are integrated into the likelihood using the same mechanism of subsidiary measurements as used to integrate systematic uncertainties. The difference lies in the choice of the additional term multiplied to the combined likelihood function. The background expectation in a bin is given as the sum of background expectations for single processes as defined in Eq. (6.9), where $\nu_{j,pc}$ denotes the nominal expectation for process p. This expectation is the result of some background estimation, for example based on a simulated event sample. In all cases, this event yield is the result of a sum of weighted events, where the event weights depend on the background estimation technique. They might for example correspond to the luminosity weighted cross section of this process in case of simulated events. The number of unweighted events n_j^{u} can be thought of as result of a subsidiary measurement which follows a Poisson distribution of unknown mean $n_j^{\mathrm{u}}\gamma$, where γ parametrises the deviation of this mean from n_j^{u}. The outcome of this subsidiary measurement can then be used to constrain the number of expected background events in the actual signal region by applying the event weight. In case of non-constant event weights, they can be replaced by a constant effective weight instead. Therefore, the nominal background expectation b_j in Eq. (6.2) is replaced by $\gamma_j b_j$, and the likelihood function multiplied by the likelihood of the subsidiary measurement:

$$P_{\mathrm{Pois.}}(\gamma_j) = \frac{(\gamma_j n_j^{\mathrm{u}})^{n_j^{\mathrm{u}}}}{n_j^{\mathrm{u}}!} e^{-\gamma_j n_j^{\mathrm{u}}} \tag{6.16}$$

To reduce the number of nuisance parameters, it is convenient to apply such a constraint term to the sum of all backgrounds in each bin rather than to each individual component. Therefore, effective weights need to be used. Often the number of unweighted events is unknown. If the relative statistical uncertainty of the expected background in bin j is given by σ_j, the effective number of unweighted events can be estimated as

$$n_j^{\mathrm{u}} = \sigma_j^{-2} \tag{6.17}$$

since the effective event weight acts as a constant scale factor and this approximation holds in the limit of constant event weights. Usually this estimate will yield non-integer values and therefore Eq. (6.16) is replaced by a Gamma distribution:

$$P_{\Gamma}(\gamma_j) = C \frac{(\gamma_j)^{\sigma_j^{-2}}}{\Gamma(\sigma_j^{-2} + 1)} e^{-\gamma_j / \sigma_j^2} \tag{6.18}$$

where C is a constant scale factor which can be neglected as it does not alter the position of the minimum.

Because the statistical uncertainty on the background estimate is small compared to the systematic uncertainties in the low BDT output region, the γ nuisance parameters are only introduced for bins in which the relative statistical uncertainty is larger than 5%. This has negligible impact on the result of the analysis, but makes the minimisation of the likelihood considerably faster. As the statistical power of the simulated signal samples is larger, no statistical uncertainty is considered for the signal expectation.

6.3. Hypothesis Testing

The results of searches for new processes are usually reported in terms of the significance of an observed excess in data over the expected number of background events, or as an upper limit on the product of the signal process cross section and branching ratio, in case no excess is observed. For this purpose, hypothesis tests are carried out to quantify the compatibility of the data with either the background-only or the signal-plus-background hypothesis. A test statistics t_μ is defined and serves as a measure of the compatibility between data and the expected event yields at a signal strength hypothesis of μ. To compute for example the significance of an excess in data, the p-value under the background-only hypothesis is computed as[2]

$$p = \int_{t^{\mathrm{obs}}}^{\infty} f(t|H_0)dt \tag{6.19}$$

where $f(t|H_0)$ is the PDF of the test statistics, given that the background hypothesis H_0 is true. It yields the probability, under the assumption of the background-only hypothesis, to observe greater incompatibility to the background expectation than actually present in data. This p-value can then be converted into the equivalent significance Z in terms of Gaussian standard deviations

$$Z = \Phi^{-1}(1-p) \tag{6.20}$$

where Φ^{-1} is the inverse of the cumulative distribution of a standard Gaussian. Commonly, the background-only hypothesis is called rejected if a p-value of $p \leq 2.87 \cdot 10^{-7}$ is found, which corresponds to a significance of 5σ. A significance larger than 3σ is usually denoted as *evidence* for the presence of a signal. If no excess is found, an upper limit is computed by finding the signal event rate which can still be rejected at a certain confidence level. For this purpose a p-value threshold of 0.05 is usually chosen. Slightly different test statistics are used for either discovery or limit setting and are defined below.

---

[2] Here it is assumed, without loss of generality, that larger incompatibility results in larger values of the test statistics.

In case of a simple likelihood function which does not depend on nuisance parameters, the Neyman-Pearson lemma [210] states that the optimal test statistics discriminating between two hypotheses is given by the ratio of the corresponding likelihood functions. Incorporating the effect of systematic uncertainties, the following test statistics is defined to test the compatibility of data with the background-only hypothesis:

$$q_0 = \begin{cases} -2\ln\left(\frac{L(\mu=0,\hat{\hat{\boldsymbol{\theta}}})}{L(\hat{\mu},\hat{\boldsymbol{\theta}})}\right) & \text{for } \hat{\mu} \geq 0 \\ 0 & \text{for } \hat{\mu} < 0 \end{cases} \tag{6.21}$$

As above, the notation $L(\mu = 0, \hat{\hat{\boldsymbol{\theta}}})$ refers to the conditional minimum of the likelihood function obtained from a minimisation with a fixed value of $\mu = 0$. Since $L(\hat{\mu}, \hat{\boldsymbol{\theta}})$ corresponds to the global minimum of the likelihood, higher values of q_0 correspond to greater incompatibility between data and the no-signal hypothesis. The test statistics is defined piecewise with respect to the best-fit value of the signal strength parameter, to ensure that a downward fluctuation of the background resulting in $\hat{\mu} < 0$ is not interpreted as incompatibility with respect to the background-only hypothesis. The PDF of this test-statistics can be either obtained by using Monte Carlo sampling methods or by exploiting asymptotic formulae. In the limit of a large sample size, the PDF $f(q_0|\mu')$ of the test statistics q_0, under the assumption of a signal strength μ', can be analytically expressed as shown in Ref. [211]. Since the number of Monte Carlo toy experiments needed to precisely determine the PDF in the tails of the distribution to allow for the computation of p-values at the level of 10^{-7} is large, these asymptotic formulae present a valuable simplification of the process. It was verified, that the use of the asymptotic formulae give accurate results for the sample sizes present in this analysis.

In order to quote the expected discovery significance in the presence of signal, the p-value under the distribution $f(q_0|0)$ is computed for the so-called *Asimov dataset*, a pseudo-dataset defined by the background-plus-signal expectation. Since it depends on the values of the nuisance parameters, it is common to first determine their values in a conditional fit with $\mu = 1$ fixed to the SM signal strength and to use these values to construct the Asimov dataset. Figure 6.5 shows the distribution of the test statistics, using the asymptotic formulae, under the background and signal-plus-background hypotheses. The dashed line corresponds to the value of q_0 given by the Asimov dataset. Computing the p-value, which corresponds to the integral indicated by the blue area, yields an expected discovery significance of 2.4σ of the combined $\sqrt{s} = 7$ TeV and $\sqrt{s} = 8$ TeV searches for $H \to \tau_{\text{lep}}\tau_{\text{had}}$ decays.

To set upper limits on the signal-strength parameter, the compatibility of data with some hypothesised values of μ is tested instead. For this, a similar test statistics is used:

$$q_\mu = \begin{cases} -2\ln\left(\frac{L(\mu,\hat{\hat{\boldsymbol{\theta}}})}{L(\hat{\mu},\hat{\boldsymbol{\theta}})}\right) & \text{for } \hat{\mu} \leq \mu \\ 0 & \text{for } \hat{\mu} > \mu \end{cases} \tag{6.22}$$

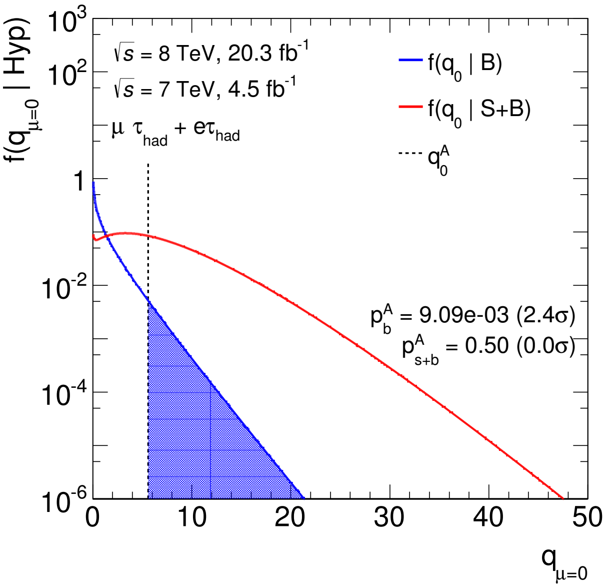

Figure 6.5. *Distribution of the test statistics* q_0 *under the background (blue) and signal-plus-background (red) hypothesis for the search for* $H \to \tau_{\text{lep}}\tau_{\text{had}}$ *decays. The dashed line indicates the expected discovery significance, as given by the Asimov dataset, corresponding to* 2.4σ.

To construct the limit, the p-value for a given hypothesised signal strength μ^{hyp} is computed, starting with sufficiently small values of μ^{hyp}. Increasing μ^{hyp} stepwise until the p-value exceeds the pre-defined confidence level threshold allows to find the smallest signal strength which can still be excluded at the given confidence level. The full procedure to construct limits and their corresponding uncertainties is further detailed in Refs. [211, 212].

6.4. Results

As discussed previously, the signal strength parameter μ is determined along with the overall normalisation parameters of the background components from $Z/\gamma^* \to \tau\tau$ and top-quark events and the estimators of all other nuisance parameters reflecting systematic uncertainties. The combined likelihood fit includes the four BDT output distributions and the four single binned top-quark control regions. Figure 6.6 shows the BDT output distributions as resulting from the maximisation of the likelihood and the ratio between data and the signal-plus-background model. In addition, the ratio between the signal-plus-background and the background-only model is shown, demonstrating the preference for a signal contribution in the high BDT score region. The best estimate of the signal strength parameter is found to be

$$\hat{\mu} \;= 0.98\ ^{+0.35}_{-0.33}(\text{stat.})\ ^{+0.36}_{-0.30}(\text{syst.})\ \pm 0.06(\text{theo. syst.})$$

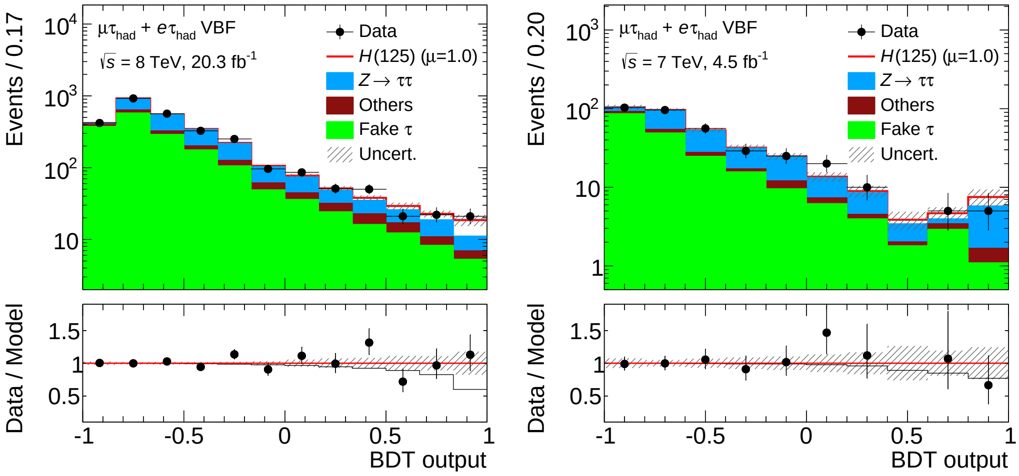

(a) 8 TeV - VBF SR (b) 7 TeV - VBF SR

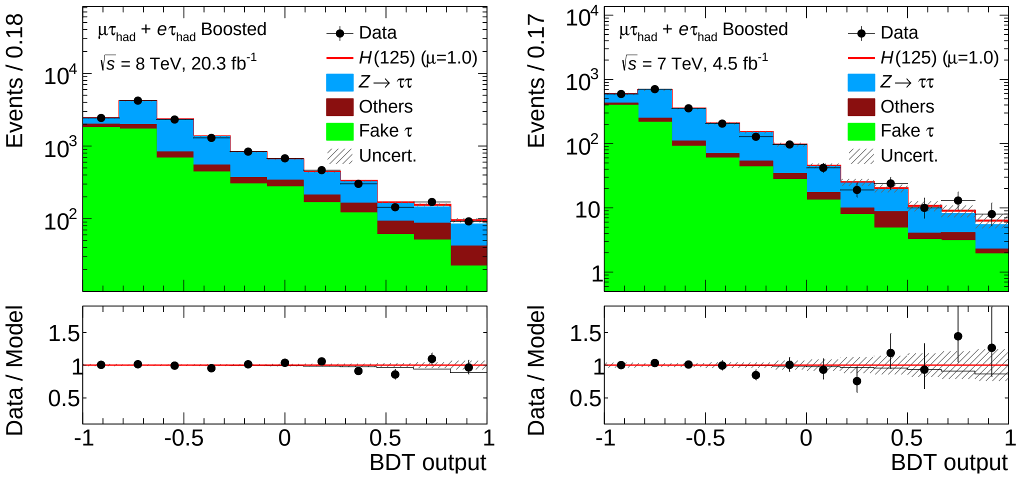

(c) 8 TeV - Boosted SR (d) 7 TeV - Boosted SR

Figure 6.6. *Distributions of the BDT output in the signal regions of the VBF (top) and Boosted (bottom) categories of the 8 TeV (left) and 7 TeV (right) analysis after the maximum likelihood fit of the combined model to data. The lower panel shows the ratio between data and the signal-plus-background model as well as the ratio between the background-only and combined model. The hatched band corresponds to the statistical and systematic uncertainty of the combined model.*

at a Higgs boson mass hypothesis of $m_H = 125$ GeV. The systematic uncertainties are split into two groups, theoretical uncertainties on the inclusive Higgs boson production cross-section and $H \rightarrow \tau\tau$ branching ratio, and all other systematic uncertainties including all experimental effects as well as theoretical uncertainties on the signal region acceptance from the QCD scale and PDF choice.

Tables 6.1 and 6.2 summarise the fitted signal and background yields in the VBF

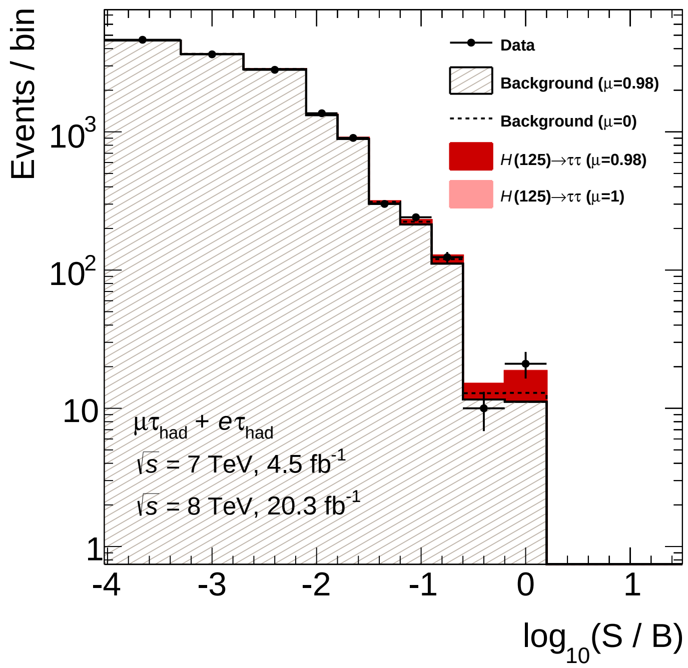

Figure 6.7. *Event yields as a function of* $\log_{10}(S/B)$ *of all categories entering the combined fit. The signal and background yields* S *and* B *are taken from the respective BDT output bin. The nominal background corresponds to the result of the unconditional fit, while the dashed line indicates the background estimate after a fit in which the signal strength parameter is fixed to zero, indicating the level of incompatibility of the background-only-hypothesis with data.*

and Boosted categories of the $\sqrt{s} = 8$ TeV and $\sqrt{s} = 7$ TeV analyses, respectively. In addition, the event yields in the two highest bins of the BDT output distributions are given. Figure 6.7 shows the event yields of all categories as a function of $\log_{10}(S/B)$ of each bin entering the fit. The fitted background contribution is shown along with the result of a fit of the background-only model, indicating the level of its incompatibility with data while taking into account all systematic uncertainties.

Testing the observed data against the background-only-hypothesis results in a p-value of $9.98 \cdot 10^{-3}$, while a p-value of $9.09 \cdot 10^{-3}$ is expected from the signal-plus-background Asimov data, as discussed in Section 6.3. This corresponds to an observed (expected) significance of 2.3σ (2.4σ) in terms of Gaussian standard deviations.

Figure 6.8 further compares the resulting $\hat{\mu}$ values when fitting individual categories or datasets, indicating a consistent result across all categories. As expected, the VBF category of the $\sqrt{s} = 8$ TeV analysis dominates the combined measurement of μ. To estimate the individual contributions of statistical, systematic and theoretical uncertainties, the fit is repeated with either all nuisance parameters, or only those sets describing experimental (theoretical) systematic uncertainties, fixed to their

Process/Category	VBF			Boosted		
	Total	2nd last bin	Last bin	Total	2nd last bin	Last bin
Fake backgrounds	1680 ± 50	8.3 ± 0.9	5.3 ± 0.7	5630 ± 170	51.0 ± 2.5	22.4 ± 1.8
$Z/\gamma^* \to \tau\tau$	883 ± 33	7.9 ± 1.0	4.2 ± 0.8	6220 ± 180	59.2 ± 3.3	43 ± 4
Top	87 ± 16	0.1 ± 0.5	0.6 ± 0.4	400 ± 60	12 ± 4	4.9 ± 1.8
Diboson	67 ± 13	1.1 ± 0.4	0.53 ± 0.22	440 ± 50	9.9 ± 2.5	5.3 ± 1.8
$Z \to \ell\ell$	49 ± 23	1.4 ± 0.9	0.52 ± 0.35	210 ± 60	14 ± 6	10 ± 4
$ggF : H \to \tau\tau$ ($m_H = 125$ GeV)	12 ± 6	0.8 ± 0.4	0.9 ± 0.6	39 ± 20	6.1 ± 3.1	6.7 ± 3.3
$VBF : H \to \tau\tau$	22 ± 10	3.2 ± 1.5	6.5 ± 3.0	11 ± 5	1.8 ± 0.8	2.0 ± 0.9
$WH : H \to \tau\tau$	0.36 ± 0.30	< 0.1	< 0.1	6.5 ± 3.0	1.0 ± 0.5	1.4 ± 0.7
$ZH : H \to \tau\tau$	0.12 ± 0.07	< 0.1	< 0.1	3.2 ± 1.5	0.54 ± 0.25	0.66 ± 0.30
Total background	2770 ± 40	18.8 ± 2.5	11.2 ± 3.3	12890 ± 110	146 ± 7	85 ± 6
Total signal	35 ± 16	4.0 ± 1.8	7.4 ± 3.4	60 ± 28	9 ± 4	11 ± 5
Data	2830	22	21	12952	170	92

Table 6.1. *Event yields as resulting from a fit to data in the two categories of the $\sqrt{s} = 8$ TeV analysis, as well as in the two highest bins of each distribution. The uncertainties on the total background and signal yields reflect the full statistical and systematic uncertainty, while the uncertainties on the individual background components reflect the full systematic uncertainty only.*

Process/Category	VBF			Boosted		
	Total	2nd last bin	Last bin	Total	2nd last bin	Last bin
Fake backgrounds	202 ± 19	2.9 ± 0.5	1.1 ± 0.4	870 ± 70	3.1 ± 0.7	1.9 ± 0.6
$Z/\gamma^* \to \tau\tau$	121 ± 9	0.5 ± 0.5	4.1 ± 1.3	1200 ± 70	4.1 ± 1.7	3.2 ± 1.1
Top	10 ± 5	0.36 ± 0.34	0.5 ± 0.4	49 ± 12	0.61 ± 0.28	0.15 ± 0.17
Diboson	6.7 ± 1.5	< 0.1	< 0.1	41 ± 5	0.20 ± 0.10	< 0.1
$Z \to \ell\ell$	4.4 ± 1.5	< 0.1	< 0.1	32 ± 7	0.22 ± 0.20	0.11 ± 0.04
$ggF : H \to \tau\tau$ ($m_H = 125$ GeV)	1.5 ± 0.8	0.21 ± 0.11	0.32 ± 0.19	6.1 ± 3.1	0.51 ± 0.27	0.53 ± 0.28
$VBF : H \to \tau\tau$	3.2 ± 1.5	0.50 ± 0.24	1.4 ± 0.7	2.0 ± 0.9	0.17 ± 0.08	0.16 ± 0.08
$WH : H \to \tau\tau$	< 0.1	< 0.1	< 0.1	1.0 ± 0.5	0.10 ± 0.05	0.12 ± 0.06
$ZH : H \to \tau\tau$	< 0.1	< 0.1	< 0.1	0.8 ± 0.4	< 0.1	< 0.1
Total background	344 ± 17	4.0 ± 0.9	5.8 ± 1.8	2190 ± 50	8.2 ± 1.9	5.5 ± 1.5
Total signal	4.7 ± 2.2	0.71 ± 0.34	1.7 ± 0.8	10 ± 5	0.8 ± 0.4	0.9 ± 0.4
Data	349	5	5	2199	13	8

Table 6.2. *Event yields as resulting from a fit to data in the two categories of the $\sqrt{s} = 7$ TeV analysis, as well as in the two highest bins of each distribution. The uncertainties on the total background and signal yields reflect the full statistical and systematic uncertainty, while the uncertainties on the individual background components reflect the full systematic uncertainty only.*

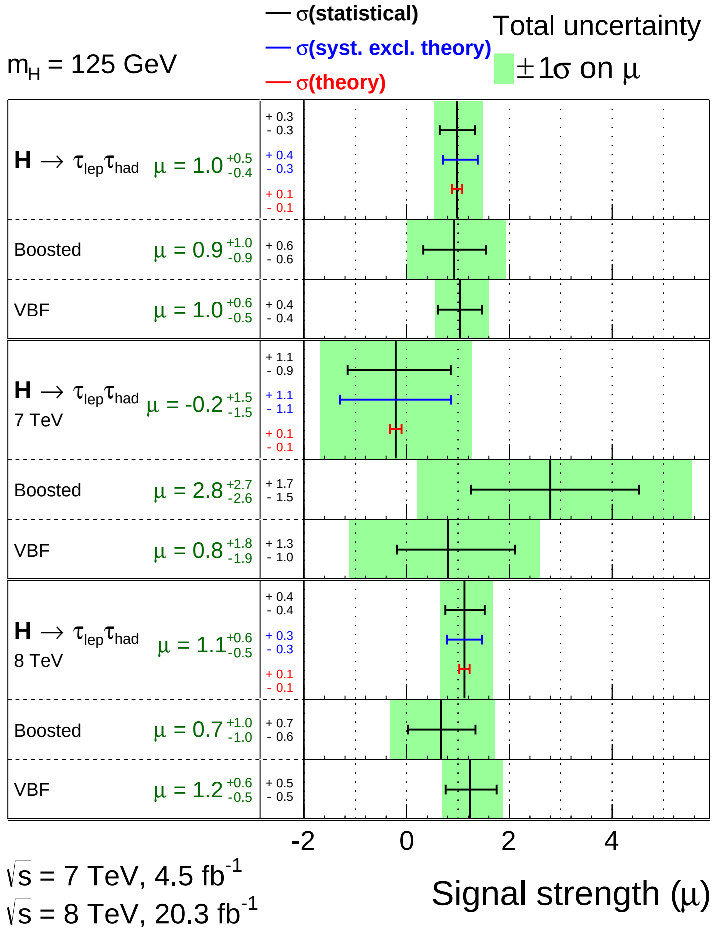

Figure 6.8. *Estimates of the signal strength parameter as resulting from fits in individual categories and datasets. While the green band indicates the total uncertainty, in addition the uncertainty contributions from statistical, experimental and theoretical systematic uncertainties are indicated.*

best estimates from the unconditional fit. The uncertainty due to systematic and theoretical uncertainties is then estimated by subtracting the uncertainty on $\hat{\mu}$ in quadrature from the total uncertainty of the nominal fit result. The overall uncertainty of the measurement is roughly equally affected by the statistical uncertainty arising from the total number of events in the signal and control regions and the systematic uncertainties. While comparing individual signal strength parameters in the categories of the analysis underlines the consistency of the results, it is physically more interesting to estimate the signal strength of the gluon-fusion production process and processes evolving through couplings between gauge bosons and the Higgs boson, as the VBF and Higgs-strahlung processes. This results in a measurement of the two parameters of

$$\begin{aligned}\hat{\mu}_{\mathrm{VBF+VH}} &= 1.19\ ^{+0.66}_{-0.60}(\mathrm{stat.})\ ^{+0.40}_{-0.35}(\mathrm{syst.})\\ \hat{\mu}_{\mathrm{ggH}} &= 0.35\ ^{+1.06}_{-1.05}(\mathrm{stat.})\ ^{+1.33}_{-1.21}(\mathrm{syst.})\end{aligned}$$

evaluated at a Higgs boson mass hypothesis of $m_H = 125$ GeV. Again, it becomes evident that the sensitivity of the measurement is dominated by the contribution from the VBF signal process. The two signal strength parameters are well compatible with the SM expectation of unity.

To further detail the impact of individual uncertainties on the result, each nuisance parameter is fixed to its $\pm 1\sigma$ estimates and the impact on $\hat{\mu}$ is evaluated after re-minimising the likelihood with respect to all other parameters of the model. The absolute change in the fitted signal strength parameter $\Delta\hat{\mu}$ with respect to the nominal estimate is then used to order all nuisance parameters based on their importance for the measurement. The black markers in Fig. 6.9 display the deviations of the best-fit values of the 25 highest ranked nuisance parameters from their prefit estimates. The parameter names are printed in black for systematic experimental uncertainties, in red for theoretical uncertainties, in cyan for statistical uncertainties of the background model and in violet for normalisation parameters. While nuisance parameters which are constrained by a normalised Gaussian subsidiary measurement, as it was discussed in Section 6.2.1, are expected to have uncertainties of the order one, previously unconstrained parameters like the normalisation factors are not normalised and therefore feature considerably smaller absolute uncertainties. In addition, the hatched blue bands indicate the impact of each nuisance parameter on $\hat{\mu}$, when varying them by $\pm 1\sigma$. For parameters constrained by subsidiary measurements, the yellow band quantifies the impact on $\hat{\mu}$ when the parameter is varied by ± 1, corresponding to the prefit uncertainty. The highest ranking parameter is a nuisance parameter parametrising the statistical uncertainty of the background estimate in the highest BDT output bin of the $\sqrt{s} = 8$ TeV VBF category. The most important systematic uncertainties are components of the jet-energy scale uncertainty, the uncertainty on the description of the probability of electrons to be misidentified as τ_{had} objects, as well as theoretical uncertainties on the Higgs boson branching ratio to tau leptons and the renormalisation and factorisation scales used in the cross-section calculation of the gluon-fusion signal process. The best-fit values of two nuisance parameters deviate significantly from their prefit estimates. The parameter describing the uncertainty of the tau-energy scale in the $\sqrt{s} = 7$ TeV data, and the parameter describing the uncertainty on the isolation requirement in the embedding procedure in $\sqrt{s} = 7$ TeV data. The TES parameter is estimated to be about 1σ lower than its nominal value. As discussed in Chapter 4, the tau-energy scale in data taken in 2012 was calibrated based on a fit to the visible mass spectrum of $Z \to \mu^+\mu^-$ events. Due to the limited amount of data available in 2011, such a correction was not derived for the $\sqrt{s} = 7$ TeV dataset. Nevertheless, a similar shift was indicated by the single particle response measurement using $\sqrt{s} = 7$ TeV data,[3] which is compatible with the preferred value of the discussed nuisance parameter. The prefit uncertainty of the NP reflecting the embedding isolation uncertainty in $\sqrt{s} = 7$ TeV data is estimated by varying the isolation requirement as detailed in Section 5.5.1. This procedure is ad-hoc in the sense that the one standard deviation estimates do not reflect the uncertainties of an actual measurement. The shift of the parameter can therefore not be interpreted

---

[3] The corresponding analysis of $\sqrt{s} = 8$ TeV data is detailed in Section 4.1.

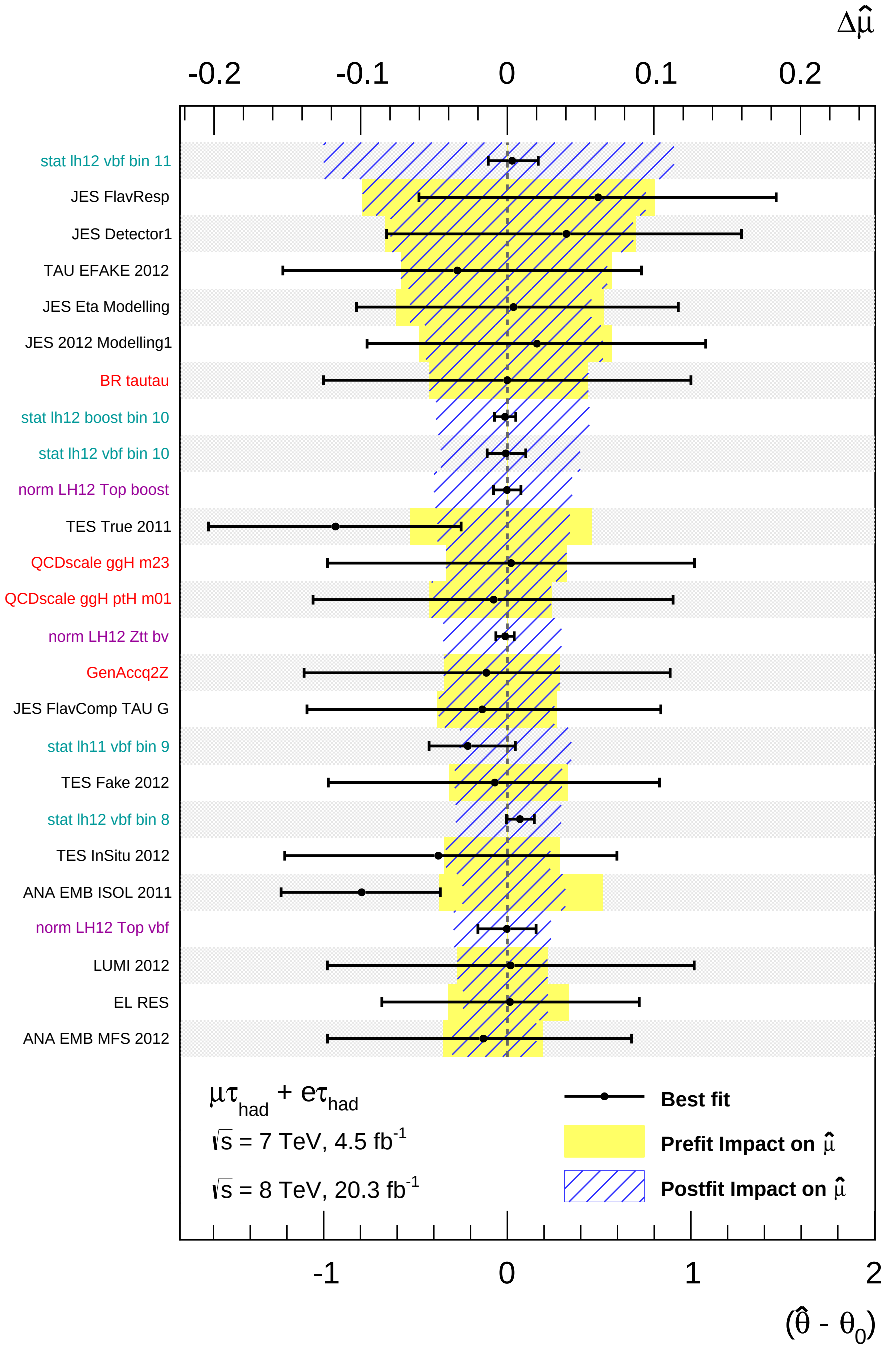

Figure 6.9. *Fitted values of the 25 nuisance parameters with the largest impact on the signal strength parameter μ. The black dots and the lower axis indicate the best-fit value of the nuisance parameter with respect to its prefit estimate. The hatched band and the upper axis shows how the best estimate of μ changes if the corresponding nuisance parameter is fixed to its $\hat{\theta} \pm 1\sigma$ values. For the systematic uncertainties, the yellow band indicates the change in $\hat{\mu}$ if the parameter is varied by its prefit uncertainties $\hat{\theta} \pm 1$. The nuisance parameter names are printed in black for systematic uncertainties, in red for theoretical uncertainties, in cyan for statistical uncertainties on the background model and in violet for freely floating normalisation parameters. An explanation of the nuisance parameter names can be found in Appendix C.*

in a standard frequentist manner. All freely floating normalisation factors are well compatible with their prefit estimates.

6.4.1. Validation of the Maximum Likelihood Fit

Different validation tests are performed to ensure the validity of the likelihood function and the minimisation procedure. As already touched upon in Section 6.2.1, special care is taken to avoid multiple minima in the likelihood function. The likelihood profiles as function of all parameters are studied and a sufficiently parabolic behaviour in the proximity of the global minimum is found. Figure 6.10 (a) shows, as one example, the likelihood profile as a function of μ with respect to the global minimum. Besides these one-dimensional profiles, two-dimensional inter-dependencies between all parameters of the model are tested. For a series of fixed values of parameter θ_1 the likelihood is minimised and the resulting value of a parameter θ_2 studied. Figure 6.10 (b) shows the dependence of six of the highest ranked nuisance parameters on μ. In the presence of concurring secondary local minima, the best-fit values of some nuisance parameters would exhibit discontinuities at the value of μ corresponding to the boundary at which the likelihood minimisation procedure would switch between the different minima. The fact that the nuisance parameters vary smoothly as a function of μ indicates the absence of such secondary local minima.

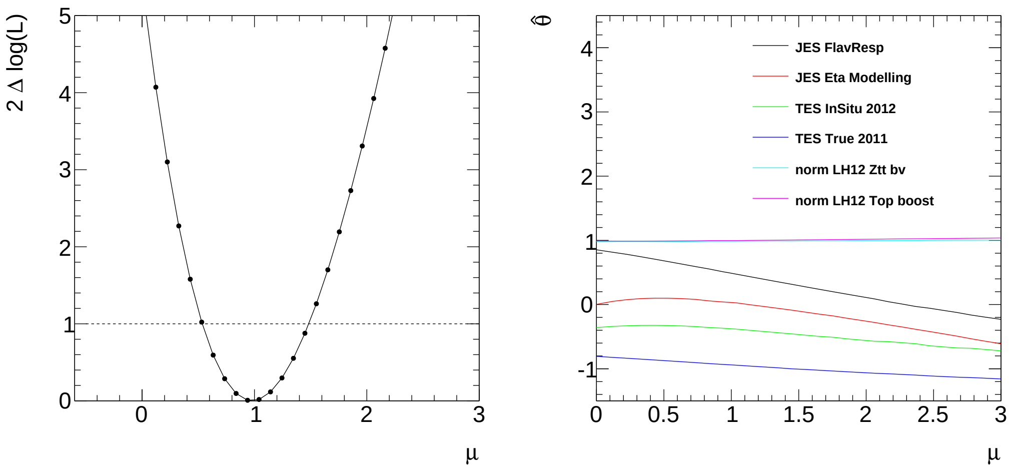

(a) (b)

Figure 6.10. *Figure (a) shows the likelihood profile as a function of μ, illustrating the parabolic shape of the likelihood if profiled as a function of the signal strength parameter. Figure (b) shows how the best-fit values of some of the most important nuisance parameters evolve with varying values of μ, demonstrating a smooth dependence of these parameters on the signal strength parameter. An explanation of the nuisance parameter names can be found in Appendix C.*

During the minimisation procedure, the covariance matrix of the model is estimated [206, 209]. Figure 6.11 shows the mutual correlation coefficients between the signal strength parameter and the same 25 top-ranked nuisance parameters which were discussed and shown in Fig. 6.9. Large correlation coefficients would indicate potential degeneracies between the parameters. The largest correlations are of the order of -25% and are found between dominant systematic uncertainty parameters and freely floating normalisation parameters as for example between the normalisation of the $Z/\gamma^* \to \tau\tau$ background and one TES parameter. Since in these cases the nuisance parameters reflect a sizeable uncertainty on the acceptance of the respective background sample, this behaviour is indeed expected.

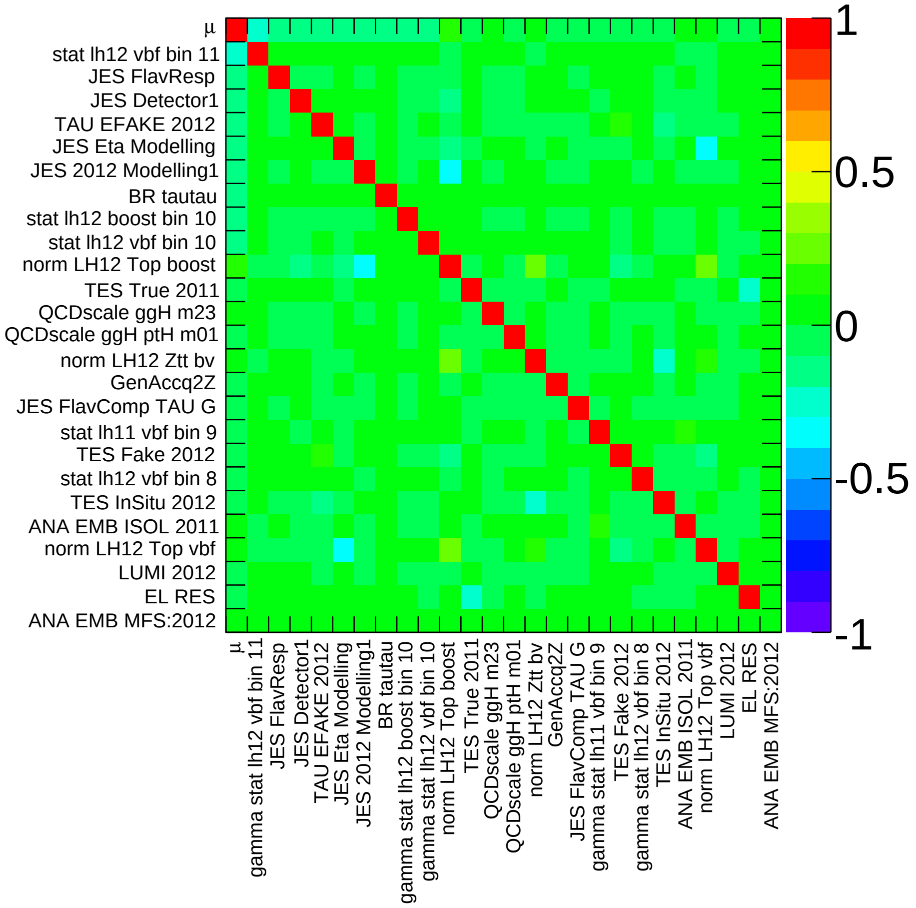

Figure 6.11. *Mutual correlation coefficients of the 25 nuisance parameter with the highest impact on μ. An explanation of the nuisance parameter names can be found in Appendix C.*

7 Combined Search for $H \to \tau\tau$ Decays

In the previous chapter, the results of the search for $H \to \tau\tau$ decays in the lepton-hadron final state were presented. The ATLAS collaboration performed similar analyses in the fully leptonic ($\tau_{\rm lep}\tau_{\rm lep}$) and fully hadronic ($\tau_{\rm had}\tau_{\rm had}$) final states. Like the analysis presented above, these searches are based on BDT classifiers trained in VBF and Boosted categories, targeting the same signal event topologies as discussed for the $\tau_{\rm lep}\tau_{\rm had}$ analysis. The event selection criteria in the three final states are fully orthogonal to each other, which allows for a statistical combination of the individual results. In this chapter, the results of the search in the two other final states as well as the results of the combined search for $H \to \tau\tau$ decays are reviewed. All analyses as well as their combination are documented in Ref. [196]. In the course of this thesis, significant contributions to the statistical combination were made.

7.1. Search in the $\tau_{\rm lep}\tau_{\rm lep}$ Final State

The fully leptonic final state accounts for a branching fraction of about 12.4% of all $H \to \tau\tau$ events. Along with the two experimentally well reconstructable leptons, four neutrinos are part of the final state and limit the resolution of the reconstructed ditau mass. The same mass-reconstruction algorithm as discussed for the lepton-hadron final state in Section 5.1.3 is used, with small modifications to account for the additional neutrino. Apart from the $Z \to \tau\tau$ background, important background contributions arise from $Z \to \ell\ell$ and $t\bar{t}$ events. Same flavour (SF) final states containing two electrons or muons of opposite electric charge are considered as well as final states with different flavour (DF) leptons ($e\mu$) with OS charge. Events are selected by single and dilepton triggers, with online p_T thresholds ranging from 6 GeV to 24 GeV, depending on the trigger object and data taking period. Different offline p_T selection criteria are applied to the leptons, ranging from 10 GeV for muons in DF final states to 26 GeV for the leading electron in ee final states. Events with a reconstructed hadronic tau candidate are rejected to ensure orthogonality to the $\tau_{\rm lep}\tau_{\rm had}$ and $\tau_{\rm had}\tau_{\rm had}$ analyses. A variety of additional preselection criteria reject background events and are chosen to be more stringent for SF events due to the higher background contamination from $Z \to \ell\ell$ decays. A veto of events with identified b-jets suppresses contributions from top-quark events. The two analysis categories are defined similarly to the $\tau_{\rm lep}\tau_{\rm had}$ analysis presented above. A VBF category is defined by requiring two jets separated by

$\Delta\eta_{jj} > 2.2$, and a requirement on the reconstructed transverse momentum of the Higgs boson candidate of $p_T^H > 100$ GeV defines the Boosted category. Two BDTs are trained in the two categories using similar input variables as discussed above for the lepton-hadron case.

The background from $Z \to \tau\tau$ events is estimated using the same embedding technique as discussed above. Its absolute normalisation is estimated in the maximum likelihood fit independently from the normalisation of $Z \to \tau\tau$ events in the other two final states, to allow for potential differences in the modelling of the selection efficiency due to the different trigger objects and final state particles. Background events from Drell-Yan $Z \to ee$ and $Z \to \mu\mu$ events, as well as background contributions from $t\bar{t}$ events with two real leptons in the final state are estimated by simulated event samples normalised to data in respective control regions. Events with misidentified lepton candidates are modelled using a template-fit method. A control region enriched in such events is constructed by reverting the isolation criteria for one of the leptons. It is then used to estimate the shape of the differential distributions, while the absolute normalisation is extracted from a fit to the p_T spectrum of the sub-leading lepton candidate.

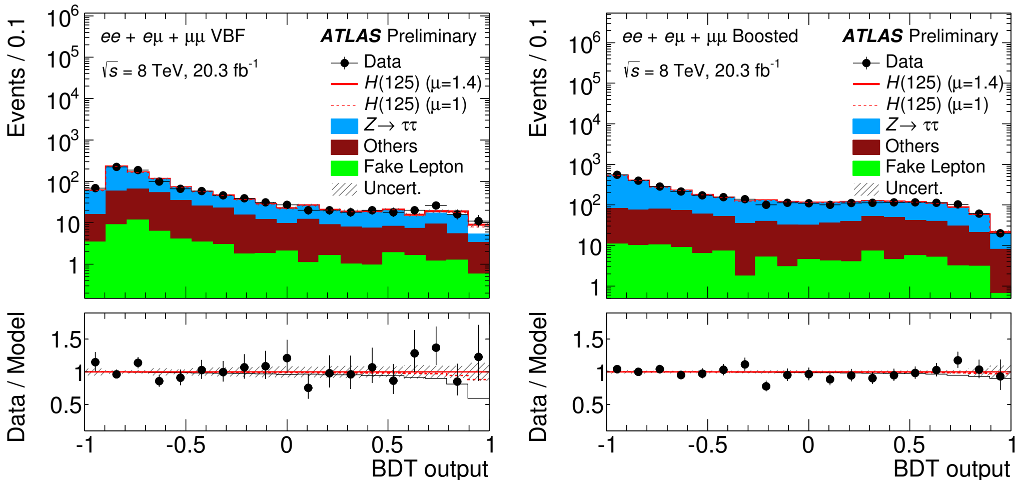

(a) (b)

Figure 7.1. *Distributions of the BDT output in the signal regions of the VBF (a) and Boosted (b) categories of the 8 TeV analysis in the $\tau_{\text{lep}}\tau_{\text{lep}}$ final state after the maximum likelihood fit of the combined model to data. The lower panel shows the ratio between data and the signal-plus-background model as well as the ratio between the background-only and combined model. The signal is normalised to the best-fit value of the combination of all three final states. The hatched band corresponds to the statistical and systematic uncertainty of the combined model [196].*

The dominant systematic uncertainties arise from the jet-energy scale calibration, uncertainties on the embedding procedure and the b-tagging efficiency calibration, as well as from statistical uncertainties of the background model. Combining all four categories, a discovery significance of 1.4σ is expected in presence of a SM

Higgs boson with $m_H = 125$ GeV. In Figure 7.1 the BDT output distributions are shown in the VBF and Boosted categories of the 8 GeV analysis. In the high BDT output region, an excess of data over the expected background is found with a significance corresponding to 2.7σ at the same mass hypothesis. The fit results in an estimate of the signal strength parameter of $\hat{\mu} = 2.10\ ^{+0.92}_{-0.83}$ [196].

7.2. Search in the $\tau_{\rm had}\tau_{\rm had}$ Final State

About 42% of all ditau decays result in a fully hadronic final state. The branching ratio therefore competes with the one of the lepton-hadron final state. The large background from multijet production nevertheless complicates the background suppression and triggering. With only two neutrinos in the final state the $\tau_{\rm had}\tau_{\rm had}$ channel offers a slightly better mass resolution than the $\tau_{\rm lep}\tau_{\rm had}$ channel, using the same mass-reconstruction algorithm as the other two final states. Background events arise from $Z \to \tau\tau$ decays and multijet events. Other electroweak processes only contribute at the percent level to the total expected event yields. Events are selected using ditau triggers and the reconstructed $\tau_{\rm had}$ objects are required to exceed transverse momentum thresholds of $p_T > 35$ GeV and $p_T > 30$ GeV, respectively. Events with electron or muon candidates are discarded and preselection criteria reduce the contribution from multijet events. The VBF and Boosted analysis categories are defined by cuts on $\Delta\eta_{jj} > 2$ and $p_T^H > 100$ GeV, respectively. Two BDTs trained on similar input variables as employed in the other two channels are used as final discriminant in the likelihood fit.

The background from $Z \to \tau\tau$ events is modelled by the embedding technique, while the multijet background is estimated by constructing a template from a control region enriched in fake background events. This control region is defined by reverting the opposite electric charge and isolation requirements. The absolute normalisation of both the $Z \to \tau\tau$ and multijet background is determined in the combined fit to data. To provide additional constraining power to this fit, an additional category is considered which contains all events not classified in one of the two signal regions. The $\Delta\eta(\tau\tau)$ distribution in this *rest* category offers good discriminating power between $Z \to \tau\tau$ and multijet events, and is included in the likelihood fit. Other backgrounds are estimated using simulated event samples.

The most significant uncertainties originate from the jet and $\tau_{\rm had}$ energy scale calibrations, the systematic uncertainty on the fake background estimate and the trigger efficiency measurement. The analysis has an expected discovery significance of 2.0σ at $m_H = 125$ GeV. In Figure 7.2 the corresponding BDT output distributions are shown in the VBF and Boosted categories of the 8 GeV analysis. As in the other two channels an excess in data over the background expectation is found, which corresponds to a significance of 3.2σ. The best-fit value of the signal strength parameter is $\hat{\mu} = 1.96\ ^{+0.93}_{-0.73}$ [196].

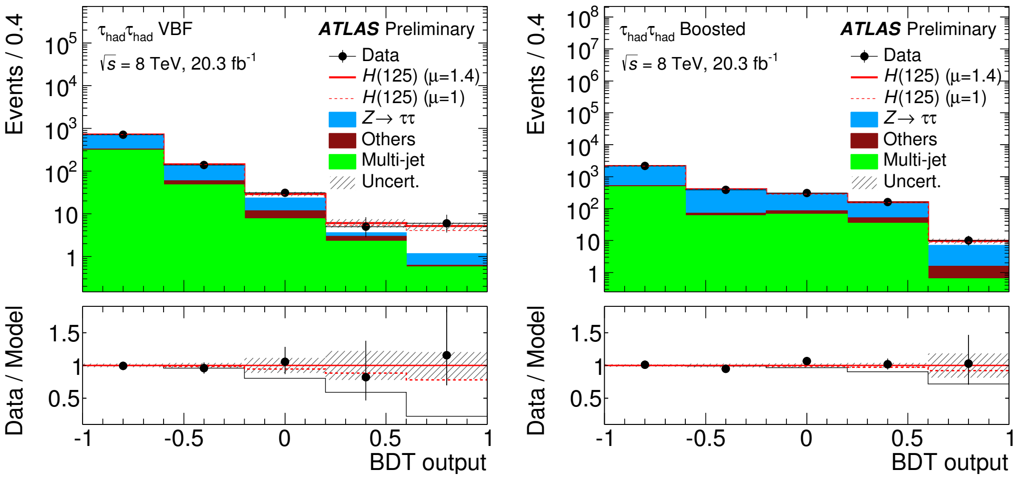

(a) (b)

Figure 7.2. *Distributions of the BDT output in the signal regions of the VBF (a) and Boosted (b) categories of the 8 TeV analysis in the $\tau_{\text{had}}\tau_{\text{had}}$ final state after the maximum likelihood fit of the combined model to data. The lower panel shows the ratio between data and the signal-plus-background model as well as the ratio between the background-only and combined model. The signal is normalised to the best-fit value of the combination of all three final states. The hatched band corresponds to the statistical and systematic uncertainty of the combined model [196].*

7.3. Results of the Combined Search for $H \to \tau\tau$ Decays

In the framework of maximum likelihood fits discussed in Section 6.2, the combination of the analyses in all three final states simply proceeds by multiplying the individual likelihood functions to obtain the combined one. Common systematic uncertainties like the components of the jet-energy scale uncertainties, the uncertainties on the luminosity measurements or on the τ_{had} identification performance are treated correlated across all final states and categories by parametrising their effect with common nuisance parameters. The minimisation and extraction of the results then proceeds exactly as discussed above.

The combined fit yields a signal strength parameter of

$$\hat{\mu} \quad = 1.40 \; {}^{+0.27}_{-0.26}(\text{stat.}) \; {}^{+0.33}_{-0.25}(\text{syst.}) \; \pm 0.09(\text{theo. syst.})$$

at a Higgs boson mass of $m_H = 125$ GeV [196]. The uncertainties are split into statistical and two systematic uncertainty components accounting for uncertainties on the product of inclusive Higgs boson production cross-section and branching ratio, and all other systematic uncertainties, as discussed in Section 6.4. If instead evaluated at $m_H = 125.36$ GeV, as measured by the ATLAS collaboration [89], the best-fit value increases by 1.4% to $\hat{\mu} = 1.42\,{}^{+0.44}_{-0.38}$, due to the decrease in the expected $H \to \tau\tau$ branching ratio. The p-value, under the background-only hypothesis, to observe a result at least as signal like as obtained here is $3.4 \cdot 10^{-6}$. This corresponds to a significance of 4.5σ in terms of Gaussian standard deviations, while 3.5σ are expected from the contribution of a SM Higgs boson of mass $m_H = 125$ GeV. This presents evidence for $H \to \tau\tau$ decays.

Figure 7.3 shows the best-fit values of μ in the individual channels and in different combinations of them, demonstrating the good agreement of the measurements across the various categories and final states. The dominant uncertainties on the measurement arise from the statistical uncertainty on the dataset, the uncertainties on the jet and tau-energy scales as well as from uncertainties on the fitted absolute normalisation of the $Z \to \tau\tau$ and other background processes. The absolute contributions of the most important uncertainties on the measured signal strength parameter are summarised in Table 7.1. A summary of the background and

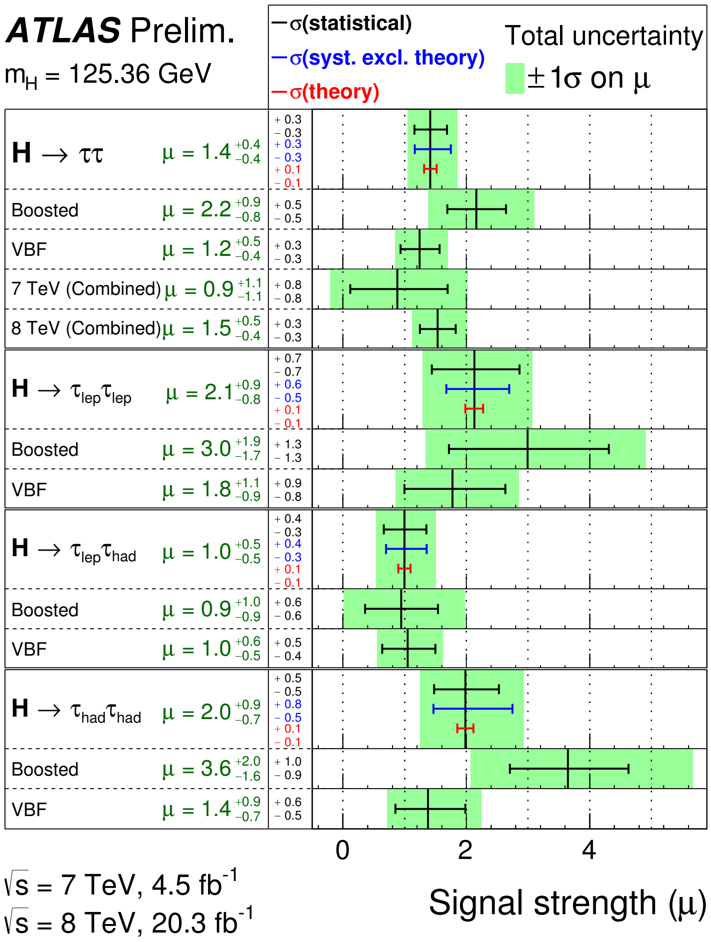

Figure 7.3. *Estimates of the signal strength parameter resulting from fits to the individual channels and different combinations of them, evaluated at a Higgs boson mass hypothesis of $m_H = 125.36$ GeV. Besides the total uncertainty, the uncertainty contributions from statistical, systematic and theoretical uncertainties are shown [196].*

signal event yields is presented in Fig. 7.4, showing the combined event yields of all

Source of Uncertainty	Uncertainty on $\hat{\mu}$
Signal region statistics (data)	$^{+0.27}_{-0.26}$
Jet-energy scale	± 0.16
Tau-energy scale	± 0.07
Tau identification	± 0.06
Background normalisation	± 0.12
Background estimate stat.	± 0.10
BR ($H \to \tau\tau$)	± 0.08
Parton shower/Underlying event	± 0.04
PDF	± 0.03

Table 7.1. *Absolute contributions of the dominant uncertainties to the measurement of the signal strength parameter $\hat{\mu} = 1.40$ at $m_H = 125$ GeV. Sub-components of uncertainties which are treated uncorrelated in the likelihood fit, are grouped together for this overview [196].*

categories as a function of $\log_{10}(S/B)$, which is determined from the estimated signal and background yields in the respective BDT output bins. Besides the nominal postfit estimates of the signal and background yields, the signal contribution at a signal strength of $\mu = 1$ is shown. Additionally, the dashed line indicates the background estimate from a conditional fit in which the signal strength parameter is fixed to zero, demonstrating the level of incompatibility between data and the background-only-hypothesis.

Like for the lepton-hadron final state discussed above, individual signal strength parameters are estimated for signal contributions from ggF or VBF and VH events. Their best-fit values are found to be

$$\begin{aligned}\hat{\mu}_{\text{VBF+VH}} &= 1.23\ ^{+0.48}_{-0.45}(\text{stat.})\ ^{+0.31}_{-0.28}(\text{syst.})\\ \hat{\mu}_{\text{ggH}} &= 1.90\ ^{+0.85}_{-0.84}(\text{stat.})\ ^{+1.15}_{-0.76}(\text{syst.})\end{aligned}$$

at $m_H = 125$ GeV. This result is summarised in Fig. 7.5 which shows contours of equal values of the likelihood function corresponding to the 68% and 95% confidence levels, in the two-dimensional plane of $\mu_{\text{VBF+VH}}$ and μ_{ggH}. These two-dimensional fit results demonstrate the strong sensitivity of the analysis towards the VBF process and the good agreement with the SM expectation.

Since the BDT output distribution itself has little sensitivity to the mass of the Higgs boson, it is interesting to study the ditau mass distribution of signal-like data events. For this purpose, the BDT output can be used to define event weights based on the expected signal-to-background ratio S/B in each BDT output bin. Figure 7.6 shows the $m_{\tau\tau}$ spectrum, where all events in the signal regions are weighted by $\ln(1 + S/B)$ based on their BDT output value. This weighting scheme enhances the contribution from events in the high BDT output regions. The data is compared

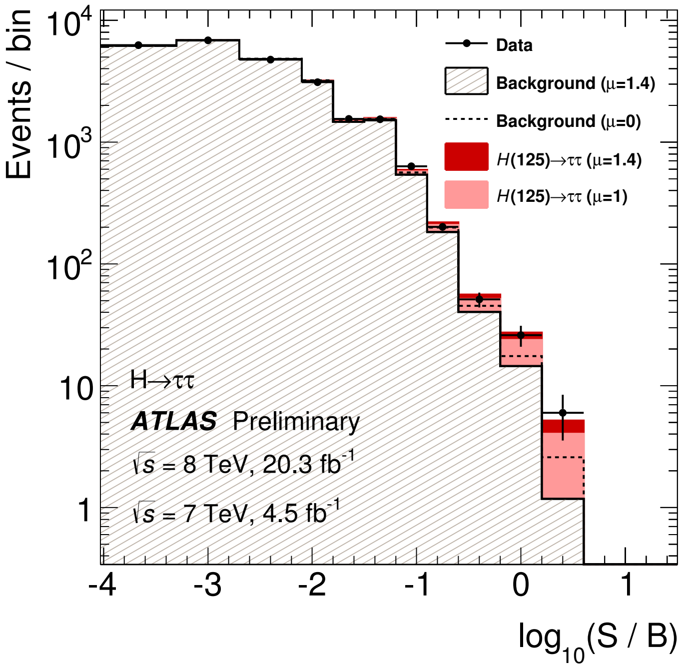

Figure 7.4. *Event yields as a function of* $\log_{10}(S/B)$, *where the signal and background yields* S *and* B *are taken from each bin of all categories entering the combined fit. The nominal background estimate results from the unconditional fit, while the dashed line indicates the fitted background yields, as estimated in a fit with the signal strength parameter fixed to zero [196].*

to the background-plus-signal model, as resulting from the combined fit to the BDT output distributions, assuming a Higgs boson mass of $m_H = 125$ GeV. In addition, alternative mass hypotheses are displayed, normalised to the best-fit value of the signal-strength parameter obtained from a fit of the corresponding signal hypothesis to the BDT output distribution. The observed excess in data is well compatible with the expectation of a Higgs boson with $m_H = 125$ GeV.

As shortly touched upon in Section 5.6.2, an alternative analysis using selection cuts to suppress background events is performed on the $\sqrt{s} = 8$ TeV dataset in order to provide a cross-check based on an independent analysis methodology. The combined cut-based analysis yields a result of $\hat{\mu} = 1.35\ ^{+0.56}_{-0.47}$ at $m_H = 125$ GeV. Using the so-called jackknife technique [213, 214] the statistical correlation between the μ values measured in the BDT and cut-based analyses is found to be of the order of 0.55 and 0.65 in all final states. The cut-based analysis result is therefore in good agreement with the result of the BDT based analysis. The significance of the excess in data when compared to the background-only hypothesis is found to be 3.2σ, while a significance of 2.5σ is expected at $m_H = 125$ GeV. Compared to the expected sensitivity of the $\sqrt{s} = 8$ TeV BDT analysis of 3.4σ, this presents a sensitivity improvement of about 35% by employing a multivariate classification algorithm. This improvement is also depicted in Fig. 7.7, which shows the local

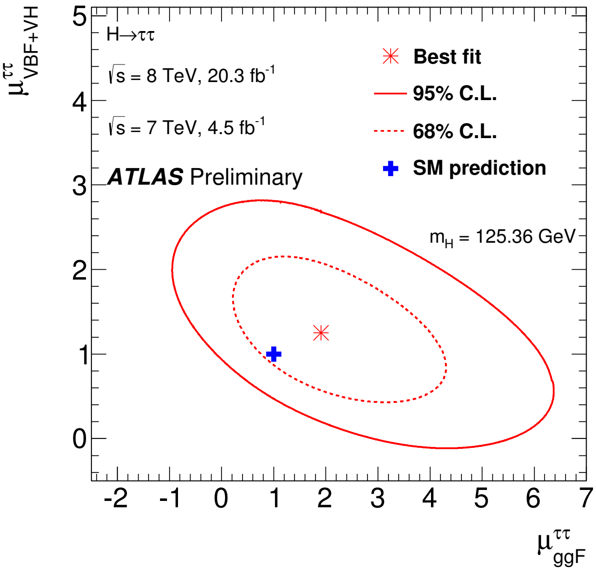

Figure 7.5. *Profile likelihood contours, corresponding to* 68% *and* 95% *confidence levels, in the* $(\mu_{VBF+VH}, \mu_{ggH})$ *plane, at a Higgs boson mass hypothesis of* $m_H = 125.36$ *GeV. The best-fit value is shown along with the SM expectation [196].*

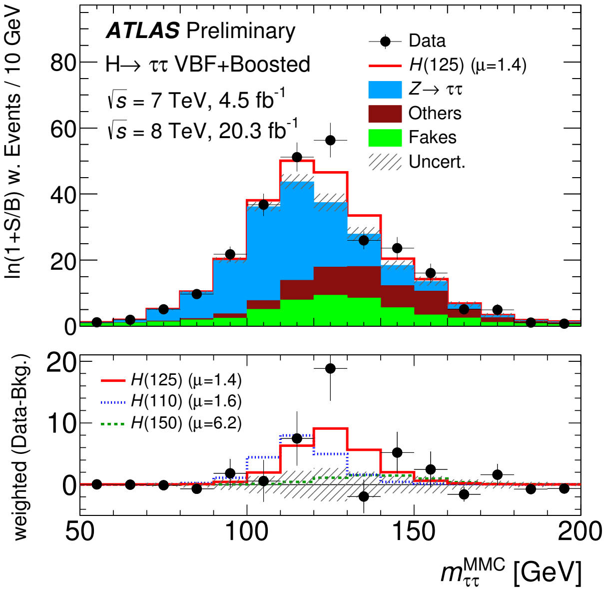

Figure 7.6. *Distribution of* $m_{\tau\tau}$ *including the contributions from all channels and categories in the* $\sqrt{s} = 8$ *TeV dataset, where each event is weighted by* $\ln(1 + S/B)$ *based on the expected event composition in the respective BDT output bin. The background and signal model are shown as resulting from the fit to the BDT output distribution. The bottom panel shows the difference between the weighted data and background events, which is compared to different signal mass hypotheses. The signal yields are normalised to the respective best-fit values of the signal strength parameter [196].*

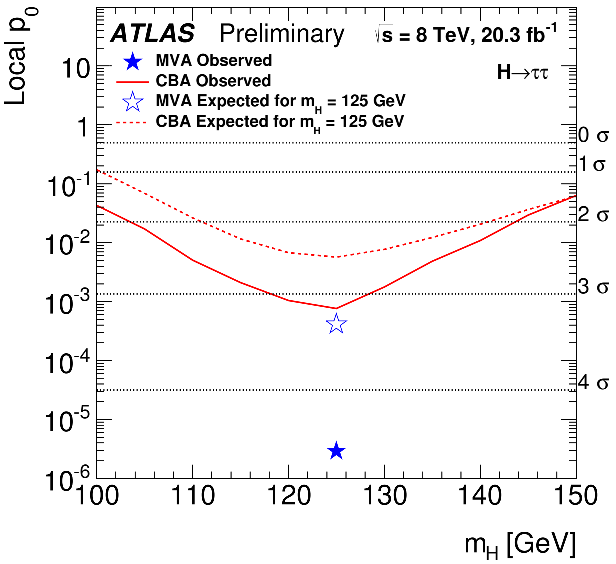

Figure 7.7. *Expected and observed p-values as a function of m_H for the cut-based analysis of all three $H \to \tau\tau$ final states in the $\sqrt{s} = 8$ TeV dataset. The sensitivity is compared to the expected and observed p-values of the BDT based analysis at $\sqrt{s} = 8$ TeV for a Higgs boson mass hypothesis of $m_H = 125\,GeV$ [196].*

expected and observed significance as a function of the hypothesised value of m_H for the cut-based analysis as well as the corresponding values of the BDT based analysis at $m_H = 125$ GeV.

7.4. Status of Higgs Boson Searches in Fermionic Final States

The combined search for $H \to \tau\tau$ decays presented above provides clear evidence that the new particle observed in the bosonic search channels also decays to tau leptons. The observed event rate is well compatible with the expectation for a SM Higgs boson. As discussed in Section 1.3, Higgs boson decays into a pair of b-quarks offer an additional search channel in a fermionic final state, with a significant branching ratio at low Higgs boson masses. The ATLAS collaboration recently reported on a search for $H \to b\bar{b}$ decays focussing on the Higgs boson production in association with a leptonically decaying vector boson [215]. In this specific final state, the lepton is used for triggering and background suppression purposes, two important aspects which can hardly be addressed sufficiently in a fully hadronic final state. The analysis is based on the full LHC Run 1 dataset at centre-of-mass energies of $\sqrt{s} = 7$ TeV and $\sqrt{s} = 8$ TeV and considers events with zero, one or two charged leptons (e, μ). These three final states target $Z \to \nu\bar{\nu}$, $W \to \ell\nu$ and $Z \to \ell\ell$ decays of the vector boson. The search heavily profits from powerful b-tagging algorithms used to identify jets originating from $H \to b\bar{b}$ decays. A BDT classifier built from various input variables including the dijet-mass spectrum $m_{b\bar{b}}$ is used to separate the signal from the various background processes. The dominant background stems from W/Z events accompanied by jets from heavy-flavour quark decays as well as from $t\bar{t}$ events. The signal strength is then estimated in a similar likelihood fit to the BDT output distribution as discussed above, along with various background-model specific nuisance parameters. The analysis observes a slight excess of data compared to the background expectation and measures a signal strength of $\hat{\mu} = 0.51\ ^{+0.31}_{-0.30}(\text{stat.})\ ^{+0.25}_{-0.22}(\text{syst.})$ at $m_H = 125$ GeV. The observed (expected) significance of this excess corresponds to 1.4σ (2.6σ) in terms of Gaussian standard deviations.

The CMS collaboration recently published evidence for Higgs boson decays into fermions [216], based on results of the searches in the $b\bar{b}$ [217] and $\tau\tau$ final states [218]. Both analyses are based on the full LHC Run 1 dataset, corresponding to an integrated luminosity of up to 5.1 fb^{-1} at $\sqrt{s} = 7$ TeV and 19.7 fb^{-1} at $\sqrt{s} = 8$ TeV. Similarly as discussed above for the $H \to b\bar{b}$ search performed by the ATLAS experiment, the CMS collaboration exploits Higgs bosons produced in association with a leptonically decaying vector boson, for background rejection and triggering purposes. In addition to W boson decays to an electron or muon and a neutrino, the search also considers $W \to \tau\nu$ decays. In this specific final state, only hadronic one-prong tau decays are considered. A BDT classifier is used to separate signal from background processes and a likelihood fit to the classification score is used to estimate the signal strength parameter. A signal strength of $\hat{\mu} = 1.0 \pm 0.5$ is measured, and found to be in good agreement with the SM expectation. The significance of the excess of data over the background expectation corresponds to 2.1σ at $m_H = 125$ GeV.

The search for $H \to \tau\tau$ decays employs the leptonic, hadronic and lepton-hadron final states. Besides these, dedicated analysis categories are optimised to provide sensitivity to Higgs boson events produced in association with a vector boson. For these categories, events with one or two additional leptons in the final state are considered. The major background contributions to the analysis are very similar to the ones presented above in the context of the $H \to \tau\tau$ search by the ATLAS experiment. The dominant $Z \to \tau\tau$ background is modelled using a sample of simulated tau decays embedded into $Z \to \mu\mu$ events. Background events from $t\bar{t}$ events are greatly suppressed by exploiting b-tagging information and the majority of background events with misidentified τ_{had} objects are modelled using data-driven methods. A major difference in the two analyses lies in the reconstruction of hadronic tau decays. While the τ_{had} four-momentum reconstruction in the ATLAS experiment is solely based on calorimeter information, the CMS experiment combines momentum measurements of charged hadrons by the inner detector with measurements of the energy deposits of neutral hadrons by the calorimeter. This allows for an improved energy resolution in the τ_{had} reconstruction compared to purely calorimeter based approaches. Events are classified into categories, based on kinematic event properties and the topology of additional jets in the event. As in the analysis presented in this thesis, VBF and Boosted categories are defined to significantly enhance the signal purity. The various subchannels employ different background suppression strategies. Stringent selection cuts are used to suppress background events and a multitude of sub-categories is defined to exploit correlations across discriminating variables. In the ditau final states alone, in total 27 categories are defined for the $\sqrt{s} = 8$ TeV analysis, while 24 are used to categorise the $\sqrt{s} = 7$ TeV data sample. The ditau mass spectrum is reconstructed using a technique based on a similar footing as the MMC algorithm presented in Section 5.1.3. It is used as discriminating variable in a combined likelihood fit in most categories. In the ee and $\mu\mu$ final states, a BDT based discriminant is used instead. Combining the ditau final states, a signal strength of $\hat{\mu} = 0.86 \pm 0.29$ is measured. Testing the data against the background-only hypothesis yields an observed (expected) significance of 3.4σ (3.6σ) at $m_H = 125$ GeV. By combining this result with the categories optimised for VH processes, an observed (expected) significance of 3.2σ (3.7σ) at $m_H = 125$ GeV is reported, in good agreement with the SM expectation.

Considering the results of these four searches for $H \to \tau\tau$ and $H \to b\bar{b}$ decays by the ATLAS and CMS collaborations, as well as the results by the CDS and D0 experiments touched upon in Section 1.4, there is clear evidence for direct Higgs boson decays into fermions across different experiments and search channels. These results are summarised in Fig. 7.8, showing the measured values of μ in searches for fermionic Higgs boson decays at the LHC and Tevatron experiments. The measured signal strength parameters in both inclusive and production mode specific fits are well compatible with the respective SM expectations. While measurements of the Higgs boson signal strength in the bosonic final states allow to indirectly access the coupling between the Higgs boson and top quarks via the gluon-fusion production process, the direct evidence for Higgs boson couplings to down-type fermions presents an additional important information for a complete assessment of the Higgs boson coupling parameters.

7.5. Current Limitations and Outlook

Since the discovery of a Higgs boson in 2012 an increasing number of measurements shows compelling agreement between experimental data and the expectations for a SM Higgs boson. The mass is measured by the ATLAS and CMS experiments to be $m_H = 125.36 \pm 0.41$ GeV [89] and $m_H = 125.03 \pm 0.30$ GeV [90], respectively. Studies of the particle's spin and parity quantum numbers have found it to be compatible with a $J^P = 0^+$ state [93–96]. Detailed fits to the production and decay rates in various analysis channels show good agreement with the SM expectations within the current experimental precision [90, 219]. Besides the interpretation in the SM framework, such combined fits can also be used to set limits on parameters in beyond the Standard Model (BSM) scenarios [90, 220].

Improving the understanding of the electroweak symmetry breaking sector will remain one of the most important physics goals of the experiments at the LHC. Upcoming data taking periods of the LHC at increased centre-of-mass energies of $\sqrt{s} = 13$ TeV will provide significantly larger data samples. Currently, integrated

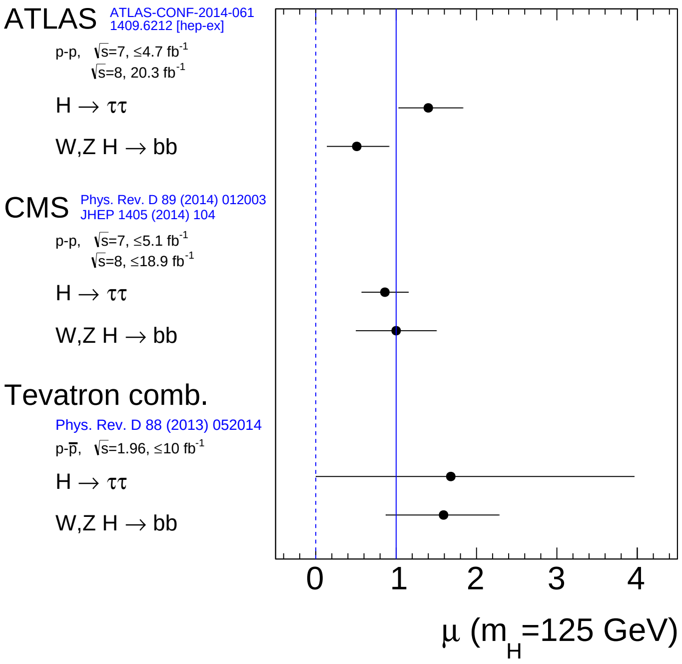

Figure 7.8. *Summary of the measured signal strength parameters in searches for fermionic Higgs boson decays at the LHC and Tevatron experiments. The results of the ATLAS experiment are taken from Refs. [196, 215], the ones of the CMS experiment from Refs. [217, 218] and the Tevatron combination is documented in Ref. [85]. While the ATLAS and CMS results are based on a profile likelihood approach, the result of the Tevatron combination is based on a Bayesian calculation with a uniform prior PDF for non-negative values of* μ.

luminosities of up to 300 fb^{-1} are envisaged until 2022, after a major upgrade of the detectors in 2018. Along with the increasing precision of the direct rate measurements, the statistical analysis of the results will move towards an improved model-independent interpretation of these measurements in an effective field theory approach [22, 221, 222]. In such frameworks, the coupling structure of the electroweak sector is parametrised in a model-independent way by identifying all operators of higher dimensions which are allowed by symmetry considerations. The general assumption for such an interpretation is that new physics phenomena are described by degrees of freedom which are sufficiently heavy to be integrated out and simply be described by effective interactions. By combining measurements of event rates and differential distributions in various combinations of Higgs boson production and decay processes and measurements of other electroweak observables like di- and triboson production, such operators can be constrained and possible deviations from the SM expectations can be searched for in a general way. In that sense, the study of the Higgs boson will provide access to study BSM physics, and it is of great interest to measure its parameters as precisely as possible to identify potential deviations from the expected SM behaviour. Apart from rate measurements, the measurement of differential cross sections, as recently reported by the

ATLAS collaboration in the $\gamma\gamma$ and ZZ^* final states [223, 224], and comparisons to precise theoretical calculations, will provide an enhanced handle to probe the SM predictions.

While the measurement of differential cross sections will remain a complicated task in ditau final states, mostly due to the high contamination by background processes which are subject to large systematic uncertainties, the $H \rightarrow \tau\tau$ analysis will provide valuable input to the combined coupling fits. As discussed above, the precision of direct measurements of the Higgs boson couplings to fermions is currently limited by the statistical power of the dataset. The search for $H \rightarrow \tau\tau$ decays by the ATLAS collaboration, as presented in this thesis, maximised the signal acceptance by employing multivariate classification algorithms in rather loosely defined signal regions. The analysis strategy adopted by the CMS collaboration instead makes use of a large number of analysis categories defined by selection cuts. In both approaches, a limited number of data events is available in rather exclusively defined areas of the kinematically allowed phase space. With the increase in size of the available dataset, various improvements to the analyses will become feasible. The $H \rightarrow \tau\tau$ channel will remain one of the most sensitive channels to the VBF production mechanism. With an increased number of signal events, an improved separation between VBF and ggF events can be achieved and will allow for strong contributions to the combined coupling measurements mentioned above. Besides the ggF and VBF production modes, dedicated studies of the VH process will further complete the measurement in the ditau final state. As several models of BSM physics consider modifications of the Higgs boson couplings to down-type fermions, also the inclusive cross-section measurement in $H \rightarrow \tau\tau$ events will help to constrain such models. In addition, the assessment of the spin and parity quantum numbers in the $H \rightarrow \tau\tau$ decay will be studied, in order to provide an independent confirmation of the findings made in the bosonic final states. The ditau final state will furthermore provide important additional information to investigate potential CP mixing effects. Improved τ_{had} identification and reconstruction algorithms will help to cope with the increase in instantaneous luminosity, leading to a higher pile-up contamination. By matching tracks in the inner detector with energy deposits in the calorimeter it will become possible to identify and reconstruct single charged and neutral pions from the τ_{had} decay. A combined four-momentum reconstruction exploiting this possibility will improve the energy resolution of reconstructed hadronic tau decays and yield additional separating power to suppress fake τ_{had} candidates. Nevertheless, systematic uncertainties connected to the matching procedure might become complicated to assess and sufficiently large datasets will be required to study and validate these approaches in single hadron and $Z \rightarrow \tau\tau$ measurements.

Summary

The spontaneous breaking of the electroweak symmetry, and with it the mechanism responsible for the generation of mass terms of the W and Z bosons, plays a key role in the Standard Model of particle physics. This breaking is described by the Brout-Englert-Higgs mechanism. A central prediction of this theory is the existence of a scalar particle, the Higgs boson. Theoretically independent of the gauge couplings between the Higgs boson and the W and Z bosons, the SM also predicts the interaction of the Higgs boson with fermions via so-called Yukawa couplings. In the SM, these couplings lead to the generation of mass terms for fermions. An experimental observation of the Higgs boson, and therefore also a confirmation of the Higgs mechanism, was lacking prior to the start of the LHC programme. The successful first data-taking period of the LHC in the years 2009 to 2012 allowed the ATLAS and CMS collaborations to discover a particle with properties consistent with those of a SM Higgs boson of a mass of approximately $m_H \approx 125$ GeV in 2012. Since then the Higgs boson production rates were measured in different final states and evidence for the main production mechanisms via the gluon fusion (ggF) and vector-boson-fusion (VBF) processes was established. By combining the results of analyses in different final states and in categories enhanced in the different signal production modes, coupling strength modifiers, parametrising possible deviations from the expected SM couplings, can be extracted and are found to be in good agreement with the SM expectations. Dedicated studies probing the spin and parity quantum numbers of the new particle established consistency with the $J^P = 0^+$ assignment of the SM.

The discovery of the Higgs boson was based on analyses of Higgs boson decays into pairs of photons, W and Z bosons. It is possible to infer indirect evidence for the coupling of the Higgs boson to fermions from the evidence for the gluon fusion process which evolves via a heavy quark loop. Nevertheless, the direct observation and measurement of the fermionic Yukawa couplings is crucial for the identification of the observed particle with the Higgs boson of the SM. For a Higgs boson mass in the proximity of $m_H \approx 125$ GeV, two fermionic decay modes are experimentally accessible at the LHC, $H \to b\bar{b}$ and $H \to \tau\tau$ decays, with branching ratios of about 57% and 6%, respectively. Since top quarks provide the dominant contribution to the gluon-fusion loop diagram, the determination of the Higgs boson coupling to tau leptons and bottom quarks, which both are down-type fermions, is in addition an important experimental test of the mechanism responsible for fermion mass generation. Due to the large multijet background emerging from QCD processes, the search for $H \to b\bar{b}$ decays is forced to focus on the production of Higgs bosons in association with a leptonically decaying vector boson to allow for an efficient triggering and background suppression.

The distinct signature of tau lepton decays allows to reconstruct all final states of $H \to \tau\tau$ events, making this decay mode a promising search channel for fermionic Higgs boson decays. Three final states arise from the decays of the tau leptons, a fully leptonic ($H \to \tau\tau \to (\ell\nu\nu)(\ell\nu\nu)$), a hadronic ($H \to \tau\tau \to (\tau_{\text{had}}\nu)(\tau_{\text{had}}\nu)$) and a lepton-hadron final state ($H \to \tau\tau \to (\tau_{\text{had}}\nu)(\ell\nu\nu)$). They account for about 12%, 42% and 46% of all decays, respectively. The dominant background arises from $Z/\gamma^* \to \tau\tau$ events, featuring an experimental signature very similar to the one of the Higgs boson signal. An important handle to suppress such background events is given by the topology of accompanying jets, especially for Higgs bosons produced via vector-boson fusion. By exploiting the presence of two high energetic jets which are well separated in pseudorapidity, background events can be suppressed to a level sufficiently low to allow for a good sensitivity to the signal. The ditau final state is therefore the most sensitive channel for the observation of fermionic Higgs boson couplings and one of the most sensitive channels for the measurement of the Higgs boson production rate via the VBF process.

This thesis presents a search for $H \to \tau\tau$ decays in the lepton-hadron final state with the ATLAS experiment. It is based on the full set of p-p collision data recorded during Run 1 of the LHC, corresponding to integrated luminosities of 4.5 fb^{-1} and 20.3 fb^{-1} at $\sqrt{s} = 7$ TeV and $\sqrt{s} = 8$ TeV, respectively. A variety of background processes contribute to the selected final state. Besides events with real tau leptons, as emerging from $Z \to \tau\tau$ decays, events with misidentified τ_{had} objects present an important source of background events. They arise, for example, from QCD multijet processes and $W \to \ell\nu$ decays. While the $Z \to \tau\tau$ background is generally hard to distinguish from the signal processes, exploiting kinematic properties of hadronic jets in ggF and VBF events allows to partially differentiate between signal and background events. Besides the characteristic jet topology in the VBF Higgs boson production process mentioned above, the p_T spectrum of Higgs bosons in ggF events is considerably harder than the one of Z bosons. For this reason, an analysis category targeting high p_T Higgs boson events was firstly introduced in the course of this thesis and provides a significant contribution to the total sensitivity of the analysis. In addition to this *Boosted* category, which is mainly sensitive to Higgs boson events produced via ggF, a VBF category is defined targeting VBF Higgs boson events. To suppress events with misidentified τ_{had} objects, a variety of angular and topological variables can be exploited. In order to efficiently combine the discriminating power arising from the various variables needed to suppress the different background processes, a boosted decision tree (BDT) algorithm is used to construct a single classification variable per category. The use of such a multivariate analysis approach yields a significantly higher signal sensitivity than obtained in analyses based on selection cuts.

A likelihood model of the expected signal and background BDT output distributions is built and fitted to data in order to measure the signal strength parameter $\mu = \sigma/\sigma_{\text{SM}}$, parametrising the signal event rate normalised to the SM expectation.

In the high BDT score regions, an excess of data over the expected background yield is found and a signal strength of

$$\hat{\mu} \; = 0.98 \;^{+0.35}_{-0.33}(\text{stat.}) \;^{+0.36}_{-0.30}(\text{syst.}) \;\pm 0.06(\text{theo. syst.})$$

at a mass hypothesis of $m_H = 125$ GeV is measured. The observed (expected) significance of this excess is found to be 2.3σ (2.4σ). The statistical and systematic uncertainties contribute roughly equally to the total uncertainty of the measurement. Important systematic uncertainties arise from the jet and tau-energy scale. To reduce their impact, a measurement of the calorimeter response to single hadrons was performed in the course of this thesis and propagated to the tau-energy scale, leading to a significant reduction of the associated systematic uncertainty with respect to previous methodologies.

A combined analysis of the result in the $\tau_{\text{lep}}\tau_{\text{had}}$ final state with the results of the analyses of the $\tau_{\text{lep}}\tau_{\text{lep}}$ and $\tau_{\text{had}}\tau_{\text{had}}$ final states is performed and yields a measurement of the signal strength parameter of

$$\hat{\mu} \; = 1.40 \;^{+0.27}_{-0.26}(\text{stat.}) \;^{+0.33}_{-0.25}(\text{syst.}) \;\pm 0.09(\text{theo. syst.})$$

at $m_H = 125$ GeV. This corresponds to an observed (expected) significance of 4.5σ (3.5σ) at $m_H = 125$ GeV. This presents evidence of $H \to \tau\tau$ decays and the first direct evidence in the ATLAS experiment for fermionic Yukawa couplings. The measured signal event rate is in good agreement with the SM expectation, not only inclusively, but also for the individual signal strength modifiers of the ggF and VBF+VH processes. The respective best-fit values are $\hat{\mu}_{\text{ggF}} = 1.9 \;^{+1.4}_{-1.1}$ and $\hat{\mu}_{\text{VBF+VH}} = 1.2 \;^{+0.6}_{-0.5}$.

Together with the results of the searches for fermionic Higgs boson decays in the $H \to b\bar{b}$ and $H \to \tau\tau$ final states by the CMS experiment and the result of the search for $H \to b\bar{b}$ decays by the ATLAS collaboration, this result is a strong contribution towards the assessment of the Higgs boson coupling strengths, and establishes the existence of Yukawa couplings to down-type fermions.

A Background Model Validation Plots

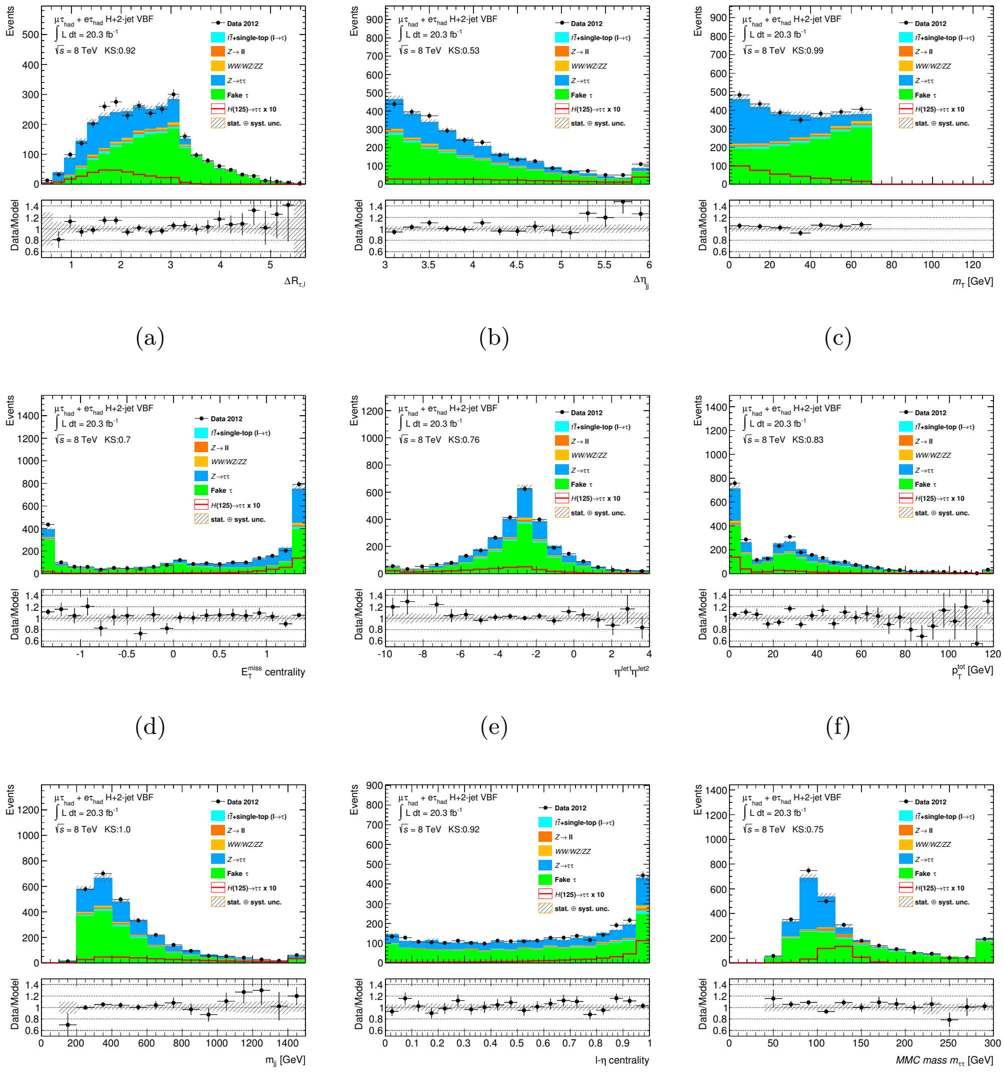

(a) (b) (c)

(d) (e) (f)

(g) (h) (i)

Figure A.1. *Distributions of the BDT input variables in the SR of the VBF category in the 8 TeV analysis. Shown are the distributions of $\Delta R_{\tau\ell}$ (a), $\Delta\eta_{jj}$ (b), m_T (c), $\mathbf{E}_T^{\rm miss}\phi$ centrality (d), $\eta_{j1}\times\eta_{j2}$ (e), $p_T^{\rm tot}$ (f), m_{j_1,j_2} (g), ℓ–η centrality (h) and $m_{\tau\tau}$ (i).*

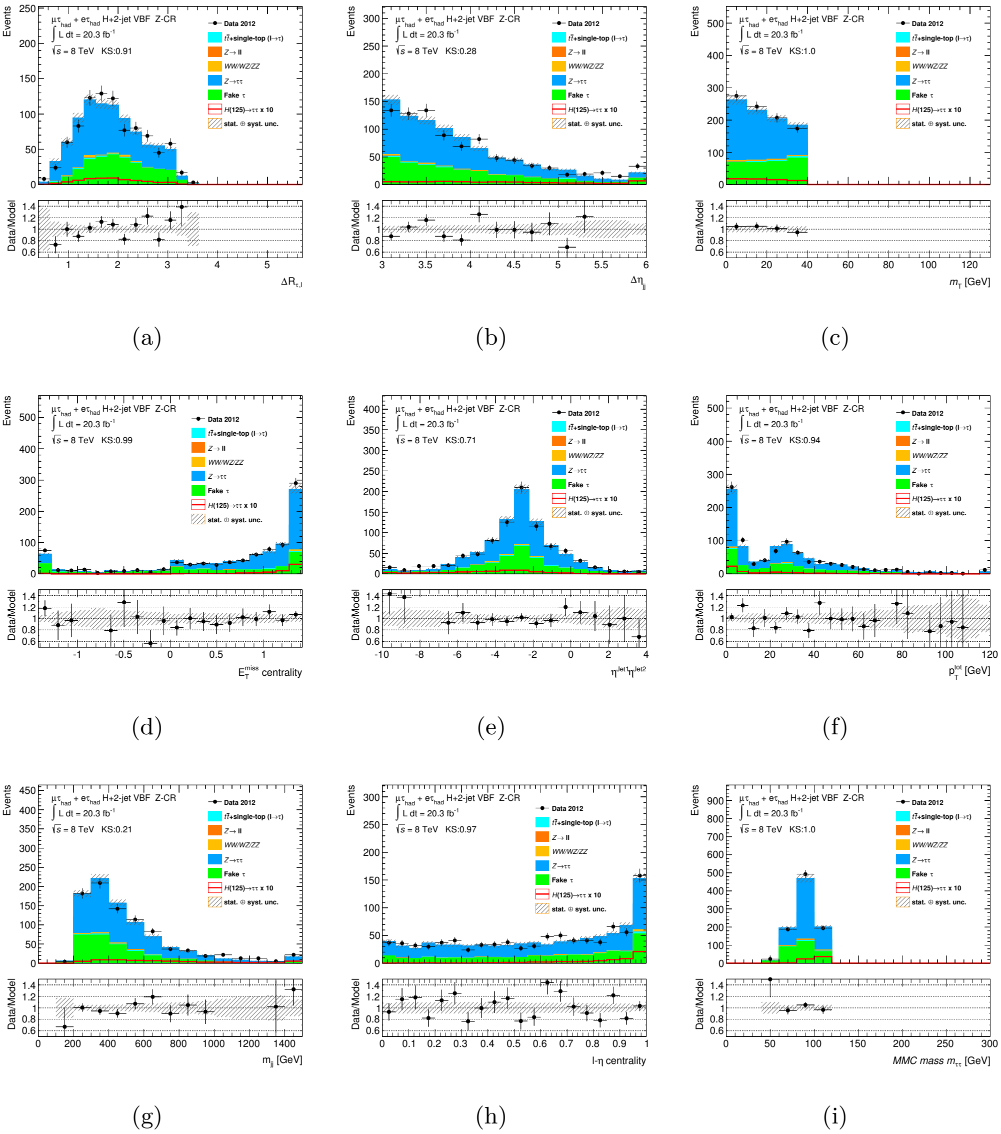

(a) (b) (c)

(d) (e) (f)

(g) (h) (i)

Figure A.2. *Distributions of all BDT input variables in the $Z/\gamma^* \to \tau\tau$ enriched CR of the VBF category in the 8 TeV analysis. Shown are the distributions of $\Delta R_{\tau\ell}$ (a), $\Delta\eta_{jj}$ (b), m_T (c), $\mathbf{E}_T^{\text{miss}}\phi$ centrality (d), $\eta_{j1} \times \eta_{j2}$ (e), p_T^{tot} (f), m_{j_1,j_2} (g), ℓ–η centrality (h) and $m_{\tau\tau}$ (i).*

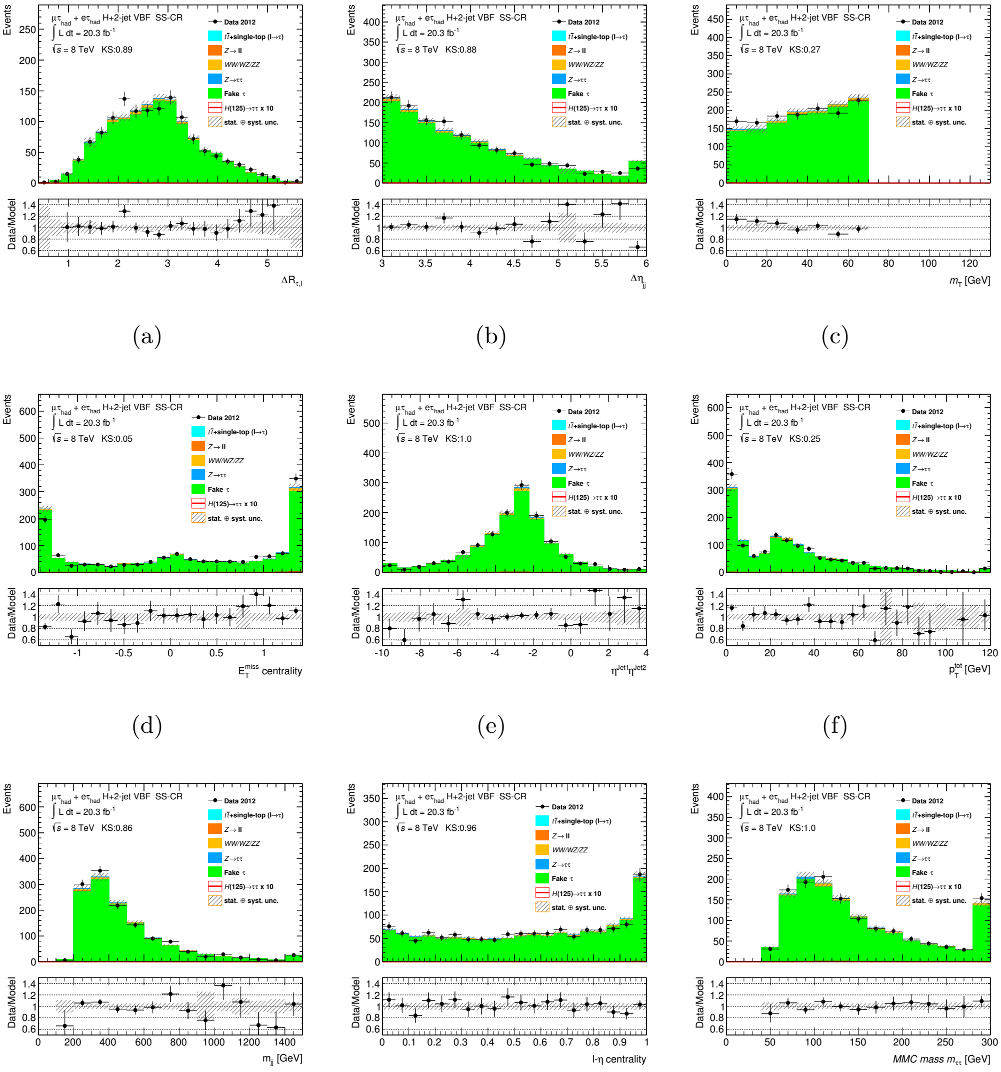

(a) (b) (c)

(d) (e) (f)

(g) (h) (i)

Figure A.3. *Distributions of all BDT input variables in the fake τ_{had} enriched CR of the VBF category in the 8 TeV analysis. Shown are the distributions of $\Delta R_{\tau\ell}$ (a), $\Delta\eta_{jj}$ (b), m_T (c), $\mathbf{E}_T^{\text{miss}}\phi$ centrality (d), $\eta_{j1}\times\eta_{j2}$ (e), p_T^{tot} (f), m_{j_1,j_2} (g), ℓ–η centrality (h) and $m_{\tau\tau}$ (i).*

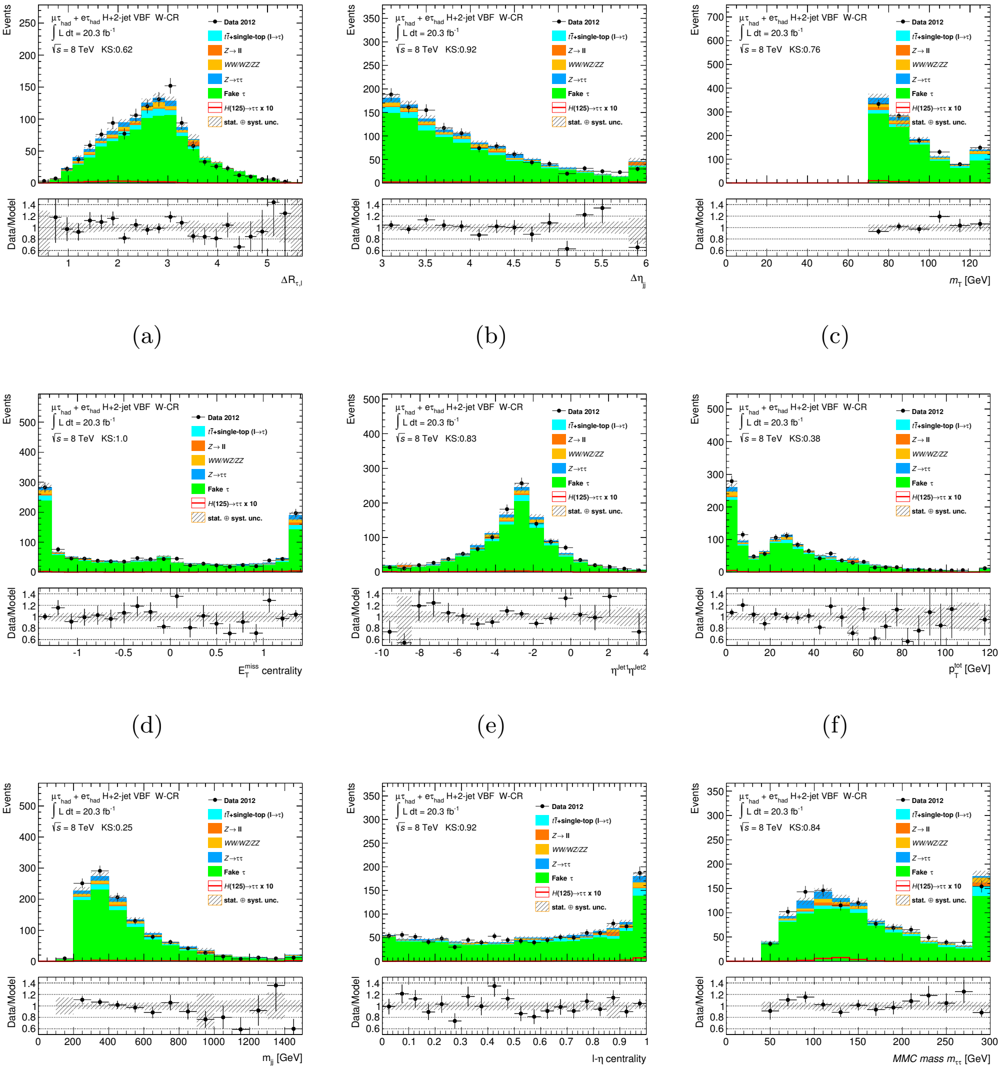

(a) (b) (c)

(d) (e) (f)

(g) (h) (i)

Figure A.4. *Distributions of all BDT input variables in the W + jets enriched CR of the VBF category in the 8 TeV analysis. Shown are the distributions of $\Delta R_{\tau\ell}$ (a), $\Delta\eta_{jj}$ (b), m_T (c), $\mathbf{E}_T^{\text{miss}}\phi$ centrality (d), $\eta_{j1} \times \eta_{j2}$ (e), p_T^{tot} (f), m_{j_1,j_2} (g), ℓ–η centrality (h) and $m_{\tau\tau}$ (i).*

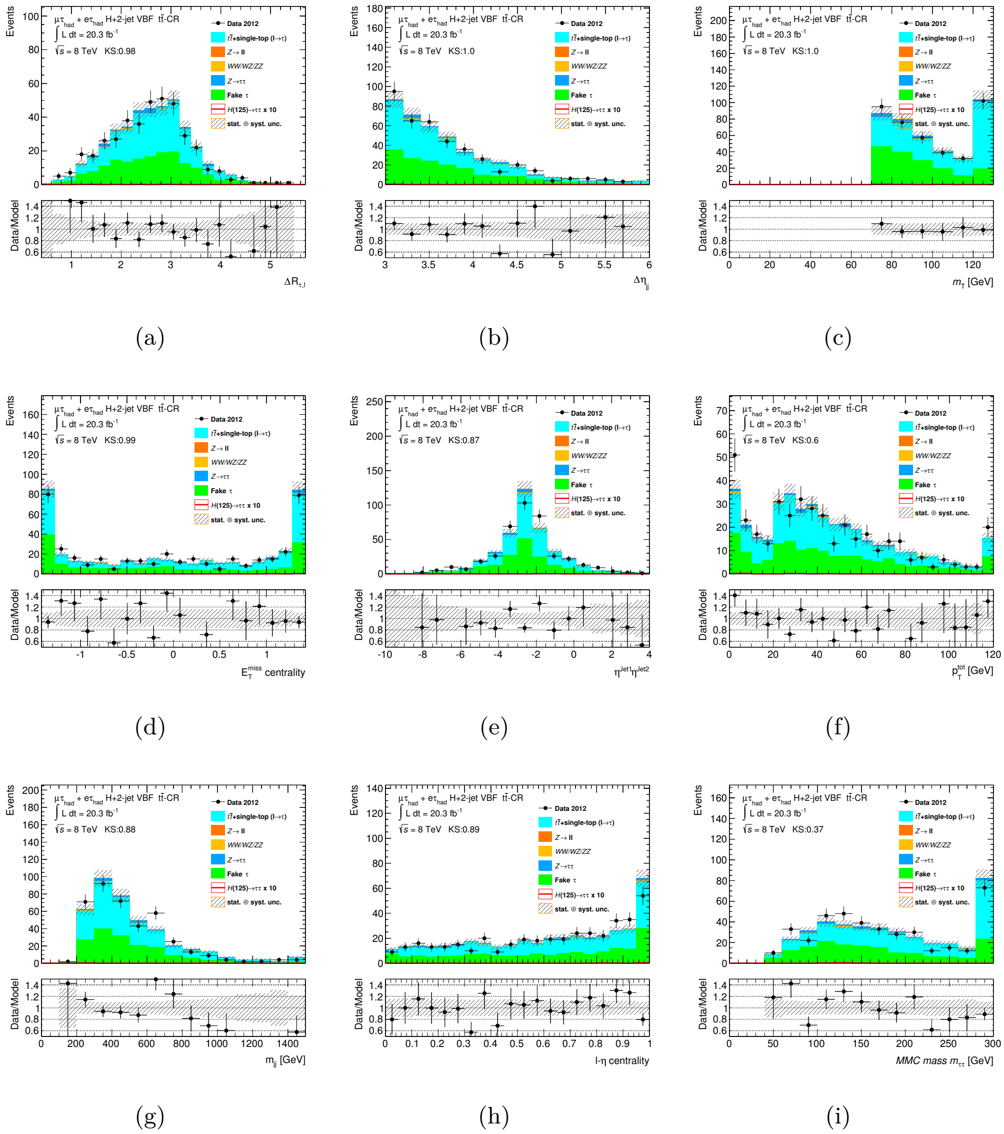

(a) (b) (c)

(d) (e) (f)

(g) (h) (i)

Figure A.5. *Distributions of all BDT input variables in the top quark enriched CR of the VBF category in the 8 TeV analysis. Shown are the distributions of* $\Delta R_{\tau\ell}$ *(a),* $\Delta\eta_{jj}$ *(b),* m_T *(c),* $\mathbf{E}_T^{\text{miss}}\phi$ *centrality (d),* $\eta_{j1}\times\eta_{j2}$ *(e),* p_T^{tot} *(f),* m_{j_1,j_2} *(g),* ℓ*–*η *centrality (h) and* $m_{\tau\tau}$ *(i).*

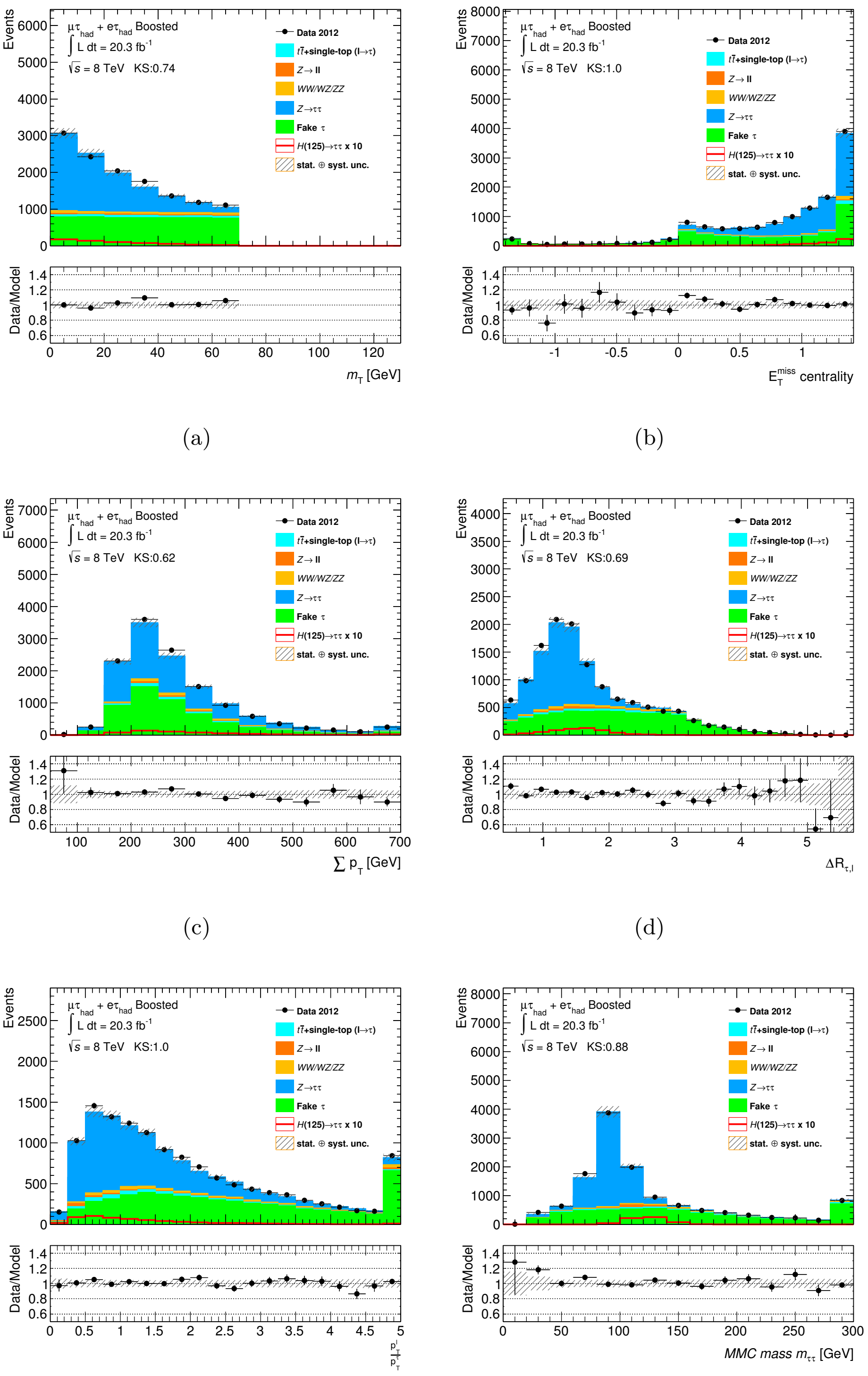

(a) (b)

(c) (d)

(e) (f)

Figure A.6. *Distributions of all BDT input variables in the SR of the Boosted category in the 8 TeV analysis. Shown are the distributions of* m_T *(a),* $\mathbf{E}_T^{\text{miss}}\phi$ *centrality (b),* $\sum p_T$ *(c),* $\Delta R_{\tau\ell}$ *(d),* $p_T(\tau)/p_T(\ell)$ *(e) and* $m_{\tau\tau}$ *(f).*

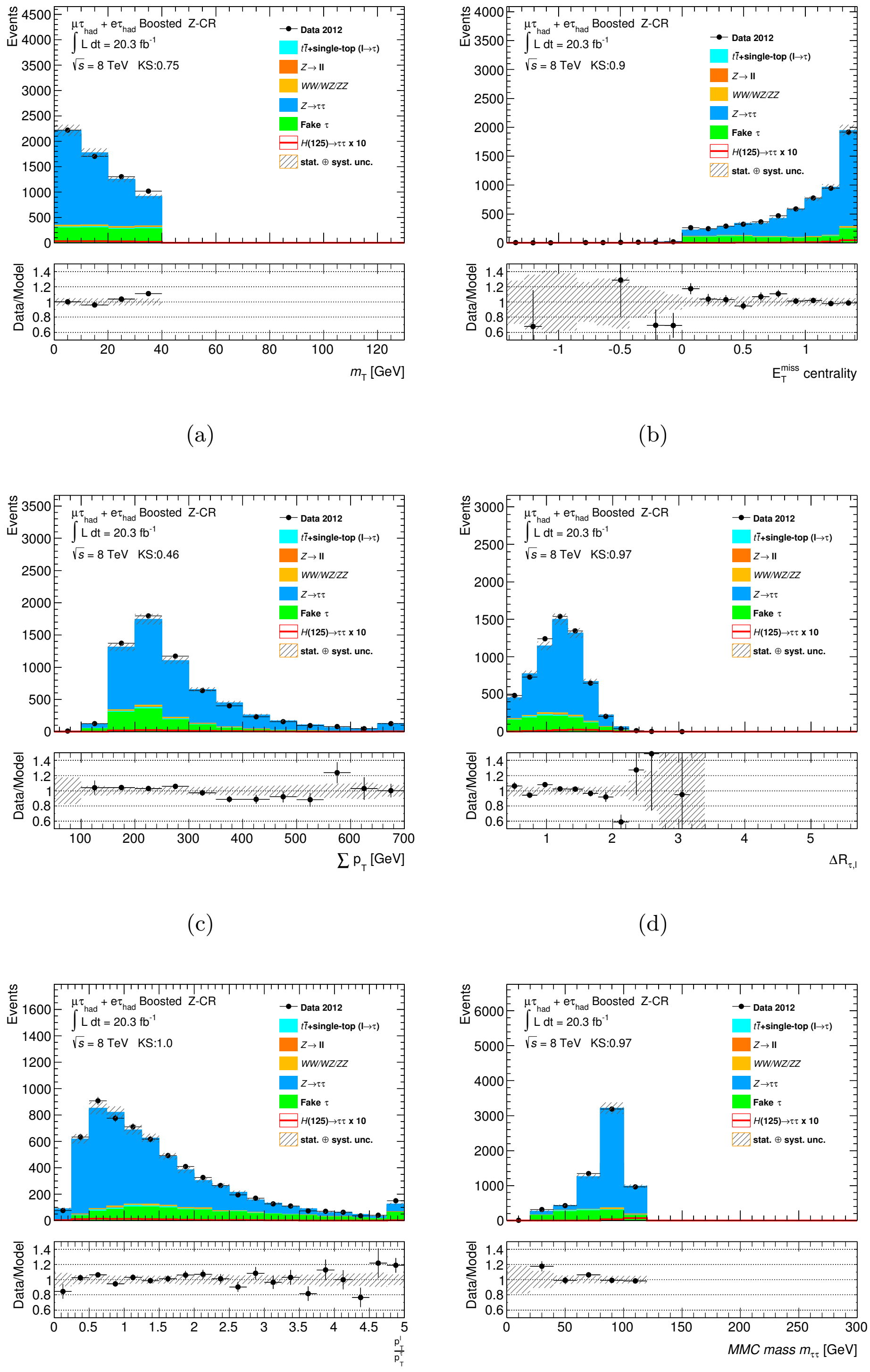

(a) (b)

(c) (d)

(e) (f)

Figure A.7. *Distributions of all BDT input variables in the* $Z/\gamma^* \to \tau\tau$ *enriched CR of the Boosted category in the 8 TeV analysis. Shown are the distributions of* m_T *(a),* $\mathbf{E}_T^{\mathrm{miss}}\phi$ *centrality (b),* $\sum p_T$ *(c),* $\Delta R_{\tau\ell}$ *(d),* $p_T(\tau)/p_T(\ell)$ *(e) and* $m_{\tau\tau}$ *(f).*

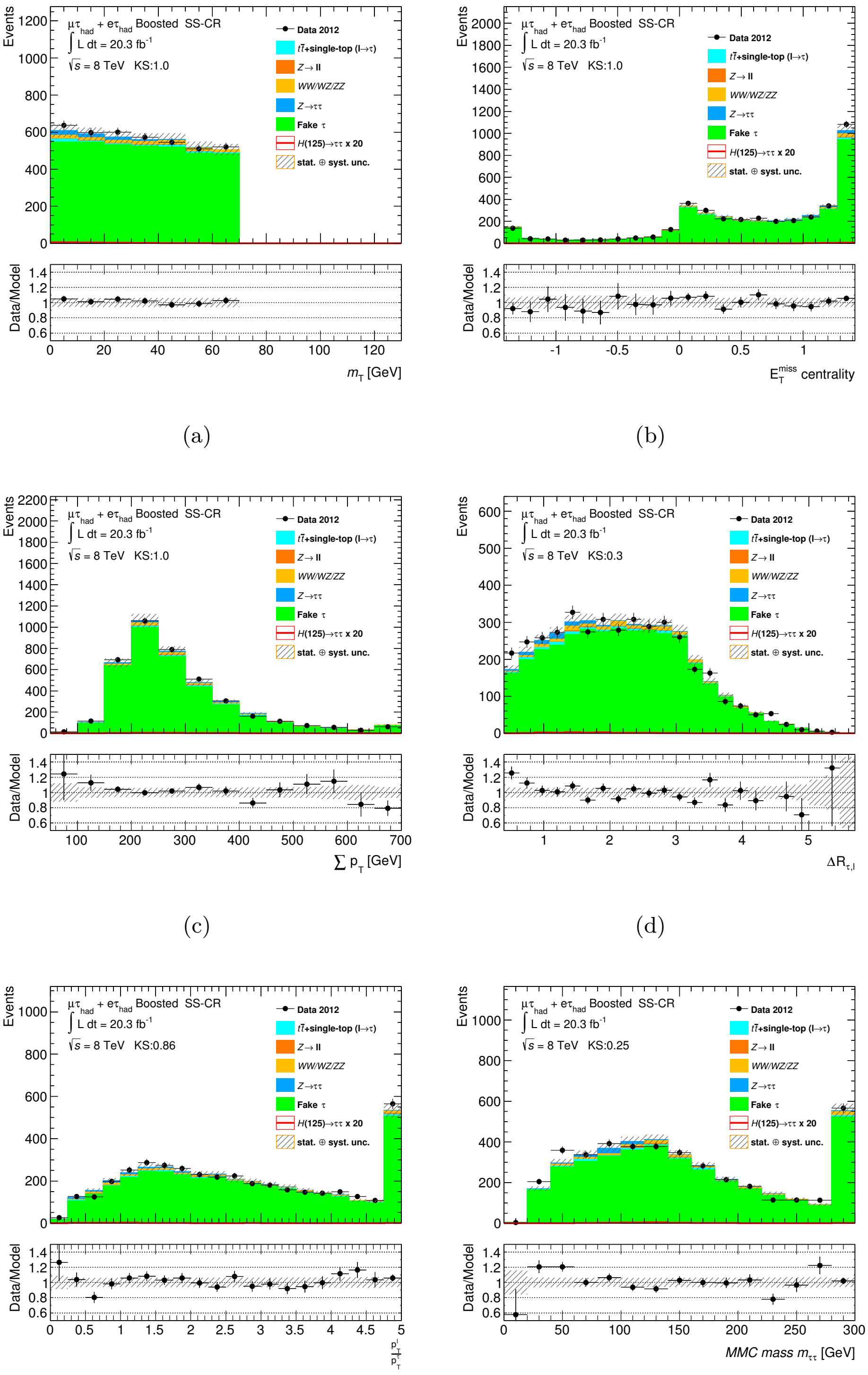

(a) (b)

(c) (d)

(e) (f)

Figure A.8. *Distributions of all BDT input variables in the fake τ_{had} enriched CR of the Boosted category in the 8 TeV analysis. Shown are the distributions of m_T (a), $\mathbf{E}_T^{\text{miss}}\phi$ centrality (b), $\sum p_T$ (c), $\Delta R_{\tau\ell}$ (d), $p_T(\tau)/p_T(\ell)$ (e) and $m_{\tau\tau}$ (f).*

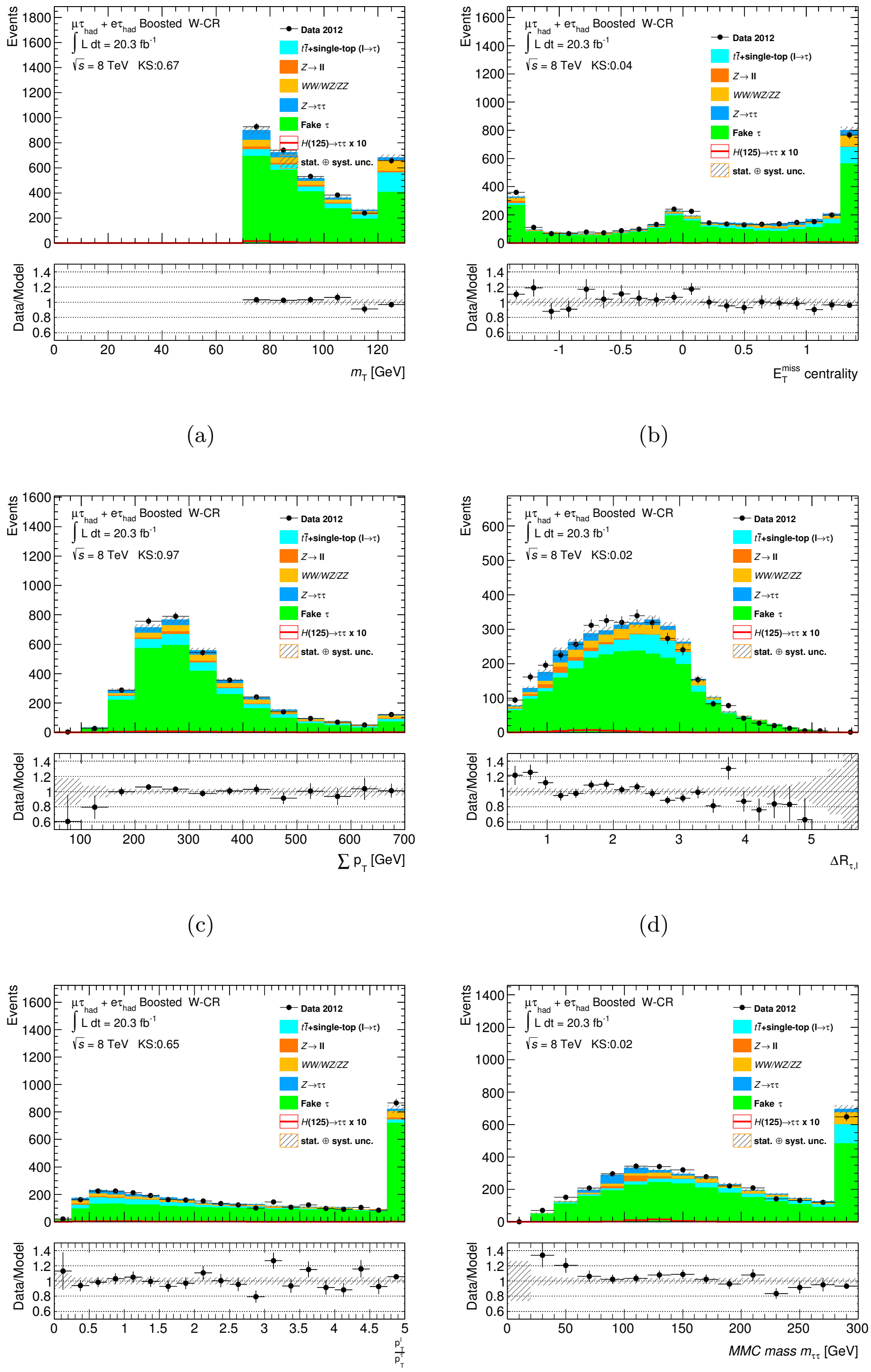

(a) (b)

(c) (d)

(e) (f)

Figure A.9. *Distributions of all BDT input variables in the W + jets enriched CR of the Boosted category in the 8 TeV analysis. Shown are the distributions of m_T (a), $\mathbf{E}_T^{\text{miss}}\phi$ centrality (b), $\sum p_T$ (c), $\Delta R_{\tau\ell}$ (d), $p_T(\tau)/p_T(\ell)$ (e) and $m_{\tau\tau}$ (f).*

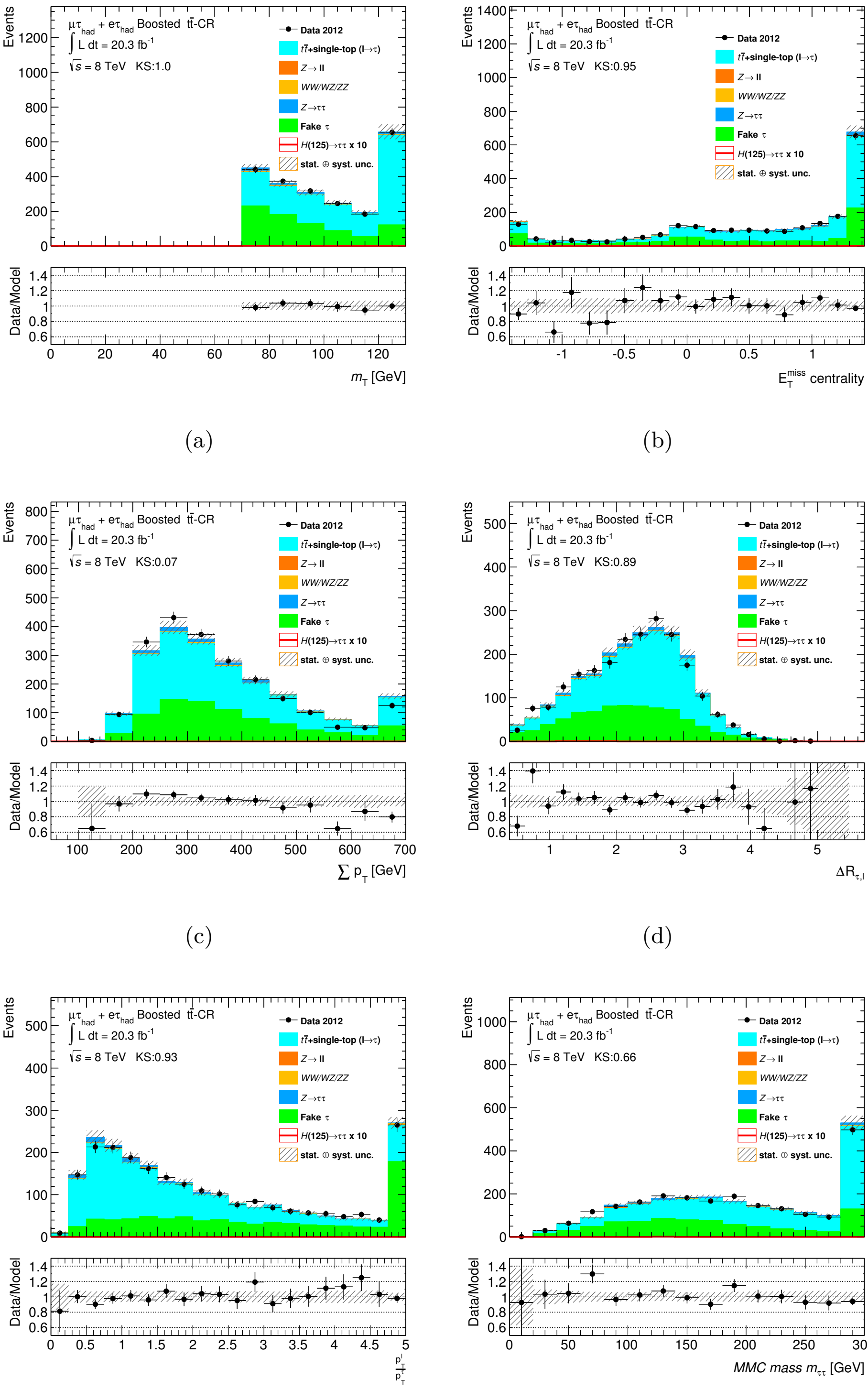

(a) (b)

(c) (d)

(e) (f)

Figure A.10. *Distributions of all BDT input variables in the top quark enriched CR of the Boosted category in the 8 TeV analysis. Shown are the distributions of* m_T *(a),* $\mathbf{E}_T^{\text{miss}}\phi$ *centrality (b),* $\sum p_T$ *(c),* $\Delta R_{\tau\ell}$ *(d),* $p_T(\tau)/p_T(\ell)$ *(e) and* $m_{\tau\tau}$ *(f).*

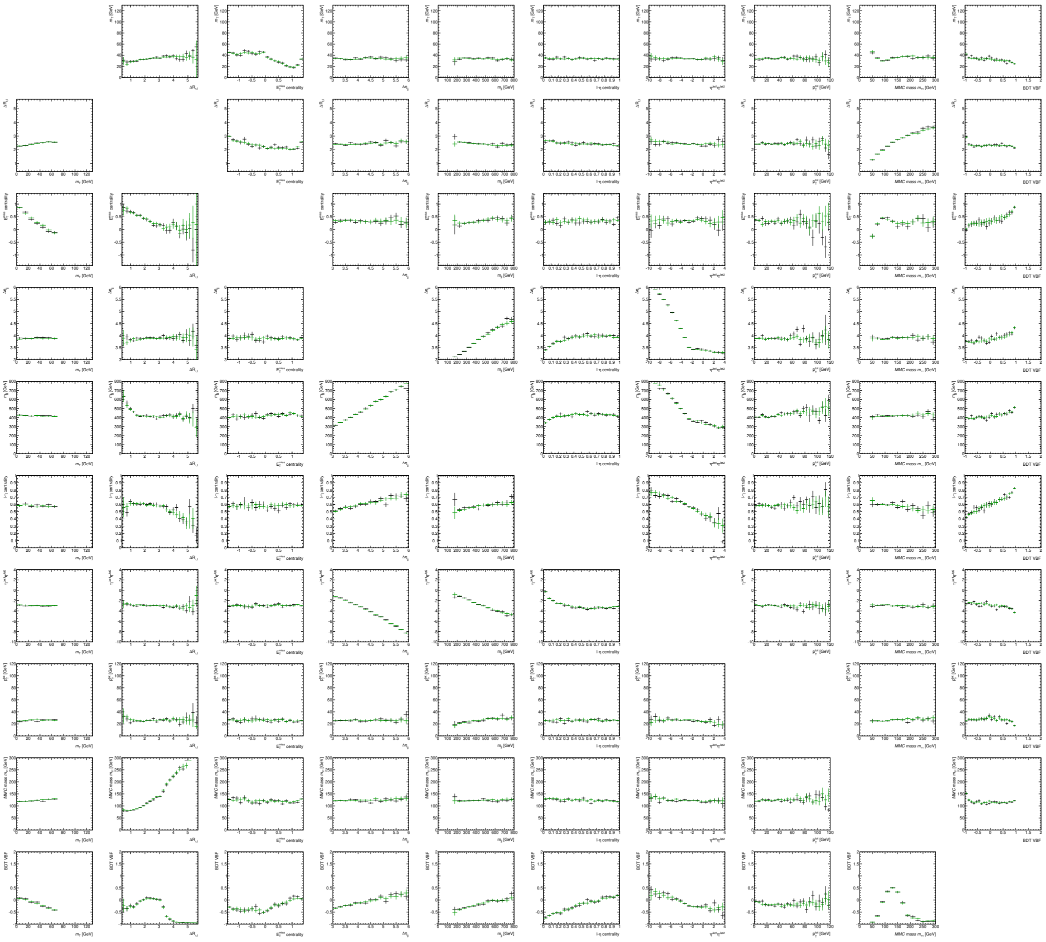

Figure A.11. *Matrix of profile plots displaying the dependence of the mean value of each input variable to the BDT in the VBF category as a function of all other input variables. The black markers are showing the behaviour found in data, while the green ones represent the background model.*

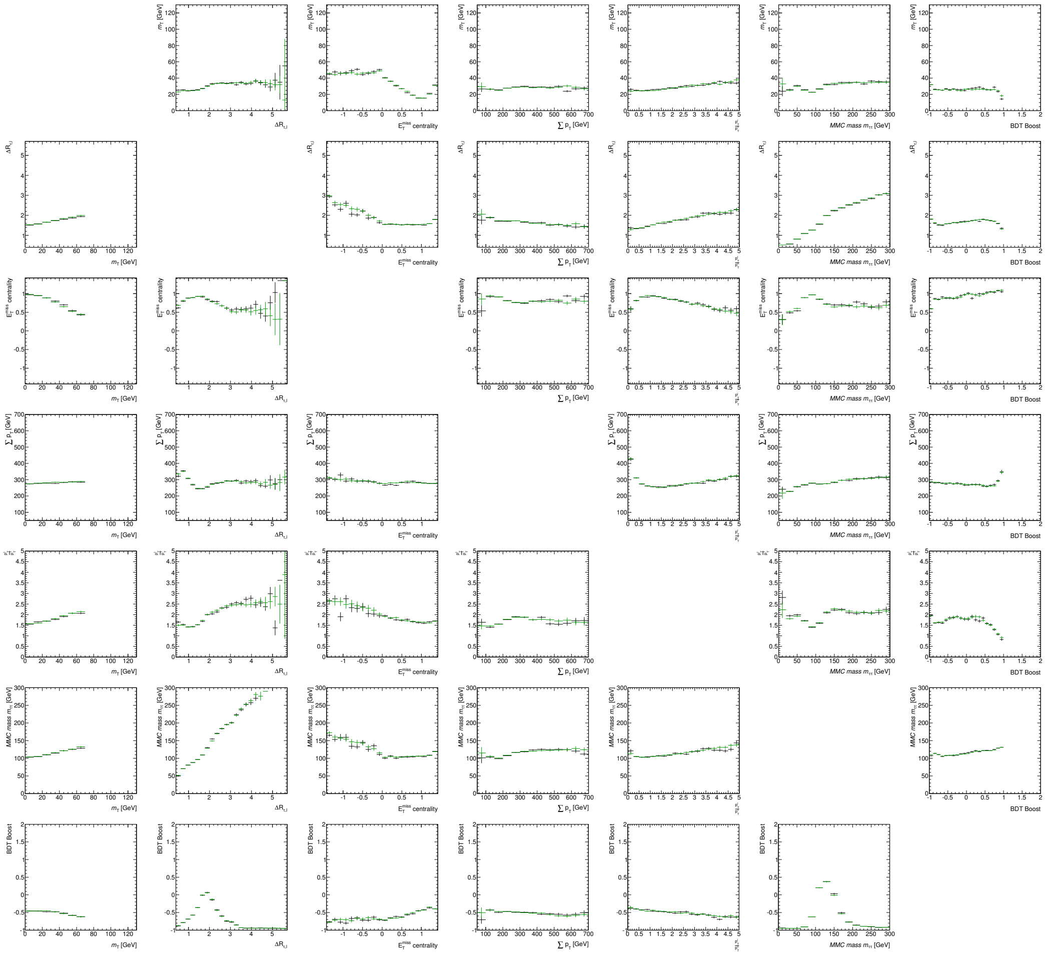

Figure A.12. *Matrix of profile plots displaying the dependence of the mean value of each input variable to the BDT in the Boosted category as a function of all other input variables. The black markers are showing the behaviour found in data, while the green ones represent the background model.*

B Additional Plots of BDT Shape Uncertainties

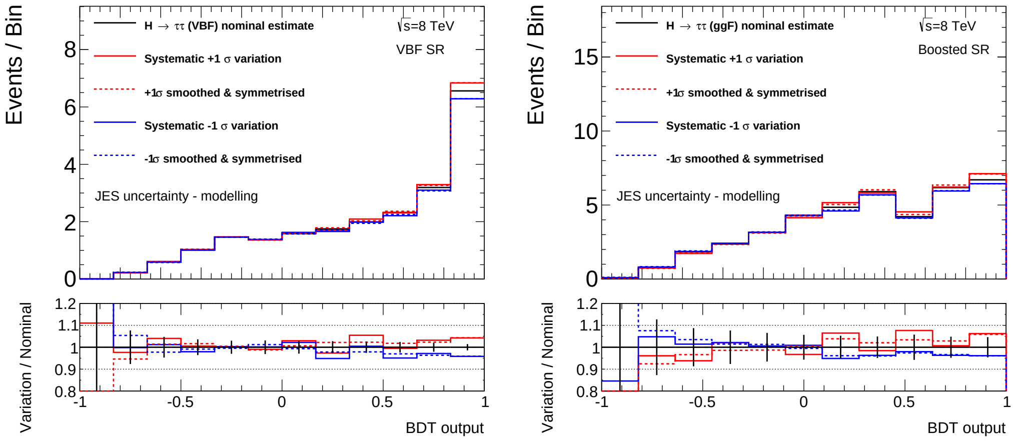

(a) (b)

Figure B.1. *BDT output distributions and the impact of the systematic JES modelling uncertainty on signal and background events in the VBF (left) and Boosted categories (right). The solid black line shows the nominal expected distribution, the solid blue and red lines indicate the distributions after shifting the corresponding parameter. The dashed lines indicate the impact of the applied smoothing and symmetrisation procedures.*

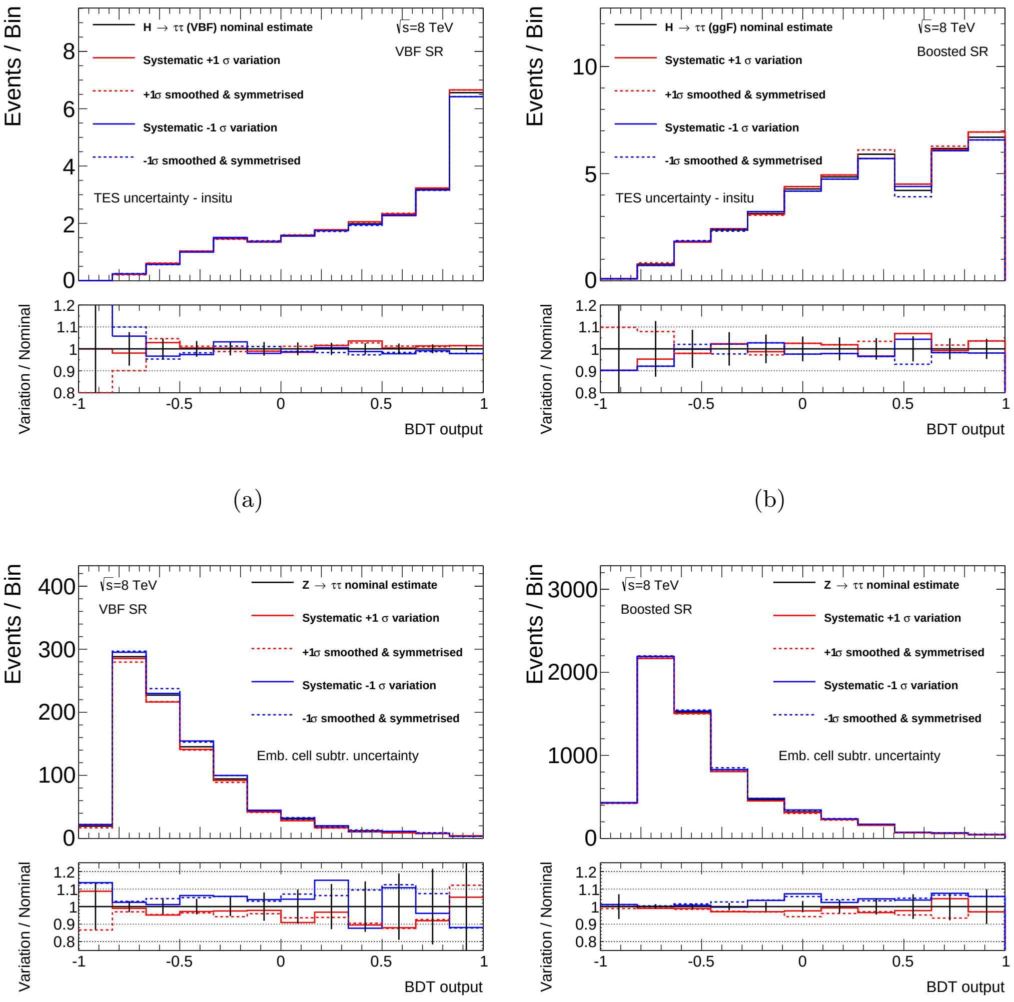

(a) (b)

(c) (d)

Figure B.2. *BDT output distributions and the impact of systematic uncertainties on signal and background events in the VBF (left) and Boosted categories (right). The solid black line shows the nominal expected distribution, the solid blue and red lines indicate the distributions after shifting the corresponding parameter. The dashed lines indicate the impact of the applied smoothing and symmetrisation procedures. Figures (a,b) show the uncertainty on the TES in situ parameter, (c,d) correspond to shifts in the energy scale used for the cell-energy subtraction in the embedding procedure.*

C Nuisance Parameter Names

In the following, a brief explanation of the meaning of the top-ranked nuisance parameters with the largest impact on the measurement of the signal strength parameter μ, as discussed in Section 6.4, is given.

stat lh12 vbf bin 11: Statistical uncertainty of the background model in the 12th bin of the 8 TeV VBF category. The same naming scheme holds for all other statistical uncertainties of the background model, lhX denotes the data taking period, vbf/boosted the category and bin Y the binnumber, where the first bin is denoted as bin 0.

JES FlavResp: Uncertainty component of the jet-energy scale to account for analysis specific jet-flavour compositions.

JES Detector1: Detector related uncertainty component of the jet-energy scale calibration.

TAU EFAKE 2012: Systematic uncertainty of the modelling of the rate to misidentify electrons as τ_{had} objects in 8 TeV data.

JES Eta Modelling: Uncertainty component of the jet-energy scale, related to the η-intercalibration.

JES 2012 Modelling1: Uncertainty component of the jet-energy scale, related to modelling and theoretical uncertainties in the calibration procedure.

BR tautau: Theoretical uncertainty on the $H \to \tau\tau$ branching ratio.

norm LH12 Top boost: Freely floating normalisation factor of the top-quark background in the 8 TeV Boosted category.

TES True 2011: Systematic uncertainty of the tau-energy scale in the 7 TeV analysis. This NP parametrises the effect on true τ_{had} objects.

QCDscale ggH m23: Theoretical uncertainty due to missing higher order corrections of the ggF signal process due to the effective suppression of 3 jet events in the high BDT score region of the VBF category.

QCDscale ggH ptH m01: Theoretical uncertainty due to missing higher order corrections for ggF signal events with at least one jet.

norm LH12 Ztt bv: Freely floating normalisation factor of the $Z/\gamma^{*} \to \tau\tau$ background contribution in the 8 TeV analysis.

GenAccq2Z: Uncertainty of the modelling of $Z \to \ell\ell$ events due to differences in the acceptance across different event generators.

JES FlavComp TAU G: Uncertainty component of the jet-energy scale in events with jets originating mainly from the fragmentation of gluons.

TES Fake 2012: Systematic uncertainty of the tau-energy scale in events with misidentified τ_{had} objects in the 8 TeV analysis.

TES InSitu 2012: Systematic uncertainty of the in situ calibration of the tau-energy scale in the 8 TeV analysis.

ANA EMB ISOL 2011: Systematic uncertainty arising from the choice of the isolation criteria in the $Z \to \mu\mu$ event selection of the embedding procedure in 7 TeV data.

norm LH12 Top vbf: Freely floating normalisation factor of the top-quark background in the 8 TeV VBF category.

LUMI 2012: Systematic uncertainty of the luminosity measurement in 8 TeV data.

EL RES: Systematic uncertainty of the electron energy resolution.

ANA EMB MFS 2012: Systematic uncertainty of the muon cell-energy subtraction in the embedding procedure in 8 TeV data.

Bibliography

[1] D. J. Gross and F. Wilczek, *Ultraviolet Behavior of Nonabelian Gauge Theories*, *Phys.Rev.Lett.* **30** (1973) 1343–1346.

[2] H. D. Politzer, *Reliable Perturbative Results for Strong Interactions?*, *Phys.Rev.Lett.* **30** (1973) 1346–1349.

[3] H. Fritzsch, M. Gell-Mann, and H. Leutwyler, *Advantages of the Color Octet Gluon Picture*, *Phys.Lett.* **B47** (1973) 365–368.

[4] S. L. Glashow, *Partial Symmetries of Weak Interactions*, *Nucl. Phys.* **22** (1961) 579–588.

[5] A. Salam, *Weak and Electromagnetic Interactions*, *Conf. Proc.* **C680519** (1968) 367–377.

[6] S. Weinberg, *A Model of Leptons*, *Phys. Rev. Lett.* **19** (1967) 1264–1266.

[7] F. Englert and R. Brout, *Broken Symmetry and the Mass of Gauge Vector Mesons*, *Phys.Rev.Lett.* **13** (1964) 321–323.

[8] P. W. Higgs, *Broken Symmetries, massless particles and gauge fields*, *Phys.Lett.* **12** (1964) 132–133.

[9] P. W. Higgs, *Broken Symmetries and the Masses of Gauge Bosons*, *Phys.Rev.Lett.* **13** (1964) 508–509.

[10] G. Guralnik, C. Hagen, and T. Kibble, *Global Conservation Laws and Massless Particles*, *Phys.Rev.Lett.* **13** (1964) 585–587.

[11] M. Kobayashi and T. Maskawa, *CP Violation in the Renormalizable Theory of Weak Interaction*, *Prog.Theor.Phys.* **49** (1973) 652–657.

[12] S. Herb et al., *Observation of a Dimuon Resonance at 9.5 GeV in 400 GeV Proton-Nucleus Collisions*, *Phys.Rev.Lett.* **39** (1977) 252–255.

[13] D0 Collaboration, *Search for high mass top quark production in $p\bar{p}$ collisions at $\sqrt{s} = 1.8$ TeV*, *Phys.Rev.Lett.* **74** (1995) 2422–2426, [`hep-ex/9411001`].

[14] CDF Collaboration, *Observation of top quark production in $\bar{p}p$ collisions*, *Phys.Rev.Lett.* **74** (1995) 2626–2631, [`hep-ex/9503002`].

[15] DONUT Collaboration, *Observation of tau neutrino interactions*, *Phys. Lett.* **B504** (2001) 218–224, [`hep-ex/0012035`].

[16] ATLAS Collaboration, *Observation of a new particle in the search for the Standard Model Higgs boson with the ATLAS detector at the LHC*, *Phys. Lett.* **B716** (2012) 1–29, [`arXiv:1207.7214`].

[17] CMS Collaboration, *Observation of a new boson at a mass of 125 GeV with the CMS experiment at the LHC*, *Phys. Lett.* **B716** (2012) 30–61, [`arXiv:1207.7235`].

[18] M. E. Peskin and D. V. Schroeder, *An Introduction to Quantum Field Theory*, Westview Press, 1995.

[19] F. Halzen and A. D. Martin, *Quarks and Leptons: An Introductory Course in Modern Particle Physics*, Wiley, 1984.

[20] D. Griffiths, *Introduction to Elementary Particles*, Wiley, 2008.

[21] S. Dittmaier and M. Schumacher, *The Higgs Boson in the Standard Model - From LEP to LHC: Expectations, Searches, and Discovery of a Candidate*, `arXiv:1211.4828`.

[22] Particle Data Group, K. Agashe et al., *Review of Particle Physics (RPP)*, *Chin.Phys.* **C38** (2014) 090001.

[23] B. Cleveland et al., *Measurement of the solar electron neutrino flux with the Homestake chlorine detector*, *Astrophys.J.* **496** (1998) 505–526.

[24] GNO Collaboration, *Complete results for five years of GNO solar neutrino observations*, *Phys.Lett.* **B616** (2005) 174–190, [`hep-ex/0504037`].

[25] KamLAND Collaboration, *First results from KamLAND: Evidence for reactor anti-neutrino disappearance*, *Phys.Rev.Lett.* **90** (2003) 021802, [`hep-ex/0212021`].

[26] Super-Kamiokande Collaboration, *Evidence for oscillation of atmospheric neutrinos*, *Phys.Rev.Lett.* **81** (1998) 1562–1567, [`hep-ex/9807003`].

[27] Super-Kamiokande Collaboration, *A Measurement of the Appearance of Atmospheric Tau Neutrinos by Super-Kamiokande*, *Phys.Rev.Lett.* **110** (2013) 181802, [`arXiv:1206.0328`].

[28] O. Greenberg, *Spin and Unitary Spin Independence in a Paraquark Model of Baryons and Mesons*, *Phys.Rev.Lett.* **13** (1964) 598–602.

[29] S. Bethke, *The 2009 World Average of* α_s, *Eur. Phys. J.* **C64** (2009) 689–703, [`arXiv:0908.1135`].

[30] T. Lee and C.-N. Yang, *Question of Parity Conservation in Weak Interactions*, *Phys.Rev.* **104** (1956) 254–258.

[31] C. Wu, E. Ambler, R. Hayward, D. Hoppes, and R. Hudson, *Experimental Test of Parity Conservation in Beta Decay*, *Phys. Rev.* **105** (1957) 1413–1414.

[32] N. Cabibbo, *Unitary Symmetry and Leptonic Decays*, *Phys. Rev. Lett.* **10** (1963) 531–533.

[33] M. Kobayashi and T. Maskawa, *CP Violation in the Renormalizable Theory of Weak Interaction*, *Prog.Theor.Phys.* **49** (1973) 652–657.

[34] Z. Maki, M. Nakagawa, and S. Sakata, *Remarks on the unified model of elementary particles*, *Prog. Theor. Phys.* **28** (1962) 870–880.

[35] J. Ellis, *Outstanding questions: Physics beyond the Standard Model*, *Phil.Trans.Roy.Soc.Lond.* **A370** (2012) 818–830.

[36] T. Hambye and K. Riesselmann, *Matching conditions and Higgs mass upper bounds revisited*, *Phys.Rev.* **D55** (1997) 7255–7262, [`hep-ph/9610272`].

[37] A. Djouadi, *The Anatomy of electro-weak symmetry breaking. I: The Higgs boson in the Standard Model*, *Phys.Rept.* **457** (2008) 1–216, [`hep-ph/0503172`].

[38] G. Degrassi et al., *Higgs mass and vacuum stability in the Standard Model at NNLO*, *JHEP* **1208** (2012) 098, [`arXiv:1205.6497`].

[39] The ALEPH, DELPHI, L3, OPAL Collaborations, the LEP Electroweak Working Group, *Electroweak Measurements in Electron-Positron Collisions at W-Boson-Pair Energies at LEP*, *Phys. Rept.* **532** (2013) 119, [`arXiv:1302.3415`].

[40] D. Y. Bardin et al., *Electroweak working group report*, `hep-ph/9709229`.

[41] D. Y. Bardin and G. Passarino, *Upgrading of precision calculations for electroweak observables*, `hep-ph/9803425`.

[42] D. Y. Bardin, M. Grunewald, and G. Passarino, *Precision calculation project report*, `hep-ph/9902452`.

[43] T2K Collaboration, *Indication of Electron Neutrino Appearance from an Accelerator-produced off-axis Muon Neutrino Beam*, *Phys.Rev.Lett.* **107** (2011) 041801, [`arXiv:1106.2822`].

[44] MINOS Collaboration, *Improved search for muon-neutrino to electron-neutrino oscillations in MINOS*, *Phys.Rev.Lett.* **107** (2011) 181802, [`arXiv:1108.0015`].

[45] Planck Collaboration, *Planck 2013 results. XVI. Cosmological parameters*, `arXiv:1303.5076`.

[46] A. D. Sakharov, *Violation of CP invariance, C asymmetry, and baryon asymmetry of the universe*, *Pis'ma Zh. Eksp. Teor. Fiz.* **5** (1967) 32–35.

[47] F.-K. Guo and U.-G. Meissner, *Baryon electric dipole moments from strong CP violation*, *JHEP* **1212** (2012) 097, [`arXiv:1210.5887`].

[48] A. Bhatti and D. Lincoln, *Jet Physics at the Tevatron*, *Ann.Rev.Nucl.Part.Sci.* **60** (2010) 267–297, [`arXiv:1002.1708`].

[49] J. C. Collins, D. E. Soper, and G. F. Sterman, *Factorization of Hard Processes in QCD*, *Adv. Ser. Direct. High Energy Phys.* **5** (1988) 1–91, [`hep-ph/0409313`].

[50] J. M. Campbell, J. Huston, and W. Stirling, *Hard Interactions of Quarks and Gluons: A Primer for LHC Physics*, *Rept.Prog.Phys.* **70** (2007) 89, [`hep-ph/0611148`].

[51] R. K. Ellis, W. J. Stirling, and B. Webber, *QCD and collider physics*, *Camb.Monogr.Part.Phys.Nucl.Phys.Cosmol.* **8** (1996) 1–435.

[52] V. N. Gribov and L. N. Lipatov, *Deep inelastic e-p scattering in perturbation theory*, *Sov. J. Nucl. Phys.* **15** (1972) 438–450.

[53] G. Altarelli and G. Parisi, *Asymptotic freedom in parton language*, *Nucl. Phys.* **B126** (1977) 298.

[54] Y. L. Dokshitzer, *Calculation of the structure functions for deep inelastic scattering and e^+ e^- annihilation by perturbation theory in quantum chromodynamics.*, *Sov.Phys.JETP* **46** (1977) 641–653.

[55] Lai, H.-L. et al., *New generation of parton distributions with uncertainties from global QCD analysis*, *Phys. Rev. D* **82** (2010) 074024, [`arXiv:1007.2241`].

[56] J. Pumplin et al., *New generation of parton distributions with uncertainties from global QCD analysis*, *JHEP* **0207** (2002) 012, [`hep-ph/0201195`].

[57] A. Martin, W. Stirling, R. Thorne, and G. Watt, *Parton distributions for the LHC*, *Eur.Phys.J.* **C63** (2009) 189–285, [`arXiv:0901.0002`].

[58] NNPDF Collaboration, *Impact of Heavy Quark Masses on Parton Distributions and LHC Phenomenology*, *Nucl. Phys. B* **849** (2011) 296, [`arXiv:1101.1300`].

[59] M. L. Mangano et al., *ALPGEN, a generator for hard multiparton processes in hadronic collisions*, *JHEP* **0307** (2003) 001, [`hep-ph/0206293`].

[60] A. Buckley et al., *General-purpose event generators for LHC physics*, *Phys.Rept.* **504** (2011) 145–233, [`arXiv:1101.2599`].

[61] T. Sjöstrand, S. Mrenna, and P. Z. Skands, *PYTHIA 6.4 physics and manual*, *JHEP* **0605** (2006) 026, [`hep-ph/0603175`].

[62] T. Sjostrand, S. Mrenna, and P. Z. Skands, *A Brief Introduction to PYTHIA 8.1*, *Comput.Phys.Commun.* **178** (2008) 852–867, [`arXiv:0710.3820`].

[63] G. Corcella et al., *HERWIG 6: An event generator for hadron emission reactions with interfering gluons (including supersymmetric processes)*, *JHEP* **0101** (2001) 010, [`hep-ph/0011363`].

[64] T. Gleisberg et al., *Event generation with SHERPA 1.1*, *JHEP* **0902** (2009) 007, [`arXiv:0811.4622`].

[65] S. Frixione and B. R. Webber, *Matching NLO QCD computations and parton shower simulations*, *JHEP* **0206** (2002) 029, [`hep-ph/0204244`].

[66] P. Nason, *A new method for combining NLO QCD with shower Monte Carlo algorithms*, *JHEP* **0411** (2004) 040, [`hep-ph/0409146`].

[67] S. Frixione, P. Nason, and C. Oleari, *Matching NLO QCD computations with Parton Shower simulations: The POWHEG method*, *JHEP* **0711** (2007) 070, [`arXiv:0709.2092`].

[68] J. Alwall et al., *Comparative study of various algorithms for the merging of parton showers and matrix elements in hadronic collisions*, *Eur.Phys.J.* **C53** (2008) 473–500, [`arXiv:0706.2569`].

[69] B. Andersson, G. Gustafson, G. Ingelman, and T. Sjostrand, *Parton Fragmentation and String Dynamics*, *Phys.Rept.* **97** (1983) 31–145.

[70] J.-C. Winter, F. Krauss, and G. Soff, *A Modified cluster hadronization model*, *Eur.Phys.J.* **C36** (2004) 381–395, [`hep-ph/0311085`].

[71] S. Jadach, J. H. Kühn, and Z. Wąs, *TAUOLA - A library of Monte Carlo programs to simulate decays of polarized τ leptons*, *Comput. Phys. Commun.* **64** (1990) 275–299.

[72] ATLAS Collaboration, *ATLAS tunes of PYTHIA 6 and PYTHIA 8 for MC11*, ATL-PHYS-PUB-2011-009. `http://cdsweb.cern.ch/record/1363300`.

[73] P. Z. Skands, *Tuning Monte Carlo Generators: The Perugia Tunes*, *Phys.Rev.* **D82** (2010) 074018, [`arXiv:1005.3457`].

[74] GEANT4, S. Agostinelli et al., *GEANT4: A Simulation toolkit*, *Nucl. Instrum. Meth.* **A506** (2003) 250–303.

[75] ATLAS Collaboration, *ATLAS Computing: Technical Design Report*, CERN-LHCC-2005-022. `http://cds.cern.ch/record/837738`.

[76] ATLAS Collaboration, *The ATLAS Simulation Infrastructure*, *Eur. Phys. J.* **C70** (2010) 823–874, [`arXiv:1005.4568`].

[77] S. Dittmaier et al. (LHC Higgs Cross Section Working Group), *Handbook of LHC Higgs Cross Sections: 1. Inclusive Observables*, `arXiv:1101.0593`.

[78] S. Dittmaier et al. (LHC Higgs Cross Section Working Group), *Handbook of LHC Higgs Cross Sections: 2. Differential Distributions*, `arXiv:1201.3084`.

[79] S. Dittmaier et al. (LHC Higgs Cross Section Working Group), *Handbook of LHC Higgs Cross Sections: 3. Higgs Properties*, `arXiv:1307.1347`.

[80] A. Djouadi, J. Kalinowski, and M. Spira, *HDECAY: A Program for Higgs boson decays in the Standard Model and its supersymmetric extension*, *Comput.Phys.Commun.* **108** (1998) 56–74, [`hep-ph/9704448`].

[81] M. Spira, *QCD effects in Higgs physics*, *Fortsch.Phys.* **46** (1998) 203–284, [`hep-ph/9705337`].

[82] A. Bredenstein, A. Denner, S. Dittmaier, and M. Weber, *Precise predictions for the Higgs-boson decay $H \to WW/ZZ \to$ 4 leptons*, *Phys.Rev.* **D74** (2006) 013004, [`hep-ph/0604011`].

[83] A. Bredenstein, A. Denner, S. Dittmaier, and M. Weber, *Radiative corrections to the semileptonic and hadronic Higgs-boson decays $H \to WW/ZZ \to$ 4 leptons*, *JHEP* **0702** (2007) 080, [`hep-ph/0611234`].

[84] LEP Working Group for Higgs boson searches, ALEPH Collaboration, DELPHI Collaboration, L3 Collaboration, OPAL Collaboration, *Search for the standard model Higgs boson at LEP*, *Phys.Lett.* **B565** (2003) 61–75, [`hep-ex/0306033`].

[85] CDF Collaboration, D0 Collaboration, *Higgs Boson Studies at the Tevatron*, *Phys.Rev.* **D88** (2013) 052014, [`arXiv:1303.6346`].

[86] CDF Collaboration, *Search for a low mass Standard Model Higgs boson in the $\tau^+\tau^-$ decay channel in $p\bar{p}$ collisions at $\sqrt{s}$ = 1.96 TeV*, *Phys.Rev.Lett.* **108** (2012) 181804, [`arXiv:1201.4880`].

[87] D0 Collaboration, *Search for Higgs boson production in trilepton and like-charge electron-muon final states with the D0 detector*, *Phys.Rev.* **D88** (2013) 052009, [`arXiv:1302.5723`].

[88] D0 Collaboration, *Search for the Higgs boson in lepton, tau and jets final states*, *Phys.Rev.* **D88** (2013) 052005, [`arXiv:1211.6993`].

[89] ATLAS Collaboration, *Measurement of the Higgs boson mass from the $H \to \gamma\gamma$ and $H \to ZZ^* \to 4\ell$ channels with the ATLAS detector using 25 fb^{-1} of pp collision data*, `arXiv:1406.3827`.

[90] CMS Collaboration, *Precise determination of the mass of the Higgs boson and studies of the compatibility of its couplings with the standard model*, CMS-PAS-HIG-14-009.

[91] ATLAS Collaboration, *Measurements of the properties of the Higgs-like boson in the $WW^{(*)} \to \ell\nu\ell\nu$ decay channel with the ATLAS detector using 25 fb^{-1} of proton-proton collision data*, ATLAS-CONF-2013-030.

[92] CMS Collaboration, *Evidence for a particle decaying to W^+W^- in the fully leptonic final state in a standard model Higgs boson search in pp collisions at the LHC*, CMS-PAS-HIG-13-003.

[93] ATLAS Collaboration, *Evidence for the spin-0 nature of the Higgs boson using ATLAS data*, *Phys.Lett.* **B726** (2013) 120–144, [`arXiv:1307.1432`].

[94] CMS Collaboration, *Measurement of the properties of a Higgs boson in the four-lepton final state*, `arXiv:1312.5353`.

[95] CMS Collaboration, *Measurement of Higgs boson production and properties in the WW decay channel with leptonic final states*, *JHEP* **1401** (2014) 096, [`arXiv:1312.1129`].

[96] CMS Collaboration, *Study of the Mass and Spin-Parity of the Higgs Boson Candidate Via Its Decays to Z Boson Pairs*, *Phys.Rev.Lett.* **110** (2013) 081803, [`arXiv:1212.6639`].

[97] ATLAS Collaboration, *The ATLAS Experiment at the CERN Large Hadron Collider*, *JINST* **3** (2008) S08003.

[98] L. Evans and P. Bryant, *LHC Machine*, *JINST* **3** (2008) S08001.

[99] Wikipedia, *Map of the CERN accelerator complex*, webpage. `http://en.wikipedia.org/wiki/File:Cern-accelerator-complex.svg`, accessed May-2014.

[100] CMS Collaboration, *The CMS experiment at the CERN LHC*, *JINST* **3** (2008) S08004.

[101] ALICE Collaboration, *The ALICE experiment at the CERN LHC*, *JINST* **3** (2008) S08002.

[102] LHCb Collaboration, *LHCb Technical Design Report: Reoptimized Detector Design and Performance*, CERN-LHCC-2003-030. `http://cds.cern.ch/record/630827`.

[103] LHCf Collaboration, *The LHCf detector at the CERN Large Hadron Collider*, *JINST* **3** (2008) S08006.

[104] TOTEM Collaboration, *The TOTEM experiment at the CERN Large Hadron Collider*, *JINST* **3** (2008) S08007.

[105] MoEDAL Collaboration, *Technical Design Report of the MoEDAL Experiment*, CERN-LHCC-2009-006. `http://cds.cern.ch/record/1181486`.

[106] ATLAS Collaboration, *ATLAS Detector and Physics Performance: Technical Design Report*, CERN-LHCC-99-014. `http://cds.cern.ch/record/391176`.

[107] ATLAS Collaboration, *Electron efficiency measurements with the ATLAS detector using the 2012 LHC proton-proton collision data*, ATLAS-CONF-2014-032.

[108] ATLAS Collaboration, *A study of the material in the ATLAS inner detector using secondary hadronic interactions*, *JINST* **7** (2012) P01013, [`arXiv:1110.6191`].

[109] ATLAS Collaboration, *Improved luminosity determination in pp collisions at $\sqrt{s} = 7$ TeV using the ATLAS detector at the LHC*, *Eur.Phys.J.* **C73** (2013) 2518, [`arXiv:1302.4393`].

[110] R. Achenbach et al., *The ATLAS Level-1 calorimeter trigger*, *JINST* **3** (2008) P03001.

[111] R. Hauser, *The ATLAS Data Acquisition and High Level Trigger Systems: Experience and Upgrade Plans*, ATL-DAQ-PROC-2012-073. `http://cds.cern.ch/record/1497132`.

[112] ATLAS Collaboration, *ATLAS Twiki: Luminosity Public Results*, webpage. `http://twiki.cern.ch/twiki/bin/view/AtlasPublic/LuminosityPublicResults`, accessed 20-Februray-2014.

[113] T. Cornelissen, M. Elsing, S. Fleischmann, W. Liebig, E. Moyse, and A. Salzburger, *Concepts, Design and Implementation of the ATLAS New Tracking (NEWT)*, ATL-SOFT-PUB-2007-007. `http://cds.cern.ch/record/1020106`.

[114] ATLAS Collaboration, *Performance of primary vertex reconstruction in proton-proton collisions at $\sqrt{s} = 7$ TeV in the ATLAS experiment*, ATLAS-CONF-2010-069. `http://cds.cern.ch/record/1281344`.

[115] ATLAS Collaboration, *Performance of the ATLAS Inner Detector Track and Vertex Reconstruction in the High Pile-Up LHC Environment*, ATLAS-CONF-2012-042. `http://cds.cern.ch/record/1435196`.

[116] W. Lampl, S. Laplace, D. Lelas, P. Loch, H. Ma, S. Menke, S. Rajagopalan, D. Rousseau, S. Snyder, and G. Unal, *Calorimeter clustering algorithms: Description and performance*, ATL-LARG-PUB-2008-002. `http://cdsweb.cern.ch/record/1099735`.

[117] T. Barillari et al., *Local Hadronic Calibration*, ATL-LARG-PUB-2009-001-2. ATL-COM-LARG-2008-006.

[118] ATLAS Collaboration, *Jet energy measurement with the ATLAS detector in proton-proton collisions at $\sqrt{s} = 7$ TeV*, *Eur.Phys.J.* **C73** (2013) 2304, [`arXiv:1112.6426`].

[119] M. Cacciari, G. P. Salam, and G. Soyez, *The Anti-k_t jet clustering algorithm*, *JHEP* **0804** (2008) 063, [`arXiv:0802.1189`].

[120] M. Cacciari, G. P. Salam, and G. Soyez, *FastJet user manual*, *Eur. Phys. J.* **C72** (2012) 1896, [`arXiv:1111.6097`].

[121] G. P. Salam, *Towards Jetography*, *Eur.Phys.J.* **C67** (2010) 637–686, [`arXiv:0906.1833`].

[122] ATLAS Collaboration, *Pile-up subtraction and suppression for jets in ATLAS*, ATLAS-CONF-2013-083.

[123] ATLAS Collaboration, *Selection of jets produced in proton-proton collisions with the ATLAS detector using 2011 data*, ATLAS-CONF-2012-020. `http://cds.cern.ch/record/1430034`.

[124] ATLAS Collaboration, *Measurement of inclusive jet and dijet production in pp collisions at $\sqrt{s} = 7$ TeV using the ATLAS detector*, *Phys.Rev.* **D86** (2012) 014022, [`arXiv:1112.6297`].

[125] ATLAS Collaboration, *Jet energy scale and its systematic uncertainty in proton-proton collisions at $\sqrt{s} = 7$ TeV with ATLAS 2011 data*, ATLAS-CONF-2013-004.

[126] ATLAS Collaboration, *Single hadron response measurement and calorimeter jet energy scale uncertainty with the ATLAS detector at the LHC*, *Eur.Phys.J.* **C73** (2013) 2305, [`arXiv:1203.1302`].

[127] ATLAS Collaboration, *Jet energy resolution in proton-proton collisions at $\sqrt{s} = 7$ TeV recorded in 2010 with the ATLAS detector*, *Eur.Phys.J.* **C73** (2013) 2306, [`arXiv:1210.6210`].

[128] ATLAS Collaboration, *ATLAS Twiki: Public Results*, webpage. `http://twiki.cern.ch/twiki/bin/view/AtlasPublic/JetEtmissPublicResults`, accessed September-2014.

[129] ATLAS Collaboration, *Commissioning of the ATLAS high-performance b-tagging algorithms in the 7 TeV collision data*, ATLAS-CONF-2011-102. `http://cds.cern.ch/record/1369219`.

[130] ATLAS Collaboration, *Calibration of b-tagging using dileptonic top pair events in a combinatorial likelihood approach with the ATLAS experiment*, ATLAS-CONF-2014-004.

[131] ATLAS Collaboration, *Measurement of the b-tag Efficiency in a Sample of Jets Containing Muons with 5 fb^{-1} of Data from the ATLAS Detector*, ATLAS-CONF-2012-043. `http://cds.cern.ch/record/1435197`.

[132] ATLAS Collaboration, *Calibration of the performance of b-tagging for c and light-flavour jets in the 2012 ATLAS data*, ATLAS-CONF-2014-046.

[133] ATLAS Collaboration, *ATLAS Twiki: Public Results*, webpage. `http://twiki.cern.ch/twiki/bin/view/AtlasPublic`, accessed September-2014.

[134] ATLAS Collaboration, *Improved electron reconstruction in ATLAS using the Gaussian Sum Filter-based model for bremsstrahlung*, ATLAS-CONF-2012-047.

[135] ATLAS Collaboration, *Electron reconstruction and identification efficiency measurements with the ATLAS detector using the 2011 LHC proton-proton collision data*, `arXiv:1404.2240`.

[136] ATLAS Collaboration, *Electron performance measurements with the ATLAS detector using the 2010 LHC proton-proton collision data*, *Eur. Phys. J.* **C72** (2012) 1909, [`arXiv:1110.3174`].

[137] ATLAS Collaboration, *Performance of the ATLAS Trigger System in 2010*, *Eur.Phys.J.* **C72** (2012) 1849, [`arXiv:1110.1530`].

[138] ATLAS Collaboration, *Performance of the ATLAS muon trigger in 2011*, ATLAS-CONF-2012-099.

[139] ATLAS Collaboration, *Expected Performance of the ATLAS Experiment - Detector, Trigger and Physics*, `arXiv:0901.0512`.

[140] ATLAS Collaboration, *Preliminary results on the muon reconstruction efficiency, momentum resolution, and momentum scale in ATLAS 2012 pp collision data*, ATLAS-CONF-2013-088.

[141] ATLAS Collaboration, *Muon Momentum Resolution in First Pass Reconstruction of pp Collision Data Recorded by ATLAS in 2010*, ATLAS-CONF-2011-046.

[142] ATLAS Collaboration, *Identification and energy calibration of hadronically decaying tau leptons with the ATLAS experiment in pp collisions at $\sqrt{s} = 8$ TeV*, `arXiv:1412.7086`.

[143] ATLAS Collaboration, *Identification of the Hadronic Decays of Tau Leptons in 2012 Data with the ATLAS Detector*, ATLAS-CONF-2013-064.

[144] ATLAS Collaboration, *Performance of the Reconstruction and Identification of Hadronic Tau Decays in ATLAS with 2011 Data*, ATLAS-CONF-2012-142. `http://cds.cern.ch/record/1485531`.

[145] ATLAS Collaboration, *Determination of the tau energy scale and the associated systematic uncertainty in proton-proton collisions at $\sqrt{s} = 8$ TeV with the ATLAS detector at the LHC in 2012*, ATLAS-CONF-2013-044.

[146] ATLAS Collaboration, *Determination of the tau energy scale and the associated systematic uncertainty in proton-proton collisions at $\sqrt{s} = 7$ TeV with the ATLAS detector at the LHC in 2011*, ATLAS-CONF-2012-054.

[147] ATLAS Collaboration, *Performance of Missing Transverse Momentum Reconstruction in Proton-Proton Collisions at 7 TeV with ATLAS*, *Eur. Phys. J.* **C72** (2012) 1844, [`arXiv:1108.5602`].

[148] ATLAS Collaboration, *Performance of Missing Transverse Momentum Reconstruction in ATLAS studied in Proton-Proton Collisions recorded in 2012 at 8 TeV*, ATLAS-CONF-2013-082.

[149] ATLAS Collaboration, *Performance of Missing Transverse Momentum Reconstruction in ATLAS with 2011 Proton-Proton Collisions at* $\sqrt{s} = 7$ *TeV*, ATLAS-CONF-2012-101.

[150] ATLAS Collaboration, *Pile-up Suppression in Missing Transverse Momentum Reconstruction in the ATLAS Experiment in Proton-Proton Collisions at* $\sqrt{s} = 8$ *TeV*, ATLAS-CONF-2014-019.

[151] ATLAS Collaboration, *Reconstruction, Energy Calibration, and Identification of Hadronically Decaying Tau Leptons*, ATLAS-CONF-2011-077.

[152] G. Folger and J. Wellisch, *String parton models in GEANT4*, *eConf* **C0303241** (2003) MOMT007, [`nucl-th/0306007`].

[153] H. Bertini, *Intranuclear-Cascade Calculation of the Secondary Nucleon Spectra from Nucleon-Nucleus Interactions in the Energy Range 340 to 2900 MeV and Comparisons with Experiment*, *Phys. Rev.* **188** (1969) 1711–1730.

[154] M. Blann, B. Berman, and T. Komoto, *Precompound Model Analysis of Photonuclear Reactions*, *Phys. Rev.* **C28** (1983) 2286–2298.

[155] B. Andersson, G. Gustafson, and B. Nilsson-Almqvist, *A Model for Low* p_T *Hadronic Reactions, with Generalizations to Hadron-Nucleus and Nucleus-Nucleus Collisions*, *Nucl. Phys.* **B281** (1987) 289.

[156] ATLAS Collaboration, *ATLAS Calorimeter Response to Single Isolated Hadrons and Estimation of the Calorimeter Jet Scale Uncertainty*, ATLAS-CONF-2011-028.

[157] ATLAS Collaboration, *ATLAS Calorimeter Response to Single Isolated Hadrons and Estimation of the Calorimeter Jet Scale Uncertainty*, ATLAS-CONF-2010-052.

[158] ATLAS Collaboration, *Jet energy scale and its systematic uncertainty in proton-proton collisions at* $\sqrt{s} = 7$ *TeV in ATLAS 2010 data*, ATLAS-CONF-2011-032.

[159] ATLAS Collaboration, *Summary of ATLAS PYTHIA 8 tunes*, ATL-PHYS-PUB-2012-003. `http://cdsweb.cern.ch/record/1474107`.

[160] E. Khramov et al., *Study of the Response of the Hadronic Barrel Calorimeter in the ATLAS Combined Test-beam to Pions of Energies from 20 to 350 GeV for Beam Impact Points from 0.2 to 0.65*, ATL-TILECAL-PUB-2009-007.

[161] A. Elagin et al., *A new mass reconstruction technique for resonances decaying to* $\tau\tau$, *Nucl. Instrum. Meth.* **A654** (2011) 481–489, [`arXiv:1012.4686`].

[162] ATLAS Collaboration, *Search for neutral MSSM Higgs bosons decaying to $\tau^+\tau^-$ pairs in proton-proton collisions at $\sqrt{s} = 7$ TeV with the ATLAS detector*, ATLAS-CONF-2011-132. `http://cds.cern.ch/record/1383835`.

[163] S. Alioli, P. Nason, C. Oleari, and E. Re, *NLO Higgs boson production via gluon fusion matched with shower in POWHEG*, *JHEP* **0904** (2009) 002, [`arXiv:0812.0578`].

[164] D. de Florian, G. Ferrera, M. Grazzini, and D. Tommasini, *Higgs boson production at the LHC: transverse momentum resummation effects in the $H \to \gamma\gamma$, $H \to WW^* \to \ell\nu\ell\nu$ and $H \to ZZ^* \to \ell\ell\ell\ell$ decay modes*, *JHEP* **1206** (2012) 132, [`arXiv:1203.6321`].

[165] M. Grazzini and H. Sargsyan, *Heavy-quark mass effects in Higgs boson production at the LHC*, *JHEP* **1309** (2013) 129, [`arXiv:1306.4581`].

[166] J. M. Campbell et al., *NLO Higgs Boson Production Plus One and Two Jets Using the POWHEG BOX, MadGraph4 and MCFM*, *JHEP* **1207** (2012) 092, [`arXiv:1202.5475`].

[167] P. Nason and C. Oleari, *NLO Higgs boson production via vector-boson fusion matched with shower in POWHEG*, *JHEP* **1002** (2010) 037, [`arXiv:0911.5299`].

[168] M. Ciccolini, A. Denner, and S. Dittmaier, *Strong and electroweak corrections to the production of Higgs + 2 jets via weak interactions at the LHC*, *Phys.Rev.Lett.* **99** (2007) 161803, [`arXiv:0707.0381`].

[169] M. Ciccolini, A. Denner, and S. Dittmaier, *Electroweak and QCD corrections to Higgs production via vector-boson fusion at the LHC*, *Phys.Rev.* **D77** (2008) 013002, [`arXiv:0710.4749`].

[170] A. Denner, S. Dittmaier, S. Kallweit, and A. Muck, *Electroweak corrections to Higgs-strahlung off W/Z bosons at the Tevatron and the LHC with HAWK*, *JHEP* **1203** (2012) 075, [`arXiv:1112.5142`].

[171] J. M. Butterworth, J. R. Forshaw, and M. H. Seymour, *Multiparton interactions in photoproduction at HERA*, *Z. Phys.* **C72** (1996) 637–646, [`hep-ph/9601371`].

[172] J. Alwall et al., *Comparative study of various algorithms for the merging of parton showers and matrix elements in hadronic collisions*, *Eur. Phys. J.* **C53** (2008) 473–500, [`arXiv:0706.2569`].

[173] K. Melnikov and F. Petriello, *Electroweak gauge boson production at hadron colliders through $O(\alpha_s^2)$*, *Phys. Rev. D* **74** (2006) 114017, [`0609070`].

[174] K. Melnikov and F. Petriello, *The W boson production cross section at the LHC through $O(\alpha_s^2)$*, *Phys. Rev. Lett.* **96** (2006) 231803, [`0603182`].

[175] S. Catani, L. Cieri, G. Ferrera, D. de Florian, and M. Grazzini, *Vector boson production at hadron colliders: A fully exclusive QCD calculation at NNLO*, *Phys.Rev.Lett.* **103** (2009) 082001, [`arXiv:0903.2120`].

[176] R. Gavin, Y. Li, F. Petriello, and S. Quackenbush, *FEWZ 2.0: A code for hadronic Z production at next-to-next-to-leading order*, *Comput.Phys.Commun.* **182** (2011) 2388–2403, [`arXiv:1011.3540`].

[177] M. Aliev, H. Lacker, U. Langenfeld, S. Moch, P. Uwer, et al., *HATHOR: HAdronic Top and Heavy quarks crOss section calculatoR*, *Comput.Phys.Commun.* **182** (2011) 1034–1046, [`arXiv:1007.1327`].

[178] M. Czakon, P. Fiedler, and A. Mitov, *The total top quark pair production cross-section at hadron colliders through* $O(\alpha_s^4)$, `arXiv:1303.6254`.

[179] M. Czakon and A. Mitov, *NNLO corrections to top pair production at hadron colliders: The quark-gluon reaction*, *JHEP* **1301** (2013) 080, [`arXiv:1210.6832`].

[180] M. Czakon and A. Mitov, *NNLO corrections to top-pair production at hadron colliders: The all-fermionic scattering channels*, *JHEP* **1212** (2012) 054, [`arXiv:1207.0236`].

[181] P. Baernreuther, M. Czakon, and A. Mitov, *Percent Level Precision Physics at the Tevatron: First Genuine NNLO QCD Corrections to* $q\bar{q} \to t\bar{t} + X$, *Phys.Rev.Lett.* **109** (2012) 132001, [`arXiv:1204.5201`].

[182] M. Cacciari, M. Czakon, M. Mangano, A. Mitov, and P. Nason, *Top-pair production at hadron colliders with next-to-next-to-leading logarithmic soft-gluon resummation*, *Phys.Lett.* **B710** (2012) 612–622, [`arXiv:1111.5869`].

[183] M. Czakon and A. Mitov, *Top++: A Program for the Calculation of the Top-Pair Cross-Section at Hadron Colliders*, `arXiv:1112.5675`.

[184] B. P. Kersevan and E. Richter-Wąs, *The Monte Carlo event generator AcerMC versions 2.0 to 3.8 with interfaces to PYTHIA 6.4, HERWIG 6.5 and ARIADNE 4.1*, *Comput. Phys. Commun.* **184** (2013) 919–985, [`hep-ph/0405247`].

[185] B. P. Kersevan and I. Hinchliffe, *A consistent prescription for the production involving massive quarks in hadron collisions*, *JHEP* **0609** (2006) 033, [`hep-ph/0603068`].

[186] N. Kidonakis, *Next-to-next-to-leading-order collinear and soft gluon corrections for t-channel single top quark production*, *Phys.Rev.* **D83** (2011) 091503, [`arXiv:1103.2792`].

[187] J. M. Campbell, R. Frederix, F. Maltoni, and F. Tramontano, *Next-to-Leading-Order Predictions for t-Channel Single-Top Production at Hadron Colliders*, *Phys.Rev.Lett.* **102** (2009) 182003, [`arXiv:0903.0005`].

[188] N. Kidonakis, *Two-loop soft anomalous dimensions for single top quark associated production with a W^- or H^-*, *Phys.Rev.* **D82** (2010) 054018, [`arXiv:1005.4451`].

[189] N. Kidonakis, *NNLL resummation for s-channel single top quark production*, *Phys.Rev.* **D81** (2010) 054028, [`arXiv:1001.5034`].

[190] T. Binoth, M. Ciccolini, N. Kauer, and M. Kramer, *Gluon-induced W-boson pair production at the LHC*, *JHEP* **0612** (2006) 046, [`hep-ph/0611170`].

[191] J. M. Campbell, R. K. Ellis, and D. L. Rainwater, *Next-to-leading order QCD predictions for $W + 2$ jet and $Z + 2$ jet production at the CERN LHC*, *Phys.Rev.* **D68** (2003) 094021, [`hep-ph/0308195`].

[192] N. Möser et al., *Estimation of $Z \to \tau\tau$ Background in VBF $H \to \tau\tau$ Searches from $Z \to \mu\mu$ Data using an Embedding Technique*, ATL-COM-PHYS-2009-446. `http://cds.cern.ch/record/1201000`.

[193] E. Barberio, B. van Eijk, and Z. Wąs, *PHOTOS - a universal Monte Carlo for QED radiative corrections in decays*, *Comput. Phys. Commun.* **66** (1991) 115–128.

[194] ATLAS Collaboration, *Search for the Standard Model Higgs boson in $H \to \tau^+\tau^-$ decays in proton-proton collisions with the ATLAS detector*, ATLAS-CONF-2012-160.

[195] ATLAS Collaboration, *Search for the Standard Model Higgs boson in the $H \to \tau^+\tau^-$ decay mode in $\sqrt{s} = 7$ TeV pp collisions with ATLAS*, *JHEP* **1209** (2012) 070, [`arXiv:1206.5971`].

[196] ATLAS Collaboration, *Evidence for Higgs boson Yukawa couplings in the $H \to \tau\tau$ decay mode with the ATLAS detector*, ATLAS-CONF-2014-061.

[197] J. Friedman, T. Hastie, and R. Tibshirani, *The Elements of Statistical Learning*, Springer, 2009.

[198] A. Hocker et al., *TMVA - Toolkit for Multivariate Data Analysis*, *PoS* **ACAT** (2007) 040, [`physics/0703039`].

[199] Y. Freund and R. E. Schapire, *A Decision-Theoretic Generalization of On-Line Learning and an Application to Boosting*, *J. Comput. Syst. Sci.* **55** (1997) no. 1 119–139.

[200] J. H. Friedman, *Stochastic gradient boosting*, *Comput.Stat.Data Anal.* **38** (2002) 367–378.

[201] I. Stewart and F. Tackmann, *Theory uncertainties for Higgs and other searches using jet bins*, *Phys. Rev. D.* **85** (2012) , [`arXiv:1107.2117`].

[202] R. J. Barlow, *Extended maximum likelihood*, *Nucl. Instrum. Meth.* **A297** (1990) 496–506.

[203] F. James and M. Roos, *Minuit: A System for Function Minimization and Analysis of the Parameter Errors and Correlations*, *Comput.Phys.Commun.* **10** (1975) 343–367.

[204] W. Metzger, *Statistical Methods in Data Analysis*, Lecture Notes (2002). `http://www.hef.ru.nl/~wes/stat_course/statist_2002.pdf`.

[205] K. Cranmer, G. Lewis, L. Moneta, A. Shibata, and W. Verkerke, *HistFactory: A tool for creating statistical models for use with RooFit and RooStats*, CERN-OPEN-2012-016. `http://cds.cern.ch/record/1456844`.

[206] W. Verkerke and D. P. Kirkby, *The RooFit toolkit for data modeling*, *eConf* **C0303241** (2003) MOLT007, [`physics/0306116`].

[207] L. Moneta, K. Belasco, K. Cranmer, S. Kreiss, A. Lazzaro, D. Piparo, G. Schott, W. Verkerke, and M. Wolf, *The RooStats Project*, *PoS* **ACAT2010** (2010) 057, [`arXiv:1009.1003`].

[208] J. Friedman, *Data Analysis Techniques for High Energy Particle Physics*, Proceedings: 1974 CERN School of Computing, Godoysund, Norway (1974).

[209] R. Brun and F. Rademakers, *ROOT: An object oriented data analysis framework*, *Nucl.Instrum.Meth.* **A389** (1997) 81–86.

[210] J. Neyman and E. S. Pearson, *On the problem of the most efficient tests of statistical hypotheses*, *Phil. Trans. R. Soc. Lond.* **A231** (1933) 289–337.

[211] G. Cowan, K. Cranmer, E. Gross, and O. Vitells, *Asymptotic formulae for likelihood-based tests of new physics*, *Eur. Phys. J.* **C71** (2011) 1554, [`arXiv:1007.1727`].

[212] A. L. Read, *Presentation of search results: The CL(s) technique*, *J. Phys.* **G28** (2002) 2693–2704.

[213] B. Efron and C. Stein, *The Jackknife Estimate of Variance*, *The Annals of Statistics* **9** (1981) no. 3 586–596.

[214] G. Bohm and G. Zech, *Introduction to statistics and data analysis for physicists*, Verlag Deutsches Elektronen-Synchrotron, Hamburg, ISBN 978-3-935702-41-6, 2010.

[215] ATLAS Collaboration, *Search for the $b\bar{b}$ decay of the Standard Model Higgs boson in associated $(W/Z)H$ production with the ATLAS detector*, `arXiv:1409.6212`.

[216] CMS Collaboration, *Evidence for the direct decay of the 125 GeV Higgs boson to fermions*, *Nature Phys.* **10** (2014) , [`arXiv:1401.6527`].

[217] CMS Collaboration, *Search for the standard model Higgs boson produced in association with a W or a Z boson and decaying to bottom quarks*, *Phys.Rev.* **D89** (2014) 012003, [`arXiv:1310.3687`].

[218] CMS Collaboration, *Evidence for the 125 GeV Higgs boson decaying to a pair of τ leptons*, *JHEP* **1405** (2014) 104, [`arXiv:1401.5041`].

[219] ATLAS Collaboration, *Updated coupling measurements of the Higgs boson with the ATLAS detector using up to 25 fb^{-1} of proton-proton collision data*, ATLAS-CONF-2014-009.

[220] ATLAS Collaboration, *Constraints on New Phenomena via Higgs Coupling Measurements with the ATLAS Detector*, ATLAS-CONF-2014-010.

[221] B. Grzadkowski, M. Iskrzynski, M. Misiak, and J. Rosiek, *Dimension-Six Terms in the Standard Model Lagrangian*, *JHEP* **1010** (2010) 085, [`arXiv:1008.4884`].

[222] W. Buchmuller and D. Wyler, *Effective Lagrangian Analysis of New Interactions and Flavor Conservation*, *Nucl.Phys.* **B268** (1986) 621–653.

[223] ATLAS Collaboration, *Fiducial and differential cross sections of Higgs boson production measured in the four-lepton decay channel in pp collisions at $\sqrt{s}$=8 TeV with the ATLAS detector*, `arXiv:1408.3226`.

[224] ATLAS Collaboration, *Measurements of fiducial and differential cross sections for Higgs boson production in the diphoton decay channel at $\sqrt{s} = 8$ TeV with ATLAS*, `arXiv:1407.4222`.

Acknowledgements

The submission of this thesis marks the temporary end of three years of interesting and challenging work within the ATLAS collaboration, and is therefore the right time to express my thanks to people who helped me during this time.

Thank you Prof. Karl Jakobs for your supervision and support and especially for your own dedication to this analysis. I enjoyed the opportunity to participate in this ambitious experimental project and to work on a topic which received much attention from the high-energy physics community in the recent years. The discovery of the Higgs boson in 2012 and the eagerly awaited results of following analyses in the months and years thereafter were remarkable events I will keep in good memory. The very same holds for Romain Madar, many thanks for your support and advise which helped me in numerous situations.

Within the Higgs working group I am especially grateful for the excellent collaboration with Thomas Schwindt, Michel Trottier-McDonald and Alex Tuna. The discussions and hands on work with you was what made the time enjoyable. Many thanks also to you Elias Coniavitis, Koji Nakamura, Lidia Dell'Asta, Katy Grimm, Sasha Pranko and Stefania Xella. It was great fun to work with and to learn from you. I was lucky to have Stan Lai, Iacopo Vivarelli and Christian Weiser at the institute. The discussions we had and your help especially during the first months were a great support. I also would like to thank the whole group in Freiburg and especially Felix, Julian, Helge, Philip, Susanne, Karsten, Sascha, George, Kristin, Mirjam, Hannah, Claudia, Francesca and Liv for the nice atmosphere in and around the offices and for bearing with me in endless complaints about this and that. A big thanks also to Christina Skorek for magically making basically everything work. And then there are of course many people outside of the physics community who have a great share in making the last years a success, and I will for sure take the chance to thank you in person. Still I want to thank you Jenny also at this place for nothing less than being here.